Durham E-Theses

Domain wall behaviour in ferromagnetic nanowires with interfacial and geometrical structuring

BURN, DAVID,MICHAEL

How to cite:

BURN, DAVID,MICHAEL (2013) *Domain wall behaviour in ferromagnetic nanowires with interfacial and geometrical structuring*, Durham theses, Durham University. Available at Durham E-Theses Online: http://etheses.dur.ac.uk/7732/

Use policy

The full-text may be used and/or reproduced, and given to third parties in any format or medium, without prior permission or charge, for personal research or study, educational, or not-for-profit purposes provided that:

- a full bibliographic reference is made to the original source
- a link is made to the metadata record in Durham E-Theses
- the full-text is not changed in any way

The full-text must not be sold in any format or medium without the formal permission of the copyright holders.

Please consult the full Durham E-Theses policy for further details.

Domain wall behaviour in ferromagnetic nanowires with interfacial and geometrical structuring

David Michael Burn

A thesis submitted in partial fulfilment of the requirements
for the degree of Doctor of Philosophy

Durham University, 2013

Abstract

The magnetic behaviour in nanoscale structures is of great interest for the fundamental understanding of magnetisation processes and also has importance for wide ranging technological applications. This thesis examines mechanisms for the enhanced control of domain walls in these structures via focussed ion beam modifications to magnetic nanowires and through the inclusion of periodic geometrical modifications to the nanowires geometry.

A detailed investigation into the effect of focussed ion beam irradiation on the structure of NiFe/Au bilayers was performed through x-ray reflectivity and fluorescence techniques. This analysis revealed the development of interfacial intermixing with low dose irradiation. This is associated with complex changes of the magnetic behaviour including a rapid decrease, followed by a recovery of the saturation magnetisation with low dose irradiation. This behaviour is attributed to changes in the local environment of the atoms at the interface; resulting in modifications to the magnetic moment on Ni and Fe. The development of an induced moment on Au and a change in the spin-orbit interaction is also suggested.

Localised control of the magnetic properties in nanowires demonstrates the ability to manipulate domain walls in these structures. Here, irradiated regions provide pinning sites where the width and dose of the irradiated region give control over the pinning potential.

The inclusion edge modulation to nanowires geometry provides additional control over their magnetic behaviour. The direct magnetisation reversal field of these structures is explained by an analytical model based on the torque on the spins following the modulated wire geometry. This model is scalable for different modulation parameters and combines with the effect of localised regions of orthogonal anisotropy along the wire; explaining the reversal behaviour over the entire parameter space.

Domain wall mediated reversal in modulated wires was also investigated in these structures. The inclusion of modulation shows an improvement in dynamic properties by the suppression of Walker breakdown. This is due to the relationship between geometrical modulations and the periodicity of micromagnetic domain wall structural changes during the Walker breakdown process. The combination of this work shows a route to the optimisation of the dynamic properties whilst minimising the detrimental increase in the de-pinning field from the modulation.

Declaration

Unless explicitly stated otherwise, the work presented in this thesis is solely that of the author and has not been submitted for examination for any other degree at any University.

Synchrotron experiments were coordinated by the author but involve the work of several team members. The x-ray reflectivity and x-ray fluorescence results presented in chapter 6 were performed at the XMaS beamline at the ESRF along with Dr. David Eastwood, Dr. Del Atkinson, Dr. Laurence Bouchenoire and Dr. Tom Hase. Initial analysis of the reflectivity data was performed by Dr. Erhan Arac which has been repeated and extended by the author in this work.

The x-ray magnetic circular dichroism measurements presented in chapter 7 were performed at the ID1011 beamline at MAXLAB in Lund along with Alex Baker, Dr. Del Atkinson, Dr. Gunnar Öhrwell, Dr. Matts Björck and Dr. Tom Hase. The preparation and irradiation of these samples along with the analysis of the data was performed by the author.

Analysis of the induced moment in Au presented in chapter 7 was performed at the XMaS beamline at the ESRF along with Dr. Del Atkinson, Dr. Jenny King, Dr. Laurence Bouchenoire, Richard Rowan-Robinson and Dr. Tom Hase. For this investigation the samples were prepared by Dr. Jenny King and irradiation was performed jointly by the author and Dr. Jenny King. The analysis of the results was performed by the author.

The fabrication of the structures and measurements of the results shown in figure 9.20 in chapter 9 were performed by Dr. Erhan Arac.

Acknowledgements

There are many people who I would like to thank for their help, support, encouragement and friendship during my PhD studies. Firstly to Dr. Del Atkinson for his supervision and guidance which has helped me throughout the whole of this project. I would also like to thank Dr. Erhan Arac with whom I have worked closely and had many fruitful discussions.

X-ray measurements at synchrotron sources make up a large proportion of this work. These would not have been possible without the many support staff involved in running these laboratories. I would like to thank Dr. Laurence Bouchenoire, Dr. Matts Björck and Dr. Gunnar Öhrwell for their assistance during these experiments. Particular thanks go to Dr. Tom Hase who has been very helpful during the experiments and for his assistance with the lengthy analysis and interpretation of the data.

I would also like to thank Dr. Jenny King, Dr. Helen Cramman and Dr. Ian Terry for their assistance and training on the various fabrication and characterisation equipment used in this investigation. Thanks also go to Leon Bowen for his support and training on the Dual Beam FIB system and to John Dobson for his technical support keeping this equipment working.

I would also like to thank the other people with whom I have worked alongside in room 12: Dr. Lara Bogart, Dr. David Eastwood, Mussab Sultan, Dr. Rachael Houchin, Alex Webb, Sarah Dempsey, Mustafa Tokac and Richard Rowan-Robinson. I have had many useful discussions with all of you.

Finally my thanks go to friends and family who have given me support and encouragement over the last few year during this PhD.

List of publications

Suppression of Walker breakdown in magnetic domain wall propagation through structural
control of spin wave emission

D.M. Burn and D. Atkinson

Applied Physics Letters **102**, 242414 (2013)

Study of focused-ion-beam induced structural and compositional modifications in nanoscale
bilayer systems by combined grazing incidence x-ray reflectivity and fluorescence

E. Arac, D.M. Burn, D.S. Eastwood, T.P.A. Hase and D. Atkinson

Journal of Applied Physics **111**, 044324 (2012)

FIB induced intermixing in nanoscale bilayers studied by x-ray reflectivity

E. Arac, D.M. Burn, T.P.A. Hase and D. Atkinson

XMaS Newsletter, **10** (2011)

Magnetization switching and domain wall propagation behaviour in edge modulated
ferromagnetic nanowire structures

D.M. Burn, E. Arac and D. Atkinson

Under review

Complex magnetic moment modification in NiFe/Au bilayers by interfacial intermixing

D.M. Burn, T.P.A. Hase, E. Arac and D. Atkinson

In preparation

Domain wall pinning in locally irradiated NiFe/Au nanowires

D.M. Burn and D. Atkinson

In preparation

Contents

Chapter 1

Introduction

1.1 Background

Magnetic domains and domain walls give rise to many of the magnetic properties that are observed in ferromagnetic materials. They form the basis for the domain wall nucleation and propagation magnetisation reversal process, which, along with coherent rotation processes, account for the majority of the ferromagnetic behaviour in these materials. Due to their important role in the behaviour of these magnetic systems, magnetic domains and domain walls have been the subject of much scientific investigation and are crucially important for understanding fundamental magnetisation processes.

In many material systems the observed behaviour results from a number of combined domain wall processes. However, the fundamental physical processes that govern the behaviour of magnetic domains and domain walls are best studied where the complexity of the system is reduced to the study of single domain walls. This has been made possible by developments in lithographic patterning techniques which allow control over material geometries on a scale where the behaviour of individual domain walls can be investigated. Coupled with the recent advances in computing power that allow for micromagnetic simulations of domain wall structures, significant contributions to the understanding of the magnetic domain wall processes have been made in the past decade or so.

Magnetisation reversal by domain wall nucleation and propagation has been studied with individual domain walls, allowing the detailed analysis of both the nucleation and propagation components.[1] Here, the propagation is driven by an applied magnetic field, which is the most common driving mechanism. Other techniques include spin transfer torque (STT)[2]

and even spin wave induced motion[3] has been demonstrated. This research has enabled the manipulation of domain walls with magnetic fields to progress to a stage where domain walls can be moved along nanowires,[1] around corners[4,5] and directed along certain paths at junctions.[6,7] The inclusion of constrictions[8–10] or notches[2,11] in a wire geometry leads to a modification in the local energy landscape introducing a pinning potential related to the constriction or notch geometry.

These studies have provided understanding of the micromagnetic spin structure of the domain walls which adopt several different structures depending on the nanowire geometry.[12] The design of asymmetrical notches[13,14] allows for the design of energy potential landscapes, which present different pinning potentials to domain walls based on their structure and propagation direction where their combination has demonstrated ratchet-like behaviour.[15–17]

There has been a large amount of work on the static properties of domain walls but now research is moving towards developing a greater understanding of the more complex and harder to measure dynamic properties of domain walls in nanowires. These studies consist of measurements of domain wall velocity along the nanowires.[18,19] This has enabled measurements of the Walker breakdown[20,21] effect, which limits domain wall mobility due to spin precessional frequency limitations and the associated energy dissipation from the wall during its motion. This breakdown results in a combination of dynamical pinning and structural transformations within the domain wall, resulting in a low time-averaged velocity. The understanding gained about the behaviour of Walker breakdown in nanowires has been used to explain unexpected behaviour occurring in more complex thin film systems.[22]

In addition to the interest in understanding the fundamental physics behind these processes, the manipulation of individual magnetic domain walls has opened many possibilities for potential applications. This has contributed heavily to the interest that has been devoted towards research in this area.

One string of applications is based upon the intrinsic memory effect from the hysteretic properties of magnetic materials. Using domains or domain walls to represent data has led to the development of devices for potential logic[23] and memory[24] applications. These have shown that there is huge potential for technological impact in areas where these spintronic devices have some significant advantages over current technological devices.

Other potential applications arise due to the stray fields produced by a domain wall, which have been identified for their ability to detect[25] and manipulate[6,26–28] magnetic

nanoparticles around magnetic nanowire circuits. Attaching biological or chemical species to the magnetic particles has opened avenues for many areas of research, including drug delivery, nanofabrication, molecular detection, nanofluidics and biomechanics. The stray fields from domain walls have even demonstrated a capability for the manipulation of cold atoms with possible applications in quantum computing.[29]

To realise the devices for these applications requires further work and greater understanding of magnetic domain walls and the relationships between the localised structure of the nanowires in which they are supported. Accordingly, this investigation considers two techniques for the modification of the nanowire properties and studies how these structural modifications lead to changes in the localised magnetic properties of the nanowires. These modifications are then demonstrated as a mechanism to control the behaviour of domain walls within nanowire structures. The first of these techniques is based on geometrical patterning of magnetic material through lithographic techniques, and the second through focussed ion beam irradiation, which allows for localised modification to the magnetic material.

Lithographic techniques are already a common mechanism for the patterning of many devices and are widely used to define geometrical structures for domain wall devices. However, work is still outstanding in the area relating to the interactions between domain walls and localised geometrical structuring. In particular, an understanding of the dynamic properties of domain walls in nanowires is still lacking. For instance, Walker breakdown remains a fundamental problem that ultimately limits potential device operation speeds, and needs to be addressed in order to secure the future success of domain wall based devices.

Additionally, the use of localised ion beam irradiation, in combination with lithographic patterning, provides an elegant method for tailoring the magnetic properties along nanowire structures. Developments in patterning technology through the development of focussed ion beam (FIB) systems allow this magnetic modification technique to be performed on the nanoscale, making this very appropriate for future device fabrication. This FIB irradiation technique is less well established than lithographic patterning so a significant proportion of this thesis is devoted towards the characterisation of the ion beam irradiation on magnetic structures, and gives a detailed understanding of the structural modifications arising from Ga^+ irradiation. A detailed analysis is also performed into the link between the structural modifications and their effect on the magnetic properties within the sample before the ability for the manipulation of domain walls is investigated.

The pioneering work by Chappert[30] demonstrated the local modification of perpendicular magnetic anisotropy (PMA) materials such as Co/Pt could be achieved with low dose ion irradiation. This was performed without significant effect on the surface roughness of the film, which is a desirable characteristic for technological device fabrication. In these multilayer materials, the PMA originates from strong magnetoelastic energy contributions due to symmetry breaking at the sharp interfaces.[31] Upon irradiation, intermixing at the interface releases the stress and reduces this anisotropy contribution. The anisotropy of the film then rotates to be in-plane as the shape anisotropy from the thin film geometry begins to dominate.[32–35] A further increase in dose leads to a ferromagnetic to paramagnetic transition, associated with damage to the sample structure.

Although a large amount of work has been performed on PMA materials, relatively little investigation has looked at the irradiation of materials with in-plane anisotropy, such as permalloy, for which the domain wall processes are well understood. These materials have no strong interfacial anisotropy giving rise to a PMA, so the anisotropy is governed by the shape and lies in the plane of the sample. Upon irradiation these films show modified magnetic properties with ion irradiation giving a decrease in saturation magnetisation for the near-surface region[36] which eventually undergoes a ferromagnetic to paramagnetic transition.[37–40] This is coupled with an increasing coercivity with dose attributed to ion induced damage to the crystal structure, the introduction of scattering defects to the thin-film and the expansion of the lattice parameter from inclusion of large defects.[41–44]

A greater understanding of the irradiation induced modifications to the structure and magnetic properties of permalloy thin films may lead towards improved mechanisms for the control of domain walls in nanowires. The combination of these material modifications with existing geometrical structuring control may ultimately allow for greater control over the properties of domain walls and lead to improvements in the efficiency of field driven, or spin transfer torque (STT) driven domain wall dynamics.[45]

1.2 Aim of this thesis

The aim of this thesis is to develop a deeper understanding of the mechanisms for the control of magnetic domain walls in nanowires through lithographic geometrical patterning and focussed ion beam modifications to the magnetic material.

The focus is on in-plane anisotropy magnetic materials, in particular the NiFe/Au bi-layer system, where the possibility of using FIB irradiation for localised modification of the magnetic material is addressed and the parameter space associated with this ion irradiation has been explored. A detailed structural analysis is presented, identifying the development of an intermixed region at the interfaces as the origin of complex modifications to the magnetic behaviour of the material. Once appropriate irradiation conditions for the control of the magnetic properties were established, the effect of localised irradiation on nanowires is demonstrated as a means of defining artificial domain structures. The effect of these on the domain wall behaviour in the nanowires is then presented.

The study also includes an investigation into the relationship between domain wall structure and lithographically prepared nanowire structures. This aimed to build on previous knowledge about the relationship between domain wall structure and localised nanowire geometrical structuring, in particular with relation to the structural transformations taking place during Walker breakdown.

Further knowledge about the behaviour and mechanisms for the control of domain walls in nanowires will be highly relevant for the design of future spintronic devices. This is important as the optimisation of the speed and reliability of controlled domain wall processes will be key to the success of future technologies.

1.3   Thesis outline

This thesis begins with the introduction of the background and physical theories describing magnetism, how it can be controlled at the nanoscale and techniques for the investigation of these magnetic properties. This leads onto a major discussion of both the structural and magnetic properties of irradiated magnetic material which, alongside lithographic patterning, are used for the control of domain walls in nanoscale structures.

Starting in chapter 2, the physical basis of magnetism relevant to this thesis is introduced. This begins with the atomic origin and leads into a full description of the magnetic properties of materials. This includes details of the complex interplay between different energetic contributions affecting a magnetic system and how these relate to the formation and existence of domain walls in ferromagnetic materials. Sample geometry can have a large effect on the properties of domain walls and the discussion here focusses on the domain wall properties in

nanowire structures in preparation for their discussion later in this thesis.

A theoretical basis for the material structure is given in chapter 3. This introduces the physics behind thin film material structures, methods for their growth and a discussion of defects in a crystal structure. The physical basis of interactions involving high energy ion irradiation of a material is introduced and describes the resulting modifications to the material structure. This section also includes a review of the literature related to modification of the magnetic properties. In addition to this modification to the thin film structure, the techniques used for the geometrical structuring, in the fabrication of structures are also introduced.

This investigation uses a wide range of different techniques for investigating the various structural and magnetic properties of interest. Chapter 4 introduces these techniques and presents the underlying physics giving rise to the particular sensitivity of each technique. Firstly, the scattering of x-rays from the samples gives information on the structural properties of thin film materials due to interference effects from the interfaces. This was combined with compositional analysis through the study of fluorescent x-ray emission from the sample. This leads into the discussion of the interaction of electromagnetic waves with magnetised materials, giving techniques for probing the magnetic properties of these systems.

Chapter 5 contains details of all the experimental procedures used in this investigation, each involving a combination of the fabrication and investigative techniques. This gives the experimental plan that shows how the measurements that are required affect the initial fabrication stages. The combination of several techniques at a time is discussed in relation to obtaining each set of results presented in the later chapters of this thesis. This chapter contains all the specific details necessary to reproduce this work.

The results of the structural and compositional investigation into the effects of Ga^+ irradiation are presented in chapter 6. This includes detailed analysis of the layer thickness and interface width as a function of irradiation dose. This interface width is then further investigated to determine its origins. Fluorescent techniques also show the way in which the elemental depth profiles of the materials change as a function of dose, demonstrating the extent to which the interfacial intermixing is taking place within these samples with elemental specificity.

The modified structure resulting from Ga^+ ion irradiation has an effect on the magnetic properties of the NiFe/Au bilayer films. Chapter 7 reports on the changes in magnetic properties that are found to result from this irradiation. These changes were investigated

using a variety of experimental techniques such as the magneto-optical Kerr effect (MOKE), superconducting quantum interference device (SQUID) and x-ray magnetic circular dichroism (XMCD) measurements to first explore the parameter space associated with ion irradiation and then to explore in more detail the origins of the magnetic changes that occur.

Chapter 8 brings together the knowledge of the irradiation control of the magnetic properties with the techniques already available for nanofabrication. This demonstrates how local modifications to the magnetic material can be introduced to magnetic nanowires to control domain walls in these structures.

Chapter 9 presents analysis of the investigation into magnetisation switching and domain wall propagation in edge modulated nanowires. The matching of Walker breakdown periodic structural transformations with geometrical structural oscillation allowed additional control and gave rise to Walker breakdown suppression in carefully tuned wires.

The thesis concludes with chapter 10 that provides a summary of the main results found in this investigation and their interpretation. It goes on to discuss the possibilities for further measurements that may be the next step towards future technological devices described above. The impact that these results may have on the direction for future spintronic devices using nanoscale magnetic structures is also discussed.

1.4   Definitions and units

In the field of magnetism, two different unit systems are commonly used: SI units and CGS units. A magnetic material which is magnetised can be described by its magnetisation, M, which is a measure of the magnetic moment per unit volume of the material. This magnetisation gives rise to a magnetic induction, or flux density, B. The application of magnetic field described by its field strength, H, also gives a contribution to the magnetic induction. Both of these contributions are related using the equation:[46]

$$B = \mu_0(H + M) \qquad \text{(SI units)} \qquad (1.1)$$

$$B = H + 4\pi M. \qquad \text{(CGS units)} \qquad (1.2)$$

Here, $\mu_0 = 4\pi \times 10^{-7}$ H/m, in the SI system, is the permeability of free space, which is a measure of the ratio, B/H, as measured in a vacuum. This becomes the dimensionless

quantity of unity in the CGS unit system.

The different unit conventions are confusing and in most areas of science and engineering, including many magnetism textbooks, the SI unit system has been adopted. However, in the literature, the CGS unit system is still widely adopted due the the numerical equivalence of the magnetic field strength, H (measured in oersteds) and the magnetic induction, B (measured in gauss).[46] Additionally, the magnetisation contribution to the magnetic induction is $4\pi M$, usually quoted in units of gauss to be numerically equivalent to B and H. Another advantage of this system is the more convenient order of magnitude for these quantities which is generally of the order of 10 - 100 Oe for typical reversal fields in the magnetic materials studied here. Despite this, it is still standard to present equations and relations in SI units.

In this thesis, the SI unit system has been adopted with the exception of magnetic fields which are presented in CGS units. Micromagnetic simulations contained in this thesis are based on the SI unit system and have been converted to CGS for consistency. These units along with the relevant conversion factors between the two systems are given in table 1.1.

In addition to this, when describing atomic magnetism contributions, a Bohr magneton, μ_B, is most appropriate to represent a small quantity of magnetic moment. In SI units it is defined as $\mu_B = \frac{e\hbar}{2m_e}$ where e is the electronic charge, $\hbar$ is the reduced Planck constant and m_e is the mass of an electron.

Quantity	Symbol	SI Unit	CGS Unit	Conversion factor
Magnetic induction	B	tesla (T)	gauss (G)	1 G = 10^{-4} T
Magnetic field strength	H	A/m	oersted (Oe)	1 Oe = $1000/4\pi$ A/m
Magnetisation	M	A/m	emu/cm^3	1 emu/cm^3 = 1000 A/m
Magnetic moment	μ_m	Am^2	emu	1 emu = 10^{-3} Am^2

Table 1.1: Units representing the principal magnetic quantities in both SI and CGS units along with the conversion factors relating the two systems.[47]

Chapter 2

Physical origins of magnetism and its behaviour in nanoscale structures

2.1 Introduction

This chapter introduces and discusses the physical origins of magnetism which give rise to the magnetic properties of materials. In particular, this chapter will focus on the factors affecting the behaviour of ferromagnetic materials discussed in later chapters.

The discussion starts with the origin of atomic magnetic moments and how they arise from electronic structure. This leads to the magnetic properties of materials which are governed by the collective behaviour of many atoms along with interactions that take place between neighbouring atoms and their environment.

In ferromagnetic materials, competition between energy contributions leads to the formation of magnetic domains separated by domain walls. These domains also have an internal spin structure and the relationship between this and the sample geometry is discussed in detail. The theory behind the micromagnetic understanding of magnetic systems is introduced as a way of describing the magnetisation configuration of these complex structures. This allows for deeper understanding of the subtle balance of energies responsible for the phenomena such as domain wall pinning and propagation, including the effects of Walker breakdown. This chapter finishes with a discussion of the current techniques that have been adopted for the control of domain walls in both their static and dynamic regimes.

2.2   Origins of atomic magnetic moments

The *magnetic moment*, μ, of an atom originates from the intrinsic spin, m_s, and the orbital angular momentum, m_L, of its electrons. In an atom with multiple electrons, these combine to give the *orbital angular momentum*, $L = \sum m_L$, and *spin angular momentum*, $S = \sum m_s$, for each atom. The sum of these gives the total angular momentum, $J = L + S$, for the atom. [48]

Atoms containing multiple electrons give rise to a range of total angular momenta depending on their electronic structure. Full shells have no net angular or spin momentum so only electrons in partially filled shells can contribute to the magnetic moment. The resulting electronic arrangement is determined by the state with the lowest ground state energy.

2.2.1   Spin-orbit interaction

In addition to the contributions from the spin and orbital angular momenta, a weak *spin-orbit interaction* also perturbs the energy of the system. This can be understood semi-classically by considering the rest mass frame of an electron in an atom with an orbiting nucleus. The positively charged nucleus has an associated current loop and hence a magnetic moment. The spin of the electron in the centre of the current loop then exhibits preferential alignment to the moment from the current loop.

This interaction forms the basis of many observed magnetic properties such as: magnetocrystalline anisotropy, magnetostriction, magneto-optic effects and anisotropic magnetoresistance which are discussed in more detail later in this chapter. [48]

2.2.2   Hund's Rules

The atomic magnetic moment can be determined from the arrangement of electrons according to their spin, orbit and the spin-orbit interaction. For an atom in its ground state energy configuration, Hund's rules provide a method to determine the order in which electrons are added to atomic subshells whilst maintaining the minimum energy and not violating the Pauli exclusion principle. The order of the rules shows the significance on the energy change of the system.

Hund's rules state that electrons are added to the atom such that:

1. The spin, $S = \sum m_s$, is maximised. This reduces the electrostatic Coulomb energy as electrons first occupy all the available orbital angular momentum states before starting double occupation.

2. The orbit, $L = \sum m_L$, is maximised whilst maintaining a spin state consistent with rule 1. Electrons with the same orbit direction can avoid each other more easily, thus reducing the Coulomb energy associated with close passing electrons.

3. Finally, the total angular momentum, J is found by considering the effect of a weak perturbation to the energy from the spin-orbit interaction. If the partially filled shell is not more than half full, the lowest value of J has the lowest energy, i.e. $J = |L - S|$, and if the shell is more than half filled then the highest value of J has the lowest energy, $J = |L + S|$.

For example, iron has 26 electrons with the electronic arrangement of Ar and 8 additional electrons. Two of these electrons fill the lower energy $4s$ sub-shell and the remaining 6 partially fill the $3d$ sub-shell of slightly higher energy giving it the atomic arrangement $[\text{Ar}]3d^6 4s^2$. To maximise S, five of the electrons occupy the spin-up state with $m_L = +2, +1, 0, -1, -2$ and the remaining electron needs to occupy the spin-down state. For this electron $m_L = +2$ to maximise L. The resulting angular momentum for the atom is $S = 2$, $L = 2$ and since the shell is more than half full, $J = |L + S| = 4$.

From the total angular momentum J, the magnetic moment of the atom, μ, is predicted by:[49]

$$\mu = g_j \mu_B \sqrt{J(J+1)} = 6.7\mu_B \tag{2.1}$$

using the Landé g factor:

$$g_j = 1 + \frac{j(j+1) + s(s+1) - l(l+1)}{2j(j+1)} = 1.5 \tag{2.2}$$

and where μ_B is the Bohr magneton.

Hund's rules are valid for isolated atomic magnetic moments but when atoms combine to form metals there are additional energy contributions from the crystal field that dominate over the spin-orbit interaction. This results in a difference between experimental results and the predicted moments from Hund's rules in equation 2.1, except in cases where the orbital momentum is zero.

2.2.3 Crystal field interaction and orbital quenching

As atoms combine to form metals the electric field from the orbitals of neighbouring atoms interact as they contribute to the bonding in the metal. This interaction, averaged over the material, can be interpreted as a *crystal field*, which interacts with the atomic moments and preferentially favours states with zero orbital momentum. A semi-classical explanation shows the orbital angular momentum precesses around the crystal field such that it has an average value of zero whilst its magnitude remains unchanged. This is known as *orbital quenching*.

In $3d$ transition metals this orbital quenching dominates over the spin-orbit interaction. A correction to the predicted moment from Hund's rules (equation 2.1) to give higher priority to the crystal field interaction gives a moment based only on the spin contribution:[49]

$$\mu = 2\mu_B \sqrt{S(S+1)}, \tag{2.3}$$

which gives much better agreement with experimental values.

In the heavier $4d$ and $5d$ transition metals the spin-orbit interaction energy increases proportionally with Z^4.[49] This becomes comparable with the crystal field so the prediction of the magnetic moment becomes more complicated.

2.2.4 Magnetocrystalline anisotropy energy

The crystal field also leads to an energy preference for particular orientations of the electronic orbitals of atoms which have asymmetrical charge distributions due to a greater overlap between the atomic orbitals in certain crystallographic directions. This leads to a preferential alignment of magnetisation along specific crystalographic axes in the sample in an effect known as *magnetocrystalline anisotropy*.

The magnetocrystalline anisotropy energy for cubic crystals such as iron and nickel is formulated by:[48]

$$E_{mc} = K_1(\alpha_1^2\alpha_2^2 + \alpha_2^2\alpha_3^2 + \alpha_3^2\alpha_1^2) + K_2(\alpha_1^2\alpha_2^2\alpha_3^2) + ... \tag{2.4}$$

where α_1, α_2 and α_3 are the cosines of the angle between the magnetisation and the x, y and z axes of the cubic crystal respectively. The anisotropy constants K_1 and K_2 are material dependent and have the values $K_1 = 4.8 \times 10^4$ J/m^3 and $K_2 = -1.0 \times 10^4$ J/m^3 for iron and

$K_1 = -4.5 \times 10^3$ J/m^3 and $K_2 = -2.3 \times 10^3$ J/m^3 for nickel at room temperature.[48] The sign of the first anisotropy constant determines the shape of the anisotropy energy landscape which is illustrated in figure 2.1(a) for nickel and 2.1(b) for iron.

For NiFe alloys the magnetocrystalline anisotropy constant varies with composition shown in figure 2.2(a) and passes through zero for compositions $\approx$ 70 - 80% Ni.[50] At these compositions the magnetocrystalline anisotropy energy landscape becomes approximately spherical giving little preference for the magnetisation to lie along any particular crystal axis.

2.2.5 Magnetostriction

A stress or strain applied to a magnetic material can result in changes to the overlap between atomic orbitals. This can lead to changes in the energetics of the system due to the interaction with the crystal field giving rise to an additional form of anisotropy known as *magnetostrictive* or *magnetoelastic anisotropy*. This energy is given by:

$$E_{me} = 1/2\lambda\sigma_s \tag{2.5}$$

where σ_s is the stress and λ is a magnetostrictive constant. For a cubic system λ_{111} and λ_{100} describe the response to stress along the [111] and [100] crystal axes respectively.

For $\lambda > 0$, magnetisation aligns parallel to the strain and for $\lambda < 0$ the magnetisation aligns perpendicular to the strain. The magnetostriction constants have the values $\lambda_{100} = 20.5 \times 10^{-6}$ and $\lambda_{111} = -21.5 \times 10^{-6}$ in iron, whilst for nickel they are $\lambda_{100} = -46 \times 10^{-6}$
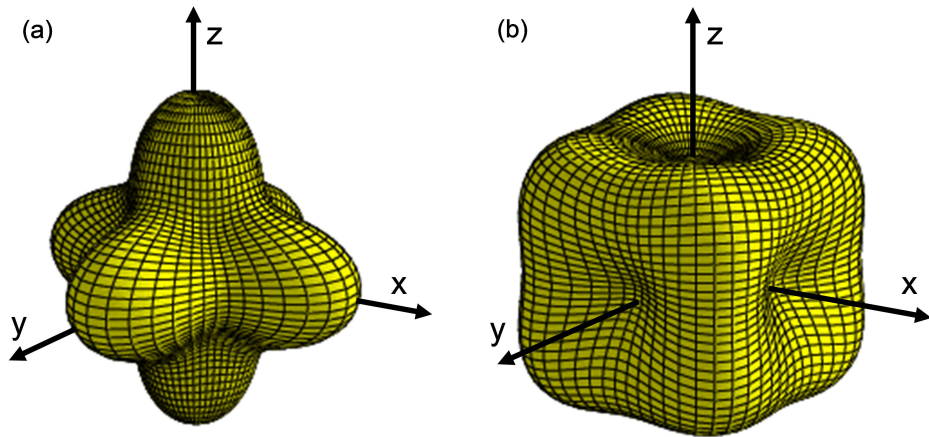
Figure 2.1: Anisotropy energy surfaces for a) nickel and b) iron plotted from equation 2.4 where minimum energy points correspond to directions of easy axes; along the x, y, z axes for iron and along the cube diagonals for nickel.[48]
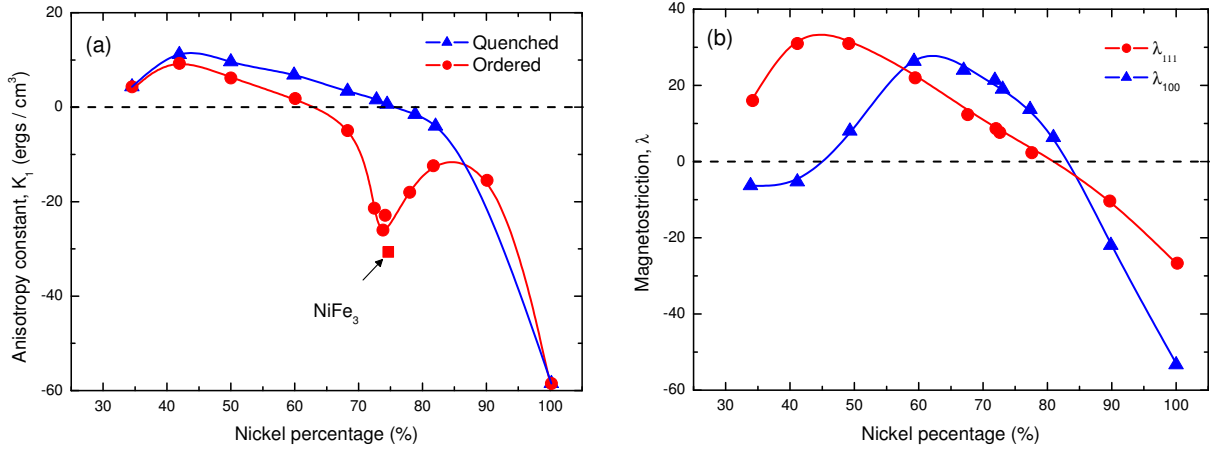
Figure 2.2: a) Magnetocrystalline anisotropy coefficient K_1 and b) magnetostriction λ for NiFe alloys as a function of Ni%, from Bozorth.[50]

and $\lambda_{111} = -25 \times 10^{-6}$.[48] In NiFe alloys λ depends on composition shown in figure 2.2(b) and at $\approx 80\%$ Ni, the magnetostriction coefficients pass through zero.

2.2.6 Polarisation of non-magnetic atoms

The overlap between atomic orbitals has been used to explain the origin of the crystal field which leads to a magnetisation dependence on the crystallographic axes in a sample. This overlap also leads to interesting behaviour when dissimilar elements are in close proximity. The overlap in atomic orbitals between magnetic and non-magnetic atoms is of particular relevance to the work presented here.

In non-magnetic atoms, the electronic arrangement is such that the spin, orbit and spin-orbit interaction result in zero magnetic moment. However, the overlap with the atomic orbitals from magnetic atoms can lead to polarisation effects resulting in an induced moment. For example, the induced magnetic moment on $4d$ and $5d$ transition metal impurity atoms in an Fe matrix has been predicted theoretically and is shown in figure 2.3 for both the spin and orbital contributions.[51,52]

The orbital contribution is small compared to the the spin due to the orbital quenching that is typical for transition metals. However, the increased orbital moments and decreasing spin moment in the $5d$ series compared to the $4d$ highlights the increasing significance of the spin-orbit interaction over the crystal field with increasing Z. The spin moments follow an S shape over the series starting with a negative value and becoming positive towards the end whilst the sign of the orbital moment changes twice over the series.
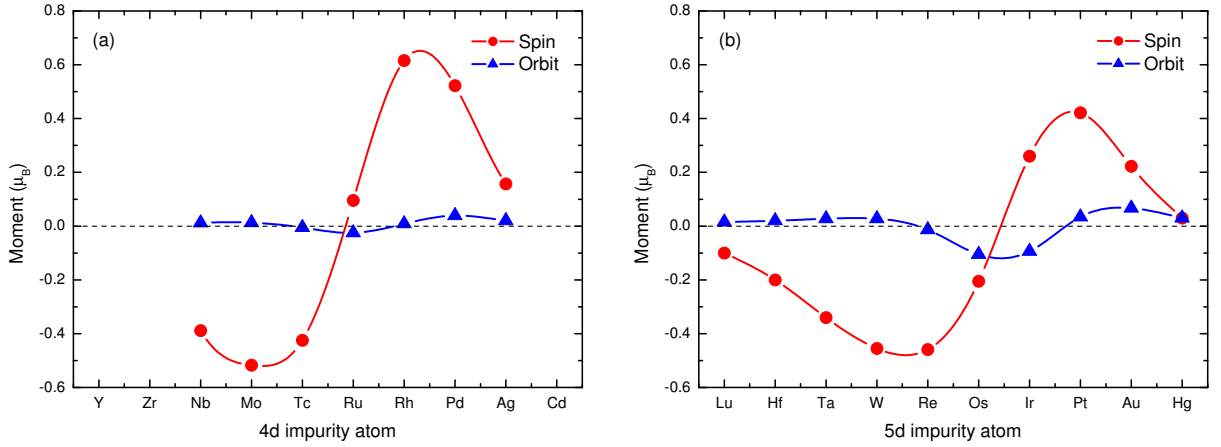
Figure 2.3: Theoretical predictions for spin and orbital moments induced on (a) $4d$ and (b) $5d$ transition metal impurity atoms in Fe.[51,52]

Element specific techniques such as XMCD experimentally confirm these results. Atomic Au with completely filled $5d$ states and no net magnetic moment gains a $5d$ moment of up to 0.03 μ_B per atom when in proximity to $3d$ ferromagnets in an $Au_{75}Fe_{25}$ alloy.[53] This moment scales with the number of Fe nearest neighbours up to 0.33 μ_B per atom.[42]

Proximity with ferromagnets can also be achieved at interfaces as demonstrated with Fe/Au,[52,54] Co/Au[55] and Fe/W[52] interfaces. The geometrical differences between impurities and interfaces suggests a local environment effect on the moment[56] but further work suggests polarisation effects are likely to dominate over any geometrical effects.[52]

2.3 Magnetism in materials

So far the origins of atomic magnetic moments have been discussed in terms of the electronic structure. The combination of atoms in a material leads to additional effects due to the interaction of the crystal field that affects the magnetisation orientation with respect to crystalline axes in the material. As well as this interaction, there is also an exchange interaction between the moments on neighbouring atoms and a Zeeman interaction between the moments and external magnetic fields. The details of these interactions are covered in section 2.4 but here considerations between the relative strength of these interactions and the strength of the magnetic moment allows different classes of magnetic materials to be identified. This section discusses the various classes of magnetic materials which are classified according to their magnetisation response to an applied magnetic field.

2.3.1 Diamagnetism

Atoms containing completely filled electronic sub-shells have no net spin or orbital angular momentum and hence do not contain a magnetic moment. However, these materials show a weak negative magnetisation in response to an applied magnetic field known as *diamagnetism*. This effect originates from induced changes in the orbital motion of the electrons due to the application of a magnetic field. This sets up a back-electromotive force that exerts a torque on the electrons which opposes their motion and reduces the orbital contribution to the magnetic moment. This classical description was developed by Langevin in 1905[57] based on Lenz's law whilst a more robust Bohr-van Leeuwen model[58] provides a quantum mechanical description of this diamagnetic behaviour.

All materials experience a diamagnetic response but this is often masked by stronger effects such as paramagnetism and ferromagnetism. Examples of diamagnetic materials include: monatomic rare gases (He, Ni, Ar, etc.); molecules with strong ionic bonding (NaCl); materials with strong covalent bonds (C, Si, Ge); and almost all organic compounds.[59]

2.3.2 Paramagnetism

For atoms with unpaired electrons in incompletely filled sub-shells a non-zero magnetic moment exists. The alignment of these magnetic moments in a material with applied magnetic field is known as *paramagnetic* behaviour. In the absence of applied magnetic field, the magnetic moments in a material are randomly orientated, which gives rise to an average magnetisation of zero. The application of a magnetic field acts to align each of these moments with the field, which gives rise to a finite positive magnetisation. This alignment from the applied field competes with the thermal motion of the atoms and maintains a degree of random alignment in the moments. This explains why only a small magnetisation response is achieved with applied field, which decreases with the effect of increasing temperature. These effects were first observed by Curie in 1895,[59] but this theoretical description was not developed until 1905 by Langevin.[57]

Paramagnetic behaviour is observed in materials where the atoms contain an incompletely filled sub-shell. For example, transition metal ions and rare earth ions contain an incompletely filled inner shell and the compounds of these elements are strongly paramagnetic.[59]

2.3.3   Ferromagnetism

In addition to the preferential alignment of magnetic moment with applied magnetic field found for paramagnetic materials, additional exchange interactions lead to the preferential alignment of the magnetic moment between neighbouring atoms. This leads to long range ordering of the magnetic moments and results in a large spontaneous magnetisation which can exist in the absence of a magnetic field, this is known as *ferromagnetic* behaviour.

The relative strength of the exchange interaction to align magnetic moments and the tendency for thermal motion to randomise the orientation of the magnetic moments is an important characteristic of ferromagnetic behaviour. At low temperatures the exchange interaction dominates, giving ferromagnetic behaviour but increasing the temperature above the *Curie temperature* leads to a transition from a ferromagnetic to paramagnetic state.

The application of a magnetic field acts to align the magnetisation direction of the moments with the field but can only overcome the effects of the exchange and the thermal energy by application of a sufficiently large magnetic field. Upon removal of the field, the material can retain a remanent magnetisation due only to the exchange interactions.

The magnetisation response of a ferromagnetic material to an applied magnetic field is often plotted as a hysteresis loop, illustrated by the example in figure 2.4. With a sufficiently strong field, overcoming the thermal and exchange effects, the magnetic moments align uni-
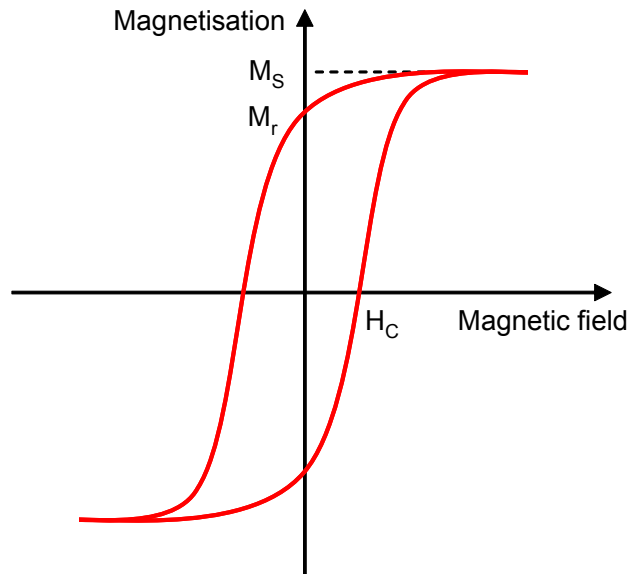
Figure 2.4: Magnetisation as a function of applied field showing a hysteresis loop typical for a ferromagnetic material. The magnetisation reaches the saturation magnetisation, M_s, at high fields, retains a remanent magnetisation, M_r, when the field is removed and requires a coercive field, H_C, to remove the net magnetisation.

formly with the field in a state known as *saturation magnetisation*, M_s. As the field is removed the magnetisation decreases to the *remanent magnetisation*, M_r, where the exchange acts to maintain a partial alignment between neighbouring moments even in the absence of applied magnetic field. Reversing the field results in the rotation of the magnetisation at the coercive field, H_c, where the effect of the field dominates over the exchange interaction.

This theory for ferromagnetic behaviour was first introduced by Weiss[60] who proposed the existence of a molecular field that acts to align the magnetic moments with an effective field given by the magnetisation of the surrounding magnetic moments. The origins of this molecular field were then explained through a quantum mechanical description of exchange developed by Dirac in 1923[61] in a formulation known as the Heisenberg Hamiltonian.[48]

Only very few materials show ferromagnetic behaviour at room temperature, these include the $3d$ transition metals iron, cobalt and nickel and the rare earth gadolinium along with some of their alloys.[59]

One such family of alloys with particular relevance to this thesis are NiFe alloys with compositions around 50% - 80% Ni which are known as permalloys. At around 50% Ni, these alloys show the highest saturation magnetisation and as shown in figure 2.2 these have a vanishing magnetocrystalline anisotropy and magnetostriction towards 80% Ni.[47,62] This gives them magnetically soft properties with a small coercivity and high permeability where a large magnetic induction can be achieved for relatively low applied fields.[47,48,59] Permalloy is technologically important and has widespread applications for electromagnetic applications such as inductance coils, audio frequency transformer cores and for magnetic shielding.[47]

2.3.4 Antiferromagnetism

The exchange interaction is also an important feature in materials which display *antiferro-magnetic* behaviour. Here, the neighbouring atomic magnetic moments display a preference for antiparallel alignment. The application of a magnetic field leads to a magnetisation in the direction of the applied field but this is small because the field acts against the effect of the exchange to remain in antiparallel alignment. A similar critical temperature exists for antiferromagnets as for ferromagnetic behaviour. Above a critical *Néel temperature* the random thermal nature of the atoms overcomes the exchange interaction and results in an antiferromagnetic to paramagnetic transition.

The underlying theory to explain antiferromagnetism was developed by Néel in a series

of papers beginning in 1932[63] based on the Weiss molecular field theorem. Examples of antiferromagnetic elements are limited to just chromium and α-manganese[48] although many antiferromagnetic ionic compounds have been discovered such as oxides, sulphides, and chlorides.[59]

2.3.5 Ferrimagnetism

The final class of magnetic materials follow *ferrimagnetic* behaviour which is very similar to ferromagnetic behaviour. These materials have a positive magnetic moment and exhibits hysteretic behaviour, becoming saturated at higher fields. They support domains and also display a temperature dependence with a transition into a paramagnetic state above a Curie temperature. The difference in behaviour arises due to the molecular structure which incorporates ions with differing magnetic moments in a lattice structure. These show preferential anti-parallel alignment but the moment contributions are different sizes which brings about the spontaneous magnetisation behaviour. Ferrimagnetism can be thought of as 'imperfect antiferromagnetism' and this theoretical understanding was provided by Néel in 1948.[64]

Ferrimagnetic materials include a divalent metal ion such as Mn, Ni, Fe, Co, Mg, etc. bound with oxygen atoms. Common examples include iron ferrite or 'lodestone', $FeO \cdot Fe_2O_3$, magnetite, Fe_3O_4 and barium ferrite, $BaO \cdot 6Fe_2O_3$.

A summary of the various classes of magnetic material is illustrated in figure 2.5. This shows the alignment between the magnetic moments on a group of neighbouring atoms in these materials with no applied field. These moments adopt random orientations in the case of paramagnetic behaviour, and align giving a spontaneous magnetisation in the ferromagnetic case. Antiferromagnetic behaviour shows the preferential anti-parallel alignment of moments which is similar to that shown in ferrimagnetism but differs due to the imbalance in magnetic moments giving a spontaneous magnetisation.

Paramagnetic   Ferromagnetic   Antiferromagnetic   Ferrimagnetic
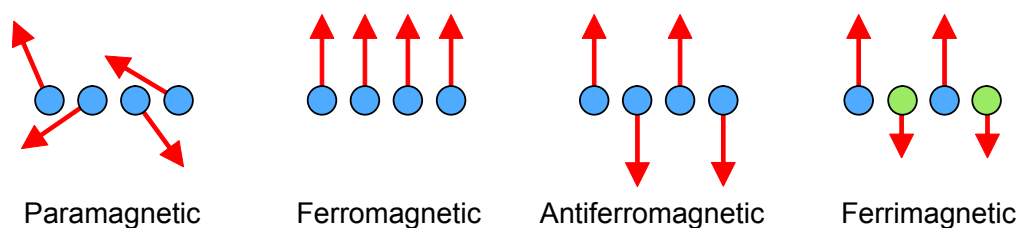
Figure 2.5: A schematic illustration of the alignment of magnetic moments in paramagnetic, ferromagnetic, antiferromagnetic and ferrimagnetic materials.

2.4 Magnetic moment interactions

The various classes of magnetic materials result from the strength of the atomic magnetic moments and the strength of the interactions between these moments on neighbouring atoms. The origins of the magnetic moments and a discussion of their strength have been presented in detail. This section discusses the various interactions between neighbouring atoms in a material, as well as with external effects such as applied field.

2.4.1 Exchange interaction

The *exchange interaction* is a very strong localised interaction that acts between neighbouring magnetic moments in a material. This interaction leads to the spontaneous magnetisation that occurs in ferromagnetic material.

This interaction originates from a combination of the Pauli exclusion principle; the quantum mechanical interactions between neighbouring spins, and the Coulomb repulsion between charges.[65] The Pauli exclusion principle limits only one fermion to occupy the same position in space with the same quantum numbers at the same time. Since electrons are indistinguishable fermions they must obey this principle so not all electrons can occupy the ground state energy and some must occupy higher energy states. The energy increase associated with the occupation of this higher energy state is known as the *exchange energy*.

The exchange energy of a magnetic system is calculated from a summation over all pairs of magnetic moments in the system. The exchange interaction is a very short range interaction so with increasing separation it very quickly becomes negligible. It is therefore common to sum over only the nearest neighbouring moments, $\boldsymbol{s_i}$ and $\boldsymbol{s_j}$ in the system:

$$E_{ex} = -2J \sum_{ij} \boldsymbol{s_i} \cdot \boldsymbol{s_j} \tag{2.6}$$

where J is the exchange integral. In the case of ferromagnetic materials, J is positive resulting in a minimum energy configuration when neighbouring spins have parallel alignment. This interaction gives rise to the spontaneous alignment of magnetic moments seen in ferromagnetic materials. When J is negative, in the case of antiferromagnetic materials, this leads to the antiparallel alignment of the neighbouring spins.

2.4.2 Zeeman energy

Magnetic moments also interact with external magnetic fields. This effect is due to the *Zeeman energy* which is described by the integral over the volume V of the dot product between the magnetisation, $\boldsymbol{M}$, and applied field, $\boldsymbol{H}$, vectors:

$$E_{ze} = -\mu_0 \int_V \boldsymbol{M} \cdot \boldsymbol{H} \, \mathrm{d}v. \tag{2.7}$$

This contribution is scaled with the permeability of free space, μ_0, and the energy is reduced when the magnetisation is aligned with the external magnetic field. This interaction is more significant for larger fields and vanishes in the case of zero applied field. This explains why the magnetisation of a system will align with a strong external magnetic field.

2.4.3 Magnetostatic energy

The *magnetostatic energy* contribution is similar to the Zeeman energy except the field originates internally from the magnetisation of the system rather than from an externally applied magnetic field. The source of this field is illustrated schematically in figure 2.6. In figure 2.6(a) a uniformly magnetised rectangular sample has an associated magnetic flux that is continuous through the sample and in the vacuum surrounding the sample. In figure 2.6(b) the magnetic fields associated with the same magnetised sample are shown. The magneti-
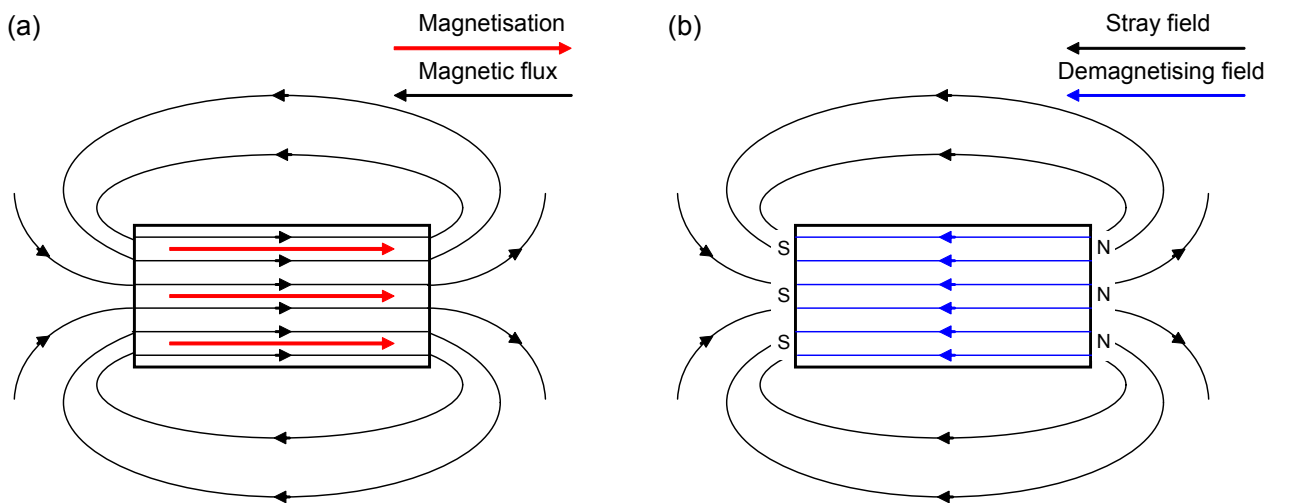
Figure 2.6: A schematic illustration of a) the magnetic flux from a uniformly magnetised sample and b) the field produced from the magnetic poles on the surface. Note the demagnetising field, $\boldsymbol{H_d}$, opposes the magnetisation, $\boldsymbol{M}$, leading to a reduced magnetic flux, $\boldsymbol{B}$.

sation leads to the development of free poles at the ends of the structure which act as a source of a new magnetic field. This follows the flux (which must be continuous) through the vacuum but opposes the flux inside the sample showing a discontinuity at the ends of the structure. The field opposing the magnetisation direction inside the sample is known as the demagnetising field, $\boldsymbol{H_d}$.

The energy of this interaction is proportional to the integral over the volume of the sample of the dot product between the magnetisation and demagnetisation field:

$$E_{ms} = -\frac{1}{2}\mu_0 \int\limits_V \boldsymbol{M} \cdot \boldsymbol{H_d} \, \mathrm{d}v \qquad (2.8)$$

This energy is minimised when the magnetic surface charges and hence the stray fields from the sample are reduced.

2.4.4   Shape Anisotropy

The geometry of a sample has an important effect on the magnetostatic energy of the system. This is due to the difference in spatial extent of the stray fields which originate from the free poles on different edges of the sample. For a non-uniform shape, this can give rise to preferential magnetisation alignment along particular easy axes of a sample due to its geometry. To align the magnetisation along a corresponding hard axis requires an increase in energy to overcome the difference in magnetostatic energy between the two axes. This shape anisotropy is described using a demagnetising factor, N, that relates the *demagnetising field*, $\boldsymbol{H_d}$, to the magnetisation, $\boldsymbol{M}$, along a given geometrical axis:

$$\boldsymbol{H_d} = -N\boldsymbol{M}. \qquad (2.9)$$

This factor is determined from the aspect ratio of the structure. In a two dimensional thin film structure, the axis perpendicular to the thin film is constrained giving it a high demagnetisation factor, $N_\perp \approx 1$, in comparison to the in-plane axes with $N_\parallel \approx 0$. The lower demagnetisation field for in-plane magnetisation has a lower magnetostatic energy and is therefore usually the ground state configuration.

Constraining the dimensions further to form a one dimensional nanowire, $N_\parallel$ to the long axis remains very small whilst for both of the orthogonal axes $N_\perp \approx 1/2$. The magnetic

easy axis thus aligns the magnetisation along the long axis of the wire so that modifying the sample geometry gives control over the preferential alignment of the magnetisation. This is particularly relevant to small scale structures and is used heavily in the control of domain structure and domain wall propagation as discussed later in this chapter.

2.4.5 Domains in ferromagnetic material

The many different interactions which govern the behaviour of a magnetic system have now been introduced. Each interaction has associated with it an energy: magnetostatic, E_{ms}, exchange, E_{ex}, Zeeman, E_{ze}, magnetocrystalline, E_{mc} and magnetostrictive, E_{me} energies respectively. The combination of these energies yields the total energy for the system, E_{tot}, given by:

$$E_{tot} = E_{ms} + E_{ex} + E_{ze} + E_{mc} + E_{me}. \tag{2.10}$$

As each of these energies is affected by the alignment of the magnetic moments, different magnetisation orientation arrangements change the energy contributions to the system. This then has an effect on the total energy of the system and, similar to other physical phenomena, the equilibrium configuration is one where the total energy is minimised. It is this minimisation of the energy that gives rise to the interesting behaviour that occurs in magnetic materials.

One of the major competitions between energies in a ferromagnetic material is due to the exchange and magnetostatic energies. The exchange energy is minimised when neighbouring moments are aligned, saturating the magnetisation. However, this leads to the generation of magnetic poles at the edges of the sample generating a large magnetostatic energy contribution. In this case the total energy can be reduced by creating multiple domains in the system separated by domain walls.

2.4.6 Introduction of multiple domains to reduce energy

Figure 2.7(a) shows a rectangular structure of magnetic material with low exchange energy at magnetic saturation but with a large magnetostatic energy from stray magnetic fields. These stray fields are dramatically reduced in figure 2.7(b) by the formation of two antiparallel *domains* separated by a domain wall. In the case of permalloy with no magnetocrystalline anisotropy, the addition of further closure domains at the end of the structure in figure 2.7(c) can completely remove these stray fields resulting in zero magnetostatic energy.
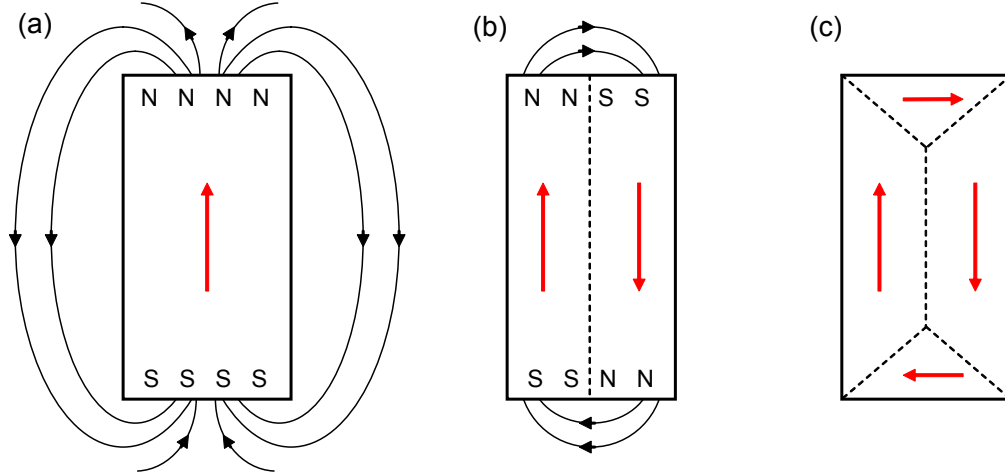
Figure 2.7: A schematic illustration of a magnetic structure showing how stray fields, and hence magnetostatic energy can be reduced by subdivision of the structure into domains.

The reduction in magnetostatic energy by the introduction of additional domains must be balanced with the increase in energy associated with the introduction of domain walls into the system. In the next section the factors affecting the energy of domain walls are considered and shown to give rise to a selection of different domain wall structures and sizes depending on the energetics of the system.

2.5   Magnetic domain walls

Domain walls form at the division between two domains of non-parallel magnetisation and incorporate a spin rotation between these two magnetisation directions. If this rotation occurs abruptly over one atomic layer, then this will give rise to a very significant exchange energy contribution associated with the domain wall. The exchange energy is minimised when the magnetisation rotates over many spins in a wide domain wall giving a small angle between adjacent spins. However, such alignments would increase the anisotropy energy as it would include many spins not aligned along an anisotropy easy axis. It is the competition between energies that determines a domain walls internal structure. These structures are considered here using simplistic analytical models and later they are discussed further using micromagnetic models of domain walls.

2.5.1   Width of Bloch type domain walls

Considering first domain walls in bulk material where magnetisation direction is dominated by the magnetocrystalline anisotropy of the material. In these materials a *Bloch wall* separating two magnetic domains comprises of a 180° rotation of the magnetisation distributed over N atomic planes. With a lattice parameter, a, adjacent spins differ by an angle of π/Na. Assuming a strong exchange interaction, the angle between neighbouring spins is small, so the exchange energy contribution from equation 2.6 gives an energy density per unit area of the domain wall as:[48]

$$\sigma_{ex} = JS^2 \frac{\pi^2}{Na^2} \tag{2.11}$$

where J is the exchange integral and S the magnitude of the spins. The exchange energy density can be reduced by distributing the rotation over a greater number of atomic planes. However, this leads to a corresponding increase in the anisotropy energy, which increases with N as:[48]

$$\sigma_K = K_1 Na \tag{2.12}$$

with the anisotropy constant, K_1. Combining the exchange and anisotropy contributions, the total energy density becomes:[48]

$$\sigma_{Bloch} = \frac{JS^2}{N} \left(\frac{\pi}{a}\right)^2 + K_1 Na. \tag{2.13}$$

An increase in the domain wall width over a greater number of spins, N, leads to a reduction in the exchange energy proportional to $1/N$, but also causes a corresponding linear increase in anisotropy energy with N. This combination leads to a total energy density, illustrated in figure 2.8, which shows a minimum corresponding to a domain wall width, δ_{DW}, with the lowest energy.

The value of N which minimises this expression is found by differentiating equation 2.13 with respect to N and taking the value at $N = N_0$ where:

$$N_0 = \sqrt{\frac{JS^2}{K_1} \frac{\pi^2}{a^3}}. \tag{2.14}$$
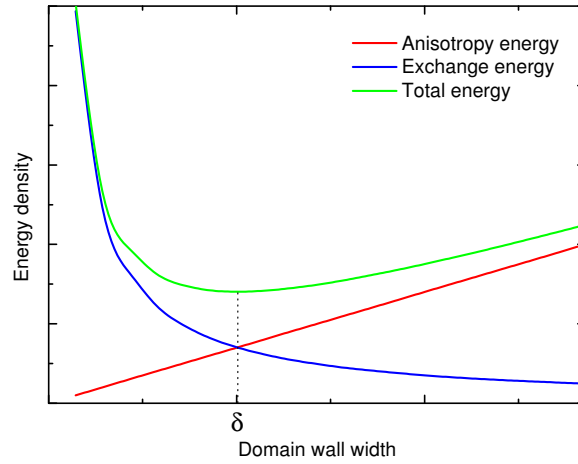
Figure 2.8: Variation in energy density with domain wall width, δ_{DW}, showing contributions from exchange energy which favours wide domain walls and magnetocrystalline anisotropy energy which favours thinner domain walls.

Using the exchange stiffness coefficient, $A = JS^2/a$, the domain wall width becomes:[48]

$$\delta_{Bloch} = N_0 a = \pi \sqrt{\frac{A}{K_1}}. \tag{2.15}$$

The total energy density of a Bloch wall can then be found by substituting this expression into the total energy density relationship in equation 2.13 to give:[48]

$$\delta_{Bloch} = 2\pi \sqrt{AK_1}. \tag{2.16}$$

This expression provides a simple relationship between the domain wall width, the exchange stiffness and the intrinsic anisotropy of the material. For example, for Fe this analysis gives the domain wall width as 30 nm and for Ni a value of 72 nm.[59]

This model is based on the assumption that the magnetisation rotates equally over N atomic planes. This is simplified, and a more detailed model can be obtained by describing magnetisation rotation by trigonometric functions.[48]

2.5.2   Domain walls in thin films

Analysis of the Bloch domain wall in bulk material ignores the effect of the magnetostatic energy from the wall itself. This is reasonable when the wall is far from the edges of the sample, however, in thin films, magnetic poles on the surface resulting from the domain wall

give rise to a magnetostatic energy contribution that cannot be neglected. When this magnetostatic energy dominates, another lower energy micromagnetic rearrangement occurs. Here, magnetisation rotation takes place within the plane of the thin film rather than perpendicular to it as in the case of a Bloch wall. This type of wall is known as a *Néel wall* and is illustrated in figure 2.9. The small magnetostatic energy resulting from free poles at the edges of the domains in figure 2.9(b) is accepted instead of the larger magnetostatic energy associated with free poles at the surface of the film from the Bloch wall in figure 2.9(a).

This gives a magnetostatic energy contribution, $-\mu_0 \boldsymbol{M_S} \cdot \boldsymbol{H_D} = \frac{1}{2}\mu_0 M_S^2 \cos^2 \theta$, where θ is the angle between the magnetisation and the demagnetisation field.[48] This is combined with the magnetocrystalline anisotropy term, K_1, to give the total energy density:[66]

$$\sigma_{\text{Néel}} = 4\sqrt{AK_1 + \frac{1}{2}A\mu_0 M_S^2} \tag{2.17}$$

with an associated domain wall width given by:[66]

$$\delta_{\text{Néel}} = \pi\sqrt{\frac{A}{K_1} + \frac{2A}{\mu_0 M_S^2}}. \tag{2.18}$$

In the limit of vanishing magnetocrystalline anisotropy in the case of $Ni_{81}Fe_{19}$, this domain wall energy density reduces to $\sqrt{8\mu_0 A M_S^2}$.

The energy for both Néel and Bloch domain walls are compared in figure 2.10 as a function of film thickness. With decreasing film thickness the Néel wall has a decreasing energy density becoming favourable over Bloch walls for films thinner than 50 - 60 nm for many thin film materials.[48] Below this thickness the Néel wall also shows a dramatic increase in width due to the larger spatial extent for spins rotating in the plane of the film.

These analytical models allow for a substantial discussion about the properties of magnetic domain walls, but they are based on assumptions such as a constant magnetisation rotation
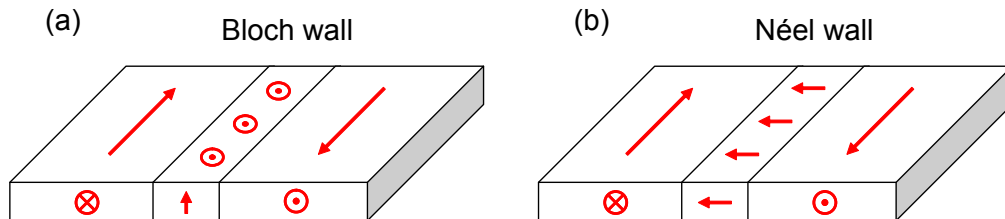
Figure 2.9: Magnetisation rotation direction in a) Bloch and b) Néel domain wall, showing the greater surface charges present for Bloch walls in thin films.
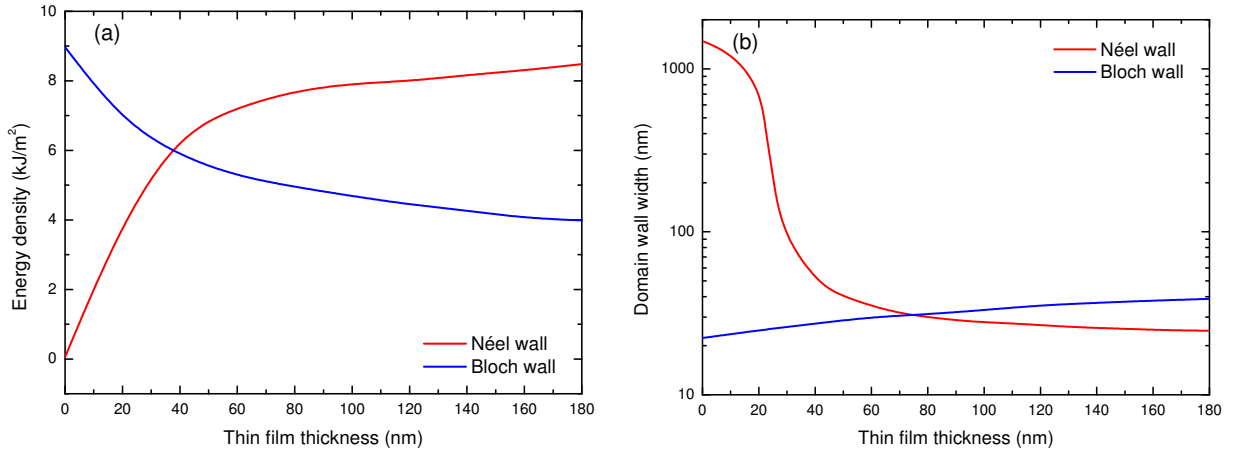
Figure 2.10: The a) energy density and b) width of Bloch and Néel walls calculated as a function of thin film thickness for a film with $M_s = 800 \times 10^3$ A/m, $A = 10 \times 10^{-12}$ J/m and $K = 100$ J/m^3. [48]

over a domain wall width which is a simplification. To progress further, a more detailed model is required giving a micromagnetic understanding of the domain walls. This theory is introduced next, and later used to explain further relationships between the domain walls and geometrical structuring of the material.

2.6 Micromagnetic understanding of magnetic materials

The current understanding of ferromagnetic materials is based on the net effect of multiple magnetic moments which combine to form domains of uniform magnetisation alignment. These domains are separated by domain walls over which the magnetisation rotation between adjoining domains takes place. The size and structure of these domain walls is determined from the competition between the various physical processes previously discussed and the study of these domain walls is of great importance. Further analysis of these domain walls requires the study of the magnetisation on a length scale that lies between that of domains and atomic scale. This intermediate scale is considered by micromagnetic theories developed by Brown[67] where the analysis is small enough to show details about domains and domain walls, whilst big enough to allow a single magnetisation vector to represent several atomic magnetic moments. [67]

Neighbouring spins have an alignment that is dominated by the exchange interaction.

This means the magnetisation vector, $\boldsymbol{M}$, can be approximated as a continuous function of position. The continuous variation of $\boldsymbol{M}$ with position can be through a large angle on a scale comparable with domains which would indicate domain walls, alternatively the rotation of $\boldsymbol{M}$ can be more gradual giving a gradual variation of $\boldsymbol{M}$ across the sample.

Viewing the magnetisation as a continuously varying quantity allows an integral over the volume of a material to be performed where calculus techniques become applicable.[67] This supersedes the previous sum over many lattice points that would have to be performed for a atomic scale model. Although it may be possible to derive formalised energy contributions from individual atoms in a lattice, the combination of these expressions for many atoms into any usable form is unrealistic for a generalised micromagnetic problem.[67]

Early micromagnetic work described only the simplest problems where it was possible to solve the integrals involved with the energy by reasonable numerical techniques. However for any generalised problem these integrals can become impossible to solve mathematically. Recent advances in computing power have given rise to simulation packages which can solve these integrals using Monte Carlo techniques which makes the computation of micromagnetics feasible. The techniques involved in using simulations to solve micromagnetic problems are described in chapter 4. Following the modelling described in chapter 5 the results from these models are presented in chapters 8 and 9; these are useful for the interpretation of magnetisation processes that occur in thin film and nanoscale structures studied here.

2.6.1   Modelling precession and damping with the Landau-Lifshitz-Gilbert equation

In the micromagnetic description of a magnetic structure, the various different energetic contributions responsible for the magnetic properties are combined to form an *effective field*, $\mathbf{H_{eff}}$ defined as:[68]

$$\boldsymbol{H_{eff}} = -\frac{1}{\mu_0}\frac{\partial E}{\partial \boldsymbol{M}}. \tag{2.19}$$

This depends on the variation of the average energy density, E, with magnetisation, $\boldsymbol{M}$, from Brown's equations[67], and represents the combined effects of exchange, anisotropy, demagnetisation and applied field in a single expression.

The minimum energy, and hence ground state of a system is therefore dependent on the magnetisation configuration. This is given by the time dependent Landau-Lifshitz ordinary

differential equation (ODE),[69] reformulated by Gilbert to form the Landau-Lifshitz-Gilbert equation[70] which is expressed as:

$$\frac{d\boldsymbol{M}}{dt} = -|\gamma_0|\boldsymbol{M} \times \mathbf{H_{eff}} + \frac{\alpha}{M_s}\left(\boldsymbol{M} \times \frac{d\boldsymbol{M}}{dt}\right).$$ (2.20)

This equation describes how the magnetisation, $\boldsymbol{M}$ evolves in time, t, in an effective field, $\mathbf{H_{eff}}$ based on two material parameters: γ_0, the gyromagnetic ratio and α, the Gilbert damping parameter.

In this equation, $\mathbf{M} \times \mathbf{H_{eff}}$ describes the precession of the magnetisation about the effective field axis and $\boldsymbol{M} \times \frac{d\boldsymbol{M}}{dt}$ describes the damping of the magnetisation which acts to align the magnetisation with the effective field. These effects are both illustrated in figure 2.11 and have relative strengths governed by their coefficients: the gyromagnetic ratio, γ_0 and the Gilbert damping parameter, α respectively.

Damping can be described by the coupling of the magnetisation with a thermal bath, allowing for dissipation of magnetic energy.[71] A more complete understanding lies within the quantum mechanical description of the spin primarily responsible for the magnetic moment, however, this concept is not well understood.[72] Suggestions of physical mechanisms include weak coupling of the magnetic moments to lattice vibrations[73,74] or spin-orbit coupling with electrons near the Fermi level.[75] For the purposes of micromagnetic analysis, it is adequate to combine these effects in the simple parameter α, which provides a phenomenological description of the approach to equilibrium configuration.[76]

Measurements for $Ni_{81}Fe_{19}$ films report a range of different measured values from $\alpha = 0.008$[71,77] to $\alpha = 0.013$.[78] The range in observations is due in part to the difficulty in
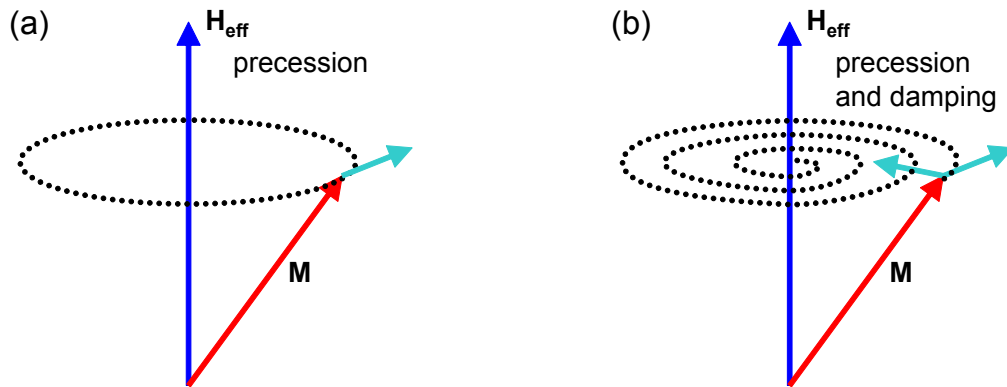
Figure 2.11: Motion of the magnetisation vector around an effective field governed by a) precessional torque and b) damping effects.

its experimental determination. One technique used to measure this parameter is known as ferromagnetic resonance (FMR), which is based on measurements of the linewidth of the resonance using small driving fields at the precessional frequency of the system. The linewidth is affected by additional effects due to an imperfect alignment between magnetisation and applied field, which acts as a large source of error in these measurements.[71]

The damping in $Ni_{81}Fe_{19}$ is found to increase when doping with other transition metals[71] and is also sensitive to the microstructure of the prepared sample.[79] Again, for the purposes of the micromagnetic modelling the damping parameter, α, is thought of as a single phenomenological constant combining several complex damping effects.[67]

2.6.2 Effect of temperature on micromagnetic simulations

Micromagnetic analysis is fundamentally a zero-temperature formalism. It assumes a fixed magnetisation density where each atom has the value of saturation magnetisation, M_s, and the effects of thermal fluctuations are not incorporated into the LLG equation upon which the energy minimisation is based.[80]

Some approaches have been developed to incorporate the effect of finite-temperature into micromagnetic models. A popular method is to introduce irregular fluctuating fields imitating the stochastic influence of temperature on the model.[68] These fluctuations are such that they have a Gaussian profile for which the time-averaged field is zero.

2.6.3 Length scales in micromagnetic simulations

Critical to the validity of the micromagnetic model is the size of the volume element in which uniform magnetisation can be assumed. This scale can be larger than the atomic structuring in the material but must be less than the length scale of domains and domain walls.

Larger cells reduce the complexity of a micromagnetic model but, beyond the scale of domains and domain walls, would lead to simplifications at the expense of the physical insight to be gained by the model. This key length scale is governed by the *exchange length* of a material, the length over which the exchange interaction acts to keep neighbouring moments aligned essentially parallel.

The exchange length is given by:[81]

$$\Lambda = \sqrt{\frac{2A}{\mu_0 M_s^2}}, \tag{2.21}$$

Using the parameters for $Ni_{80}Fe_{20}$: the saturation magnetisation, $M_s = 860 \times 10^3$ A/m,[62] and exchange stiffness, $A = 13 \times 10^{-12}$ J/m[48] yields an exchange length of $\Lambda = 5$ nm for $Ni_{80}Fe_{20}$.[82] Therefore a cell size of 5 nm is typically chosen to give a good representation of the magnetic behaviour of permalloy samples.

To solve a micromagnetic problem, the volume of a structure such as the planar nanowire illustrated in figure 2.12 is divided into cells. In this case a regular array of cubic cells fill the volume and each is assigned a spin to represent the net spin of the atoms within the volume of that cell. Further practical consideration of the division of a more generalised sample into cells will be discussed further in chapter 4.

2.7 Micromagnetic understanding of domain walls

The micromagnetic framework allows for a more realistic explanation of domain wall physics based on the minimisation of the energy from interactions between many spins in the system. A further in-depth discussion of the domain walls is based on this theory, in particular, looking at the domain wall structure in geometrically structured materials. The micromagnetic understanding also allows for a discussion of domain wall motion and dynamic properties as well as the effect of local features on the domain wall energy leading to the understanding of domain wall pinning that is difficult to explore experimentally.
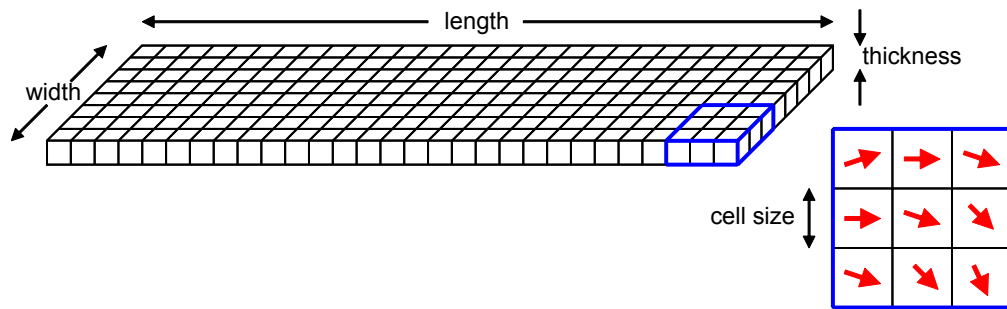
Figure 2.12: Division of a micromagnetic problem into cells. Each cell is assigned a spin vector representing the average magnetic moment of the atoms within the cell.

2.7.1 Domain walls in planar nanowires

Previously, Néel type domain walls were found to be preferable in thin film magnetic materials. Further constraining the material in two dimensions gives rise to planar nanowire structures defined by their width, w, usually of the order of hundreds of nanometres and their thickness, d of the order of tens of nanometres. Nanowires are typically micrometres in length, much greater than the size of a domain wall so this is less significant in determining their structure.

$Ni_{80}Fe_{20}$ nanowires have negligible magnetocrystalline or magnetostrictive anisotropy so the magnetisation direction is governed by the shape anisotropy. Magnetostatic energy favours states of flux closure but as sample dimensions are reduced, domain walls occupy an increasing proportion of the structure giving increasing significance to the exchange energy. Below certain dimensions the exchange energy cost to support a domain wall becomes greater than the magnetostatic energy advantage from the presence of multiple domains, so the lowest energy configuration becomes one supporting just a single domain aligned with the nanowires long axis due to shape anisotropy.[65,83]

As nanowires are thin, Néel domain walls are expected which have a simple structure of spins which rotate largely in-plane and traverse the wire width. Different forms of in-plane magnetisation rotation give rise to vortex, symmetric or asymmetric transverse domain wall structures, as illustrated in figure 2.13.

The *transverse wall* (figure 2.13(a)) shows a triangular arrangement of spins with non-zero magnetisation perpendicular to the wire axis with, in this case, a wider structure at the top edge than the bottom. With increasing wire width this asymmetry becomes more prominent bringing about an increase in magnetostatic energy due to the free poles on the nanowire edge. Wider wires allow a rearrangement of the spin structure to an *asymmetric transverse wall* (figure 2.13(b)) and then to a *vortex wall* (figure 2.13(c)) where the larger cross section allows for an in-plane flux closure structure to develop with just a localised core
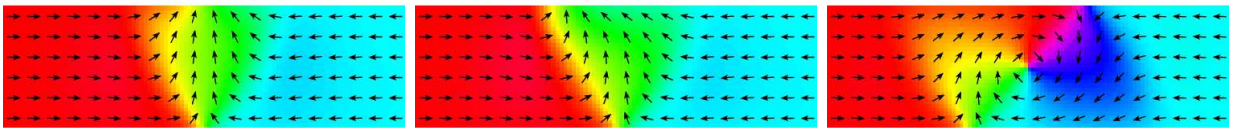
Figure 2.13: Micromagnetic simulations showing a) symmetric transverse, b) asymmetric transverse and c) vortex type domain wall structures in a 150 nm wide, 10 nm thick permalloy wire.

with out-of-plane magnetisation.[84] The reduction in magnetostatic energy outweighs the increase in exchange energy, and as a result the vortex wall becomes energetically favourable in wider wires whilst transverse walls are stable with lower energy in thinner wires.

A phase diagram of the stable domain wall structures in a permalloy nanowire of width, w, and thickness, d, developed by McMichael and Donahue[84] and later improved by Nakatani[12] to include asymmetric domain walls is shown in figure 2.14. This phase diagram shows that for large cross sectional areas, vortex walls are expected whilst transverse wall structures are more energetically favourable in wires with smaller cross sectional area. The transition between these structures occurs at $wd = (60 \pm 2)\Lambda^2$ and is first order, where the energy must overcome an energy barrier for the transition to occur. This allows both structures to be metastable outside of their region of stability.[85] The transition between asymmetric and symmetric transverse wall structures is second order, so structures cannot be separated under a field.[12]

The wall width, δ_{DW}, can be approximated by $\delta_{DW} \approx w/\pi$ for symmetric transverse walls and $\delta_{DW} = 3w/4$ for vortex walls,[12] showing a linear increase with wire width that is more pronounced for vortex walls. Both of these structures show little dependence on the nanowire thickness but for asymmetric transverse walls δ_{DW} increases with nanowire width and thickness.

The illustrations of domain walls in figure 2.13 separate two domains with magnetisation directed towards the domain wall, known as head-to-head domain walls. Corresponding tail-to-tail domain walls have inverted magnetisation but have similar properties. Domain wall
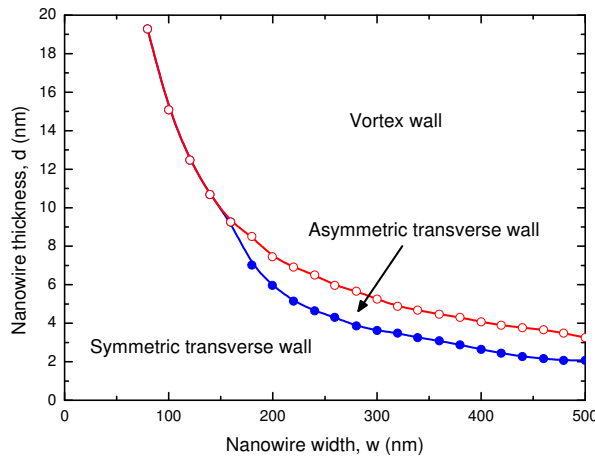
Figure 2.14: Phase diagram showing stable domain wall structures in a NiFe nanowire of thickness, d, and width, w.[12]

structures also have chirality depending on the orientation of the perpendicular magnetisation component of a transverse wall. In vortex walls a four-fold chirality exists depending on the direction of the out-of-plane component of the vortex core combined with the winding direction of the magnetisation.

2.8 Domain wall pinning

In addition to the extended structure of a nanowire, further modifications of the energy landscape can be achieved by the introduction of localised features within the nanowire design. This can be used to artificially introduce pinning sites to investigate domain wall pinning. A greater understanding of this is important, in some cases unwanted pinning hinders domain wall motion and is avoidable and in other cases it is very important for the control over the positioning of domain walls.

Domain wall pinning originates due to the stray fields from domain walls which interact with defects in the material leading to variations in the energy landscape of the wire. This can lower the domain wall energy at a particular location or present a potential barrier which needs to be overcome and both of these effects can result in domain wall pinning.[86,87] Pinning occurs naturally from roughness or defects in the material but can also be introduced artificially for control over the positions of domain walls in domain wall devices.

2.8.1 Pinning by structural defects

A defect such as a non-magnetic inclusion eliminates the need for a change in magnetisation over the defect. A domain wall over this defect has a reduced volume giving it a lower energy which acts to pin the domain wall. A magnetic defect presents a barrier for the domain wall as it takes a larger energy to rotate the magnetisation within the defect.

Defects can be divided into two regimes depending on the relative size of the defect, D, in comparison with the domain wall, δ_{DW}. For sharp transitions between the material and defect parameters the model developed by Friedberg and Paul[88] and later refined by Paul[89] gives the reduced coercivity as:

$$h_c = \frac{H_c M_1}{K_1} \tag{2.22}$$

which increases in proportion with the magnetisation, M_1, and inversely with the anisotropy

constant, K_1, in the crystal lattice. Here the subscript 1 denotes the parameters of the crystal lattice whilst 2 represents the differing values for the defect.

The reduced coercivity is found in terms of the following dimensionless parameters: $F = A_2 M_2 / A_1 M_1$, representing the saturation magnetisation of defect, $E = A_2 K_2 / A_1 K_1$, representing the anisotropy of the defect, $\delta_{DW} = \sqrt{A_2 / K_2}$, the domain wall width in the defect and $w = D / \delta_{DW}$ the ratio of the defect size to the domain wall width.

This theory gives a linear increase in coercivity as $H_c \sim D / \delta_{DW}$ for $D \ll \delta_{DW}$ explained as the defect fills a greater proportion of the domain wall width leading to a greater reduction in local energy and hence a greater pinning effect.[48] For $D > \delta_{DW}$ the coercivity saturates at a value determined by the difference between defect and matrix anisotropy.[89]

An alternative model for $D > \delta_{DW}$ exists for the case of a fuzzy defect experiencing a gradual change in magnetic properties between the material and the defect.[90] Here, the coercivity:[48]

$$H_c \approx \frac{2 H_a}{\pi} \frac{\delta_{DW}}{D} \left[\frac{\Delta A}{A} + \frac{\Delta K}{K} + \frac{3}{2} \frac{\lambda_s \Delta \sigma}{K} \right] \tag{2.23}$$

scales as δ_{DW} / D multiplied by terms representing fluctuations in the exchange stiffness, anisotropy and magnetoelastic anisotropy in the defect and gives a decrease in coercivity when $D > \delta_{DW}$.

Figure 2.15 illustrates this behaviour based on the relative size of a defect and the domain wall. The linear increase of coercivity as $H_c \sim D / \delta_{DW}$ for $D \ll \delta_{DW}$ can be compared with the saturated coercivity for the larger defect case and with the reduction as $H_C \sim \delta_{DW} / D$
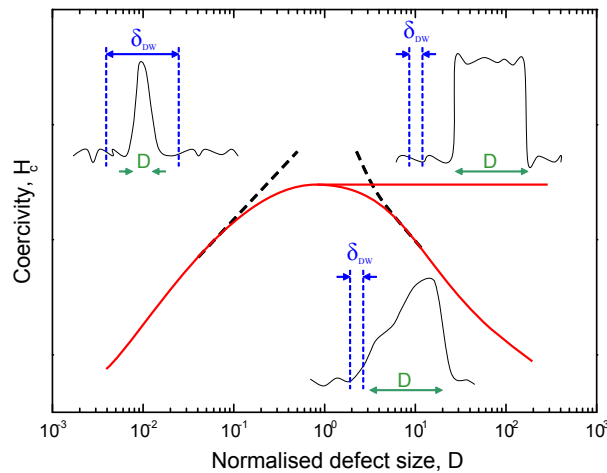
Figure 2.15: Illustration of the variation in coercivity of a domain wall pinned on a defect as a function of the relative size of the defect, D, and domain wall, δ_{DW}.

for the fuzzy defect case.

In materials sharp defects commonly result from grain boundaries and dislocations. Fuzzy defects result from strain, diffusion or composition fluctuations within a material.

2.8.2 Pinning by geometrical features

In nanowires, non-magnetic defects can be introduced artificially by the omission of magnetic material in the form of a notch. Magnetic defects can also take the form of an inclusion of additional magnetic material as anti-notches in a nanowire geometry.[91,92] The engineering of these structures is easily achieved using lithographic techniques giving control through the geometrical size and shape of the features[11] along with the combination of multiple features to form constrictions[9,10] and allow for greater control over the de-pinning field.

The micromagnetic structure of a domain wall, in addition to the notch/anti-notch geometry, has a large influence on the pinning potential. This has led to the design of notches for pinning different domain wall structures[93,94] including differential pinning potentials between head-to-head and tail-to-tail domain wall varieties[95] and domain wall chirality sensitive pinning.[14,96]

The combined understanding of domain wall structure and nanowire geometry allows for the manipulation of domain walls through in potential devices. These include domain wall diode structures requiring a higher de-pinning field in one direction than the other effectively only allowing the propagation in one direction. This is demonstrated both with micromagnetic simulations[14] and experimental results[13,17] with a single feature, whilst ratchet behaviour is displayed with multiple asymmetric anti-notches along a nanowire geometry.[15,16,97]

2.8.3 Pinning by modified material

A lot of work has been performed on the behaviour of domain wall pinning through the inclusion of artificial geometrical features for the pinning of domain walls in nanowires. However, the modification to the magnetic properties of the nanowire by the localised inclusion of defects is becoming another viable method for domain wall control. The control over the domain wall properties has been demonstrated in both perpendicular magnetic anisotropy (PMA)[98] and in-plane anisotropic materials;[99,100] however this area has not been fully ex-

plored. This is the theme of chapter 8 looking at the use of localised modification of the magnetic properties in nanowires for the control of domain wall pinning by ion irradiation.

Localised regions of modified magnetic material along a nanowire may also be preferable to the inclusion of artificial notches for domain wall pinning. The irradiation allows the nanowire to retain its geometrical structure and this is less likely to modify other properties such as the electrical resistance along the wire which may be important for device applications.

2.9   Domain wall propagation

The application of magnetic field to domain walls in nanowires, as well as supplying energy for de-pinning from pinning sites, can provide a driving force for domain wall propagation. The Zeeman energy from a field along the wire axis favours one domain orientation over the other. This means that the domain with parallel alignment increases in size at the expense of the anti-parallel domain effectively moving the domain wall.[20] The spins that make up a transverse domain wall have a large magnetisation component orthogonal to the nanowire axis. Under the influence of an applied field along the nanowire axis these spins feel a torque leading to a rotation of the spins out of the plane of the nanowire. This out of plane magnetisation component sets up a demagnetising field which also acts on the orthogonal magnetisation component of the domain wall to provide a torque, rotating the spins in the direction of the applied field.

These torques set up by the applied field drive the precession of the spins in the material. This precessional motion is damped by the damping in the material allowing the spins to ultimately align with the applied field direction. The passage of a domain wall over a section of a material can then be understood by the increase in the precessional motion of the spins which then rotate and precess around the new magnetisation direction parallel with the field. As the domain wall passes these spins are damped to their final state.

The patterning of magnetic material into nanowire structures has enabled experiments showing the propagation of domain walls under low fields[18,101] where control of the geometry can be used to guide domain walls around corners[4,5,11,18,19,102] and through tapered wire sections.[7,102] This level of control is useful for technological applications but an alternative method of manipulation of domain walls through spin transfer torque (STT) is predicted to ultimately be more convenient and allow for a greater degree of manipulation over the domain

walls.[103] However, the theory of field driven domain wall propagation will be discussed here as this is well established and also more appropriate for experimental investigation.

Domain wall dynamics were first investigated in the Sixtus-Tonks experiments[104,105] which gave rise to the concept of domain wall mobility, defined as the ratio of the velocity to applied field. This is useful for describing dynamics at low fields where velocity, v, increases linearly with field, H_x, due to the Zeeman energy gradient given by:

$$v = \frac{\gamma_0 \delta_{DW}}{\alpha} H_x \tag{2.24}$$

where γ_0 is the gyromagnetic ratio, δ_{DW}, the domain wall width and α, the Gilbert damping parameter.[106] Figure 2.16(a) demonstrates this linear increase in domain wall displacement with time for 4 Oe and 10 Oe driving fields giving rise to a velocity with a linear dependence on field shown for low fields in figure 2.16(b).

2.9.1 Walker breakdown in domain wall propagation

A further increase in field beyond the *Walker field* leads to the onset of *Walker breakdown* where a dramatic change in domain wall dynamics occurs resulting in a rapid decrease in time-averaged domain wall velocity. This is predicted from the dynamic solution to the 1D Bloch wall equation by Walker[21] and is caused by a limit imposed by the precessional frequency of
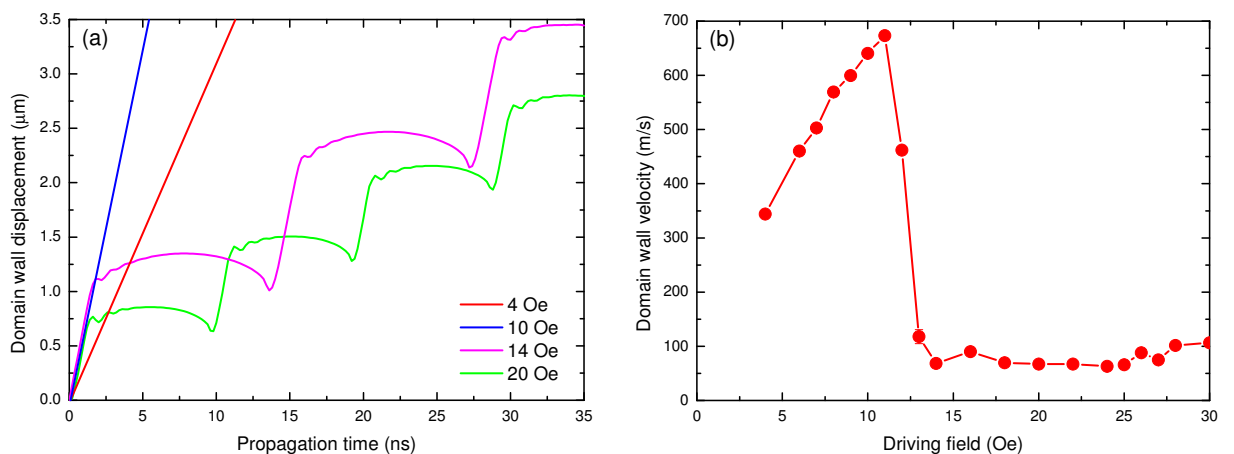
Figure 2.16: Propagation of a transverse domain wall in a 250 nm wide 5 nm thick NiFe nanowire at fields above and below the Walker field. a) The domain wall displacement shows a change from linear to periodic motion b) giving an average velocity with a dramatic reduction at the Walker field.

the spins where the rotation rate of the spins cannot maintain the fast domain wall velocity. This phenomenon has been confirmed experimentally in many structures including NiFe nanowires.[20]

Micromagnetic analysis shows that during Walker breakdown, the internal structure of the domain wall undergoes periodic oscillation between a transverse wall structure and antivortex core structures. The fast transverse walls are interrupted by the nucleation and slow traverse of the wire width, by the antivortex structure which even includes a phase of retrograde wall motion. The periodic nature of the wall propagation and retrograde motion is shown in figure 2.16(a) for the 14 Oe and 20 Oe driving fields giving a dramatically reduced domain wall mobility in comparison to the mobility below the Walker field shown in figure 2.16(b).

The physical mechanism for this change in behaviour originates from the pinching end of the 'V' shaped transverse wall structure where the rapid rotation of the spins required for the domain wall motion exceeds the precessional frequency of the spins in the material. This results in the incomplete switching of spins at the nanowire edge and hence the pinching end of the transverse domain wall moves into the wall in the form of an antivortex core. This has an out-of-plane M_z component and winding direction governed by the precession of the magnetisation around the applied field.[107]

The dynamic Slonczewski equations[66] can be used to model the 1D domain wall motion and give the Walker field as:

$$H_W = \frac{\alpha H_K}{2} \tag{2.25}$$

based on the damping parameter, α, and transverse anisotropy, H_K. One can also find the Walker velocity:

$$v_W = \frac{\gamma_0 \delta_{DW}}{\alpha} H_W = \frac{\gamma_0 \delta_{DW}}{2} H_K \tag{2.26}$$

which depends on the gyromagnetic ratio, γ_0, the domain wall width, δ_{DW}, but not on α.[107]

2.9.2 Walker breakdown suppression

Surprisingly, nanowires with rough edges show improved domain wall dynamics where high mobility is found beyond the Walker field.[82,108] Micromagnetic analysis shows the regions of high M_z develop but then dissipate with the emission of waves in magnetisation before the creation of a full antivortex core is completed.[82] Turbulence due to a system of fine amplitude interacting spin waves are left in the wake of the propagating domain wall as it

interacts with many roughness facets. This can be interpreted as allowing a new energy dissipation channel to be opened up in Thiele's formula.[109]

By the very nature of edge roughness, it is hard to control, so other methods for preventing the formation of the antivortex core have been explored. The application of a transverse field to a nanowire provides Zeeman energy which maintains the spins in the 'V' shaped transverse wall configuration.[106] The nucleation of the antivortex core is then suppressed up until a higher energy. The application of external quasi-static perpendicular fields[110] or oscillating axial fields[111] also have a similar effect maintaining the transverse wall structure. As an alternative to external fields modified structures including magnetic underlayers[112] or lateral comb structures[113] incorporated into the nanowire design also show the suppression of Walker breakdown from intrinsically supplied field.

2.10   Injecting domain walls into nanowires

In order to study the properties of domain walls in nanowires, techniques for the nucleation and injection of the domain walls into the nanowires are important. To understand these techniques, it is best to start with an understanding of domain wall nucleation in larger scale materials. For a domain wall to nucleate, the spins in a region of the material need to rotate which can be achieved through the application of a magnetic field leading to an increase in the Zeeman energy. Once this field overcomes an energy barrier associated with the spin rotation, the domain wall can nucleate. Normally this effect occurs near defects or as a result of edge or surface roughness in a structure due to the localised magnetostatic energy of the defect.[114] This additional energy allows the energy barrier to be overcome at a reduced applied field where the defect or edge roughness becomes the nucleation point in the system.

For experiments on domain walls, control over the nucleation process is desirable. Here, two different techniques were adopted for the nucleation of domain walls at low fields. These include the geometrical patterning of a nucleation pad onto a nanowire structure and the addition of a stripline for applying localised pulsed magnetic fields.

For completeness, a further domain wall injection technique can be achieved through the localised ion beam irradiation of PMA material.[115,116] This is a popular technique in these materials due to the rotation of the anisotropy, however permalloy has in-plane anisotropy so this is not a suitable method for the nucleation of the domain walls in this investigation.

2.10.1   Nucleation pad domain wall injection

Nanowires have a high aspect ratio with strong shape anisotropy aligning the spins along the wire axis and high coercive field is required to overcome this anisotropy to switch the magnetisation. In comparison, a wider structure has much less shape anisotropy and will therefore switch at a lower field. A wide pad structure can be included on the end of a nanowire to create a structure that displays a combination of both of these properties. The nucleation of a reverse domain and domain wall occurs at a relatively low field, governed by the large size and reduced aspect ratio of the nucleation pad, and domain walls can be investigated in the nanowire, as the pad is connected to the wire. This approach gives control over the nucleation location and propagation direction in the structure.[1,117] Likewise, a thinner structure such as a tapered end reduces the chance of nucleation. It is common to include both structures, one on each end of a nanowire, for domain wall experiments.

Figure 2.17 shows a nanowire geometry including a nucleation pad and tapered end for the nucleation and injection of a domain wall from the left hand end of the nanowire. Propagation along the wire continues with the driving force of the applied field until annihilation of the domain wall occurs at the tapered end of the wire after the successful switching.

This technique allows domain wall dynamics to be investigated at fields above the injection field with control over the nucleation position and therefore propagation direction. Careful design of the nucleation pad and applied field sequence can also give control over the domain wall type and chirality that is injected into the wire.[94]

The limitations of this technique are that domain walls in the nanowires can only be investigated at fields greater than the injection field of the pad. Some approaches have adopted complex bent structures to separate the injection field from the propagation field.[18] This methodology means that an additional transverse field component is also present during the measurements which may have other undesired effects on the results.
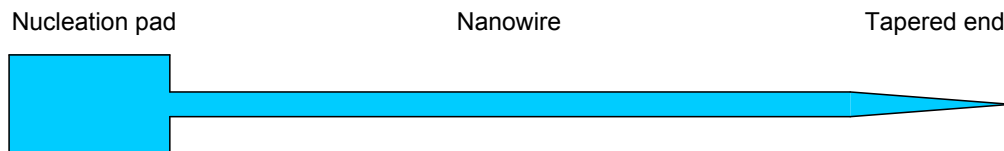
Figure 2.17: The inclusion of a wider nucleation pad onto a nanowire structure for the injection of domain walls into the nanowire. The tapered end restricts nucleation at that end allowing the propagation direction to be controlled.

2.10.2 Localised pulsed field domain wall injection

Another technique for the nucleation of domain walls is through the application of a localised pulsed field to overcome the coercivity of the wire in a specific location along the nanowire. This is performed by passing a pulsed current through a conductor, perpendicular to the nanowire.[10] The schematic in figure 2.18 shows the typical arrangement of a nanowire with a stripline injection circuit.

The field generated from a stripline nucleates a reversed domain and pair of domain walls at the intersection point with no limits on additional bias fields as in the nucleation pad case. There is also the added advantage that the nucleation process can be triggered electronically allowing it to be synchronised with other field sequences allowing for many complex dynamic domain wall experiments which are not possible with nucleation pads.[118,119] This technique also gives more control over the injection as it can be separated from the domain wall propagation therefore allowing the injection of multiple domain walls into a nanowire.[120] The choice of pulsed field amplitude, pulse length and current direction even allows for a choice of domain wall structure rather than relying on device geometry during the fabrication stages.[121]

This technique comes at the price of a more complex sample fabrication process requiring multiple lithographic steps (discussed further in chapter 3). The experimental protocol is also more involved requiring electrical connection to the sample and synchronisation between pulsed fields and external bias fields. In this thesis both domain wall injection techniques will be adopted. Initially the nucleation pad injection technique can give a basic domain wall injection scheme but the requirements for domain walls at low bias fields led towards the use of the pulsed injection technique too.
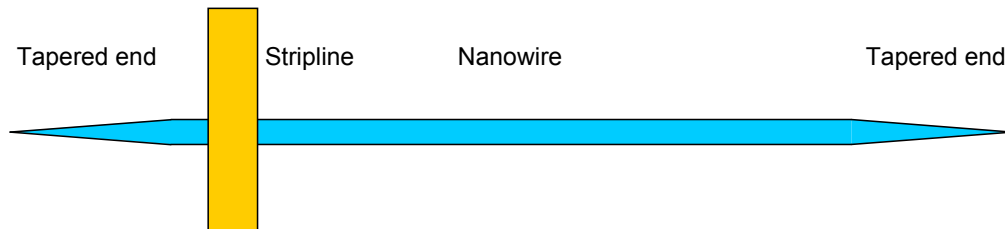
Figure 2.18: Schematic illustration of a domain wall injection stripline carrying a current pulse perpendicular to a magnetic nanowire for the nucleation of a domain wall at the intersection point.

Chapter 3

Preparation and patterning of thin ferromagnetic films and nanostructures

3.1   Introduction

This chapter considers the processes involved with the fabrication of thin-film magnetic samples, including their growth and the effect of ion irradiation on their structural and magnetic properties. This is combined with further patterning techniques to explain the process for fabricating the magnetic structures and devices that were introduced in chapter 2.

Material properties such as crystal structure and defects are also introduced with emphasis on thin film materials. Techniques for the growth of thin films are discussed, in particular growth by thermal evaporation as this method was used extensively in this investigation.

Modifications to the structure of the thin films following ion irradiation are discussed in some detail as this is key to this thesis. This includes the ion implantation and the sputtering of material from the sample surface at high doses, but more relevantly, the intermixing at the interfaces in multilayered structures. The modifications to the magnetic properties of the sample are discussed in relation to the changes to the sample structure as a function of irradiation dose.

The patterning capabilities of the dual ion and electron-beam system, which allow for the fabrication and modification of nanostructured samples are then described. These give control over the magnetic properties of nanostructures, both via their shape anisotropy (chapter 2)

and through the modification of the magnetic properties of the material.

3.2 Structural background to materials

This section describes the theoretical background governing the structure that is formed from the arrangement of many atoms when they combine to form materials. This structure, along with the defects occurring within the structure, has a major influence upon the physical properties of the material.

3.2.1 Crystalline structure of materials

When atoms combine together to form materials, a crystalline arrangement is common where a repeating *basis* is arranged in a regular *lattice* structure. There are 14 different lattice structures but only the simple cubic (sc), body-centred cubic (bcc) and face-centred cubic (fcc) lattice structures are relevant to this investigation. The *unit cell* representing the smallest repeat unit of the lattice is illustrated in figure 3.1.

These unit cells have a spacing known as the lattice parameter, d. For Ni, Fe and Au the crystal structures are fcc, bcc and fcc with lattice parameters 3.52 $\mathring{A}$, 2.87 $\mathring{A}$ and 4.08 $\mathring{A}$ respectively.[122] In NiFe alloys the crystal structure is bcc for Ni content below 30%. For higher compositions there is a phase transition to a fcc structure[48] which represents the alloy compositions of interest, in the range $Ni_{81}Fe_{19}$[123] where the lattice parameter decreases with increasing Ni content.[124] An ordered state, $FeNi_3$, also exists; however the magnetic properties of this alloy are inferior to the disordered alloy. Luckily this has a slow ordering time and can be avoided with a reasonable cooling rate to avoid crystallisation.
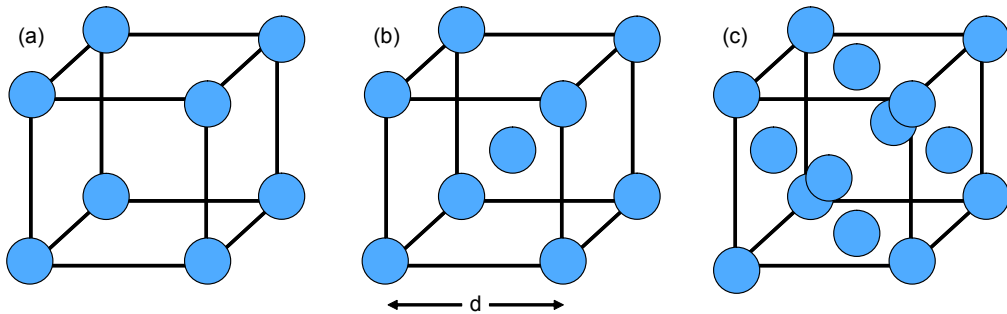
Figure 3.1: Unit cell of a a) simple cubic (sc), b) body-centred cubic (bcc) e.g. Fe and c) face-centred cubic (fcc) e.g. Au, Ni, NiFe lattice structure with lattice parameter, d.

3.2.2 Crystal defects

Materials rarely form single crystals with perfect crystalline arrangement and it is common for most materials to contain crystal defects, which have a large influence upon the macroscopic properties of the material.

A crystalline structure that grows from multiple nucleation sites will form regions with the same crystal structure but each is likely to have a different orientation of the crystal axes. This results in crystallite *grains* separated by *grain boundaries* as illustrated in figure 3.2(a). Polycrystalline material results from a high density of initial nucleation sites, while reducing the number of nucleation sites results in fewer, larger grains.

Defects also form at the interface between two layers with different lattice parameters and this is known as *lattice mismatch*. This can lead to elastic compression or expansion of the unit cell (figure 3.2(b)), or, if the mismatch is too great, the energy associated with the deformation exceeds an energy barrier and formation of a dislocation defect occurs. In this case the lattice returns to its original size and dislocation defects are introduced where an atomic plane is skipped (figure 3.2(c)).

The addition or omission of a single atom from a crystal structure is known as a *point defect* of which there are several variations as illustrated in figure 3.3. *Vacancy defects* occur when an atom is omitted from the crystal, and *interstitial defects* occur when an extra atom of the same kind is present in the crystal. If a crystal is doped with a different element this is known as a *substitutional defect*. This distorts the lattice spacing depending upon the relative size of the defect and matrix.
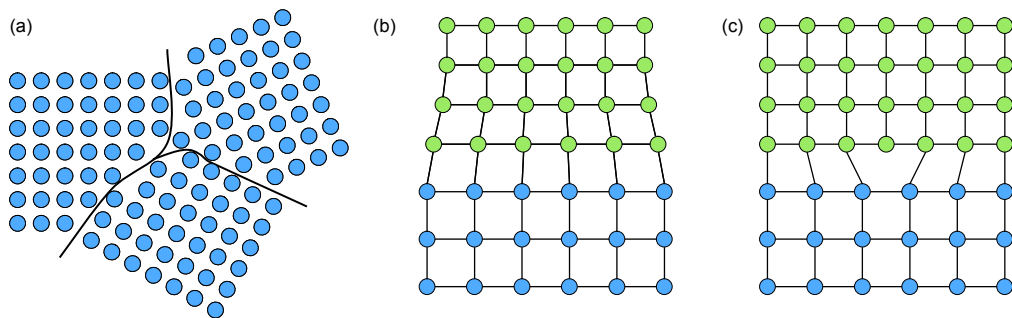
Figure 3.2: a) Grains of crystalline material separated by grain boundaries and lattice mismatch at an interface causing b) elastic deformation and c) the inclusion of a dislocation defect.
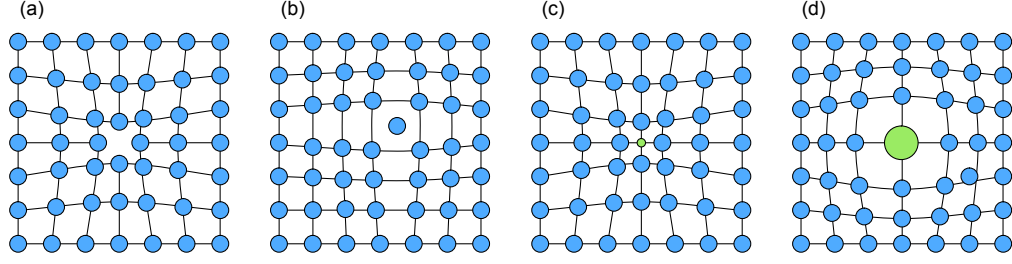
Figure 3.3: Types of point defects in a crystal structure: a) vacancy defect, b) interstitial defect, and substitutional defects with c) smaller and d) larger atoms.

3.3 Growth of thin film magnetic materials

This section describes the different growth modes that can occur during the growth of metallic thin films. These are typically grown on a substrate by either sputtering or thermal evaporation techniques where the source material is gradually added to the substrate increasing the layer thickness.

3.3.1 Thin film growth modes

When material from a vapour-phase source reaches a substrate it becomes adsorbed onto the surface and remains attached to the surface either by physical Van-der Waals forces or more strongly if chemical bonding occurs with the substrate. If the energy of the adatom exceeds the adatom-surface binding energy, the adatom is free to move around the sample surface or even leave the surface.

There are different modes of material growth, illustrated in figure 3.4, that depend upon
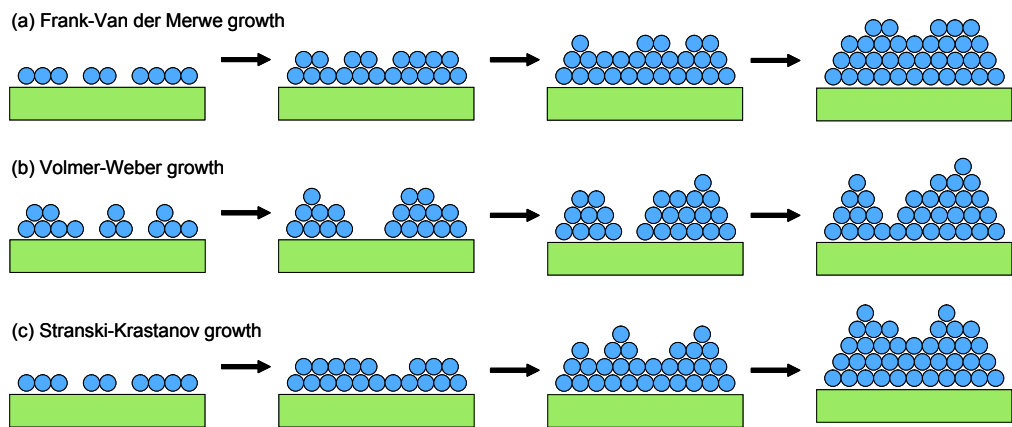
Figure 3.4: Thin film growth depends on the relative strength between adatom-adatom and adatom-surface binding energies. This gives rise to different growth modes known as a) Frank-van der Merwe growth, b) Volmer-Weber growth and c) Stranski-Krastanov growth.

the relative strength of the adatom-adatom and adatom-surface binding energies. [125] When the adatom-substrate system is more strongly bound than the adatom-adatom system, the deposition tends to form continuous epitaxial layers in a process known as *Frank-Van der Merwe* or layer-by-layer growth. In the opposite case where adatom-adatom binding dominates, then the growth of islands and droplets of material is favoured for energy minimisation. This mode is known as *Volmer-Weber* or island growth. *Stranski-Krastanov* growth is another mode where initially Frank-van der Merwe growth takes place up to a critical thickness where strain in the layer results in a change to Volmer-Weber type island growth.

For NiFe films on Si or SiO$_2$ Frank-Van der Merwe growth is expected, [123] but for Au it is possible that Volmer-Weber growth will dominate. [126] Weak bonding between Au and the substrate also means that an adhesive layer, such as $\approx$ 3 nm Cr, is required before each Au deposition.

3.3.2 Thin film deposition by thermal evaporation

In this investigation, the thin magnetic films were grown using the thermal evaporation technique that was first used for NiFe films by Blois. [127] Material is heated by passing a DC current through a resistive crucible until the material melts and begins to evaporate at a constant rate. In high vacuum the material travels ballistically to a substrate where it is then adsorbed onto the substrate, forming a layer of the source material. For metals and alloys, these layers are typically polycrystalline with a grain size of the order of 10 nm[128] and films can be grown with a thickness from nanometres to micrometres.

For thermal evaporation, source material must melt at a reasonable temperature and maintain a reasonable partial vapour which explains why this technique is good for metals but more complex for insulators with higher melting temperatures. For alloyed source materials there may be a differential evaporation rate between the components, but for the case of NiFe the change in composition is small. [127] Therefore the thin film composition can be chosen using the appropriate source alloy mixture.

To produce high quality films, the evaporation must be performed in a good vacuum to reduce film contamination and oxidation, which may otherwise result in defects in the film during deposition. It is common to bake out the crucibles and chamber prior to deposition to allow contaminants adsorbed onto the source material and gases diffused in the chamber structure an opportunity to diffuse out.

With a multi-source system it is possible to fabricate devices with different layers by heating different sources in turn or by co-evaporation to create alloys. This allows multilayered structures to be created with high quality interfaces since the sample remains under vacuum for the whole growth.

A simple way to introduce lateral patterning is to perform thermal evaporation through a shadow mask, shielding regions of the substrate to leave deposited material only on the exposed regions. This is a relatively simple technique which is good for large structures as it produces structures the same size as the mask, although the patterning resolution is limited by machining capabilities when creating the mask; here features down to $\approx 0.1 - 0.5$ mm have been produced. To achieve even smaller feature sizes, patterning with electron beam lithography has been performed: this is discussed in more detail in section 3.7.

3.4 Ion - solid interactions

Now that the basics of material structure have been established, this section describes the physical background behind the processes involved as an energetic ion is incident on a target material. There are three main processes: ion implantation, sputtering and intermixing, all of which are illustrated schematically in figure 3.5 and discussed in detail below. These processes are all characterised in terms of the irradiation dose, which is a measure of the
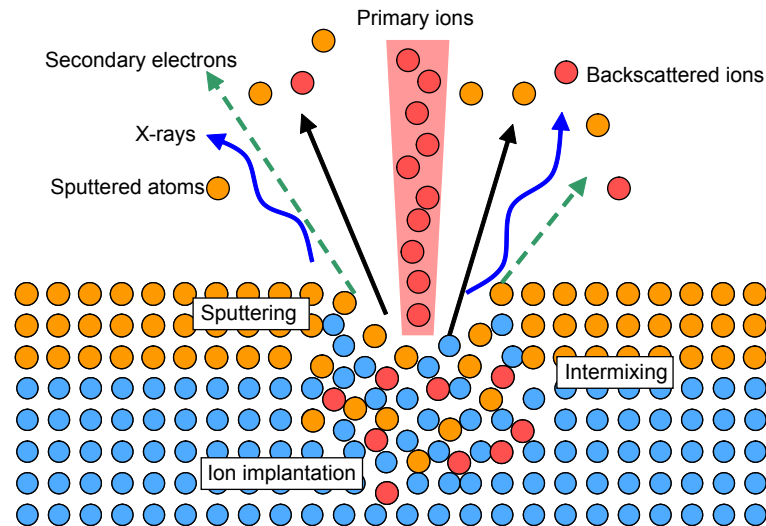
Figure 3.5: Illustration of the physical processes resulting from energetic ion irradiation on a bilayer sample including sputtering, intermixing and implantation. Various backscattered ions, sputtered atoms, secondary electrons and x-rays are also emitted into the vacuum as a result of the irradiation.

number of incident ions per unit area of the irradiated sample and which is expressed with the units Ga^+/cm^2 throughout this thesis.

3.4.1   Irradiation induced ion implantation

The implantation of ions can lead to structural changes in the sample due to both physical and chemical processes. Physical changes result from the inclusion of defects in the sample lattice which generates regions of local stress due to the dissimilar atomic size. Chemical effects may also take place if the implanted ion forms chemical bonds in the lattice to make an alloy.

The degree of implantation can be formulated by considering energetic incident ions that are scattered by atoms in the sample, reducing their energy and modifying their initial trajectory. After multiple scattering events the ions may return to the vacuum as backscattered ions or come to rest within the sample as implanted ions when their energy falls below the displacement threshold energy. The number of ions implanted at a depth, x, can be approximated by a Gaussian distribution described by the average range of an ion, its projected range, R_p, with a peak concentration, n_0, and a standard deviation, σ_p:[129]

$$n(x) = n_0 \exp\left(\frac{(x - R_p)^2}{2\sigma_p^2}\right).$$ (3.1)

This can be integrated to find the peak concentration, n_0, based on the incident ion dose per unit area, ϕ, giving

$$n_0 = \frac{1}{\sqrt{2\pi}}\frac{\phi}{\sigma_p}.$$ (3.2)

A more robust analytical approach to predicting the range of implanted ions by Lindhard, Scharff and Schiott is known as the LSS theory.[130] This is based on the probabilities of scattering from binary collisions and can predict the ranges of ions to within 20% which is usually acceptable. More commonly, the predicted range can be obtained from Monte Carlo simulations using the projected range algorithm (PRAL) developed by Biersack, Littmark and Ziegler.[131,132] The application of these simulation techniques to this work is discussed further in chapter 4.

Equation 3.2 shows that an increase in the irradiation dose leads to a linear increase in the concentration of implanted ions. A sample can initially be thought of as having an increasing

number of defects, but there is also the possibility of a phase change where the sample may then be better described as an alloy of the initial sample material and the implanted atoms. Ga^+ ions implanted into Fe leads to a phase change at a Ga fraction of around 15 at. %.[133] However, the maximum doses used in this investigation give at most a 1% Ga fraction, so the formation of new phases was unlikely.

3.4.2   Sputtering of surface atoms

As previously mentioned, the incident ions transfer some of their energy to the atoms in the sample with each scattering event. If a near surface atom gains enough energy to overcome its surface binding energy, it can be ejected from the surface and enter the vacuum in a process known as sputtering. This has a significant effect on the structure, as it means material from the surface is removed from the sample.

The amount of sputtered material per incident ion is known as the *sputter yield*. This depends upon the surface binding energy, the atomic mass of the ions and the target atoms and can be predicted from Sigmund's theory for polycrystalline samples based on the linear Boltzmann transport equation.[134] This shows that sputtering is proportional to energy acquired by surface atoms and agrees well with experiments for a wide range of energies and ion-target combinations (see figure 3.6(a)).[135]

More recently this theory has been extended to accurately predict the angular dependence to the sputter yield.[135] This is illustrated in figure 3.6(b) for Ga^+ ions incident on a Si target
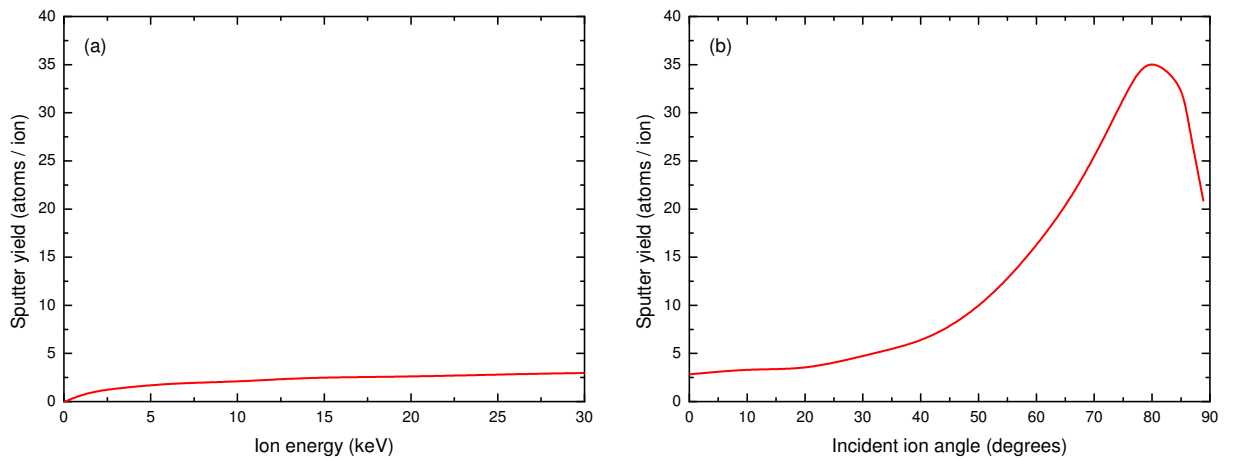
Figure 3.6: Sputter yield as a function of a) incident ion energy at normal incidence and b) incidence angle at 30 keV for Ga^+ ions on a Si target.[136]

showing a maximum yield at 80° incidence angle.

This characterisation of the sputtering assumes a single crystal silicon target. However, sputtering of a polycrystalline film shows variations in the behaviour due to the relative alignment of the beam direction with the different crystallographic axes in each grain of the material. The crystalline orientation of some grains can lead to a channelling effect where incident ions travel deep into the sample. Here, the energy loss from the ion is more gradual so the sputtering and damage to the sample is greatly reduced.[137]

3.4.3   Interfacial intermixing

Atoms far from the surface are also affected by momentum transfer from the primary beam causing a relocation of atoms within a sample. This is particularly noticeable near an interface between different materials where atoms relocate across the interface in a process known as *interfacial intermixing*. The efficiency of this mixing, given by the number of mixed atoms per incident ion, for an Au/Cu system mixed with Xe is more than 10 times as efficient compared with the direct implantation of Au into Cu.[138]

Ballistic mixing

The *ballistic model* can be used to describe ion beam mixing based on elastic collisions between incident ions and target atoms. The simplest form of ballistic mixing is known as *recoil mixing* where a proportion of the incident ion's kinetic energy is transferred to a single target atom near an interface. With high energy incident ions, the target atom recoils deeply into the target ($\approx$ 50 nm), where the maximum range corresponds to a head-on collision. The number of recoil events increases linearly with the irradiation dose and is independent of temperature: however, head-on collisions are not common so recoil mixing is not a large contributing factor.[139,140]

Recoil mixing is also an entirely forward-momentum model and fails to give an explanation for the isotropic broadening observed with ion irradiation on thin film marker structures.[141] Expanding this model to include further collisions between recoiled atoms and additional target atoms shows that many atoms can undergo multiple low-energy uncorrelated collisions in a process known as *cascade mixing*. The net effect is a collision cascade where atomic relocations follow a random walk showing a diffusion-like process according to Fick's law.[142]

The initial momentum direction of the incident ion is lost and displacement becomes isotropic about the interface and proportional to the concentration gradient at the interface.

Following the derivations by Nastasi,[129] the diffusivity, D, from thermally activated diffusion is given by:

$$Dt = \frac{n\alpha^2}{6} \tag{3.3}$$

which, following Anderson's[143] adaptation for collision cascades, effectively becomes:

$$D_c t = \frac{dpa(x)\langle r^2 \rangle}{6} \tag{3.4}$$

where the square of the jump distance, α^2, is replaced with the mean squared range of the displaced target atoms, $\langle r^2 \rangle$, and the number of jumps, n, is replaced with the number of displacements per atom, dpa. This is given by:

$$dpa = \frac{2}{5}\frac{F_D \phi}{E_d N} \tag{3.5}$$

using the damage energy per unit length, F_D, the atomic displacement energy, E_d, the ion dose, ϕ, and the atomic density, N. Combining these equations gives:

$$D_c t = \frac{F_D \langle r^2 \rangle \phi}{15 N E_d}. \tag{3.6}$$

An alternative approach to this formulation by Sigmund and Gras-Marti,[141,144] based on linear transport theory includes the mass difference between ion and target atoms and gives a very similar result. Both of these equations show the effective diffusion constant, $D_c t$, scales with both the dose, ϕ, and damage energy, F_D.

Since ballistic intermixing is a diffusion-like process, the resulting composition variation over the interface can be described by an error function with an associated interface width.[145] This width is given by $\sqrt{4D_c t}$ which scales as the square root of the ion dose, $(\sqrt{\phi})$,[143] and is shown in figure 3.7.

Thermodynamic effects

Models by Anderson (equation 3.6), Sigmund and Gras-Marti[141,144] suggest that mixing is independent of the temperature and the chemical properties, and further suggest that
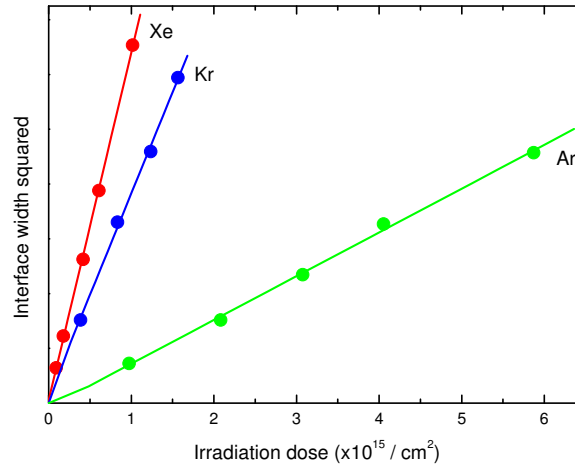
Figure 3.7: Interface width squared increases linearly with dose for 300 keV ions accelerated onto a Pt/Si bilayer. Interfacial broadening occurs at a greater rate for the heavier ions which carry a greater momentum.[138]

interfaces with similar physical properties should experience the same amount of mixing. However, differences in the mixing are found to result due to the chemical properties of the atoms at the interface that originate from *thermodynamic effects*.[129]

The enthalpy difference, ΔH_{mix}, is the difference between the enthalpy of the components A and B, and the enthalpy of their alloy AB. Negative ΔH_{mix} shows a greater preference for alloy formation, whilst positive ΔH_{mix} gives rise to preferential de-mixing (if the temperature is high enough) which competes with the ballistic mixing effects.

Since ballistic mixing gives rise to a square root relationship between irradiation dose and the interface width, a plot of the squared interface width is linear with dose only when ballistic intermixing takes place. In the thermodynamic case of preferential mixing, an alloy layer of fixed composition is expected to develop between the two layers, resulting in an enhancement to the interface width. Alternatively, preferential demixing will result in a reduced interface width. In this way, the plot of squared interface width with dose can be used to identify any contributions from thermodynamic effects.[146]

For an Au marker layer in Fe the heat of mixing is +38 kJ/mol and for Ni it is +34 kJ/mol.[147] These are both positive suggesting that preferential de-mixing is likely to be a competing effect for Au mixed in NiFe.[148,149]

Thermal spike model

Another deviation from the ballistic model comes from so-called *thermal spikes*, which occur as a result of the collision cascades.[150] Here, the incident energetic ion creates a collision cascade moving many target atoms away from their original location, resulting in a region of vacancies along the ion path with an over-dense region surrounding it. These vacancy-interstitial pairs are known as *Frenkel pairs*. Shortly after the collision cascade, the atoms return to fill the vacant sites, releasing energy equivalent to a short, sharp rise in temperature. This spike in thermal energy is sufficient that the atomic displacement energy is reduced, which can lead to mixing rates appearing up to ten times larger than rates predicted by ballistic models.[151]

Thermal spike effects are negligible for lighter elements ($Z_{ave} < 20$) and where the deposition energy, F_D, is low.[144] However, the elements relevant to this investigation are above this limit, so athermal mixing by thermal spikes can be expected.[145]

3.5 Structural effect on magnetic properties

The structural changes resulting from ion irradiation as described above give rise to changes in the magnetic properties when the irradiated sample is a magnetic thin film. In this section the previous work on irradiated magnetic thin film structures is discussed, with a focus on the relationship between the structural changes and changes to the magnetic properties.

3.5.1 Perpendicular magnetic anisotropy (PMA)

Many multilayered magnetic materials show perpendicular magnetic anisotropy (PMA), which originates from a strong magnetostrictive interfacial anisotropic component from stress due to symmetry breaking at the interfaces.[31] This effect depends on the interface sharpness[152] and variation in mixing at the interfaces during preparation allows for control of the magnetic anisotropy.[153] The pioneering work by Chappert in 1998[30] showed how ion beam irradiation can be used to tailor the magnetic properties of Co/Pt films with out-of-plane anisotropy, where regions of magnetic material can be patterned without affecting the topological surface roughness. Since this pioneering work, much attention has been paid towards these PMA systems due to their high coercivity and large magneto-optical response making

them well suited for high density recording media.[154]

The physical mechanisms leading to these changes in magnetic properties are attributed to the development of an intermixed region at the interfaces during the irradiation process. This mixing destroys the sharp interface structure, relieving the stress at the interface which then lowers the magnetostrictive anisotropy contribution.

As the interfacial anisotropy contribution is reduced, the shape anisotropy from the thin film geometry begins to dominate. This leads to a rotation of the anisotropy from PMA to an in-plane geometry, resulting in a decrease in the out-of-plane coercivity and an increase of the in-plane coercivity.[31–35,154–158] By a similar mechanism to the mixing at the interfaces, ion beam induced surface roughening has also been demonstrated to lead to a lowering of the surface contribution to PMA.[31,33,155–159]

Additionally, Co and Pt are miscible so the irradiation leads to the formation of Co-Pt alloy regions, which also contribute to the reduction in PMA.[30,31,33,154,155,157,158] Similar investigation with Co/Au interfaces where Co and Au are not miscible still leads to a reduction in PMA but not significant enough that the in-plane anisotropy becomes dominant.[154]

3.5.2 Loss of magnetic texturing

Most of these investigations in PMA materials also report a ferromagnetic to paramagnetic transition, which occurs with a further increase in irradiation dose.[30,33,155,159] This effect also agrees with the decrease in saturation magnetisation for the surface of in-plane anisotropic materials.[36,37,39,40] This eventually renders the surface as a non-magnetic dead layer with a thickness that increases with irradiation dose.[38,39]

These effects are accounted for by a reduction in magnetic moment from irradiation-induced damage in the near-surface region of the samples. This damage includes the amorphisation of the crystal structure, the introduction of scattering defects and the expansion of the lattice parameter by the inclusion of large defects.[41] The increase in defect density throughout the material also gives an explanation for the increase in coercivity due to an increasing number of domain wall pinning centres.

The implanted ions in the magnetic material give rise to only a small change in the magnetic moment due to their chemical alloying effects and the physical stress resulting from a large ion in a lattice. This is demonstrated by the reduction in moment of FeGa and NiGa with increasing Ga content.[38,160] In NiGa, the irradiation beyond a critical dose

leading to more than 20% Ga implantation leads to the complete quenching of the magnetic moment.[38] This quenching occurs due to a phase transition from crystalline to amorphous texturing which occurs above the critical dose threshold.[161]

3.5.3   Modified magnetic moment at intermixed interfaces

As discussed above, the intermixing at an interface can lead to a much greater mixing efficiency than by direct implantation, as a larger effect occurs due to the energy of the incident ion rather than its presence in the lattice following the irradiation.[156] The structural models show that the width of the intermixed region scales with the square root of the irradiation dose. This is consistent with the variation of the square root of the dose required to quench the magnetic properties as a function of sample thickness.[37] This shows that the interface region is responsible for the modification in the magnetic properties.

At the interfaces, several effects can account for changes in magnetism as a result of the intermixing.[162] Substitutional and interstitial point defects, due to the intermixed atoms, form localised regions of lattice stress. In the case of $3d$ transition metals this gives an increase in the magnetostriction coefficient which may lead to preferential magnetisation alignment along directions of applied stress.[163,164] At a magnetic/non-magnetic interface, polarisation effects, discussed in chapter 2, can modify the magnetic moments of both the magnetic and non-magnetic components. Interfacial intermixing modifies the local environment at the interface and can lead to changes in moment that result in macroscopic effects on the saturation magnetisation of the irradiated material.[39] The grain size is another property of the material that is modified by the irradiation. Materials with small grain size typically have soft magnetic properties with a low coercivity.[38] Irradiation-induced grain growth, due to effective annealing from the energy of the beam, gives rise to a reduced moment and an increased coercivity.[36]

3.5.4   Removal of magnetic material by sputtering

Finally, in the regime of very high irradiation doses, sputtering is the dominating mechanism for the modification of the sample structure. This also affects the magnetic properties by a reduction in the quantity of magnetic material in the sample.[165] A linear decrease in NiFe magnetisation is found to occur with high dose Ga irradiation.[38]

3.6 The dual ion and electron beam microscope

Most of the previous work on the irradiation of magnetic structures has been performed with large area irradiation, or irradiation through lithographically-prepared masks.[30] With the development of focussed ion beam systems it is possible to perform local irradiation allowing for direct patterning without the need for additional resist preparation steps. This has been demonstrated with a patterning resolution sub 5 nm;[166] however, for the most common applications, beams in the 50 - 100 nm range are more than adequate.[167] In this investigation, the FEI dual beam Helios Nanolab 600i system was used. This combines the functionality of both a scanning electron microscope (SEM) and focussed Ga^+ ion beam (FIB) system. It is widely used for rapid prototyping and device fabrication in a research environment and has the ability to define patterns for producing the magnetic nanostructures described in chapter 2, as well as to perform the local ion irradiation.

3.6.1 SEM and FIB operation

The SEM and FIB are very similar in their operation principles, in that a charged particle is produced at a source, accelerated by an electric field, focussed with electromagnetic lenses and positioned on the sample by deflection with electric fields from an octopole. The difference between the electron and ion columns is that the sign of all the fields is reversed to account for the opposite charge of the electrons and Ga^+ ions.

Schematics of the columns are shown in figure 3.8. These also contain other components such as apertures to limit the beam current and a beam blanker to effectively turn the beam on and off, both important during lithography and patterning.
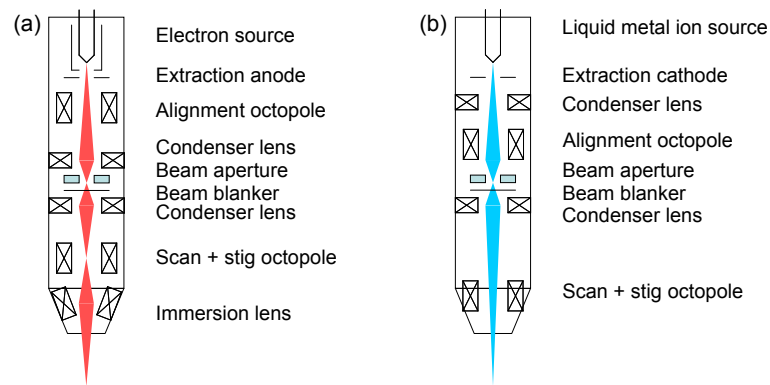
Figure 3.8: Schematic layout of the electron/ion optical components inside the a) electron and b) ion columns of the dual beam system.

Ions are produced from a liquid metal ion source (LIMS) where a tungsten filament heats a reservoir of gallium to its melting point (302 K[168]) which then wets a tungsten tip. A potential between the source tip and an extraction electrode produces a large electric field at the tip, drawing the liquid metal into a conical shape known as a Taylor cone,[169] in which the electrostatic forces and surface tension remain in equilibrium. The electric field at the apex of the Taylor cone leads to field extraction of the ions from the tip.[167] The extracted ions are then accelerated down the column by an acceleration voltage (typically 30 keV).

Electrons are produced from an Elstar Schottky field-emission source,[170] which works by field-assisted thermionic emission. This produces a large beam current[171] from a small source area, which is needed for high-resolution imaging and very useful for e-beam lithography.

3.6.2 Dual beam system

In the FEI Helios Nanolab system, the two columns are combined in a single vacuum chamber with the beams converging at 52° to a single focal point known as the *eucentric point*. The sample stage can be manipulated to move the sample to the eucentric point as illustrated in figure 3.9 which can be rotated for normal incidence ion or electron beams.

Beams incident on the sample produce backscattered and secondary electrons with an intensity giving information about the surface topology and composition. By scanning the beam over the sample, the intensity at each position can be combined to generate an image. Whilst imaging can be performed with both beams, the electron beam is preferred due to
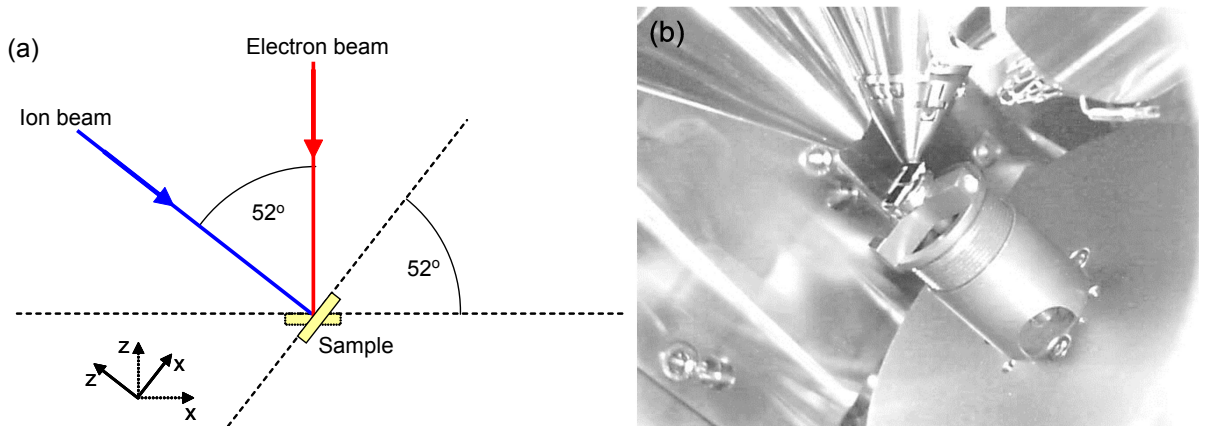
Figure 3.9: Electron and ion beams converge at 52° to a eucentric point in the dual beam system. During operation the sample is positioned at this point and can be rotated for normal incidence ion or electron beam. a) Shows a schematic illustration of the geometry of the sample space and b) shows a photo of the stage positioned at 52° at the eucentric point.

the damage caused by exposure from the ion beam. As the two beams are aligned at the eucentric point, the electron beam can be used for aligning the sample before irradiation to limit the Ga^+ exposure and allow more precise positioning of irradiation patterning.

3.7   Patterning magnetic material

So far in this chapter the techniques for the preparation of thin films, and the modification of their properties using ion irradiation have been discussed. Now, using lateral patterning, further control over the magnetic properties can be gained through control of the shape anisotropy. This section describes how micro and nanoscale structures can be fabricated and how local ion irradiation was performed using the dual electron and ion beam system.

3.7.1   Patterning with electron beam lithography

As previously discussed, shadow masks can be used to give control over the geometry of deposited material but these have a resolution limited by mechanical machining capabilities. However, smaller structures can be made through lithographic processes where a mask is created in a resist layer. With electron beam lithography, structures down to 30 nm can be fabricated in a process illustrated schematically in figure 3.10.

First, the substrate is spin-coated with a resist layer, such as the positive tone resist, polymethyl-methacralate (PMMA). Regions of the resist are then exposed by an electron beam which is scanned over the desired pattern. When the dose is in excess of the *clearing dose*, the secondary electrons provide enough energy to break apart the resist polymer molecules into shorter lengths, in a process known as *scission*. Chemical development of the
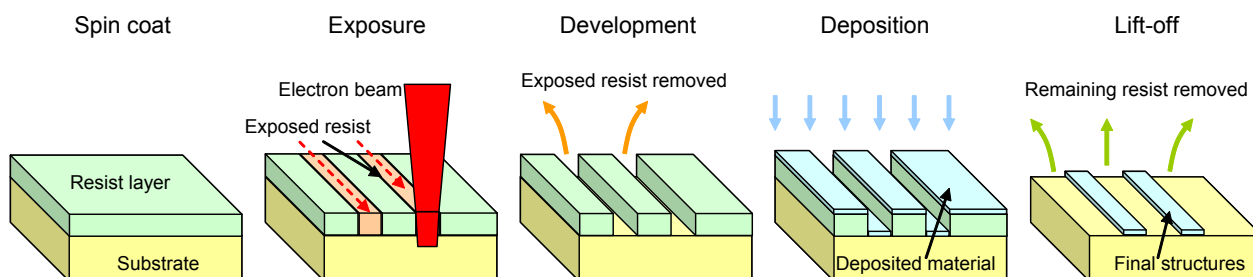
Figure 3.10: The process of lateral patterning using electron beam lithography. An electron beam exposes a pattern in a resist which is developed to leave a nanoscale stencil. Following deposition of the desired material, the remaining resist is removed in a lift-off procedure leaving the desired pattern on the substrate.

sample dissolves the more soluble shorter polymer chains, leaving only the unexposed PMMA remaining on the substrate to create a micro or nanoscale stencil on the substrate. At this stage, material can be deposited onto the substrate, in this case by thermal evaporation, and the process is completed by a 'lift-off' process where any remaining PMMA is removed, leaving only material deposited on the exposed regions of the substrate. Further details about the lithographic methods used here are given in chapter 5

3.7.2   Exposure of the patterns

For electron beam imaging, the beam is raster scanned over the field of view. In contrast, during patterning the scanning of the beam is controlled using scan-processing software where only the desired area of the sample is exposed. This area is divided up into pixels with a given footprint that is exposed for a selected dwell time, such that the area dose reaches the clearing dose for the resist. For simple shapes, the beam is scanned over the area in a raster or serpentine fashion but for more complicated patterns the scanning strategy is determined from comparison of the desired pattern with the available pixels on the raster grid.[172]

To achieve larger area patterning, greater than the size of the field of view, a more complex strategy is used where the pattern is divided into smaller sub units which are exposed separately. The sample stage is translated between exposures, effectively stitching adjacent patterns together.

3.7.3   Multiple layer alignment

Some sample designs require multiple lithographic steps, such as the preparation of NiFe nanowire structures with Au electrical connections. To ensure suitable alignment between subsequent steps this process relies on markers deposited during the first lithography step, which are then used to align the system in subsequent steps. The dual beam FIB/SEM incorporates various automated control mechanisms so the whole alignment process can be performed through the use of automation scripts.

Since structures are generally patterned in regular arrays on a substrate, the approximate location of the markers on the sample is known and only the fine tuning of the alignment requires imaging using the beam. The imaging area can then be minimised to reduce the unnecessary exposure of the regions of the sample where the structures are to be fabricated.

3.7.4   Patterning with ion beams

A similar approach can be used for patterning regions with localised ion irradiation on the samples. Here, the scan-processor is used to manipulate the positioning and blanking of the ion beam on to a sample following the deposition of magnetic material. This allows for local intermixing of interfaces, which can then be combined with the nanostructures created by electron beam lithography.

The ion beam patterning strategy is, in the first instance, copied from electron beam lithography. However, differences in the physics involved in exposing a resist and the immediate changes from ion exposure mean that the patterning strategies need to be adjusted. Short pixel dwell times and multiple pass irradiation sweeps produce a more uniform effect from irradiation in comparison to the single pass, longer dwell time applicable to the electron beam lithography exposure.[173]

3.8   Summary

In summary, this chapter introduces all of the physics relevant to the preparation of the magnetic thin films and nanostructures investigated in this thesis. This includes the basic theories about sample structure and crystallography, before discussing the mechanisms for the modification of this structure through ion beam irradiation and how that affects the magnetic behaviour. Finally, the focussed ion beam system was discussed, including the patterning capabilities that can be achieved with both the ion and electron beams.

Chapter 4

Investigative techniques

4.1 Introduction

In this chapter the experimental methods are discussed for the investigation of the structural and magnetic properties of irradiated bilayer thin films and nanoscale structures.

First, the investigation of the structure of thin films using the grazing incidence x-ray reflectivity (XRR) technique is discussed; this gives structural information from buried interfaces being sensitive to interface roughness and interfacial intermixing. X-ray fluorescence measurements give additional and complementary information about the element specific depth dependence from the structure.

X-ray magnetic circular dichroism has also been used as it is sensitive to element specific magnetisation and can even be used to differentiate between spin and orbital contributions to the magnetism. Combining this with the grazing incidence reflectivity allows an element specific depth profile to the magnetisation to be probed.

Magneto-optical Kerr effect (MOKE) measurements have been important too in this work. The effect relies on the interaction between the magnetisation of the samples and polarised electromagnetic waves in the optical part of the spectrum. This gives information on the magnetisation orientation as a function of applied field. With a focussed laser, this system can probe magnetisation behaviour in nanostructures and is well suited for investigating the effect of geometrical patterning and local ion irradiation of nanowires.

Measurements on a superconducting quantum interference device (SQUID) also add to this project and provide a direct measure of the magnetic moments and their variation with irradiation in the thin film samples.

In addition to these experimental techniques, simulations of ion-solid interactions and micromagnetic behaviour have been used to aid in the understanding of the physical processes taking place in the structures studied in this work.

4.2 X-ray reflectivity of thin films

Electromagnetic radiation incident on a material is generally scattered as the electron cloud of an atom is driven into oscillation by the absorption of an incident photon. This oscillation then acts as a source, instantly re-radiating a photon with the same energy in an elastic process known as non-resonant scattering. [174]

When the incident photon energy is sufficient to promote an electron to an incompletely filled orbital the atom transitions to an excited state in a process known as *absorption*. This energetic state can either decay in a dissipative process by the emission of phonons and other thermal energy, or radiatively by the spontaneous emission of a photon with energy matching the transition energy back to the ground state. When the incident photon energy matches the transition energy, resonant enhancement of the scattering occurs, where the process of excitation and spontaneous emission is rapidly repeated. [174]

Illumination of a material containing many atoms shows these scattering and absorption effects which are better described in terms of waves where atoms are considered as a source of spherical wavefronts that propagate out in all directions. These waves interfere with each other in such a way that it is possible to determine the material structure by measuring the scattered beam from a sample. In this investigation the structural properties of NiFe/Au bilayers were investigated with sub-nanometre spatial resolution. This was achieved with the scattering of x-rays as they cover the region of the electromagnetic spectrum with wavelengths from 0.01 nm to 10 nm. [175]

Grazing incidence x-ray reflectivity is a well established scattering technique for determining the layered structure of thin films. It can give quantitative information about the layer thickness, interface width and the layer density. The penetration of x-rays into a sample allows subsurface layers and interfaces to be characterised non-destructively. This section introduces the theory behind the interaction of x-rays with a material and how this technique can be used to investigate the structure of thin films.

4.2.1 Theory of reflection and total external reflection

The theory that underpins x-ray reflectivity is based on the interaction between x-rays electrons where elastic or Thompson non-resonant scattering takes place. The model relies on the kinematic approximation, where scattering is weak such that only one scattering event per wave is included. The Fraunhofer or far-field approximation is also assumed in which the observation point is far from the sample compared to the size of illuminated sample area. This means that the scattered waves can be considered parallel at the detector.

The scattering of x-rays from a surface results in both reflection and transmission of the beam, as illustrated schematically in figure 4.1. The angles of the reflected, α_r, and transmitted, α_t, beams depend on both the incident beam angle, α_i, and the refractive indices either side of the surface, n_0 and n_1.

The refractive index is defined as:

$$n = \frac{c}{v}, \tag{4.1}$$

where c is the speed of light in a vacuum and v is the speed of light in a medium. This is governed by the electron density in the material and it is often expressed as:

$$n = 1 - \delta + i\beta, \tag{4.2}$$

using the dispersion, δ, and absorption, β, coefficients. In the case of x-rays, both of these coefficients are small and of the order of 10^{-6} and 10^{-8} respectively, resulting in a refractive index $n \approx (1 - 1 \times 10^{-5})$.

At the interface between two materials with different refractive indices, Snell's law and the Fresnel equations can be derived from the continuity of waves and their derivatives over
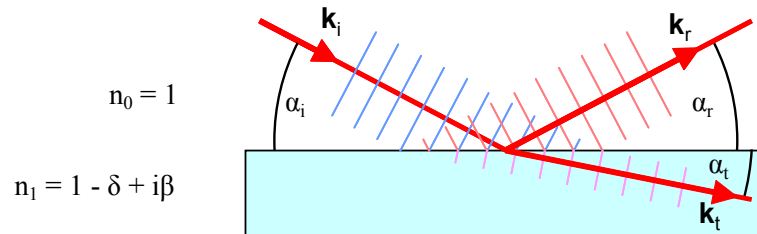
Figure 4.1: Schematic showing the wavefronts and wavevector, $\boldsymbol{k}$, of an incident x-ray beam at angle, α_i, that is reflected and transmitted from an interface between materials of refractive index n_0 and n_1.

the interface. Snell's law is given by:[175]

$$n_0 \cos(\alpha_i) = n_1 \cos(\alpha_t). \tag{4.3}$$

Total external reflection occurs when the real part of the transmitted beam vanishes, i.e. when $\alpha_t = 0$. With $n_0 = 1$ for a vacuum and for small α_i the cosines can be expanded to get the critical angle, α_c:

$$\alpha_c = \sqrt{2(1 - n_1)} = \sqrt{2\delta} \tag{4.4}$$

using the real part of the refractive index from equation 4.2.

The Fresnel equations for reflectivity, r, and transmission, t, describe how electromagnetic waves travel between layers of different refractive index. In angular terms these are given by:

$$r = \frac{n_0 \alpha_{i,r} - n_1 \alpha_t}{n_0 \alpha_{i,r} + n_1 \alpha_t} \tag{4.5}$$

$$t = \frac{2 n_0 \alpha_{i,r}}{n_0 \alpha_{i,r} + n_1 \alpha_t}. \tag{4.6}$$

The measurable intensity from reflection and transmission are $R = |r|^2$ and $T = |t|^2$. Below the critical angle only a reflected component exists. As the angle is increased above the critical angle, transmission increases whilst the reflectivity drops as α_i^{-4}.

4.2.2   Scattering from a thin film

A thin film illuminated with x-rays at grazing incidence sets up a series of infinite reflections from both the top and bottom interfaces within the film, as illustrated in figure 4.2. The observed reflectivity of the film, r_{slab}, is found from the addition of the initial reflectivity, r_{01},
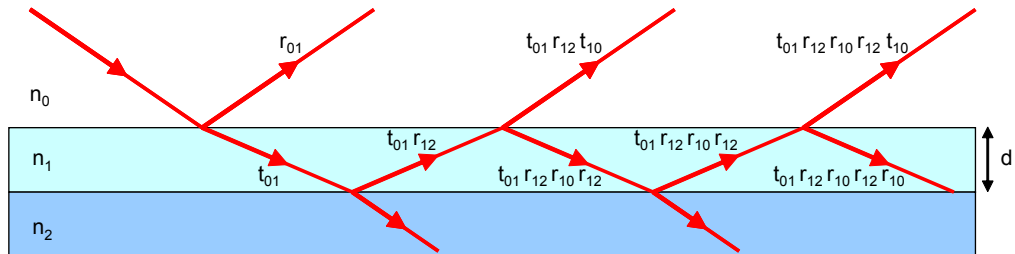
Figure 4.2: Schematic illustration of the combination of transmitted and reflected x-rays from a thin slab of material with refractive index n_1 on a substrate, n_2.

with the transmitted component from each subsequent reflection at the surface:

$$r_{slab} = r_{01} + t_{01}r_{12}t_{10}p^2 + t_{01}r_{12}r_{10}r_{12}t_{10}p^4 + \dots \tag{4.7}$$

$$= r_{01} + t_{01}r_{12}t_{10}p^2 \sum_{m=0}^{\infty} (r_{10}r_{12}p^2)^m. \tag{4.8}$$

These reflectivity components are combined with their appropriate phase factors, p, to account for the path difference, $p^2 = \exp(iqd)$ where d is the thickness of the layer, $q = 2k_1 \sin(\alpha_1)$ and k_1 is the incident wavevector. This forms a geometric series which can be summed and then simplified using Fresnel's equations following the method by Als-Nielsen[175] to get the Fresnel reflectivity:

$$r_{slab} = r_{01} + \frac{t_{01}r_{12}t_{10}p^2}{1 - r_{10}r_{12}p^2} = \frac{r_{01} + r_{12}p^2}{1 + r_{01}r_{12}p^2}. \tag{4.9}$$

4.2.3 Parratt's recursive method for multilayered films

In multilayered films the total reflectivity is affected by further transmission and reflection of the beam from the sub-surface layers and interfaces. To account for this, each layer, j, with its respective refractive index, n_j, and thickness, d_j has a Fresnel reflectivity as before, based on the reflection from the top and bottom interfaces given by equation 4.9. The reflectivity from any layer is then found from the reflection from all layers below it using Parratt's recursion relation:[176]

$$r_{j-2,j-1} = \frac{r_{j-2,j-1} + r_{j-1,j}p_{j-1}^2}{1 + r_{j-2,j-1}r_{j-1,j}p_{j-1}^2}. \tag{4.10}$$

The phase factor, $p_j^2 = exp(id_j q_j)$, accounts for the phase difference between reflected beams where $q_j = 2k_j \sin(\alpha_j)$ and k_j is the wave vector incident on layer j at an incidence angle α_j. This process is repeated recursively starting at the substrate (where the transmitted intensity from underlayers is zero) until the reflectivity from the surface/vacuum interface, $r_{0,1}$, is determined.

An example simulation of the specular reflectivity, $R = |r|^2$, as a function of the incidence x-ray angle, α_i, for a thin NiFe film on an infinite SiO_2 substrate is shown in figure 4.3 for both 5 nm and 10 nm thick NiFe layers. The reflected intensity shows a decreasing trend superimposed with interference fringes which are known as Kiessig fringes after the author of the first experimental observations.[177] The Kiessig maxima are found when the phase

factor, $p^2 = \exp(idq)$, with $q = 2k_1 \sin(\alpha_1)$ between reflected waves from the bottom and top interfaces of the film of thickness, d, results in constructive interference. i.e. when:

$$d \sin(\alpha_t) = m\lambda \qquad (4.11)$$

where m is an integer representing the fringe number with an x-ray wavelength, λ. Using the angle of incidence with equations 4.2 and 4.4 this becomes:

$$d\sqrt{\sin^2(\alpha_{im}) - \sin^2(\alpha_c)} = m\lambda \qquad (4.12)$$

which, in the case for small α_c and α_{im} simplifies to:

$$\alpha_{im}^2 = \alpha_c^2 + m^2 \left(\frac{\lambda}{d}\right)^2. \qquad (4.13)$$

Then the angular difference between two consecutive fringes, m and $m+1$, is found from:

$$\alpha_{m+1} - \alpha_m = \frac{\lambda}{d}. \qquad (4.14)$$

This gives a clear way to determine the layer thickness based on the angular positions of the Kiessig fringes at high angles where the separation decreases linearly with increasing layer thickness as shown in figure 4.3.
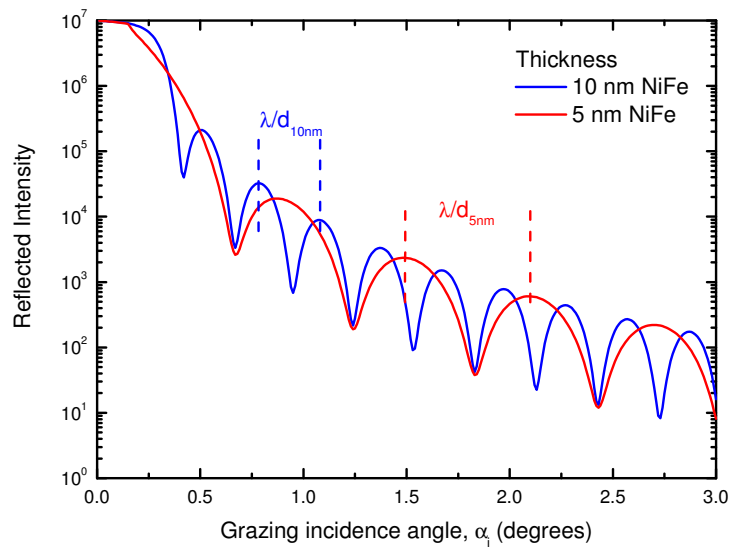
Figure 4.3: Simulated specular reflectivity for 5 nm and 10 nm $Ni_{85}Fe_{15}$ thin films on an infinite SiO_2 substrate with perfect interfaces. Incident x-ray energy was 11.8 keV.

At low angles, close to the critical angle, refraction effects also contribute to changes in the Kiessig fringe positions and the model derived for the kinematical regime breaks down. Névot and Croce[178] found that that by modifying the Fresnel coefficient of transmission as well as the coefficient of reflection by replacing p^2 with $p_i \times p_r$ to include the effects of a complex p_i near the critical angle, their model is more valid around the critical angle.

4.2.4   Scattering from interfaces

So far perfectly smooth interfaces have been considered. Actual interfaces have a finite width due to topological roughness and chemical intermixing that are illustrated in figure 4.4. Specular x-ray reflectivity cannot differentiate between these two roughness mechanisms as it is sensitive to only the average change in electron density in the z-axis and can only be used to find the total interface width, σ.

Following the derivation by Als-Nielsen,[175] the interface between two layers of different refractive indices can be described in the kinematical regime for angles much greater than the critical angle, $\alpha \gg \alpha_c$. The interface can be represented by an ensemble of flat surfaces with depths given by a Gaussian distribution with a standard deviation, σ. There is no in-plane structuring so the scattering vector, q, only has q_z components and hence this technique is sensitive only to out-of-plane changes in roughness. The reflectivity from this interface can be found from the reflected contributions from each of these surfaces (equation 4.9) integrated over the interface width in z with a density profile described by an error function, $\mathrm{erf}(z)/\sqrt{2}\sigma$. This also needs to take into account the change in phase from each component of the reflection given by $p^2 = \exp(iqz)$ where $q = 2k\sin\alpha$.
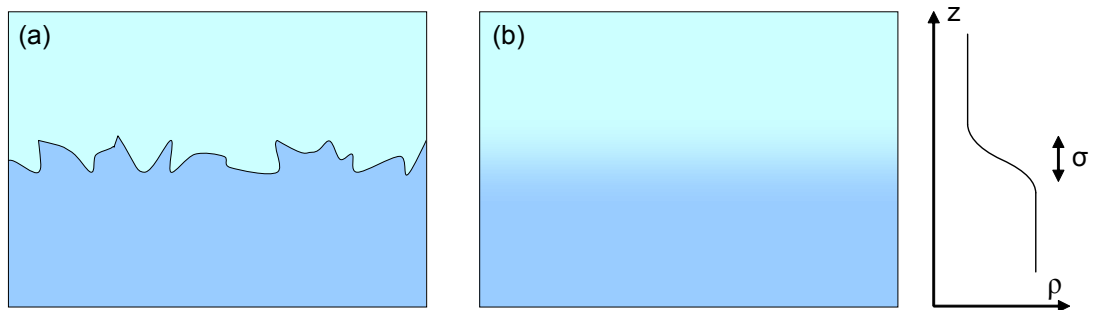
Figure 4.4: Graphical representation of an interface with a transition between two electron densities, ρ, over a total interface width, σ. a) Topologically rough interface or b) chemically intermixed interfaces show the same averaged electron density variation in z.

The Fresnel reflectivity for a thin slab then becomes:

$$r = r_{smooth} \times \int_0^\infty \frac{\mathrm{d}}{\mathrm{d}z} \left(\mathrm{erf} \left(\frac{z}{\sqrt{2}\sigma} \right) \right) \exp(iqz)\mathrm{d}z \qquad (4.15)$$

consisting of the reflectivity of the smooth interface, r_{smooth}, multiplied by the Debye-Waller factor.[175] The differential of the error function is a Gaussian:

$$\frac{\mathrm{d}}{\mathrm{d}z} \left(\mathrm{erf} \left(\frac{z}{\sqrt{2}\sigma} \right) \right) = \frac{1}{\sqrt{2\pi\sigma^2}} \exp \left(-\frac{1}{2} \left(\frac{z}{\sigma} \right)^2 \right) \qquad (4.16)$$

whose Fourier transform is also another Gaussian:

$$\exp \left(-\frac{q^2\sigma^2}{2} \right) \qquad (4.17)$$

resulting in the reflectivity from this model with a rough interface given by:

$$r = r_{smooth} \exp \left(-\frac{1}{2}q^2\sigma^2 \right). \qquad (4.18)$$

The total reflection thus becomes:

$$R = R_{smooth} \left| \exp \left(-\frac{1}{2}q^2\sigma^2 \right) \right|^2 = R_{smooth} \exp \left(-q^2\sigma^2 \right). \qquad (4.19)$$

Figure 4.5(a) compares simulations based on equation 4.19 for a 10 nm NiFe film with zero and 0.5 nm roughness introduced to the NiFe/vacuum interface.

The main effect is the reduction in amplitude of the Kiessig fringes at higher incidence angles. The angle up to which the Kiessig fringes remain can give an indication of the extent of the interface width. The surface roughness also affects the beam transmitted into the layer giving rise to interference effects which explain the enhanced Kiessig minima at $\approx$ 1°.

This derivation has shown how the interface width, σ, affects the specular reflectivity from a sample. However, the intermixed or topologically rough nature of the interface (see figure 4.4) cannot be found from the specular reflectivity. Information on this can be obtained from the off-specular scatter from a sample.
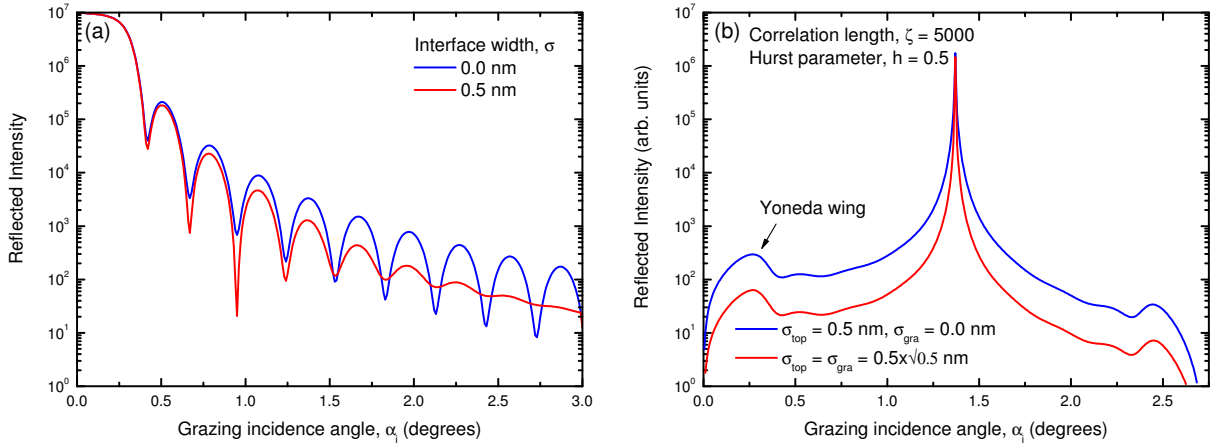
Figure 4.5: Simulation of x-ray reflectivity from a 10 nm $Ni_{85}Fe_{15}$ film on a SiO_2 substrate with a NiFe/vacuum interface width of 0.5 nm with 11.8 keV incident x-rays. a) The specular reflectivity is compared with the same structure with perfect interfaces. b) An interface formed entirely of topological roughness is compared with an interface with equal amounts of topological roughness and chemical grading.

4.2.5 Differentiating between chemically graded and topologically rough interfaces

The two contributions to the interface width shown in figure 4.4 have the same electron density variation in the z-axis when averaged over x and y which explains why the specular reflectivity is not sensitive to the interfacial differences. Diffuse scattered x-rays do have an in-plane component to the scattering vector and hence have sensitivity to the in-plane structuring, so can be used to determine the nature of the interfaces.

An intermixed interface can be described by a slowly varying electron density over many layers which scatter out-of-phase resulting in a decrease in specular reflectivity due to destructive interference effects. For topologically rough interfaces, abrupt changes in the electron density result in scattering but at a range of different angles. This also results in the decrease in specular reflectivity but with an increase in diffuse reflectivity.

Real interfaces are composed of both topological roughness, σ_r, and intermixing, σ_i, contributions which are related to the total interface width from specular reflectivity measurements by:[179]

$$\sigma = \sqrt{\sigma_i^2 + \sigma_r^2}. \tag{4.20}$$

Figure 4.5(b) shows a simulated reflected intensity as a function of grazing incidence angle, α_i where exit angle, 2θ has been positioned at a Kiessig fringe maxima at $\alpha_i = 1.37°$.

The figure shows a sharp specular reflection at the specular condition, superimposed on a broad diffuse scattered background. The diffuse scatter is bounded in angle by features called Yoneda wings where diffuse scatter is enhanced at the critical incidence and exit angles due to electric field at the surface.[180] Figure 4.5(b) shows an interface composed of 0.5 nm topological roughness with no intermixing compared to the the reflectivity of a sample with the same total interface width but equal amounts of topological roughness and chemical grading. It can be seen that whilst the roughness and intermixing affect the specular reflectivity in the same way, only the topological roughness contributes to the increased diffuse scatter.

Other parameters such as the fractal Hurst parameter, $h = 0.5$, and the height-height correlation length, $\zeta = 5000$, are needed to accurately predict the shape. It is possible to fit the data to these models but this is computationally intensive. There may also be no unique solution to fit the data with four parameters.

Another simpler approach to determine the nature of the interfaces is based on the fact that the diffuse, I_d, and specular, I_s, scattered intensities are related to a first approximation by:[179]

$$\frac{I_d}{I_s} = \exp(q_z^2 \sigma_t^2) - 1 \tag{4.21}$$

where q_z is assumed to be large in order to measure all of the diffuse scatter. This is given by:

$$q_z = \frac{2\pi}{\lambda} \sin \theta \tag{4.22}$$

where θ is the detector angle and σ_t is the topological roughness. By integrating the intensity under the transverse diffuse curve and separating the specular reflected component, it then becomes possible to eliminate the topological roughness. This allows the contribution from intermixing to be obtained using equation 4.20.

4.3 X-ray fluorescence

Another technique useful for investigating thin film structure is *x-ray fluorescence* which gives elemental specific information about the composition of the sample. Performing these measurements as a function of angle at grazing incidence allows for depth dependent analysis through a layered material.

Non-resonant x-ray scattering was used to explain the x-ray reflectivity technique, whereas x-ray absorption processes are involved in the fluorescence measurements. Here, an incident energetic x-ray photon ejects a core electron from an atom into the continuum known as a photoelectron. An outer electron in the atom can then undergo spontaneous emission when it fills the hole in the core shell, emitting a photon characteristic of the energy transition. This process is known as fluorescent x-ray emission.

4.3.1 Atomic absorption and fluorescent decay

There is a threshold energy associated with the ionisation of a core electron. Once the incident x-ray energy overcomes this threshold known as an *absorption edge*, a sharp increase in the absorption coefficient is found. Figure 4.6(a) illustrates this absorption as a function of energy with several absorption edges corresponding to the ionisation of an electron from shells labelled with the quantum number of the shell: K-edge ($n = 1$), L-edge ($n = 2$) and M-edge ($n = 3$). Each edge also shows fine structure resulting from spin-orbit splitting in that level giving rise to five steps at the M-edge, three steps at the L-edge and one step at the K-edge. This is discussed in more detail in section 4.4. These jumps at the absorption edges are superimposed on an E^{-3} trend in the absorption, which is explained by a decrease in the electron's oscillitatory response as the incident x-ray energy is increased beyond the absorption edge.[175]

For a given atomic series (K, L and M) there are multiple possible fluorescent transitions
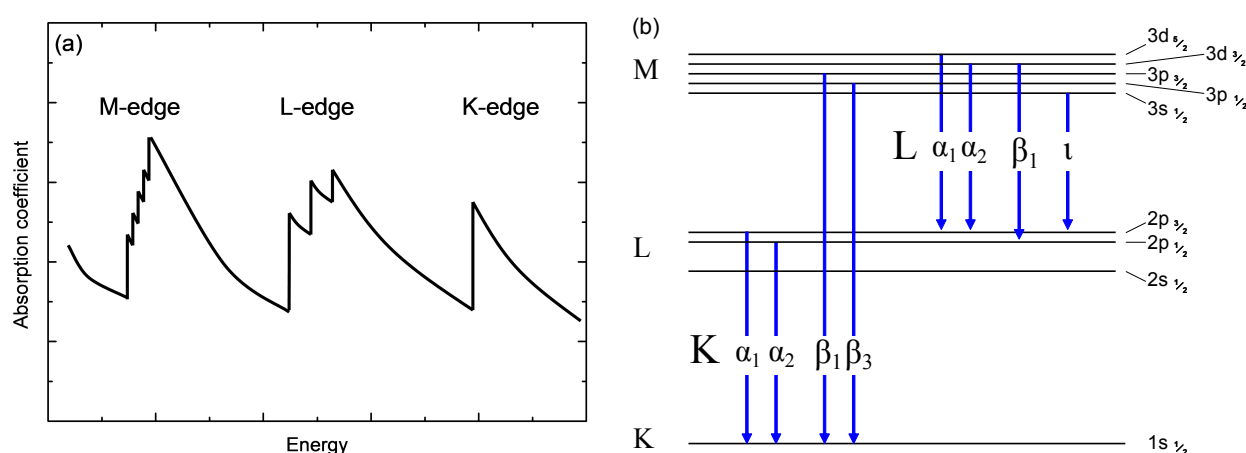
Figure 4.6: a) X-ray absorbtion as a function of x-ray energy showing the K, L and M absorption edges. b) The allowed fluorescence transitions that can occur following a K or L shell ionisation.

from the outer electrons that could fill the vacancy in the inner shell, giving rise to different energy x-rays. Figure 4.6(b) illustrates the possible energy transitions between shells in an atom relevant to to this work. These transitions are governed by quantum mechanical selection rules which only allow certain transitions between electronic orbitals:

- The principal quantum number must change by at least one ($\Delta n \geq 1$)

- The angular quantum number must change by one ($\Delta l = \pm 1$)

- The total angular momentum must change by zero or one ($\Delta j = 0, \pm 1$)

The allowed fluorescent transitions are based on the electronic structure of the atom which gives this technique its elemental specificity. By counting the number of fluorescent x-rays as a function of energy a spectrum can be obtained where each peak represents an atomic transition at a particular energy. An example spectra is shown in figure 4.7 for an irradiated NiFe/Au bilayer with an x-ray beam incident at $\theta = 1°$.

Since each element has a characteristic x-ray fingerprint, the different elements contributing to the peaks can be identified. Figure 4.7 also shows how the peaks from Ni, Fe, Au, and Ga contributions sum to produce the measured spectrum. Some peaks lie very close in energy, for example Ni $K\alpha_1$ and Ni $K\alpha_2$. In the measured spectra these cannot be resolved and so appear as one peak.
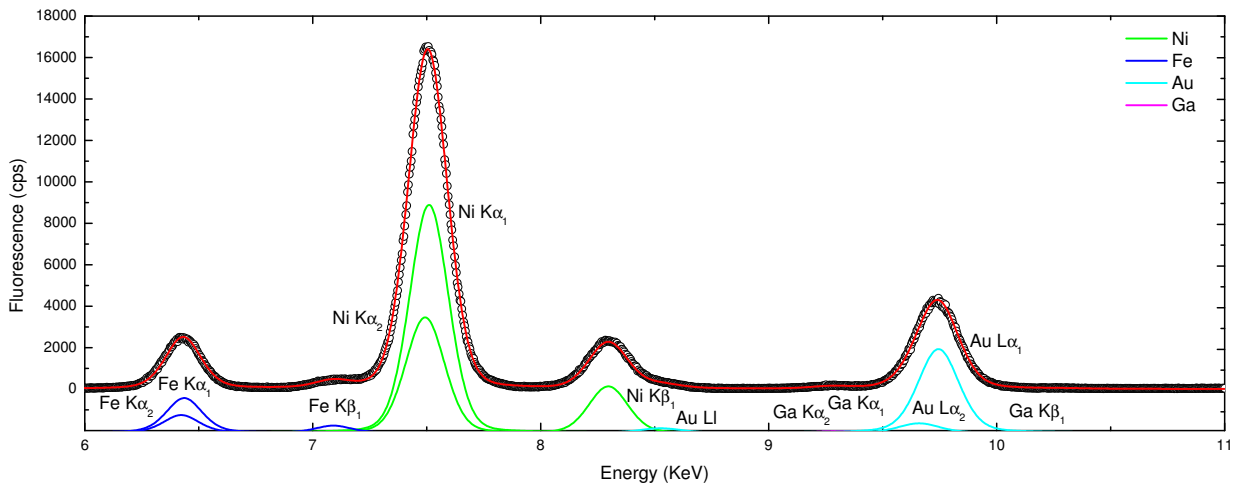
Figure 4.7: Example x-ray fluorescence spectra for a 0.31 $\times 10^{15}$ Ga$^+$ /cm^2 irradiated NiFe/Au bilayer. The spectra is recorded at 12.5 keV and at an angle of 1° . The data fitted with multiple Pseudo-Voigt curves for each element (offset for clarity) and the sum of the model is shown by the red line.

The intensity of the peaks represents the relative number of fluorescent x-rays collected from each element in the sample. This is determined by the number of incident photons multiplied by a number of factors representing the probability that the photon results in the emission of a fluorescent x-ray photon.

The mass fraction, C_a, of a particular element a in a medium of density ρ and the photo-electric part of the mass absorption coefficient, $\tau_{a\lambda}$ give the probability for the absorption of the incident x-ray photon. The absorption jump factor, $J_{a\lambda}$, at a wavelength λ then determines the probability of that event creating a hole in the electron shell of interest of element a. The fluorescence yield, ω_a, gives the ratio of the decay of excited states by radiative fluorescent x-ray emissions to the total number of ionisation events. It can be approximated by:

$$\omega_a = \frac{Z^4}{A + Z^4} \tag{4.23}$$

where Z is the atomic number and A is a constant approximately 10^6 for K shell ionisations and 10^8 for L shell ionisations.[181]

The competing non-radiative decay process is known as the *Auger process* where the energy from the electronic transition ionises a less tightly bound outer electron known as an Auger electron, instead of producing a fluorescent x-ray photon. This process is more common for lighter elements and since the efficiency of producing Auger electrons is inversely proportional to the production of fluorescent photons, this gives rise to the improvement in fluorescence yield with Z.[182]

The relative emission rate, g_a, of one fluorescent emission line related to other possible radiative decay paths from the same ionisation is shown along with the energies of the transitions relevant to this investigation in table 4.1.

	Transition energy (keV)[183]			Relative emission rate[184]	
Element	$K\alpha_1$	$K\alpha_2$	$K\beta_1$	$K\alpha_2$ / $K\alpha_1$	$K\beta$ / $K\alpha$
Ni	7.47815	7.46089	8.26466	0.506	0.135
Fe	6.40384	6.39084	7.05789	0.508	0.135
Ga	9.25174	9.22482	10.2642	0.512	0.143
Element	$L\alpha_1$	$L\alpha_2$	L_l	$L\alpha_2$ / $L\alpha_1$	L_l / $L\alpha$
Au	9.7133	9.6280	8.4939	0.1117	0.0473

Table 4.1: Table showing transition energies and relative emission rates for the relevant transitions of the elements investigated.

Each peak in the spectrum has a natural linewidth for the transition due to the lifetime of a hole in the core energy level of the atom. The changing electronic configuration of the atom leads to broadening of the energy levels when atoms are brought together to form metals. This effect results in a considerable broadening of the linewidth. A detailed discussion on the fluorescence linewidth along with other factors affecting it can be found elsewhere.[185] For $Z < 13$ (Al) K transitions and $Z < 30$ (Zn) L transitions, the core energy levels can be considered sufficiently deep that the transitions are not affected by broadening from bonding and can be assumed to have the natural linewidth.[185]

4.3.2 Fluorescence from a layered sample

In layered samples there are several geometrical factors that also affect the fluorescence in addition to those discussed for a free atom. For this method the electric field due to the incident x-ray radiation must be known at every point in the sample structure.

Following the derivation by de Boer[186] the fluorescence intensity of an element from a sample of thin layers can be found by considering the electromagnetic plane wave which penetrates the sample surface. The energy supplied to the material varies as a function of position due to interference that forms standing waves within the layers.

The energy absorbed by a volume of material bounded by a surface, S, can be converted to the number of absorbed photons by dividing by the energy of a photon, hc/λ. The fluorescent intensity is then found by integrating the rate of energy transfer per unit area, P_{jz}, over the thickness of material, d_j, and multiplying by factors describing the probability of fluorescence emission. An exponential factor based on the linear absorption coefficient, μ_{na}, is also included to describe the re-absorption of a fluorescent x-ray as it exits the material at an angle, ψ_d, which is assumed to be greater than the critical angle. The total fluorescent intensity, I_{aj}, of atom a in layer j from the sample is then given by:

$$I_{aj} = \frac{\lambda}{hc} \frac{C_{aj}\rho_j\tau_{aj}J_{a\lambda}\omega_a g_a S}{\mu_{j\lambda}} \exp\left(-\sum_{n=1}^{j-1}\frac{\mu_{na}d_n}{\sin\psi_d}\right) \times \int_0^{d_j} \mathrm{d}z \left(-\frac{\partial P_{jz}}{\partial z}\right) \exp\left(-\frac{\mu_{ja}z}{\sin\psi_d}\right). \quad (4.24)$$

To extend this to a multilayered sample, Parratt's recursion theorem can be used again to find the electric field at any point within the sample. This is found from the sum of a down-going transmitted component, $\boldsymbol{E_j^d}$, and up-going reflected component, $\boldsymbol{E_j^u}$, of the

electric field at the top of layer j:

$$\boldsymbol{E_j} = \boldsymbol{E_j^u} + \boldsymbol{E_j^d}. \tag{4.25}$$

Combining this with the integration of the energy over the thickness of each layer gives the number of fluorescent photons from a sample based upon the absorption factors and the re-absorption by surface layers. This is modulated by the plane-wave amplitude of the transmitted, reflected and incidence x-rays to give an intensity relation:

$$I_{aj} = I_0 C_{aj} \rho_j \tau_{aj} J_{a\lambda} \omega_a g_a S \exp\left(-\sum_{n=1}^{j-1} \frac{\mu_{na} d_n}{\sin \psi_d} \right) \frac{|\boldsymbol{E_j^t} + \boldsymbol{E_j^r}|^2}{|\boldsymbol{E_0}|^2} d_j \tag{4.26}$$

where:

$$I_0 = \frac{|\boldsymbol{E_0}|^2 \lambda}{2Z_0 hc} \tag{4.27}$$

is the intensity of the incident irradiation per surface area per unit time. The impedance of vacuum, Z_0, is related to the permeability, μ_0, and permittivity, ϵ_0, of free space by $Z_0 = \sqrt{\mu_0/\epsilon_0}$.

This equation shows that the fluorescence intensity is proportional to the amplitude of the electric field of the incident x-rays into the sample. It is also dependent on both the transmitted, $\boldsymbol{E_j^t}$, and reflected, $\boldsymbol{E_j^r}$, components of the electric field, so the electric field forms a standing wave through each layer. This can be used to investigate the depth dependence of the fluorescence as the standing waves can be controlled by the x-ray incidence angle.

4.3.3 X-ray penetration depth

Below the critical angle there is a component of beam intensity that penetrates the sample surface known as the evanescent field. The penetration depth, Λ_p, is the depth into the sample surface where the intensity drops to $1/e$ and is given by:[187]

$$\Lambda_p = \frac{\lambda}{\sqrt{2}\pi} \left(\sqrt{(\alpha_i^2 - \alpha_c^2)^2 + 4\beta^2} - (\alpha_i^2 - \alpha_c^2) \right)^{-\frac{1}{2}}. \tag{4.28}$$

As the angle of incidence, α_i, tends to 0, the penetration depth tends to $\Lambda_p = \lambda/(2\pi\alpha_c)$ which for most materials is ≈ 1 nm.[187] For larger α_i the penetration depth can be approximated as $\Lambda_p = \alpha_i \lambda/(2\pi\beta)$, shown as a function of incidence angle in figure 4.8(a) where a dramatic rise in the penetration depth occurs as the beam passes through the critical angle.
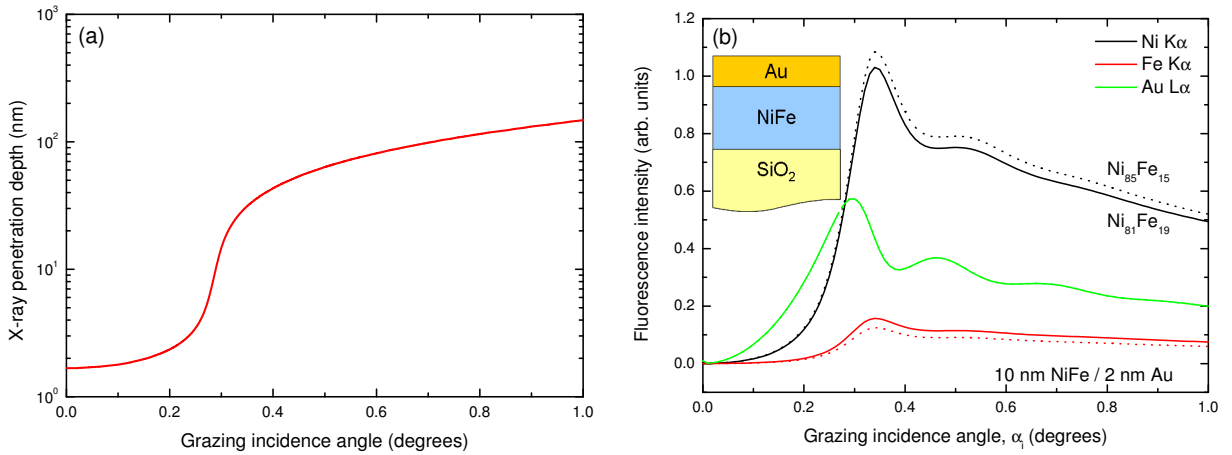
Figure 4.8: a) Penetration depth of the x-ray beam into a $Ni_{85}Fe_{15}$ sample. b) Simulation of fluorescence intensity for the Ni K_α, Fe K_α and Au L_α transitions as a function of 12.5 keV x-rays incidence angle for a 10 nm NiFe / 2 nm Au bilayer sample. The solid lines show the stoichiometry at $Ni_{81}Fe_{19}$ and the dotted line at $Ni_{85}Fe_{15}$ showing the sensitivity of fluorescence measurements to the elemental composition.

4.3.4   Depth resolution using grazing incidence

By varying the x-ray incidence angle the geometry of the electric field can be varied from the evanescent field to the transmission of the x-ray beam into the sample, which sets up standing waves as described earlier. Further increases in angle modify the standing wave and lead to an angular dependence of the fluorescence intensity.

When the incidence angle corresponds to a Kiessig minimum in the reflectivity data the standing wave in the sample has nodes at the interfaces and an anti-node in the centre of the layer. This acts as a waveguide leading to resonance giving a maximum fluorescence intensity.[186] As the incident angle is increased the standing wave decreases in wavelength. Each harmonic of the standing wave fits exactly inside the layer results in an enhanced fluorescence signal that brings about fringes in the fluorescence data. These fringes are π out-of-phase with the Kiessig fringes in the x-ray reflectivity since the Kiessig fringes result from the interfaces between layers whilst reflectivity fringes originate from the centre of the layers.

Beyond incident angles of $\approx 0.6°$ these modulations of the fluorescence signal are damped leaving a fluorescence signal that is proportional to the amount of material fluorescing. This damping is more significant than for the reflectivity fringes. At larger angles many harmonics of the standing wave fit between the interfaces, as a result, the effect of adding additional half wavelengths becomes less pronounced.

Fluorescence enhancement is a second order effect caused by excitation of other atoms by the fluorescent radiation. Elements with an absorption edge below the fluorescent x-ray energy can be excited by these x-rays as well as by the incident beam. This has the effect of reducing the fluorescence of high energy x-rays but enhancing the fluorescence observed from low energy elements.

Simulations of the angular dependence of fluorescence are shown in figure 4.8(b). The fluorescence intensity increases from zero with increasing incidence angle as the evanescent field moves deeper into the sample. Around 0.3°, the critical angle, the fluorescence reaches a maximum before a gradual decrease. The fringes occurring at angles just above the critical angle are caused by the interference effects discussed earlier.

The sharp rise in fluorescence intensity at the critical angle gives information on the surface layer of the sample. Here the Au fluorescence rises at a lower angle than the Ni and Fe indicating that the Au is a surface layer. The Au fringes are more distinct and carry on to higher angles, indicating that the Au layer is thinner than the NiFe layer.

This figure also illustrates the fluorescence of $Ni_{81}Fe_{19}$ compared to that of $Ni_{85}Fe_{15}$. The difference in the fluorescence intensity results from the C_{aj} mass fraction term in equation 4.26 which gives the fluorescence technique its compositional sensitivity. The Au layer is not affected by the change to the composition of the NiFe layer.

This simulation method can be extended to include the effects of small amounts of roughness at the interfaces, by modulating the initially smooth surface with a root-mean-square deviation, σ_j.

4.4   X-ray magnetic circular dichroism (XMCD)

As well as their use in structural characterisation, x-rays are also a useful tool for characterising the magnetic properties of a sample through a technique known as x-ray magnetic circular dichroism. This technique has advantages over other magnetic sensitive techniques as it is sensitive to specific elements and can reveal differences in orbital and spin contributions to the magnetism. It is also sensitive to moments down to $0.001\mu_B$ per atom.[188] This magnetic sensitivity comes about due to changes in the polarisation dependent absorption of the sample which depends on the part of its electronic structure responsible for magnetism.

In 1975, Erskine[189] first predicted that magnetic information could be obtained from

the absorption spectra of circularly polarised x-rays. This XMCD effect was first observed in 1987 on the K edge of Fe[190] and subsequent measurements at the L edges of transition metals gave a much a greater effect.[191] This is because the p - d electronic transition is probed which encompasses the region of the electronic structure responsible for the magnetic properties in these materials.

In the discussion on x-ray fluorescence the concept of absorption edges was introduced, where a sharp increase in x-ray absorption occurs at the ionisation energies in a material. For the L and M transitions these absorption edges show fine structure resulting from the spin-orbit splitting of the core levels.

Here, just the L absorption edge will be considered for the $3d$ transition metals as these transitions involve the states responsible for the magnetism in these materials. Figure 4.9 shows in more detail the L absorption edge, composed of the L_3 and L_2 peaks originating from the spin-orbit splitting of the $2p$ shell into the $2p_{3/2}$ and $2p_{1/2}$ levels respectively. The spin-orbit energy difference, E_{SO} between these levels gives rise to the difference in energy between the two absorption peaks.

4.4.1   The two step model

The XMCD sensitivity is best explained using the simple two-step model of Kapusta *et al.*[192] involving first the absorption of a photon leading to the excitation of an electron from the ground state to a final state at the Fermi level. Secondly, the occupation of the final state acts as a filter, further restricting the absorption based on the occupation of the final state.
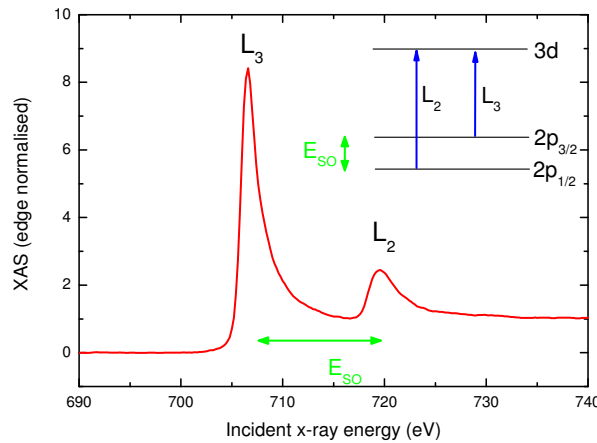
Figure 4.9: Fine structure results in splitting of the Fe L x-ray absorption edge where two peaks: L_3 and L_2 arise due to absorption from the $2p_{3/2}$ and $2p_{1/2}$ levels respectively.

Here, transitions between the $2p$ and $3d$ states are considered as they are commonly used for investigating the magnetic properties in $3d$ transition metals.

The spin-orbit coupling in the p state of the atom acts to align the spin and orbital momenta of the electrons. Right handed circular polarised (rcp) x-rays preferentially excite more spin-up (62.5%) than spin-down (37.5%) electrons at the L_3 edge since their spin and orbital moments align parallel. At the L_2 edge the moments are antiparallel so rcp x-rays preferentially excite more spin-down (75%) than spin-up (25%) electrons.[193] The opposite case occurs for photons with the left handed circular polarisation (lcp). In this way the core shell is seen as a source of spin polarised electrons, as illustrated in figure 4.10(a) which shows the proportion of the spins excited into an empty $3d$ state for each helicity of light.

The selection rules that govern the allowed fluorescence transitions discussed in section 4.3 also govern the allowed absorption transitions in an atom. Upon absorption the angular momentum of a photon is transferred to the electron, so the orbital angular momentum quantum number of the new shell must differ from the original by $\Delta l = \pm 1$. Following the definition by Feynman[194] $\Delta l = +1$ for rcp photons and $\Delta l = -1$ for lcp photons. This limits the absorption to the excitation of only certain transitions giving rise to preferential absorption.

The second step which introduces the magnetic sensitivity relies on the spin-split nature of the density of states at the Fermi level. This results in a difference in the absorption when the x-ray helicity is flipped with respect to the magnetisation of the sample. For non-magnetic materials there is no exchange splitting of the d band, the spin-up and spin-down transitions are equal for lcp and rcp and this is illustrated in figure 4.10(a). However, in a
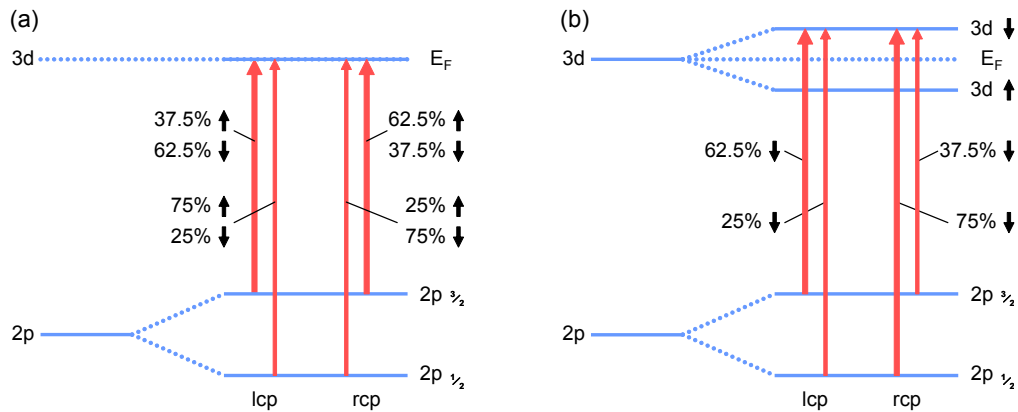
Figure 4.10: The two step model for XMCD showing a) the spin polarisation of photoelectrons excited by circurlarly polarised x-rays from spin-orbit split $2p$ subshell. b) The spin filtering by the spin-split $3d$ final state giving this technique its magnetisation sensitivity.

magnetised sample there is an imbalance in the number of empty states at the Fermi level for each spin. Figure 4.10(b) shows the case of a completely occupied spin-up state below the Fermi level so only transitions to the spin-down $3d$ state are allowed.

These effects result in an imbalance in the absorption where the $2p_{1/2}$ sees greater absorption of one helicity and $2p_{3/2}$ sees greater absorption of the other. Hence, the absorption over the $L_{3,2}$ edge becomes sensitive to the spin of the valence states at the Fermi level which represents the magnetisation of the sample. This imbalance in the absorption is maximised when the magnetisation of the material is orientated parallel to the wavevector of the incident x-ray illumination, otherwise the effect is scaled by $\cos\theta$ where θ is the angle between the magnetisation and the wavevector of the illumination.[193] Figure 4.11(a) shows two example x-ray absorption spectra for lcp and rcp x-rays over the $L_{3,2}$ edge and their associated difference spectra.

Integration of the difference spectra over the L_2 and L_3 edges allows information about the $3d$ band to be obtained ignoring the initial spin-orbit coupling in the $2p$ level. The sum of the areas of both the L_2 and L_3 edges shows only changes in the orbital moments of the final states whilst the difference between the areas of the peaks shows only the spin polarisation of the final states. It then seems trivial to extract the spin and orbital moments but it is more common to report the relative ratio of these contributions based on the sum rules.[193,196]
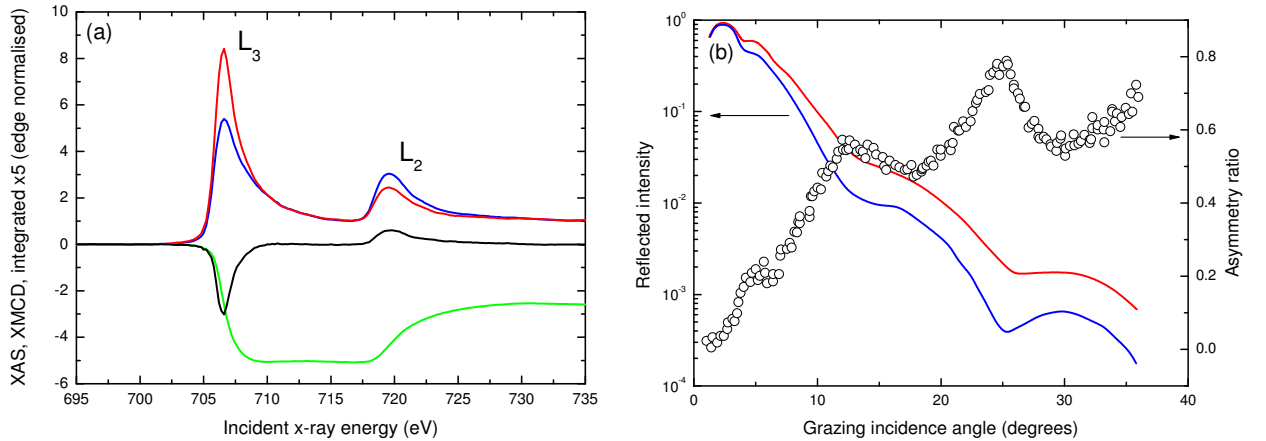
Figure 4.11: a) Example x-ray absorption spectra for a 20 nm NiFe / 2.5 nm Au sample at the Fe $L_{3,2}$ edge measured for both helicities of incident light. The difference spectra (black) is integrated (green) and from this the spin and orbital contribution to the magnetic moment can be found. b) Example specular reflectivity of Co L_3 edge (786.5 eV) for opposing saturating magnetisation directions and the associated asymmetry ratio.[195]

4.4.2   Sum rules to find the spin to orbital moment ratio

The sum rules by Thole and Carra[197,198] are a convenient way to find the ratio between spin and orbital contributions to the magnetic moment using experimentally measured data integrated over the L_2 and L_3 edges. This avoids needing to know the number of holes at the Fermi level which is hard to measure experimentally.

The difference between the absorption spectra measured for each helicity is integrated over the ionisation edge:

$$\Delta A_i = \int_{L_i} \mu^+(E) - \mu^-(E) dE. \tag{4.29}$$

From this the orbital, m_l and spin, m_s magnetic moments are found from:

$$\Delta A_3 + \Delta A_2 = -\frac{C}{2\mu_B} m_l \tag{4.30}$$

and

$$\Delta A_3 - 2\Delta A_2 = -\frac{C}{3\mu_B}(m_s - m_D). \tag{4.31}$$

Here, C is an unknown material constant relating to the polarisation of the photons and number of holes per unit area, μ_B is the Bohr magneton and m_D is a dipole term which is assumed to be negligible for Ni and Fe which have a cubic crystal structure.[196,197]

Hence, it is thus common to find the ratio of orbital to spin contributions, m_l/m_s, which can be expressed as:

$$\frac{m_l}{m_s} = \frac{2}{3} \frac{\Delta A_3 + \Delta A_2}{\Delta A_3 - 2\Delta A_2} \tag{4.32}$$

where the additional unknown terms cancel out.

4.4.3   XMCD difference as a function of applied magnetic field

The difference in peak heights represents both the number of holes at the Fermi level and the relative orientation of the magnetisation and helicity of incident light. The preceding discussion assumes the magnetisation is at saturation along the axis of the incident beam, but when the energy is fixed at the L_3 absorption edge, the height of the peak can give a relative measure of the magnetisation in the sample. By performing this measurement as a function of magnetic field, element specific hysteresis loops can be extracted using this XMCD technique.

4.4.4 Dichoric x-ray scattering from magnetic interfaces

In XMCD, the asymmetry between the absorption at each helicity depends on the magnetisation of the sample and has an energy dependence showing a maximum at the absorption edges. Combining this technique with grazing incidence x-ray reflectivity can also give depth sensitivity to the element specific magnetisation behaviour through a thin film.

Conventional x-ray scattering techniques give results dominated by the charge scattering. However, Hannon[199] and Gibbs[200] found that with circularly polarised x-ray tuned to an absorption edge, resonant enhancement of the scattering occurs due to electronic transitions between the core shell and empty states at the Fermi level. The magnetic sensitivity originates in a similar way to XMCD where the spin-orbit interaction in the core shell and exchange split density of states at the Fermi level gives a difference in the resonance depending on the incident x-ray helicity. By measuring the difference in scattering with opposite helicities or opposite magnetic fields, an asymmetry ratio is found that can give an indication of the magnetisation state.

This technique has mainly been performed in a scattering geometry, i.e. Ni multilayers,[201] but it has been tried in specular reflectivity from a buried thin film of Fe[202] and Co.[195] This originates from changes to the reflected and transmitted components of the beam at the interface of a magnetic layer due to the dichoric absorption in that layer. This results in a change in total reflectivity from the layered sample using Parratt's recursive algorithm.

The grazing incidence x-ray reflectivity from opposite axial magnetic fields, I^+ and I^-, with circularly polarised x-rays tuned to an ionisation edge gives results with contributions from both the charge scattering and magnetic scattering in the sample. By taking the sum $(I^+ + I^-)$, only structural effects are found, relating to the electron density giving the characteristic reflectivity curve with Kiessig fringes indicating the thin film nature of the sample. The difference, $(I^+ - I^-)$, is related to electronic transitions between shells and depends on the field due to spin-orbit splitting in the inner shell and polarisation of the conduction band.[199,200] By taking the difference and normalising by the sum of the intensities, the asymmetry ratio defined by $(I^+ - I^-)/(I^+ + I^-)$ removes the effect of the charge scattering leaving only a measure of the magnetic signal from the sample. An example of I^+, I^- and the asymmetry ratio is shown in figure 4.11(b) for the magnetic signal from Co L_3 in a multilayer system.

4.5   Magneto-optical Kerr effect (MOKE)

Following from the XMCD effect where the polarisation of x-rays can be used to probe magnetism, a similar effect also occurs for other parts of the electromagnetic spectrum such as at optical wavelengths. Here, the interactions between visible light and magnetic materials are known as magneto-optical effects where rcp and lcp photons experience different refractive indices when they interact with the magnetic material. This technique differs from XMCD in that the energies are not matched with the absorption edges and therefore do not give element specific results. However, the availability of optical laser sources and the ability to focus the beam to a small spot size on to a sample makes this technique valuable for the investigation of nanowires and nanostructures using in-house equipment. It has also become an important technique for studying surface magnetism and is widely used for magnetic thin film characterisation.

The rotation of the plane of polarised light passing through magnetic material was first reported by Faraday in 1845[203] which was followed by the discovery of a similar effect for the reflection of light by Kerr in 1877.[204,205] In both effects the rotation angle depends on the strength of magnetisation of the material. Even though the Faraday effect is stronger than the Kerr effect, the applications of this are limited because the sample under investigation must be transparent. Therefore, the Kerr effect is the most commonly used magneto-optical approach where the analysis of the change in polarisation angle of light upon reflection from a magnetic surface is proportional to the magnetisation state of the material.

4.5.1   Physical interaction between polarised light and magnetic materials

Linearly polarised light can be represented by a combination of left, lcp, and right, rcp, handed circularly polarised light in equal proportions as illustrated in figure 4.12(a). The magneto-optical effects arise from magnetisation dependent birefringence of magnetic materials that give an asymmetry in the refractive index for the two circular polarisations. A mathematical formulation of this macroscopic description is given by dielectric tensor theory, the details of which can be found elsewhere.[206] In summary, this predicts the occurrence of a differential absorption and a phase shift for the two polarisations.

The phase shift between rcp and lcp is illustrated schematically in figure 4.12(b) and
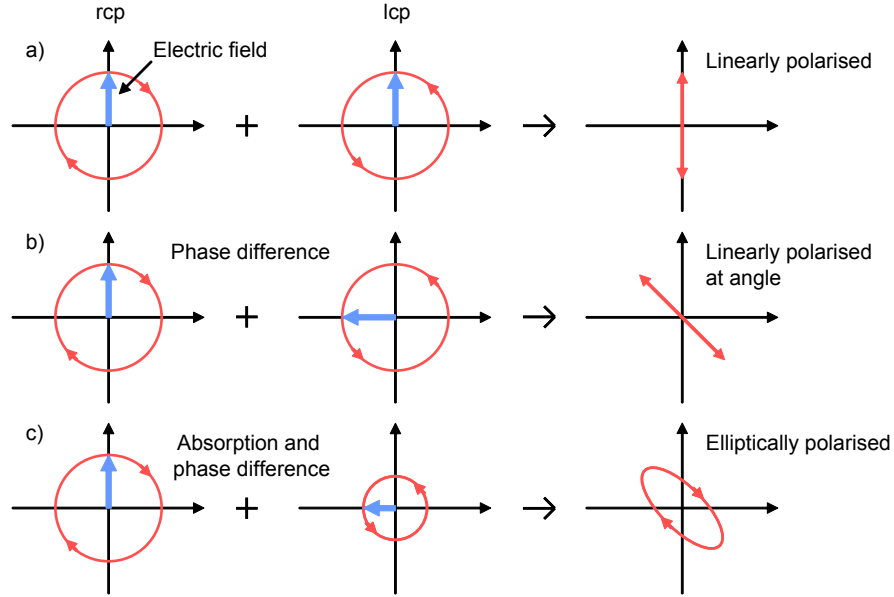
Figure 4.12: Illustration of the polarisation dependent absorption and phase shift acquired during reflection from a magnetic surface that renders the reflected light elliptically polarised.

results in a linearly polarised reflected beam with a rotation of the plane of polarisation. This effect is combined with a differential absorption of rcp and lcp illustrated in figure 4.12(c) leading to a final beam with elliptical polarisation.

4.5.2   Geometries of the magneto-optical Kerr effect

Measurements of the magneto-optical Kerr effect can be performed in three different geometries: transverse, longitudinal and polar which are illustrated in figure 4.13 and defined by the relative orientation of the magnetisation with respect to the plane of incidence of the illumination. The different geometries are best explained using a model where, upon reflection, a Lorentz force gives rise to an additional component of polarisation orthogonal to the incident electric field vector and the magnetisation of the sample. The addition of the original reflected polarisation with the Kerr component results in elliptically polarised light.
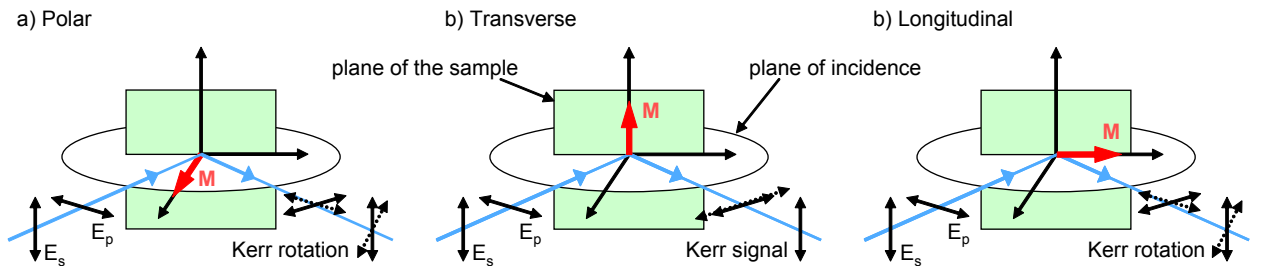
Figure 4.13: Schematic showing MOKE measurements of samples with magnetisation in a) longitudinal, b) transverse and c) polar geometries.

In the polar geometry, which is sensitive to magnetisation that lies out-of-plane of the sample, incident p and s light both experience a Kerr rotation. Measurements in the polar MOKE geometry are often performed with normal incidence illumination to maximise the orthogonality between the electric field vectors and sample magnetisation and hence produce a larger Kerr signal.

For transverse and longitudinal geometries the magnetisation lies in the plane of the sample and the incident beam must enter at an oblique angle or else the electric field would either be parallel with the magnetisation, producing no Kerr effect, or the Kerr effect would be along the beam direction and would not be measurable. For the transverse geometry the magnetisation is perpendicular to the plane of incidence of the light. This gives a magneto-optical enhancement of the amplitude of p-polarised light. In the longitudinal geometry, the magnetisation is parallel to the plane of incidence of the light giving rise to a rotation of the angle of polarisation.

4.5.3 Measuring magnetic properties of thin films and nanostructures

The MOKE technique provides surface sensitivity as the incident light probes only a certain depth into the sample known as the *skin depth*. This is defined as the depth at which the intensity is attenuated to $1/e$ of its initial value. The skin depth is governed by the absorption of the material and for most magnetic metals, has a value of 10-20 nm.[207] Measurements of films thinner than the skin depth give a Kerr signal proportional to the thickness of the film with additional effects from the interaction of the underlying substrate. For thicker films or bulk samples, the Kerr signal gives sensitivity only to the near surface region within the skin depth of the surface.

For investigating geometrical structuring in-plane the focussed spot size allows for localised probing of the magnetic behaviour. Individual nanomagnets cannot be resolved optically as their dimensions are smaller than the wavelength of light used to interrogate them. However, individual sub-wavelength nanostructures can still produce a detectable Kerr signal.[208] Further details about the measurements performed on the nanostructures in this investigation are given in chapter 5, which covers in more detail procedures for locating structures to be measured and maximising their signal to noise ratio.

4.6 Superconducting quantum interference device (SQUID) magnetometer

The magnetic characterisation techniques discussed so far in this chapter give great insight into the properties of magnetic materials but are limited to only giving magnetisation measurements on a relative scale. However, with a superconducting quantum interference device (SQUID) magnetometer direct measurements of the magnetic moment can be obtained. This technique is very sensitive and has a resolution below 10^{-14} Tesla[209] but does however require a larger sample volume and samples separated on individual substrates for the measurements. There are two varieties of SQUIDs, RF and DC. This discussion will focus on the operation of the RF SQUID as this was used in this investigation.

4.6.1 Design of the Josephson junction

The SQUID technique relies on the discovery by Deaver and Fairbank in 1961[210] where flux quantisation was observed in a superconducting ring in units of $\Phi_0 = h/2e$.[211] Supercurrents in the ring respond to changes in external flux, inducing an opposing flux to maintain the constant total flux through the inside of the ring.[212] The introduction of a Josephson junction[213] to the ring disrupts the supercurrents leading to an oscillating supercurrent contribution where the frequency scales with the internal flux contribution from the supercurrent.

4.6.2 Detecting changes to the supercurrents in a SQUID

To detect changes in flux using a SQUID, the superconducting ring is coupled to external circuitry. For the RF SQUID a resonant detection method[214] is used where the inductor of a resonant LC 'tank' circuit, illustrated in figure 4.14(a), is coupled to the superconducting ring in parallel with a capacitor chosen so that the tank circuit has a resonance and drives the SQUID at 20-30 MHz.[212] Externally applied DC flux damps the oscillating supercurrents and results in a change in power required to maintain the resonance frequency of the tank circuit. This is measured by amplifying and detecting the small change in the AC voltage across the tank circuit.[215]

The magnitude of the detected RF voltage shows a triangular shaped response with
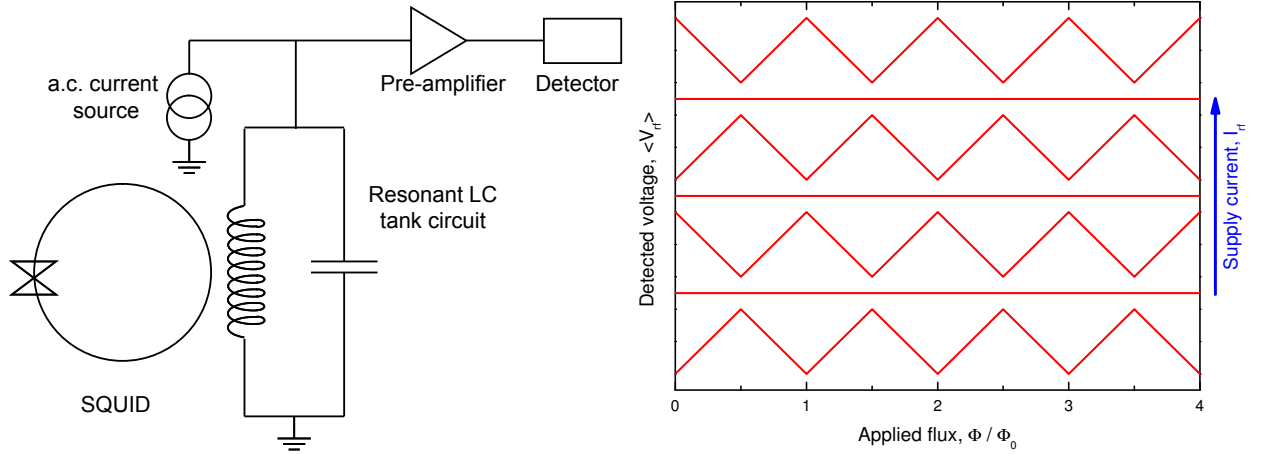
Figure 4.14: Resonance detection method for an a.c. SQUID showing a) schematic drawing and b) output voltage[212]

increasing flux, illustrated in figure 4.14(b). These oscillations correspond to the quantised states of the ring and depend on the tuning of the RF current supply. This response contains regions where the voltage increases linearly with flux as long as the changes in flux are less than $\pm\frac{1}{2}\Phi_0$.[212] To achieve a greater range than this, external feedback is incorporated to reduce the signal from the pickup coils to maintain the SQUID in the linear sensitive range. The reduction in the signal from the feedback is accounted for later with data correction factors.[216]

The SQUID device can measure change in magnetic flux on its own but it is often coupled to additional coils through a flux transformer. In chapter 5 the use of a SQUID as a magnetometer for measuring thin NiFe/Au films is discussed.

4.7 Micromagnetic investigation into the magnetic properties of nanostructures

To assist with the interpretation of results from the various experimental techniques outlined above and to gain insight into the physical processes occurring, micromagnetic simulations have been performed alongside the experimental work presented in this investigation. These simulations are based on the micromagnetic framework introduced in chapter 2 and offer a powerful way to model and visualise the time evolution of the microscopic magnetic structuring on a length scale smaller than that of domains and domain walls. This section will

cover the techniques involved in performing these simulations for the investigation of nano- and micro-scale thin film structures.

There are a variety of micromagnetic simulation packages available. SimulMag[217] is well suited for educational use or initial characterisation of magnetic device design before rigorous analysis. More in-depth analysis is suited to packages such as Magpar[218] or NMag[219] which has the main advantage of non-cuboidal cells allowing more generalised geometries to be investigated.[220] Here the discussion will focus on the object orientated micromagnetic framework (OOMMF)[221] used in this investigation due to its extensibility, general acceptance and adoption by a large proportion of the magnetics community. The simulations here were all performed at 0 K as the effect of temperature is not accounted for in this package and techniques for the inclusion of a temperature effect are not the aim of this investigation. Any results are therefore discussed knowing that micromagnetic results give an overestimate of reversal fields in comparison to the expected values from finite temperature samples. In a real system at a finite temperature, stochastic thermal fluctuations contribute energy to the spins in the system giving a lower effective energy barrier that needs to be overcome by field energy. In the simulations, this thermal energy is not present and therefore a larger field is required to achieve the same total energy. However, symmetry breaking issues were considered.

4.7.1   Performing micromagnetic simulations

To solve a micromagnetic problem using a simulation the sample is first represented as an array of cells containing a volume of magnetic material where the magnetisation is assumed to be uniform. Each cell is assigned a single spin which interacts with the effective field formed from a combination of the exchange with its eight nearest neighbour cells and energies from the interaction with magnetic field.[222] A Monte Carlo approach is then used to evolve the system in time, minimising the energy arising from the ensemble of spins in the system according to the LLG equation (equation 2.20).[69] This gives the time evolution of the magnetic spin state of the sample from which the magnetisation, energy contributions and spin arrangement can be extracted.

4.7.2 Division of generalised shapes into cuboidal cells

The division of a sample into cells was trivial in the example presented in chapter 2 where a rectangular planar nanowire structure was represented by a rectangular array of cubic cells. To represent a more generalised sample geometry, the cubic mesh is overlaid on the desired structure geometry and the shape is approximated to a collection of squares as illustrated in figure 4.15(a). Where the centre of a cell lies within the magnetic material the cells are assigned a M_s value for the material. Alternatively, if the centre of the cell lies outside the magnetic material then it is assigned a value, $M_s = 0$.[223]

Due to the square nature of the cells, this can result in step-like staircase edges to a magnetic structure which may result in behaviour or effects that are artefacts of the model compared to a structure with smooth edges. However, there are techniques available to reduce this problem. The cell size can be reduced, but this increases the computational load. Alternatively, corrections can also be made to the model to account for the differences in magnetostatic energy from step-like and uniform edges.[223] In this work, the step-like edges lead only to a small artefact in comparison to the geometrical structures investigated. This is then insignificant compared to the trends observed in the magnetic properties as a function of a wide range of sample geometries.
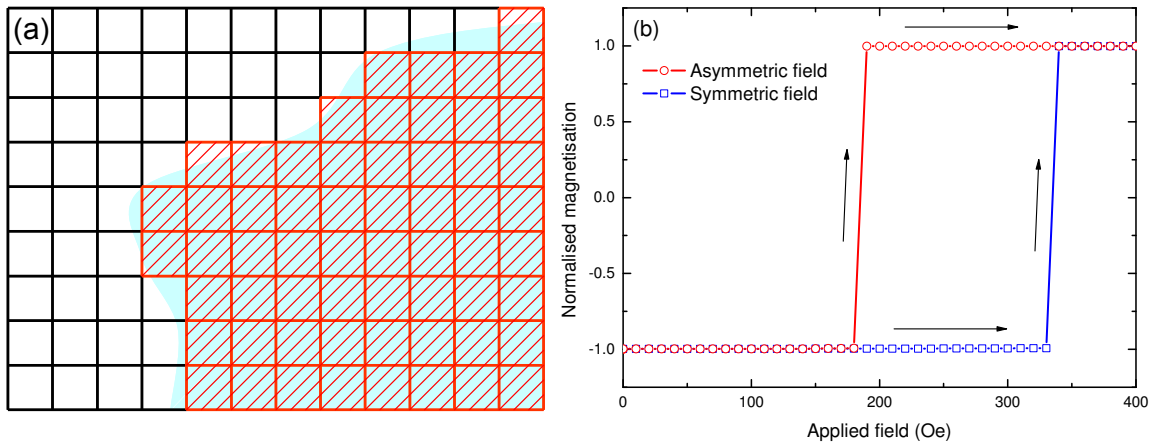
Figure 4.15: a) The division of a non-regular sample geometry into a cubic mesh where cells take the value of M_s of the material where their centre point overlaps the magnetic structure whereas other cells have $M_s = 0$. b) The effect of initial symmetry in the model gives an artificial increase in the reversal field that does not occur in real physical systems.

4.7.3 Removing symmetry

Micromagnetic simulations are often initiated with uniform magnetisation along a particular axis in the structure. For the case of a nanowire for example, it is typical to investigate the switching from negative to positive magnetisation where the initial magnetisation is saturated along the wire axis. Since there are no stochastic thermodynamic effects incorporated into the model it is necessary to remove the perfect symmetry from the model to prevent computational problems. This is typically achieved by adding a small off-axis field (in this case 0.1 Oe) which does not appreciably affect the model except to break the symmetry.

For the case of a 300 nm $\times$ 1 μm elliptical structure that is 5 nm thick, figure 4.15(b) demonstrates the reversal behaviour with applied field along the long axis with and without a small perpendicular 0.1 Oe symmetry breaking field. A considerable 150 ± 10 Oe difference in the reversal field is found which is higher without the symmetry breaking field. In a real system, imperfections in the structuring would lead to localised variations in the demagnetisation energy. Additional stochastic thermal effects are also not taken account of in the model. Both of these effects result in the breaking of symmetry in real systems so it is appropriate to compare these with simulations with a symmetry breaking initial field.

4.7.4 Damping in quasi-static and dynamic simulations

In magnetic systems the speed at which magnetisation rotation processes take place is governed by the damping in the system. This is a complex phenomenon and can be associated with the dissipation of magnetic spin energy into the thermal energy of the system. A more complete discussion of this is given in chapter 2. For the purposes of micromagnetic analysis the damping is described by a single Gilbert damping parameter, α, which is a phenomenological constant describing the rate at which precessing spins settle to the effective field.

For quasi-static simulations where the magnetisation and energetics of the system as a function of applied field are of interest, this damping is not important. Therefore, α is often set to a value of 0.5 which is significantly larger than measured value for most ferromagnetic materials but allows the simulation to converge to an equilibrium in a shorter computation timescale with little effect on the results of the simulations.[68,222] For simulations of dynamic magnetisation processes where the magnetisation as a function of time is the important quantity, α has a more significant impact on the outcome of the simulations. It must therefore

be set to a lower, more realistic value of 0.01 for $Ni_{80}Fe_{20}$.[224]

Figure 4.16 shows quasi-static micromagnetic simulations of the de-pinning of a domain wall from a trap structure (discussed later in chapter 8) with a damping parameter of $\alpha = 0.5$ and $\alpha = 0.01$. The graph shows that both damping parameters give consistent results supporting the validity of artificially increased damping for quasi-static simulations. The larger error bars for the $\alpha = 0.01$ points are artefacts arising from the torque stopping criteria which has been artificially increased in this simulation to gain the results on a reasonable computational timescale.

In quasi-static simulations it is common to progress through a range of applied fields where the magnetic configuration achieves an energy minimum at each field. During simulation the damping has the effect of reducing the energy of the system which converges to a minimum as the simulation evolves. Since this convergence may never reach the minimum point, an appropriate stopping condition must be defined to enable the simulation to finish or progress to the next field step. This is known as the torque stopping criteria where the torque, $|\boldsymbol{m} \times \boldsymbol{H}|$, must drop below this criteria for the simulation to progress. If this value is set too low then the simulation will continue to evolve for longer simulation times without a significant improvement in the validity of the simulations. On the other hand, if the criteria is set too high, the simulation will progress before the minimised energy state can be found. In this case the results from the simulations will not be realistic of the intended magnetic system.
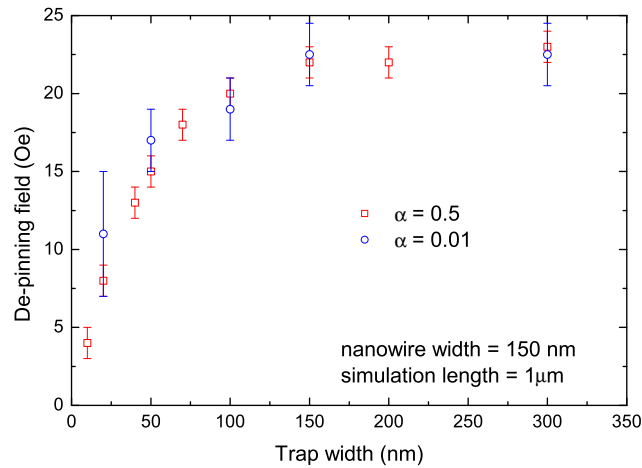
Figure 4.16: The de-pinning field of a domain from a reduced M_s trap giving a comparison between the damping parameters $\alpha = 0.5$ and 0.01 on the quasi-static nature of the micromagnetic simulations. Both damping parameters agree with the same trend but $\alpha = 0.5$ is generally accepted for this job as it is considerably quicker.

In the quasi-static simulations here, the default torque stopping criteria of 1×10^{-5} A/m is used, and for the dynamic simulations, the torque stopping criteria is removed from the simulation.[222]

4.7.5   Removing the effect of the ends of nanowires

Micromagnetic simulations are ideally suited to investigating the magnetic properties of finite micro- and nanoscale structures. Nanowires, on the other hand are finite in their width and thickness but have an extended length that can be approximated as infinite. Simulations on infinitely long structures are unrealistic so simulations on nanowires must consider only a finite length structure.

The introduction of ends to a nanowire will create free poles which set up a demagnetising field. This leads to a rearrangement of the spins which becomes significant towards the ends of the nanowire as shown in figure 4.17(a). A domain wall structure in a nanowire feels a force driving it towards the nearest end of the nanowire which adds complexity to the investigation of domain wall behaviour. To reduce the significance of this problem, the nanowire length can be extended to maximise the region towards the centre of the wire with uniform magnetisation but this comes at the expense of a significant increase in computation time.

Manipulation of the geometry at the ends of the wires can be used to gain a certain amount of control over the orientation of the spins.[225] The abrupt square end shown in figure 4.17(a) shows significant curling of the magnetisation towards the corners. The introduction of an elliptical end shape in figure 4.17(b) shows an improvement where the magnetisation points more uniformly along the axis of the wire with minimal edge effects. A nanowire with tapered ends in figure 4.17(c) can be used to arrange the spins to point inwards.

Another more involved method to account for the free poles at the end of a nanowire is to introduce boundary conditions where fixed spins produce a correction field which counteracts the field from the free poles at the end of the structure. This has the effect of maintaining
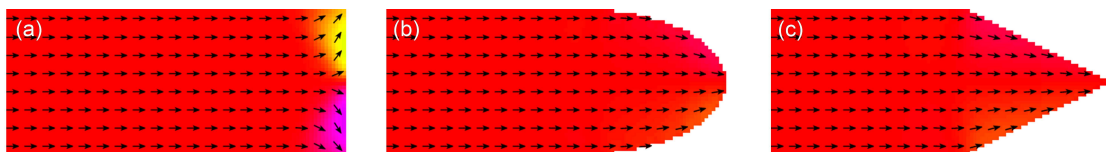
Figure 4.17: Micromagnetic simulations of 200 nm wide, 15 nm thick nanowires comparing the effect of a) rectangular, b) elliptical and c) tapered end sections extending over the last 200 nm of the structure.

uniform magnetisation along the nanowire all the way to the end. This methodology is illustrated schematically in figure 4.18.

A simulation is first performed on a nanowire, saturated along its axis, to find the stray field which develops as a result of the free poles on the end of the nanowire. This initial simulation has the same cross-sectional area, but a length 10 times larger than the desired simulation size, allowing the ends to be considered as independent. The free poles from this initial simulation are then fixed at the ends of nanowires in subsequent simulations with inverted polarity. This has the effect of cancelling out the poles created from the demagnetisation effects and allows the spins near the end of a nanowire not to 'feel' the effect of the nanowire end. This results in uniform magnetisation along the entire length of the nanowire.[226]

4.7.6 Micromagnetic simulations on domain wall dynamics

Dynamic effects are investigated through micromagnetic simulations by removing the torque stopping criteria, allowing the simulation to evolve as a function of time. Particularly appropriate to this project is the dynamic properties governing the propagation of domain walls along nanowire structures. These walls travel with a velocity which can be derived from the micromagnetic simulations by the analysis of the net magnetisation along the nanowire axis. For a fixed nanowire length the domain wall propagation increases the size of one domain at the expense of the other leading to an increase in magnetisation. The velocity of the domain wall can then be found from the gradient of the magnetisation with time as illustrated in figure 4.19(b).
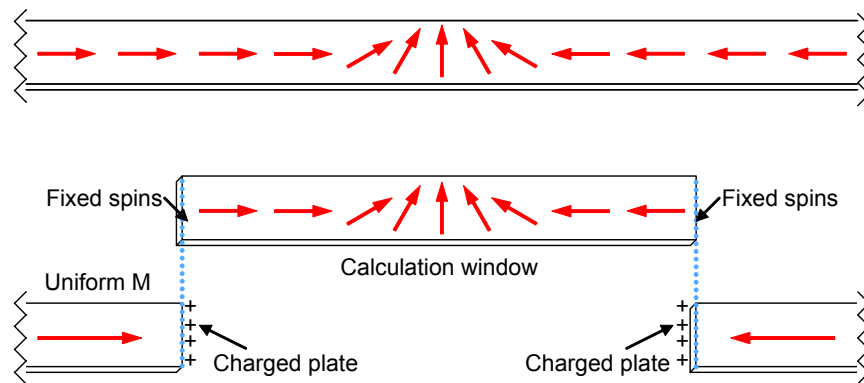
Figure 4.18: End correction where fixed spins at the nanowire ends counteract the demagnetisation effects from the wire end allowing the simulation of an effectively infinitely long wire.[226]
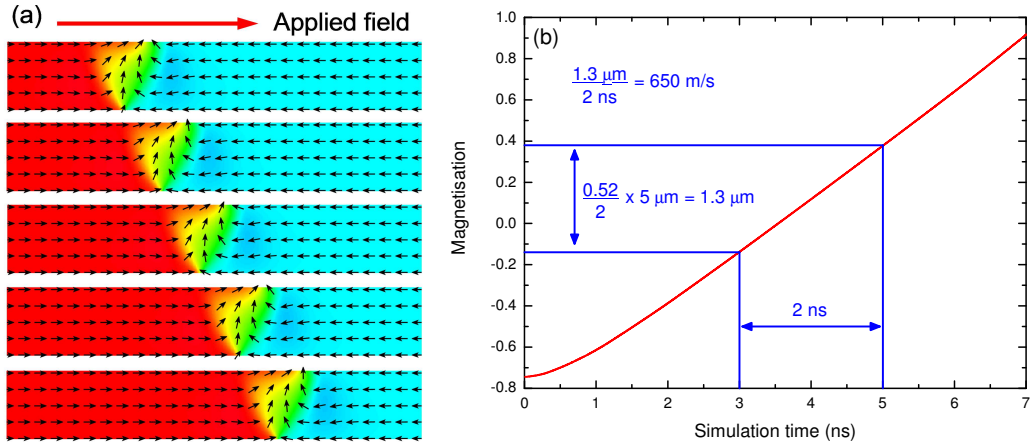
Figure 4.19: a) Evolution of domain wall position in time with applied field of 10 Oe in a section of a 250 nm thick, 5 nm wide, 5 μm long NiFe wire. b) The rate of change of position is used to determine the domain wall velocity.

The example shown here describes the velocity of a domain wall determined in its steady state but to achieve this state the domain wall must go through an acceleration phase better illustrated by the example in figure 4.20. Here a domain wall accelerates due to the application of an 8 Oe field. The domain wall takes up to 3 ns to achieve its maximum velocity, travelling up to ≈ 2 μm along the wire. Disturbances in the internal spin structure that affect the energy contributions continue for up to 8 ns.

These acceleration effects are a dynamic property of the domain wall which may be very interesting for the nanowire structures presented in chapters 8 and 9; however this is beyond the scope of the current work and here techniques for achieving the steady state domain wall
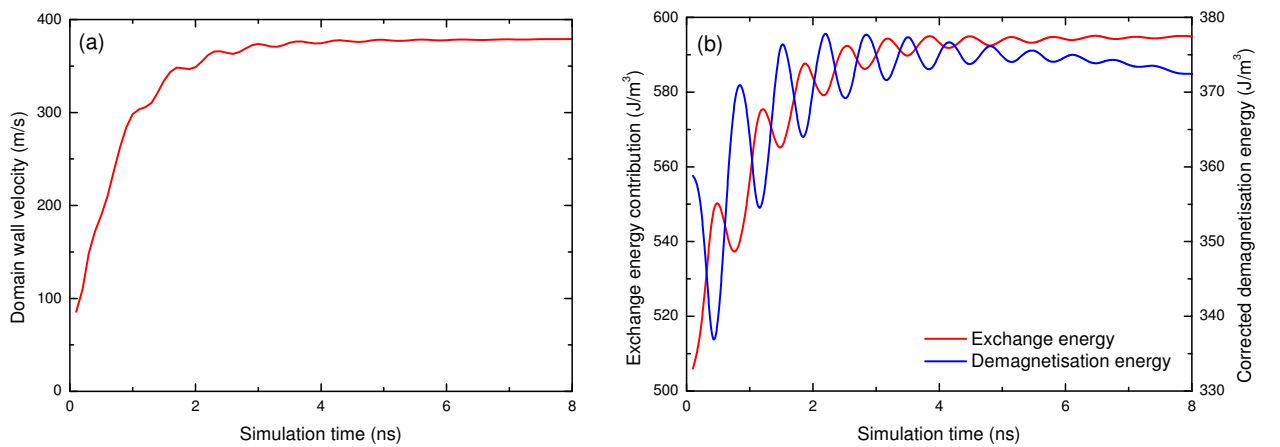
Figure 4.20: Change in a) domain wall velocity, b) exchange and magnetostatic energy as a function of time during the acceleration of an initially stationary domain wall in a 150 nm wide, 10 nm thick nanowire under the effect of an 8 Oe applied field.

motion without the the additional acceleration effects are considered.

One technique is to ignore the results collected for the first 3 - 8 ns of each simulation. This is a simplistic approach but it gives reliable results. However, domain walls can propagate a considerable distance in this time requiring an increase in the nanowire length and therefore an increase in computation time to achieve these results.

Another approach is to start a simulation with an initial magnetisation representing a domain wall already in a dynamic state. This would require starting a simulation based on the spin structure of a previous simulation but this would not hold information about the current state of precession or damping in these spins. This would likely still result in an initial phase where the domain wall needs to recover its steady state motion. This would be likely to take less time than the initial acceleration phase but this technique adds to the complexity of the simulation protocol.

In this investigation the dynamic properties were investigated for a wide range of nanowire geometries. Because of this the simplistic approach was adopted by increasing the simulation length. This was adopted due to the many different initiation steps that would need to be repeated for each nanowire geometry which would not significantly reduce the computation time in this case.

4.8 Simulating ion - solid interactions

The use of simulations provides insight into the magnetisation processes that take place in magnetic systems and helps with the interpretation of the experimental results. Simulations also provide additional understanding in relation to the structural and compositional analysis work performed in this thesis. These help to provide further understanding of the results from the experimental structural analysis techniques. Following from the theory of ion-solid interactions introduced in chapter 3, this section follows Eckstein in his review of simulation approaches to ion-solid interactions and describes how these theories are formulated into simulations.[227]

The basic principles show that an energetic ion incident on a target will undergo scattering and lose energy as a result of collisions with the target atoms. This results in multiple processes taking place such as sputtering of the target surface, ion implantation, and interfacial intermixing (already discussed in chapter 3). These processes can all be studied by

following the histories of incident ions and subsequent recoils in a step-by-step fashion by
the analysis of many collisions taking place in a collision cascade. This must be repeated for
many incident pseudoparticles to obtain reasonable statistics.[227]

There are two main approaches to performing these simulations, either the binary collision
approximation method or the classical or molecular dynamics approach. The binary collision
model approximates the interaction as a series of binary collisions between moving ions and
target atoms. This differs from the classical or molecular dynamics model which take into
account interactions with all nearest neighbouring atoms to study the movement of atoms
as a function of time using many body Newtonian mechanics. The discussion here focusses
on the binary collision approximation model as this is the most common for this type of
simulation. It is also the method used in the TRIDYN simulation package which was used
for the simulations presented in chapter 6.[228] TRIDYN is a dynamic version of the TRIM
code so this discussion first considers the operation of the TRIM code before the extension
towards the dynamic simulations in TRIDYN.

4.8.1   Simulation method

Models using the binary collision approximation such as the TRIM[229] code are commonly
solved by Monte Carlo simulations instead of analytic analysis of the formulations based on
transport theory. The advantage of this is that it gives a better treatment of the elastic
scattering process in a model where it is easier to define surfaces and interfaces and make it
easy to determine the energy and angular distributions following scattering events. Monte
Carlo simulation techniques, however, come at the expense of a large computational load
so simulations usually result as a compromise between the accuracy and processing time
constraints.[229]

These simulations consider a large number of incident pseudoprojectiles which represent
a differential fluence, $\Delta\phi$, that is equal to the total fluence, ϕ_0, divided by the number of
pseudoprojectiles, N_H.[227] Each pseudoprojectile has an initial energy, position and velocity
and is sequentially directed towards the target composed of an amorphous collection of atoms
with random locations.[230] Interactions during a binary collision result in the elastic energy
transfer between ion and target and also modify the ion's trajectory. Further energy losses
also occur due to nuclear and electronic inelastic scattering.[229] The history of the pseudo-
projectile is terminated when its energy falls below a cut-off energy, $E_{f,i}$, or when its cascade

results in it ending up outside the simulated target region.

There are two assumptions that dramatically increase the efficiency of the simulation:

- An analytic formula is used to determine atom-atom collisions rather than evaluating the complete scattering integral.

- A free-flight-path approach is used so only significant collisions are evaluated.

Analytic expression for binary nuclear collisions

The analytic formula approximation developed by Molière[231] can be used to increase the processing speed of the simulation by up to 50 times in comparison to the numerical analysis of the scattering integral.[232]

For high energy collisions the target atom can be assumed to be an unscreened nuclear coulomb potential as the electron density has little effect on the scattering. This assumption puts the collisions into the Rutherford regime, making use of a derivable fitting parameter, Δ. For lower energy collisions the nuclear screening is important and the fitting parameter is modified to include two parameters that are tuned so that the simulations fit correctly with the experimental results. With these parameters the potential can accurately represent scattering with most atomic potentials where the range from low to high is accounted for by an interpolation scheme to bridge the gap.[233]

Free flight path assumption to reduce computation time

Between collisions, ions are assumed to travel in straight free-flight paths where they do not lose momentum or kinetic energy. The length of this path depends on the pseudoprojectile energy which is used to calculate a maximum jump length. This length is then divided randomly to determine the position of the next collision event. After each collision the energy decreases along with the maximum jump length. When the jump length would extend over a boundary into a different layer, the length is reduced to a random distance within that length which is then repeated until the interface is crossed in monolayer steps.

The maximum path length is given by $\lambda_l = n^{-\frac{1}{3}}$ based on the local atomic density n. This underestimates the nuclear energy loss so $\lambda_l = 0.5n^{-\frac{1}{3}}$ was chosen as a satisfactory approximation adopted for simulations.[234]

4.8.2   Energy transfer during binary collisions

When an ion of energy E is involved in a collision with a target atom, the energy is divided between the final energy of the ion, E_1, and the final energy of the target atom, E_2. Each target atom also has an associated displacement energy, E_d, and binding energy, E_b, which represent the physical bonding strength between atoms in the target.

In collisions where $E_2 < E_d$, the final energy of the target atom is not sufficient to overcome the displacement energy barrier. It therefore remains in its original location in the target and the remaining energy, E_2, is dissipated away by phonon emission in the target. When $E_2 \geq E_d$ the target atom is displaced from its initial location in the target matrix. It leaves behind a vacancy and joins the cascade of moving ions with an energy given by $E_2 - E_b$. Similar comparisons are made with the incident ion energy, E_1, which remains in the cascade if $E_1 \geq E_d$ and becomes an implanted defect if $E_1 < E_d$.

As ions in the cascade take part in more collisions their energy is depleted. When the energy falls below a cut-off energy, $E_{f,i}$, the history of the pseudoparticle is terminated. This cut-off energy should be set below the surface binding energies to ensure correct sputtering yield and atomic relocations are represented by the simulations.[228]

4.8.3   Dynamic relaxation of the target structure

TRIDYN is a dynamic version of TRIM code which has been extended to account for dynamic changes in target composition as a function of fluence.[230] These changes are significant for highly energetic ions where atomic reordering may occur, e.g. in layered structures or polyatomic materials.[234]

Again this uses the binary collision approximation in an amorphous target, but there are differences in how the target reacts to the incident fluence. Initially the target is divided into arbitrary regions of constant thickness. During the collisional transport stages of the simulation, atomic rearrangement results in vacancies in some atomic sites and interstitial defects at others along with sputtering of the surface. This is illustrated in figure 4.21(a) and (b).

In TRIDYN a dynamic relaxation step is introduced following the collision cascade, when the energy of all of the particles involved in the collision cascade has decreased below the cut-off energy. The defects result in a change in density of the layer and the thickness is
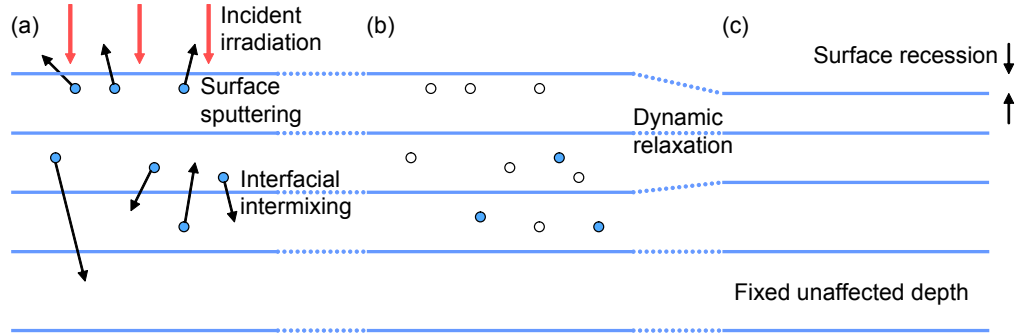
Figure 4.21: Schematic showing process involved in the TRIDYN simulation starting with a) ion cascades that cause surface sputtering and interfacial intermixing b) resulting in a modified density in each layer c) which then relaxes to give layers of varying thickness with constant density during the dynamic part of the simulation.[230]

adjusted so that the density relaxes in a process illustrated in figure 4.21(c). The simulation of the collision cascade, followed by dynamic relaxation is repeated for each pseudoparticle involved in the simulation.

Following a simulation, the layers with modified sizes are interpolated to give composition profiles as a function of equal depth increments. These results are particularly useful near interfaces where these effects show isotropic broadening of initially abrupt interfaces. The output profiles also contain the location at which the incident ions come to rest within the target matrix giving estimates for the range of the ions in the material.

4.9 Summary

In this chapter various techniques have been introduced relating to the investigation of the structural and magnetic properties in thin films and nanostructures. First, structural studies by x-ray reflectivity are described that give insight into the thickness and interfaces between layers of a thin film while elemental profile can be obtained using x-ray fluorescence techniques. Modifications to the structure resulting from energetic ion irradiation can also be simulated, adding to the understanding of the work presented in chapter 6 on the nature of ion irradiation on the structure of thin films.

Magnetic analysis techniques including XMCD, MOKE, SQUID and micromagnetic simulations have also been discussed. Each technique has advantages for understanding a certain aspect of the magnetisation behaviour in this investigation. For the analysis of changes in magnetism resulting from ion irradiation, the change in magnetisation found from both

MOKE and SQUID techniques. This was further investigated in terms of the spin and orbital contributions using the element specific XMCD technique, which in combination with x-ray reflectivity also gives rise to depth sensitivity. These results are presented in chapter 7. The focussed nature of the MOKE allows for interrogation of magnetic properties on a local scale allowing for magnetic characterisation of nanoscale structures. Structures on this scale show properties that are well explained by comparison with micromagnetic simulations and are presented in chapters 8 and 9.

Chapter 5

Experimental Procedures

5.1 Introduction

In this chapter the experimental procedures that were used to obtain the results in this investigation are discussed in an order relating to the objectives of each area of the investigation. Firstly, the experimental procedures for the detailed structural analysis that used both x-ray reflectivity and fluorescence techniques are discussed. An important aspect of this part of the investigation is the trade-off between relatively large areas needed for x-ray measurements and the small areas most suitable to focussed ion-beam irradiation. Secondly, the experiments are discussed for the investigation of the change in magnetic properties as a function of ion beam irradiation. This uses a combination of MOKE, SQUID and XMCD experiments that combine to give an understanding of the irradiation induced changes in the magnetic properties discussed in chapter 7. MOKE measurements were performed in the first instance to gain an understanding of the magnetic behaviour for a wide range of irradiation parameters whilst the SQUID and XMCD techniques were performed on samples with selected irradiation conditions to further investigate the origins of the changes in magnetic behaviour of these materials.

Finally the experimental work performed on magnetic nanowire structures is described. This combines the techniques involved in the fabrication and measurement of nanoscale magnetic samples using focussed MOKE measurements. Local ion irradiation was also performed along the nanowires to investigate the effects of local magnetic modification upon the propagation of domain walls in the nanowires.

5.2   Sample preparation details

Before providing a detailed discussion of the specific experimental details for each stage of this investigation, an outline of the sample preparation procedure is first given that is appropriate to every sample presented in this work.

5.2.1   Preparation of Si/SiO$_2$ substrates

Samples were prepared on substrates of single crystal Si wafers with a 500 nm thick amorphous hydrothermally grown oxide layer. This amorphous oxide acts to stop the effects of the underlying crystal structure affecting the growth of subsequent layers and also acts as an electrically insulating layer which is important for samples with electrical connections. These wafers were scored using a diamond scribe and diced into ≈ 5 mm square substrates.

It is important to keep samples free from dirt and grease, particularly when experimenting with nanoscale structures where the size of dust particles become comparable, or even larger than the structures under test. Therefore all the preparation steps were performed in a cleanroom and the sample substrates were cleaned, first in acetone and then isopropanol (IPA) for two minutes in each under ultrasonic agitation and then blown dry with N$_2$ gas.

5.2.2   Thin film deposition by thermal evaporation

Deposition of metallic thin films was performed by thermal evaporation. Substrates were placed at the top of a vacuum chamber, 50 cm above crucibles containing the source material. These crucibles were ceramic coated tungsten wires, or in the case of Cr, a pre-coated tungsten wire. These were heated ohmically with a DC current (typically 30 - 60 A) to achieve a steady evaporation rate, typically 0.6 $\mathring{A}$/s for NiFe (nominally Ni$_{81}$Fe$_{19}$) from a single alloy powdered source followed by Au at 0.3 $\mathring{A}$/s without breaking the vacuum. Once a stable rate was established the sample shutter was opened, allowing deposition on to the sample. Deposition was monitored using an in-situ quartz crystal rate monitor to determine the deposition rate and thickness in real time. The rate monitor was calibrated against x-ray reflectivity data for films of different thicknesses and is accurate to 0.1 nm. Once the desired thickness was achieved, the shutter was closed, the current stopped and the chamber allowed to cool before venting with N$_2$ gas.

The vacuum achieved by the combination of backing and turbo pumps gave a typical base

pressure of 10^{-7} Torr, this rose to 10^{-6} Torr during deposition. Baking-out the crucibles prior to evaporation helps to achieve lower pressures by allowing absorbed gases to be released from the crucibles, the source materials and to some extent the chamber walls.

5.2.3 Electron beam lithography

Geometrical structuring was achieved by electron beam lithography prior to the deposition of the thin film material. The methodology was introduced in chapter 3 and here the specific experimental steps that were useful in many different parts of this investigation are outlined.

First a ≈ 70 nm resist layer was deposited by spin coating a 2% solution of PMMA-495 in anisole at 3000 rpm for 30 seconds onto a substrate. This was then baked on a hot plate for 90 seconds at 120°C to evaporate the anisole solvent.

The samples were then loaded into the dual beam FIB/SEM system, positioned at a 4 mm working distance and aligned using the electron beam with a 21 pA beam current and 30 keV acceleration voltage. This beam was focussed onto an edge of the substrate in a sacrificial region where additional exposure was not critical to the final sample. The centre of the substrate was then located and patterning was controlled by patterning software relative to this centre point. Patterns were exposed with a single pass of the electron beam remaining at each pixel for a dwell time of 8 μs delivering an electron dose of 400 $\mu C/cm^2$, suitable to break enough polymer links in the PMMA allowing it to be cleared during development.

The exposure was followed by development of the resist in a 1:3 solution of methyl-iso-butyl-ketone (MIBK) : IPA at 21°C for 20 seconds followed by a wash in IPA for 20 seconds and blown dry with N_2 gas. This created a nano or microscale stencil through which a thin film was subsequently deposited by thermal evaporation. Following deposition, lithographically patterned samples were soaked in acetone for 1 hour followed by 2 minutes in acetone then IPA with ultrasonic agitation to remove any unexposed PMMA and deposited material, to reveal the desired pattern on the substrate.

5.3 Structural investigation of NiFe/Au bilayers

Structural modifications to NiFe/Au bilayers resulting from Ga^+ irradiation were investigated using grazing incidence x-ray reflectivity and fluorescence techniques. This section describes the experimental procedure for fabricating, irradiating and characterising the struc-

tural properties of the samples using these techniques. The results along with their discussion are presented in chapter 6.

5.3.1 Choice of sample geometry

Measurements using x-ray reflectivity and fluorescence techniques require relatively large area samples. The x-ray beam spot size when focussed was ≈ 50 μm diameter (see section 5.3.5) but when projected at grazing incidence, the footprint of the beam on the sample becomes much larger. For these measurements it was also important to have adequate separation of the samples to ensure that the beam probes only one sample at a time and to make it easy to identify and align with the beam. It was therefore necessary to produce samples that were several millimetres long and with a comparable separation between structures.

Since these structures were intended for analysis of the modification to the structural properties resulting from Ga^+ irradiation large sample areas needed to be irradiated. To accurately represent the structural modifications that occur in nanoscale systems from local ion irradiation, similar irradiation conditions were needed for this large area irradiation to allow for a direct comparison. Performing such localised irradiation on a large area was also challenging as this process was performed serially over a long timescale. This can introduce problems due to drift in the ion beam current or the sample position over time.

The sample size was chosen as a compromise between the large areas required for x-ray measurements and the timescale required for performing Ga^+ irradiation on these structures. This led to the choice of strip samples with dimensions 1.3 mm $\times$ 5.5 mm separated by 1 mm gaps which were prepared by thermal evaporation of 20 nm NiFe followed by 2.5 nm Au cap through a shadow mask onto a SiO_2 substrate.

5.3.2 Irradiation of large area samples

To perform this large area irradiation the techniques discussed in section 3.7.2 have been adopted. The 1.3 mm $\times$ 5.5 mm strips were divided into an array of 200 μm $\times$ 200 μm write fields. Each of these were irradiated by raster scanning the beam over an array of 20 μm $\times$ 20 μm regions. Following the irradiation of each write field, the stage was moved in 200 μm steps covering first the 1.3 mm width of the samples before repeating multiple rows covering the entire area of the strip in a scheme illustrated in figure 5.1. Each stage movement had a
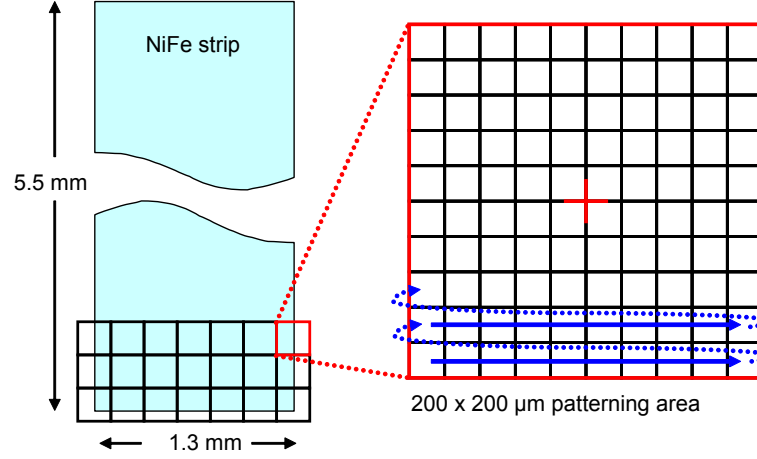
Figure 5.1: Irradiation of a large area strip was performed over 200 μm write fields where the beam was raster scanned over an array of 20 μm patterning areas. This was followed by successive stage movements to cover the entire area of the strip.

stitching error of at worst ≈ 1 μm which is negligible compared to the millimetre scale x-ray beam footprint. The irradiation area was intentionally larger than the strip to ensure the entire NiFe/Au structure was irradiated in the case of a misalignment or drift of the sample position over time. Excess irradiation on the Si/SiO$_2$ substrate does not significantly affect the results.

The irradiation was performed with normal incidence Ga$^+$ irradiation at 30 keV as these conditions transfer the maximum energy to the sample without leading to significant amounts of surface sputtering (see figure 3.6). A 6.7 nA beam current with a 66 nm beam diameter was rastered over the area with a pitch of 33 nm and held at each position for a dwell time of 1 μs. The dose, determined by the number of repeat exposures, was chosen to be in a region where interesting magnetic properties were found which are presented in chapter 7.

In total the irradiation of each strip took from several hours up to days depending on the irradiation dose. During the irradiation the damage to the beam defining aperture was significant resulting in a steady increase in beam current throughout the irradiation. A measurement of the beam current before and after irradiation was performed and the average used to give an improved estimate of the dose received by the sample.

5.3.3   X-ray reflectivity and fluorescence measurements

The x-ray reflectivity and fluorescence measurements were performed using synchrotron x-rays from the bending magnet, BM28 on the XMaS beamline at the ESRF in Grenoble. The use of synchrotron x-rays allows for a high brightness giving a large number of photons per

second compared to a standard laboratory source. This allows for the measurement of weakly scattered diffuse scatter with reasonable counting times which is important for characterising the roughness and intermixing at the interfaces. The radiation from a bending magnet is polychromatic allowing the use of a monochromator to give x-rays tuned to a particular energy allowing for the investigation of fluorescence, where the excited transitions can be chosen.

Both the x-ray reflectivity and fluorescence measurements were performed using the same experimental setup illustrated by the simplified schematic in figure 5.2. Synchrotron x-rays pass through the beamline optics which condition the beam to a 50 μm spot incident on the sample. The x-rays reflect off the sample at an angle of θ into the detector located at 2θ. These incident x-rays are also absorbed, ejecting a core electron from the elements in the sample (depending on the incident energy) giving rise to fluorescent x-ray emission which can also be detected with a detector above the sample.

Reflectivity scans were performed with 11.8 keV x-rays in the θ - 2θ configuration scanning 2θ from 0° - 7° with a step size of 0.02° and a counting time of 1 - 4 s at each point. At low incidence angles this was measured with a photodiode detector positioned at 2θ with beam attenuators to limit the intensity and avoid saturation of the detector. At higher angles as the reflected intensity decreases, the attenuators were removed and a more sensitive avalanche photodiode detector was used. The datasets for different levels of attenuation and detector
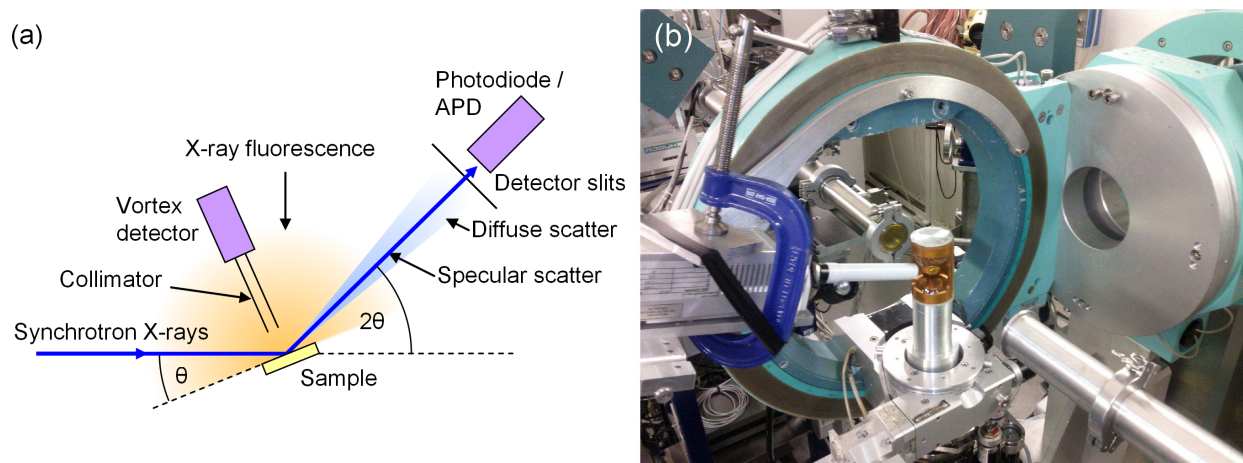
Figure 5.2: a) Simplified schematic layout and b) photograph of the experimental setup for grazing incidence x-ray reflectivity and fluorescence measurements performed at the XMaS beamline at the ESRF in Grenoble. Synchrotron x-rays incident on the sample produce specular and diffuse scatter which is measured by a detector at 2θ as well as fluorescence x-rays which are measured from above the sample.

were combined and normalised against the monitor signal from an Au grid located before the attenuators to account for minor changes in the incident beam intensity and losses in the ring current. A corresponding off-specular scan (offset by -0.1° in θ) was also performed and subtracted from the specular scan to obtain the true specular reflectivity of the sample. This allows an approximation of the forward diffuse scatter from any topological roughness in the film to be removed from the specular reflectivity results.

Transverse diffuse scans in θ with a fixed 2θ at Kiessig maxima or minima were also used to measure the diffuse scatter and give information about the in-plane structure, such as topological roughness and chemical intermixing in the sample. θ was scanned from 0° to 2θ in 0.05° steps counting for 4 s per point. This was followed by more detailed scans in the central 0.3° region of the specular peak in steps of 0.005°.

The x-ray fluorescence measurements were performed with incidence x-ray energies of 12.5 keV and 11.8 keV, i.e. above and below the Au L_3 edge (11.919 keV[235]). The fluorescence signal was measured with a Vortex Si-drift diode detector positioned perpendicular to the beam direction and fixed at 75° to the sample plane to avoid detecting any signal directly from the beam such as air scatter. The detector measures the energy of the fluorescent x-rays from the sample by converting each detected x-ray into a charge proportional to its energy which is counted with a multi-channel analyser (MCA). By combining the individual counts at each energy, spectra were produced representing all of the intensity from each fluorescence emission taking place within the sample. Fluorescence scans were performed at grazing incidence for θ from 0° to 1° in 0.01° steps with data collected for 30 - 60 seconds at each step. These measurements were used to gather information about the depth dependent composition throughout the sample. Fluorescence was also measured as a function of position across the width of the irradiated samples in 50 μm steps with a constant incident angle of $\theta = 1$°, i.e. above the critical angle. This gave information about the average composition of each sample. Reflectivity and fluorescence scans followed a similar method but were not performed simultaneously. For the fluorescence measurements the saturation of the detector at low angles was not a problem, so the beam attenuators were not used and the reflectivity detector was moved away from the specular condition.

5.3.4   Fitting of the peaks in the fluorescence spectra

The fluorescence spectra showed the x-ray energy from all of the fluorescence transitions taking place within the sample. These were separated into the contributions from each element by fitting the spectra with a set of peaks corresponding to the individual atomic transitions. This fitting was performed using the Levenberg-Marquardt method[236] and an example was illustrated previously in figure 4.7 where multiple peaks were combined to form a model that fits to the experimental data.

Pseudo-Voigt shaped peaks were used to best represent the peaks constituting the fluorescence emission as they incorporate the linewidth of the transition convoluted with the energy resolution of the detector (100 - 150 meV minimum[237]). The full width half-maxima and shape parameters of the peaks were constrained to be the same for all transitions from the same element due to the negligible broadening of inner shells in heavy elements. The peaks are centred on the transition energies given in table 4.1 and the energy axis was allowed to shift and stretch to account for changes in the energy calibration of the vortex detector, which affects all transitions in the same way. The ratio of peak heights between the transitions was constrained to be in the ratio of the relative emission rates, also given in table 4.1 and the heights of all the peaks were varied together when fitting the model to the data.

Once the model was fitted to the data, peak areas give the fluorescence intensity originating from each element. These were then normalised against the beam monitor to account for any small changes in incident beam intensity during the measurements. Fluorescence intensity as a function of grazing incidence x-ray angle was then fitted to a model describing the depth dependence to the composition of the sample.

5.3.5   Fitting grazing incidence XRR and XRF data

The angular dependent x-ray reflectivity and fluorescence data were fitted using the commercial software package Bede REFS.[238] This uses a model based on the nominal sample structure containing free parameters to describe the thickness, roughness and composition of each layer. A reflectivity or fluorescence curve is then simulated using these model parameters and the theoretical framework discussed in chapter 4. The parameters are then adjusted to find a model which best fits to the data. When a suitable fit is found, the model parameters are then taken to be representative of the sample structure.

A goodness of fit (GOF) parameter was calculated from each model fit to the experimental data. For reflectivity data where intensities vary over many orders of magnitude, a logarithmic GOF parameter was used but with fluorescence a linear GOF parameter is more suitable. A genetic algorithm[239] was used to modify the model parameters within a certain range and the changes to the parameters are accepted if the GOF parameter is reduced.

Some model parameters such as the sample size and beam dimensions have been fixed prior to fitting based on other measurements. The exact sample size is found from travelling microscope measurements and beam dimensions are determined from half cut measurements of the beam shown in figure 5.3. As the sample height was increased the beam became obscured by the sample and the intensity dropped to zero. The shape of this curve represents the Gaussian profile of the beam[240] so fitting the shape of this curve with a sigmoidal function gave an estimate of the beam width of 50 ± 3 μm in the z direction.

5.3.6   Ion - solid simulations on multilayered samples

To support analysis of the structural experimental results, models of incident energetic ions on bilayer system were performed following the technique discussed previously in chapter 4. These were performed using the TRIDYN simulation package.[230,234] Here a model for the NiFe/Au bilayer sample with amorphous texturing was assumed. Normal incidence Ga$^+$ irradiation was applied to the sample at 30 keV and simulated using 10,000 pseudoprojectiles to give good statistical averaging without excessive computation time.

Table 5.1 shows the parameters used to describe the atoms and their energies that are
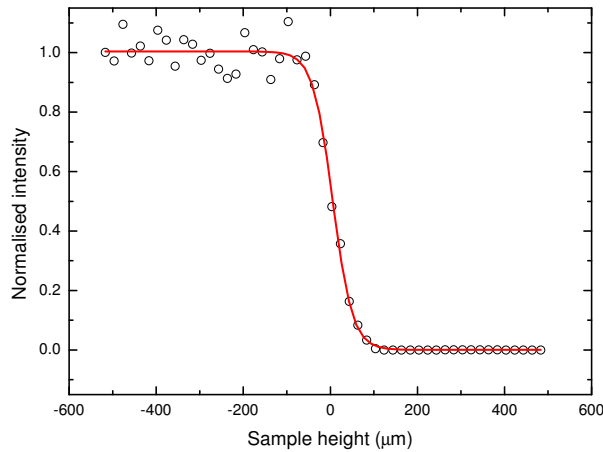
Figure 5.3: X-ray beam intensity as the beam is cut by the sample. This is fitted with a sigmoidal function and used to determine the beam width of the beam with Gaussian profile.

Element	Ga	Au	Ni	Fe
Atomic number	31	79	28	26
Atomic mass (amu)	69.72	196.97	58.71	55.85
Atomic density ($\times 10^{22}$ cm^{-3})	5.10	5.90	9.14	8.49
Bulk binding energy (eV)	0	0	0	0
Surface binding energy (eV)[143,241]	2.8	3.8	4.46	4.34
Relocation threshold energy (eV)[143]	12	36	23	17
Cut off energy (eV)	1	1	1	1
Electronic stopping correction factor	1	1	1	1

Table 5.1: Table of parameters used by TRIDYN for the simulation of energetic Ga$^+$ ions incident on a NiFe/Au bilayer system.

used in the simulations. The results given by the simulations are ultimately be determined by these values so it is important they are representative of the real physical parameters.

The bulk binding energy is the energy needed for an atom to leave its initial location in the bulk of the material. This energy is subtracted from the energy transfer to the recoil atom during every collision. The value for this was hard to obtain so was set to a recommended value of zero, which is reasonable when surface binding energies are more significant.[228] These are similar to the bulk binding energy but are associated with atoms at a surface or interface. The value for these can be taken from the enthalpy of sublimation, the energy taken to convert the solid into a gas. This assumption works well for multi-atomic targets which have a low heat of fusion such as metallic alloys.[234]

Once an atom or ion joins the collision cascade, the cut-off energy determines the energy at which particle histories are terminated. This needs to be set less than the surface binding energy, but otherwise a higher value reduces the computation time. Here a value of 1 eV was chosen for all elements, suitably below the lowest surface binding energy at 2.8 eV. Once its energy is depleted the particle then occupies a new position in the sample and it can either relax back to its original position or remain in the new position if the energy change is greater than the relocation threshold energy. Ion beam mixing, preferential sputtering and the resulting composition profiles after irradiation are critically determined by this parameter as the width of these collisional mixing profiles scales inversely with the square root of the relocation threshold energy.[143] Finally the electronic stopping correction factor is a means to correct for deviations from the Lindhard-Scharff stopping potential, important for light projectiles, it is set to a recommended value of 1.[229]

The simulations returned results showing changes to the structure and composition of the

model sample as a function of the applied dose. This contains information including the areal density of implanted Ga$^+$ ions, the sputtering yield and the predicted surface recession of the target resulting from the incident irradiation. The simulations also produce depth profiles for each atomic component showing the intermixing for various selected doses.

5.4 Investigating the magnetic properties of irradiated magnetic material

Following irradiation, modifications to the sample structure resulted in changes in the magnetic properties of the NiFe/Au bilayer structures. This section describes the experimental methods used to investigate these effects. The investigation starts with the initial characterisation of a wide range of irradiation conditions followed by more specific techniques to confirm and further investigate the magnetism for selected doses.

5.4.1 Magnetic characterisation of irradiation parameter space

Initially MOKE measurements were used for the measurement of a wide range of samples under different irradiation conditions. The MOKE magnetometer has a beam spot size of ≈ 10 μm making it ideal for probing the magnetic properties of microscale structures. The irradiation procedure for these smaller structures was much less complicated and was performed on a reasonable timescale. Structures on the 10 micrometer scale were also easier to locate and align on the MOKE system.

Ellipses of size 50×10 μm were chosen so that the samples had an easy axis from shape anisotropy but also curved edges to reduce the complicated spin structures that can arise from sharper edge structures. Multiple ellipses were fabricated by electron beam lithography followed by thermal evaporation of NiFe/Au with a variety of thicknesses onto a single Si/SiO$_2$ substrate giving a large number of test structures that are nominally identical. The pitch of 100 μm gave sufficient separation between each ellipse such that any interference effects between neighbouring elements could be ignored.[208] However, this was small enough to allow fabrication on a single substrate and for easy navigation between structures using the MOKE system.

Following fabrication, the samples were irradiated using the dual-beam FIB/SEM system.

The sample was positioned at the eucentric point, the focal point of both the ion and electron beams. Alignments and identification of the structures were mainly performed using the electron beam to avoid unnecessary ion beam irradiation of the samples during imaging. Once positioned, a snapshot image with the Ga^+ beam confirmed the alignment and allowed for the precise positioning of an irradiation window over the elliptical structure. This short exposure with a 50 ns dwell time should only contribute at most a small systematic error in the dose to all of the measurements.

A rectangular irradiation window of 55×14 μm was used which was slightly larger than the ellipses. This allowed the beam some lead-in time and lead-out time where any deviations from the beam blanking or positioning would lead to dose variations outside the desired structures at the edge of the scan. However, the irradiation window was kept relatively small to avoid excessive time spent irradiating the substrate rather than the sample.

The beam conditions were kept similar to those used in the structural investigation; this used a 30 keV Ga^+ beam at normal incidence irradiation to keep sputter yields to a minimum. Beam currents of 28 pA and 515 pA were used and the required dose was achieved by repeated exposures of each pixel in the pattern with a dwell time of 1 μs. The magnification was $2000\times$, giving a 64 μm wide field of view.

The measurements of the magnetic properties of these samples were performed using longitudinal MOKE measurements with the experimental setup illustrated by the schematic in figure 5.4.
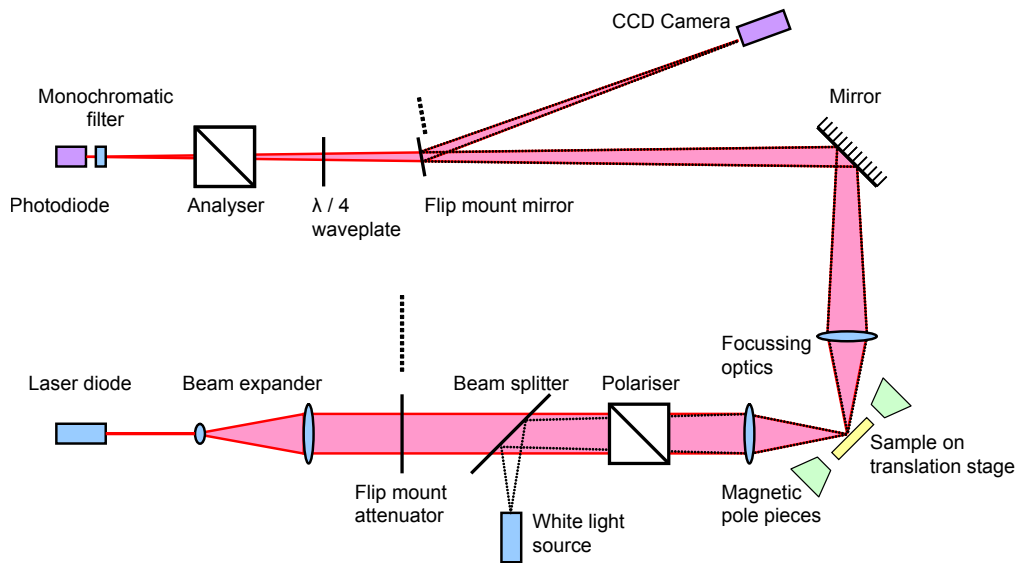
Figure 5.4: Schematic diagram of the focussed longitudinal MOKE system showing the optical path for both the laser and white light source.

The sample was mounted on a translation stage with the long axis of the ellipse aligned along the MOKE sensitivity direction and the direction of applied field. The structures were located through the use of a white light source and CCD camera which shows an image of the structures on the chip and the position of the semiconductor diode laser ($\lambda = 658$ nm) spot which was also focussed to a spot with an elongated ≈ 10 μm long footprint on the sample. The laser spot was aligned with the structures by positioning using the motorised translation stage. Once aligned the $\lambda/4$ waveplate was adjusted so that the elliptically polarised light reflected from the magnetic sample was shifted back to linear. This condition was found from iterative adjustments of the $\lambda/4$ waveplate and the analysing polariser angle to achieve extinction of the beam. The analysing polariser was then rotated to give an offset so that changes in magnetisation gave a monotonic response to the photodiode signal.

The sample stage was positioned within an electromagnet and a field was generated typically at 27 Hz along the MOKE sensitivity direction to reverse the magnetisation in the sample. The variation in the photodiode signal was recorded along with the field measured with pickup coils and averaged over many field cycles for approximately 1 minute. The photodiode signal was plotted against the integrated pickup coil signal to give the variation of magnetisation with applied field.

5.4.2   Measurements using SQUID magnetometry

The MOKE was a useful technique to show how magnetic properties vary over a wide range of irradiation conditions. However, the interesting changes arising in the magnetic properties presented later in chapter 7 needed to be confirmed as originating from the magnetic moment in the sample and not occurring from other complicating magneto-optical effects. Here SQUID magnetometry was used to investigate the true magnetic moments on an absolute scale for selected irradiation conditions.

Samples for SQUID analysis needed a larger volume of magnetic material than that of the microstructured ellipses and the samples also needed to be mounted individually into the SQUID system as this technique does not have local sensitivity. Here, the same 1.3 mm $\times$ 5.5 mm samples used for the x-ray structural characterisation studies were used, where the doses were chosen from the region of interest from the MOKE results. The samples were diced into individual substrates and each strip was mounted separately in gelatine capsules and attached to a measurement straw with the long axis of the strip orientated vertical in

the SQUID sensitivity direction.

The SQUID magnetometer, described in chapter 4, can detect very small changes in magnetic flux through a superconducting ring. In the magnetometer however, the flux from the sample is not measured directly with the SQUID ring, but from a series of pickup coils that are coupled to the SQUID device through a flux transformer. As a magnetic sample is passed through a coil set, the change in flux in the coils results in a detected voltage that varies linearly with the flux from the sample. To account for any field drift from the environment or the superconducting magnet incorporated into the system, the pickup coils are arranged as a balanced second-derivative coil-set (see figure 5.5(a)) where counter-wound coils are designed to reject any flux contribution not originating from the sample.

Superconducting magnets allow measurements to be performed in fields up to ±7 Tesla and a helium cryogenic system allows for temperature measurements down to 1.9 K.[216] This investigation focussed on the room temperature response of these samples as a function of field rather than transitions through the Curie temperature, so the measurements were performed at 290 K.

Samples were loaded into the SQUID magnetometer on a rod to the approximate position of the coil-set. This was done through a load lock which was evacuated and purged with He gas to reduce the chance of contaminants entering the sample space. A scan of the sample position was performed in a field of 100 Oe and used to fine-tune the centre position of the magnetic sample before the start of the measurement sequence.
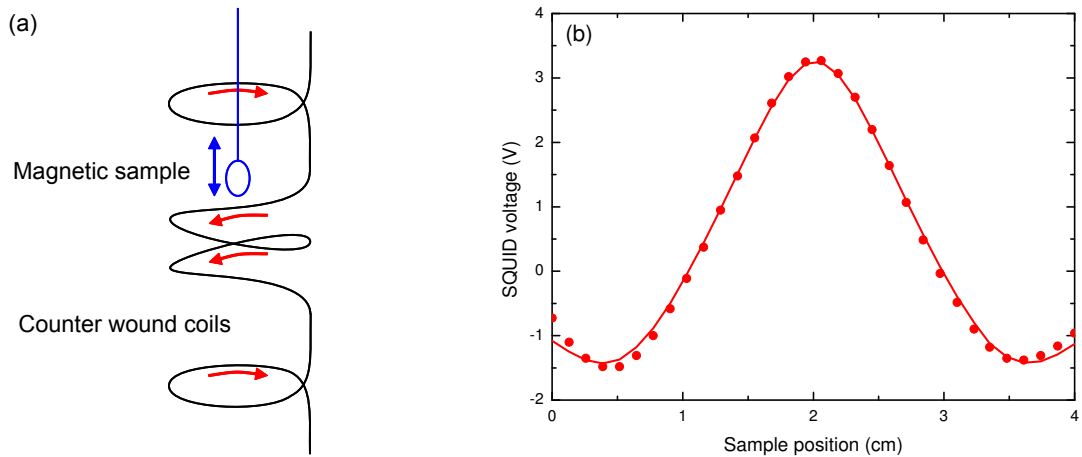
Figure 5.5: a) Schematic of the measurement of a magnetic sample in a counter-wound coil set to remove the effect of flux not originating from the sample.[216] b) The variation in SQUID voltage as a function of position of a magnetic sample as it is scanned through the detection coils.

During the measurement the SQUID voltage was measured as the magnetic sample was moved through the detection coils. This signal was fitted with a typical magnetic dipole and the fitting parameters were used to determine the magnetic moment of the sample. Figure 5.5(b) shows an example of the SQUID voltage as a magnetic sample is moved through the coils where the line indicates the fit to the data. This procedure was repeated as a function of applied field in the range ±30 Oe with 1 Oe step size with high resolution field mode. This was sufficient to saturate the sample in both directions and the combination of results shows the response of the magnetisation to the applied field of the sample as a hysteresis loop shown in figure 5.6(a).

All of these samples were fabricated on a Si/SiO_2 substrate which also adds a diamagnetic contribution to the detected moment. The effect of this was found by measuring the magnetic response of a blank substrate at the same temperature at 290 K but the fields were increased to ± 5 Tesla with 1 Tesla steps to detect this small magnetic signal. Figure 5.6(b) shows these results which have a linear trend passing through the origin with a negative gradient indicating the substrate is diamagnetic with a value of $(-2.317 \pm 0.009) \times 10^{-8}$. This linear response is subtracted from all subsequent measurements of NiFe/Au samples to remove the contribution from the substrate.
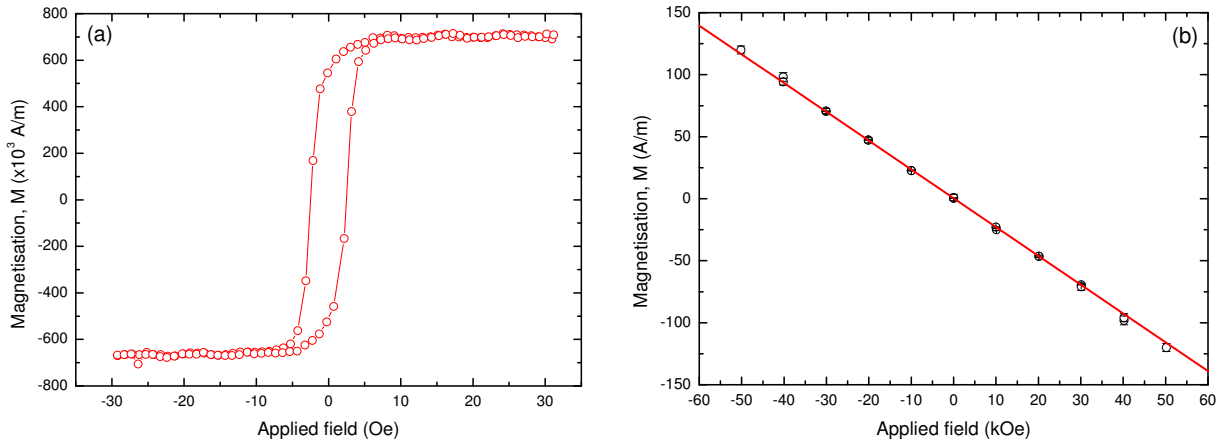
Figure 5.6: a) Example SQUID hysteresis loop formed from the fitted dipole to many scans with increasing and decreasing field. b) Magnetisation contribution from the diamagnetic Si/SiO_2 substrates that is subtracted from all measurements to leave only contributions from the magnetic samples.

5.4.3 Investigating the element specific magnetism changes in NiFe

The XMCD technique provides a way to further investigate the origins of the changes in magnetism that result from Ga^+ irradiation. The technique is element specific and sensitive to both the spin and orbital contributions to the magnetisation. The technique uses the absorption spectra of a material, which is proportional to the fluorescence of the sample. For $3d$ metals the fluorescence yield is low so the absorption is either determined from transmission measurements or through drain current measurements. For drain current measurements electrical connections are needed, requiring larger area samples, which increases the area that needs to be irradiated. Measurements of the transmitted beam were more appropriate for this investigation as they can be performed on smaller samples; however this requires samples to be fabricated on electron transparent substrates, in this case 200 nm thick SiN membranes covering 1.5×1.5 mm and supported by a 5×5 mm frame. These are easily damaged, for example by cleaning with ultrasound, so special measures were taken to avoid this.

The substrate requirements for XMCD measurements required new samples and the changes in magnetic properties occurring on SiO_2 substrates were verified on SiN substrates before continuing. Again the samples were a compromise between the large areas for x-ray measurements and the small areas more appropriate for focussed ion beam irradiation. The x-ray beam here was focussed to a 0.8 mm wide and 0.2 mm high spot, but in this case no extended footprint occurs as the beam is not incident at a grazing angle. Rectangular structures, with dimensions 1.5 mm by 1 mm with curved corners were used and were prepared by deposition through a shadow mask aligned with the centre of the SiN windows. The irradiation conditions for these samples followed the same procedure for irradiating the large area samples for structural investigation with the total patterning area reduced to 1.2 mm $\times$ 1.6 mm.

XMCD measurements require circularly polarised x-rays with energies that can be tuned over the absorption edges of the material of interest. For Ni and Fe $L_{3,2}$ edges at energies 708 eV and 721 eV for Fe, and 855 eV and 872 eV for Ni [235] require the use of soft x-rays so the experiment was performed at ID1011, a soft x-ray beamline at the MAXLAB synchrotron source in Lund, Sweden. This beamline uses an elliptically polarising undulator insertion device to generate the x-rays where the choice of helicity and energy of the x-ray photons was manipulated by controlling the geometry of the magnet array within the undulator device. [242] A monochromator was used along with the undulator to further refine the energy

of the x-ray photons and these two devices were adjusted together by an automated control system to ensure the maximum photon flux was achieved.

When using soft x-rays, the scattering from air becomes significant so the entire experiment was performed in ultra-high vacuum, requiring a bake out of the system after changing the samples. A simplified schematic of this experimental setup is shown in figure 5.7.

The incident synchrotron x-rays travel through a series of beam defining optics which focus the beam onto the sample with an elliptical spot size 0.8 mm wide and 0.2 mm high. The x-rays are then transmitted through the sample and the intensity is measured using a photodetector diode in-line with the beam. This intensity was normalised against the monitor signal from an Au grid located before the sample, and used to detect changes in beam intensity and to account for the gradual decrease in beam intensity with time resulting from synchrotron current losses. Unfortunately this did not completely account for changes in polarisation or variation in the beam positioning resulting from changes in the orbit of the electron beam around the ring.

Multiple samples were mounted on a Cu stage allowing for the investigation of several samples without breaking the vacuum. The long axis of each sample was orientated along the applied magnetic field axis and the sample windows were aligned with holes drilled through the back of the stage, illustrated in figure 5.8(a).

The dichoric effect is maximised when the magnetisation is orientated along the incident x-ray beam direction. However, for permalloy samples with in-plane anisotropy, the magnetisation lies in the plane of the film so the samples were rotated so that a component of the magnetisation lies along the beam direction. This rotation was achieved up to an angle
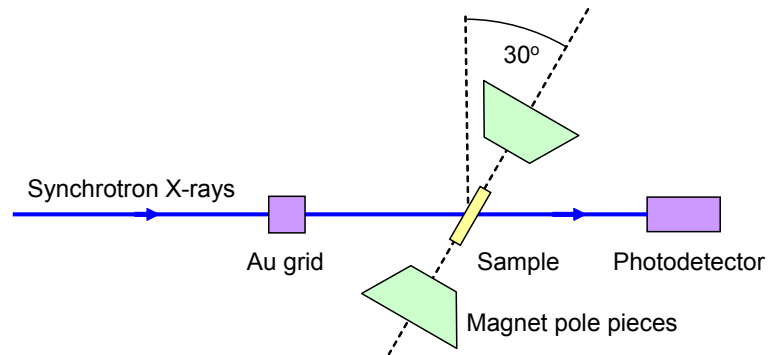
Figure 5.7: Simplified schematic illustration of the experimental setup for performing XMCD measurements in transmission mode. Incident synchrotron radiation passes through a sample in a magnetic field environment and the transmitted component of the beam is measured by a photodiode detector.
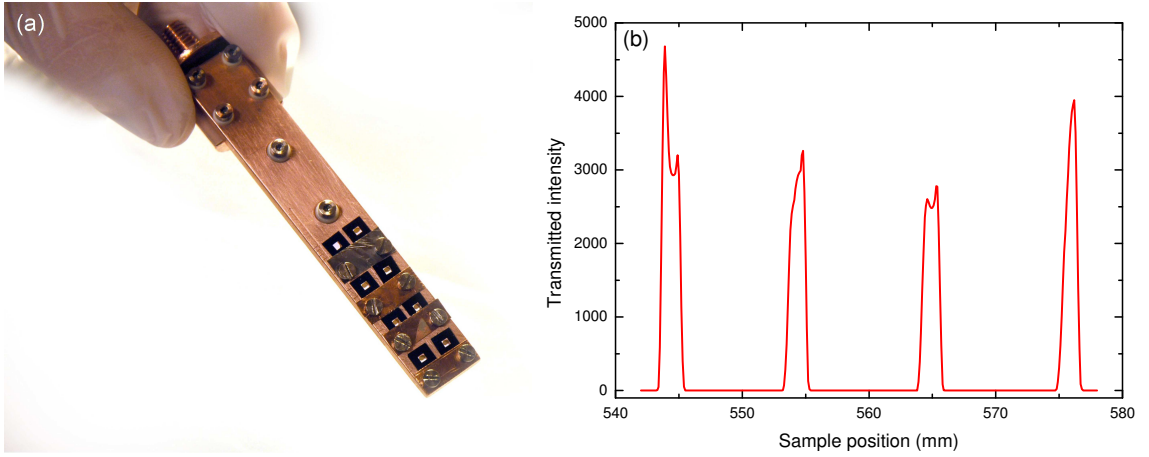
Figure 5.8: a) Photograph of samples mounted on the XMCD sample stage. b) A scan showing the intensity of transmitted x-rays as a function of sample stage position used for the alignment of the samples with the x-ray beam.

of 30° beyond which a loss in intensity occurred due to the beam clipping the edges of the sample stage. An applied field of ± 90 Oe was also rotated by 30°, to align with the plane of the sample.

Samples were aligned with the x-ray beam by measuring the transmitted intensity of the beam as a function of the stage position shown in figure 5.8(b). The peaks indicate the locations where the transmitted intensity through the sample was detected and correspond to the location of the SiN windows. The sample positioned at 576 mm shows the transmitted x-ray beam through a blank SiN window. At 544 mm and 565 mm a dip in the centre of the peak shows the absorption by the NiFe sample which has a gap on either side of the sample on the window. The sample at 554 mm was slightly offset during deposition and has only one side without absorption from NiFe. Serial measurements of four samples at a time were automated by driving the stage to these positions, however to access the other four structures required manual adjustment.

To perform XMCD measurements on a sample, the undulator and monochromator were scanned through the x-ray beam energies in the range 845 - 875 eV for Ni and 700 - 730 eV for Fe in 0.25 eV steps with an additional 15 eV below and 30 eV above this range in steps of 3 eV. The normalised transmission was used to determine the absorption as a function of the photon energy. Each scan was performed with a fixed helicity and magnetic field. Each scan was then repeated to obtain measurements with both helicities of circularly polarised light and both orientations of the applied magnetic field to obtain difference spectra.

Scans performed on a blank substrate show a decrease in absorption with energy which was subtracted from the results obtained from the magnetic samples to obtain just the absorption due to the absorption peaks. This measurement also removed the effect of a slight Ni contamination found in the Au grid. The energy scans were then normalised between the pre and post edge regions allowing the difference spectra to be found from pairs of scans with opposite helicity or magnetic field. These difference spectra were then integrated over the $L_{3,2}$ peaks and analysed by the sum rule approach introduced in chapter 4.

In addition to the energy scans over the $L_{3,2}$ peaks, the energy was also tuned to the maximum at the L_3 peak and scans were performed as a function of applied magnetic field. This allows hysteresis loops to be obtained for specific elements in the sample.

5.5   Experimental procedure to investigate the presence of a magnetic moment on Au

Experiments to investigate any dichoric x-ray signal originating from the Au atoms were also investigated at the XMaS beamline, BM28 at the ESRF which can produce x-ray energies at the Au L_3 edge (11.919 keV[235]). This beamline was set up to perform reflectivity measurements at grazing incidence so the combination of XRR and XMCD effects give a technique with elemental sensitivity to the depth dependence of any induced magnetic signal originating from the Au. Again the x-ray measurements at grazing incidence probe a large footprint so large strip samples (1.3 mm × 5.5 mm) were required.

This experimental setup was very similar to that used for x-ray reflectivity measurements where the x-rays from the bending magnet on this beamline pass through a series of x-ray optics, are focussed to a point on the sample from which they reflect into the detector in the same setup described for structural x-ray reflectivity measurements. A simplified experimental setup is illustrated in figure 5.9 where the addition of a diamond phase plate gives circularly polarised x-rays and the sample was positioned in a magnetic field.

The magnetic field was applied along the axis of the x-ray beam and in the plane of the sample. It was powered by a bi-polar amplifier capable of producing both positive and negative fields. The field was calibrated according to the coil current shown in figure 5.10(a) and during the field flipping measurements the field was flipped between ±300 Oe.

A synthetic diamond phase plate inserted along the incident x-ray path was used to
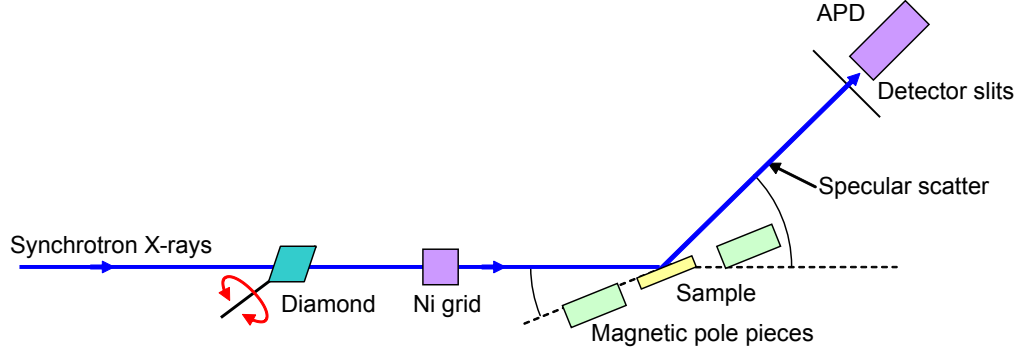
Figure 5.9: Simplified schematic of the experimental setup at the XMaS beamline for performing x-ray magnetic resonance scattering measurements. The reflected x-ray intensity was measured as a function of grazing incidence angle. The asymmetry ratio in the reflected intensity was compared whilst flipping the magnetic field or incident x-ray helicity.

select the circular polarisation of the beam by rotation about an axis perpendicular to the beam. Figure 5.10(b) shows the 'batman curve' of the x-ray intensity transmitted through the diamond phase plate as a function of its rotation angle; this is used to identify the angle at which the phase plate transmits circularly polarised x-rays.[243] A Ni grid included in the path of the beam gives a monitor signal with which the reflected intensity was normalised.

In this experiment, measurements of the dichoric signal were obtained directly by flipping either the helicity (with a fixed field) or the applied field (with a fixed helicity) in the sequence '+ − − + +−' for each measurement. The averages of the data recorded for + and − were combined and recorded along with their sum, difference and asymmetry ratio.

First, reflectivity scans were performed with the incident x-ray photon energy tuned to
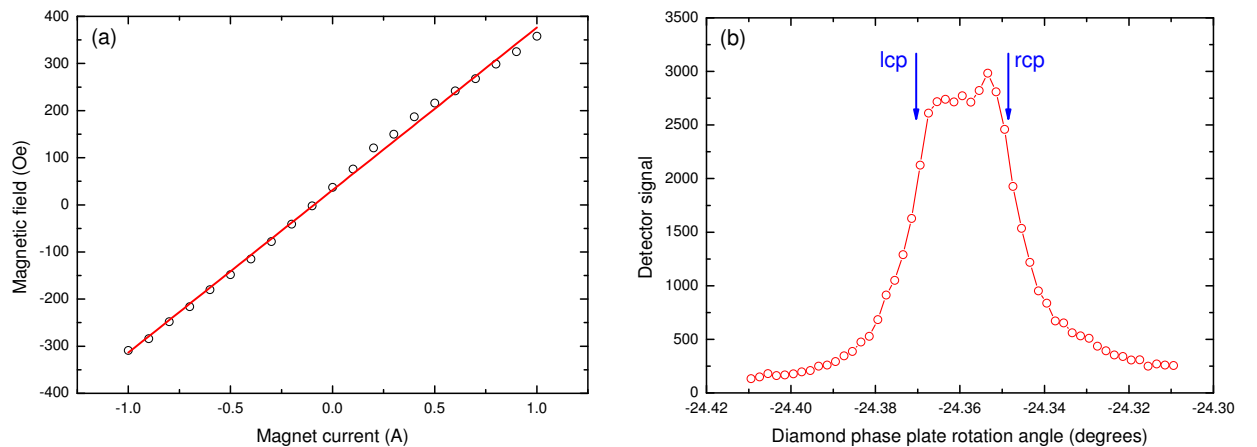
Figure 5.10: a) Calibration of the applied magnetic field at the XMaS beamline. b) X-ray intensity as a function of the rotation of the synthetic diamond which is used to identify the incident x-ray helicity at the XMaS beamline.

the Au L_3 absorption edge. The sample and detector angle were then fixed at the specular condition where the greatest asymmetry ratio was detected when flipping the field or helicity. This allowed for a scan of the incident x-ray energy to be performed to locate the precise energy over the absorption edge at which the largest asymmetry ratio was detected.

Reflectivity scans were then performed for 2θ: $0.2°$ - $4°$ and θ: $0.1°$ - $2°$ in 120 steps. At each point the reflected intensity was measured six times whilst the magnetic field was flipped with a constant helicity. These measurements were then repeated for each sample with the opposite helicity where any magnetic response should give an equal and opposite response in the data.

The field dependence of the asymmetry ratio was measured at the specular condition giving the highest asymmetry ratio at the saturation. The magnetic field was varied between negative and positive saturating field where the helicity was flipped at each field step to give a measure of the asymmetry ratio. The magnetic field was scanned between -350 Oe and $+350$ Oe in 30 steps and then repeated from $+350$ Oe to -350 Oe to obtain data for both increasing and decreasing fields.

5.6   Investigation of the magnetic properties of nanowires

Combining the work on the irradiation control of magnetic properties with lithographic patterning techniques gives a potential new way for controlling the behaviour of domain walls in nanowires. This section discusses the experiments involved in the investigation of the magnetic properties of nanowires as a function of both their geometrical structuring and the irradiation induced interfacial structuring.

In chapter 2 the idea of geometrical confinement of a magnetic material into a nanowire geometry was introduced to reduce the complexity to a system where individual domain walls can be studied. Typical dimensions for observing these properties in permalloy are of the order 100 nm in width, 10 nm in thickness and micrometres in length. This means that electron beam lithography techniques are essential for the fabrication of these nanowire structures. As well as being optimised to support simplified domain wall structures, these wires must also be optimised so that magnetic measurements can be achieved using the MOKE magnetometer.

The best signal-to-noise ratio was obtained from the MOKE when the area of the spot

fully illuminates the magnetic material; however for nanostructures this was not possible so the signal was reduced in proportion to the area of the nanostructure. The length of nanowires was the only dimension that could be extended so the minimum length of wire was set by the width of the laser spot footprint (≈ 10 μm). Longer nanowires also become easier to locate using the CCD camera on the MOKE system, but take longer to expose during the lithography process. Most importantly the magnification of the electron beam microscope had to be decreased for fabricating longer nanowires, this can result in a decrease in the quality of the geometrical structuring obtained.

A further increase in the signal-to-noise ratio of the MOKE measurement was achieved by fabricating arrays of identical nanowires to increase the area of the magnetic material probed by the laser spot. In this way the signal was reduced by the filling factor of the array instead of the relative size of the nanostructure in the illuminated spot.[208] The magnetic properties of the entire array represent the properties of each wire within it, as long as they are nominally identical and are suitably spaced with at least a 1:1 mark space ratio to avoid interactions.[208]

To measure the magnetic properties of these structures using the MOKE system, a similar method was followed to that described above for the microscale ellipses. The samples were mounted onto the translation stage and the CCD camera was used to align the structures with the focussed laser spot. It was possible to see an array of nanowires using the CCD camera but the use of marker structures was particularly important for identifying the structures on the substrate.

For individual nanowires that could not be observed optically with the CCD camera, an additional alignment step was performed following approximate alignment using marker structures. Here a map of reflected intensity was generated by scanning over the x and y coordinates of the stage.[244] This was then plotted as an image which represents the shape of the structure convoluted with the shape of the laser spot shown by the example in figure 5.11. Maps were made over a 16 μm length with 0.5 μm resolution whilst averaging for 3 s/point. Following the scan, the stage was moved back to the location where the maximum reflected intensity was obtained. This maximum in the reflected intensity represents the position of the nanowire structure that is likely to give the most significant Kerr signal. At this point the $\lambda/4$ waveplate and analyser were optimised as before.

The measurement of an individual nanowire or a nanowire array followed the same method
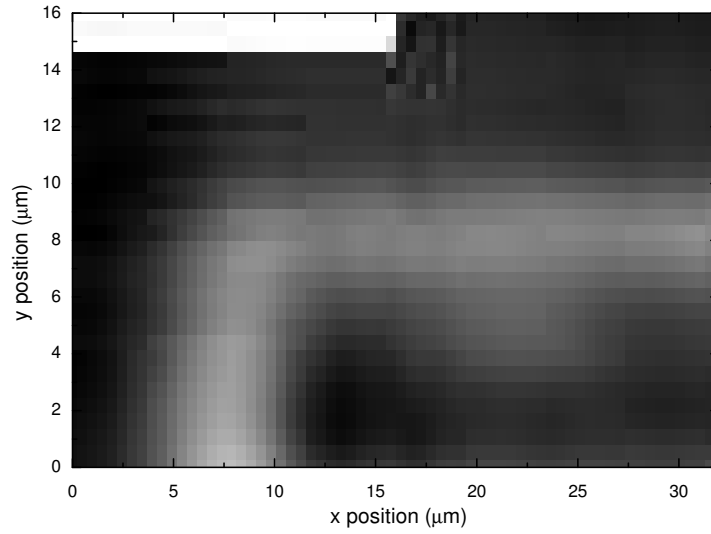
Figure 5.11: Map of the reflectivity of an individual L-shaped magnetic nanowire generated from two scans stitched together along the x axis. The light regions represent the greater reflectivity of the NiFe/Au structure.

as for the larger scale structures except that the averaging was increased to several thousand field cycles over approximately 2 minutes. This allowed the signal to noise ratio on the hysteresis loops to be maintained even though the signal size was much smaller due to the reduced area of magnetic material. MOKE measurements on the nanowires and nanostructures also showed the effects of higher order Kerr signals which made the results more complex to interpret. These appear as a higher frequency modulation of the Kerr signal with field superimposed upon the hysteresis loops. These are not observed from measurements performed on thin films and are likely to occur due to complex reflection and interference conditions from the patterned samples. As long as features such as the reversal field in the loops were dominant, these higher order terms were removed from the hysteresis loops for clarity.

The fabrication and measurement procedure for both individual nanowires and arrays of nanowires has now been discussed. The discussion now focusses on the different experiments performed on nanowires that have structural modifications arising from different mechanisms. The first investigation involved nanowires where local Ga^+ irradiation caused a modification to the magnetic properties at a point along the wire and the second involved nanowires affected by edge modulation geometry along the entire nanowire length.

5.6.1 Local ion irradiation of nanowires

In this part of the investigation, planar permalloy nanowire structures were modified by local Ga^+ irradiation to locally modify the magnetic material and hence investigate the influence of this upon the domain wall behaviour.

Information about domain wall propagation along a structure can be obtained by MOKE measurements of the magnetisation behaviour at various points along a nanowire where a change in magnetisation corresponds to the passage of the domain wall past the probed region of the nanowire. Comparison of the reversal field at different locations along the wire gave insight into the domain wall propagation field. A uniform wire with a domain wall nucleation pad should have a constant reversal field at all points along the wire representing the field required to inject and propagate a domain wall along the nanowire. The introduction of pinning defects along the wire leads to a rise in the reversal field for the remainder of the wire beyond the defect, where this reversal field then corresponds to the de-pinning field for that defect.

As the MOKE spot needs to be positioned at several different locations along the wire the wire length needs to be considerably longer than the projected length of the laser spot. Nanowires with dimensions of 400 nm wide and 100 μm long were chosen with a 2 μm wide, 4 μm long domain wall nucleation pad at one end and a 4 μm tapered end at the other to inhibit domain wall nucleation. To pattern these structures the magnification was reduced during lithography and a 120 μm wide write field was used. Several identical wires were fabricated on the same substrate with a pitch of 200 μm in x and 100 μm in y, allowing for easy navigation of the sample on the MOKE whilst leaving adequate separation to avoid magnetic interference effects.[208] Following patterning, thermal evaporation was used to deposit 10 nm NiFe capped with 2.5 nm Au.

Prior to the irradiation process, the position of the nanowire structures was located using only the electron beam imaging in the dual-beam FIB/SEM system. Multiple irradiation windows were positioned every 25 μm along the 100 μm long nanowire allowing the effect of three different sets of irradiation parameters to be investigated on each nanowire. The 25 μm separation was a suitable gap to confirm regions of constant magnetic properties between irradiation windows and to allow the location of the irradiation windows to be determined from the MOKE measurements afterwards.

The irradiation was performed using normal incidence 30 keV Ga^+ ions and a 29 pA

beam current with a spot size of 9 nm. Irradiation areas were 4 μm high rectangular regions with widths varying from 100 nm up to 30 μm. The beam was scanned from the bottom to the top in a raster scan fashion with a 1 μs dwell time at each point. The variation in dose was achieved by repeat exposure at each pixel. The rectangles were larger than the width of the wire to allow for any misalignment in the beam positioning. This allowed for a 'lead-in' time before the beam arrives at the structure of interest and also so that the position of the irradiation can be inspected by electron beam imaging following the irradiation. Even though low doses do not cause significant surface damage, the irradiated regions can still be seen due to the localised electrical charging of the substrate.

5.6.2   Edge modulated nanowire structures

For investigation into nanowire properties affected by geometrical edge structuring, shorter wires were used as the measurements did not need to be position sensitive. The use of shorter wires allowed a higher magnification, with a 65 μm field of view, to be used during lithography which allowed higher quality geometrical patterning to be produced. A nanowire length of 20 μm was chosen so the overall structure size was also easy to locate and measure using the MOKE system and the average width of the wires was again chosen to be 250 nm.

These wires were patterned in 8 μm arrays of nanowires with a pitch of 800 nm. Multiple arrays of wires were patterned on the same substrate with a pitch of 100 μm which avoids magnetic interference between structures, but is suitable for easy navigation between structures using the MOKE system. Each array had different edge modulation parameters where the wavelength ranged between 0.2 μm and 2 μm and the amplitude was varied between 15 nm and 50 nm. This set of wires was fabricated in one case with 500 nm tapers at each end. This was then repeated on another identical set of wires with a 1 μm long, 500 nm wide domain wall nucleation pad on one end and a 500 nm tapered end on the other. Following patterning, thermal evaporation was used to deposit 10 nm NiFe followed by a 2.5 nm Au cap without breaking the vacuum.

The arrays were all measured on the MOKE magnetometer where wire structures with two tapered ends gave information about the nucleation field in these structures. The wire structures including the domain wall nucleation pad gave information about the domain wall propagation field along these structures.

5.6.3 Pulsed field domain wall injection experiments

In addition to the domain wall injection into nanowires with nucleation pads, localised pulsed fields from a stripline were also used to inject domain walls. This was performed in the nanowires with two tapered ends. The addition of pulsed and quasi-static fields at the intersection of the stripline and nanowire produces an enhanced magnetic field. With suitable length and magnitude pulses the fields were sufficient to nucleate domain walls. The change in magnetisation resulting from the application of the pulsed field was then probed using MOKE measurements to investigate the properties of the domain walls in these structures.

The stripline approach follows the methods adopted by Hayashi[121] for injecting an individual (pair of) domain walls into planar permalloy nanowires. Adaptations were made to fit in with the methods and techniques already being used in this investigation. The basic design, follows the theory in chapter 2, where a pulsed current along a conductor perpendicular to the nanowire creates a localised axial field component. This field can switch the magnetisation in that local region and therefore creates two domain walls in the nanowire.

Domain wall injection striplines were fabricated using a second step of lithography involving the alignment of the second layer on top of the first. This was followed by thermal evaporation of 3 nm Cr followed by 30 nm Au to produce a conductive strip. The 500 nm wide stripline regions were kept to a short length of 16 μm, long enough to cover the 8 μm height of the array of nanowires with excess length to account for any misalignment. These striplines were joined together with wider 10 μm connections to keep the overall resistance low. The arrangement of striplines on the substrate then had to match the position of the arrays of nanowires so 10 parallel groups each containing 5 striplines in series were fabricated on the substrate. This arrangement is illustrated in figure 5.12(a) and an individual array of nanowires intersected by a stripline is shown in figure 5.12(b).

1 mm wide contact pads extending to the edges of the substrate ($\approx$ 3 mm) were also included onto both ends of the stripline array to give a large area for making electrical connections. Conductive silver paint was used for electrical connections to a sample holder which then allowed for connection to further instruments through co-axial 50 Ω cabling. Ideally the stripline circuit should have zero ohmic resistance so that an applied voltage pulse travels freely along the stripline and the energy is dissipated into a 50 Ω load. In reality the resistance was measured at 20 Ω which leads to a small amount of reflection of the pulse; this was not significant compared to the initial pulse height.
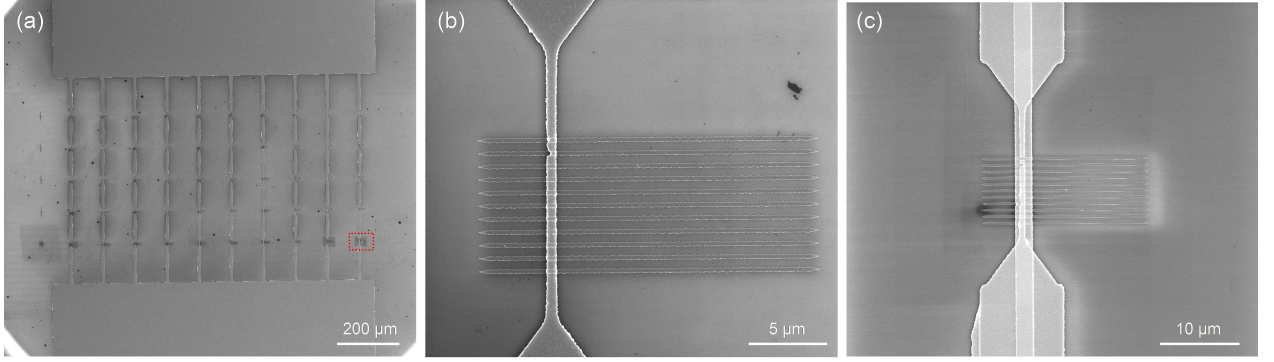
Figure 5.12: Scanning electron microscope images of stripline structures fabricated over arrays of nanowires. a) Connection of multiple striplines to contact pads, b) a single 500 nm wide stripline fabricated on an array of nanowires and c) a wider 2 μm striplines produced during an additional lithographic step.

During preliminary testing of the stripline circuit it was found that the thin stripline regions were easily damaged by the application of pulsed currents. To enable these measurements to continue, the striplines were repaired with a wider 2 μm strip that was aligned using a third lithographic step with the original two layers. Again, this was followed by the thermal evaporation of 2.5 nm Cr and 30 nm Au and the result illustrated in figure 5.12(c).

The stripline was connected to a pulser circuit illustrated in figure 5.13(a) supplying a pulsed voltage into a 50 Ω load resistance to generate a current pulse through the stripline. This circuit used a pulse forming line that was charged by a DC voltage. Upon triggering a Hg-wetted relay, the voltage was divided between the pulse forming line and the load resistance creating a current that flows through the stripline. The pulse length was determined by the length of the pulse forming line and the amplitude by the initial charge voltage.
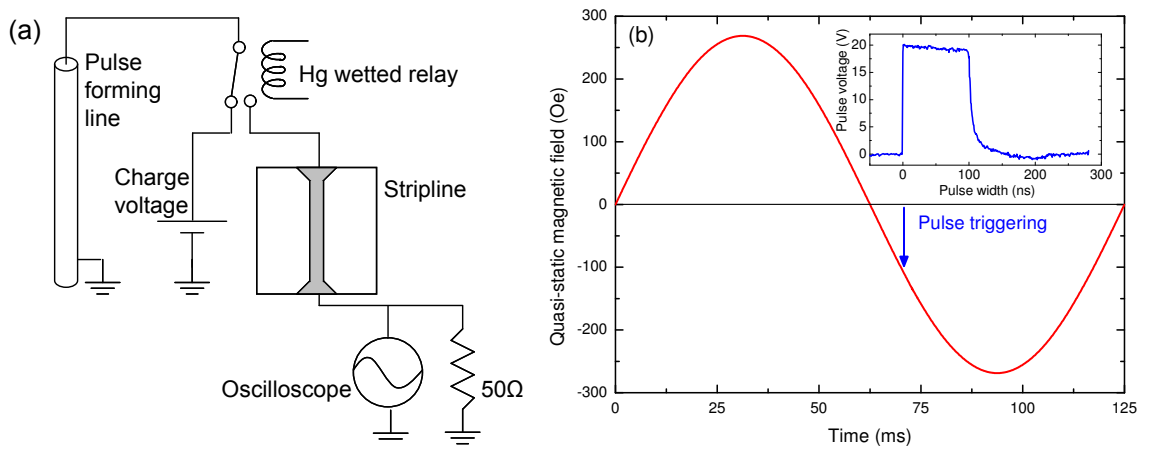
Figure 5.13: a) Circuit diagram of the pulser circuit and b) pulsed field triggering position on the quasi-static waveform. The insert shows a typical pulse shape.

The pulse was triggered by a digital to analogue converter (DAC), synchronised to the additional quasi-static field applied to the sample ($\pm$270 Oe). The field sequence is illustrated in figure 5.13(b) which also shows an example of a 100 ns long, 40 V pulse produced by the circuit. To prevent samples from burning out a slower, 8 Hz, repetition rate was used compared to previous MOKE measurements. Various pulse lengths were investigated and showed little difference in the domain wall injection, so 150 ns was chosen as this gave a reliable pulse shape but with reduced energy that helped prevent burn out of the stripline.

Figures 5.14(a-c) show three hysteresis loops from an array of nanowires where the pulse was triggered at different decreasing quasi-static fields. This triggers switching at a field lower than the nucleation field as long as the combination of quasi-static and pulsed fields overcome the nucleation field and the propagation field is lower than the nucleation field. These two conditions determine first whether or not a domain wall is nucleated, followed by whether it will propagate along the wire. These conditions are met in two different ways: in the case where the quasi-static field at the trigger point exceeds the propagation field, the magnetisation will switch immediately after the pulse triggering point. Otherwise the domain wall is nucleated but remains pinned until the quasi-static field increases to the propagation field and then the domain wall will de-pin and complete the switching of the wire.

This effectively results in the reversal field measured on the hysteresis loops showing
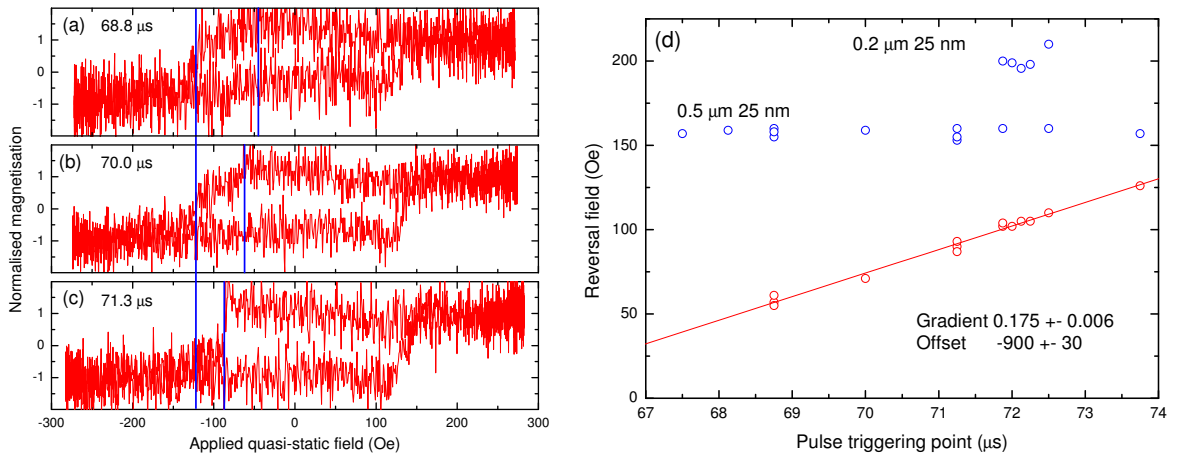
Figure 5.14: a) Hysteresis loops with pulsed fields triggered at various points on the decreasing field section of the waveform illustrated by the blue line. The combination of the quasi-static and pulsed fields leads to a) no effect, b) intermittent and c) repeatable domain wall nucleation. d) The combination of reversal fields as a function of pulse triggering time. The blue points show the reversal of the wire without pulses from just the quasi-static field and the red points show a decrease in the reversal field as the pulses are triggered earlier in the field cycle.

either the propagation field of the wire or giving an upper bound to the propagation field where switching is determined by the field limitations of the stripline circuit. These results, in relation to the magnetic properties of the wires are discussed in more detail in chapter 9 but they are presented here to facilitate the discussion of the method for obtaining results from the stripline circuit.

Figure 5.14(d) shows the fields where magnetisation switching occurs from a collection of hysteresis loops measured on two different structures. The blue points show the reversal field for the wire structures with increasing fields representing the usual magnetic reversal field for these structures. The red points illustrate the reversal field that is obtained for decreasing field with the addition of the pulse field. This is plotted against the trigger point on the quasi-static field cycle. The linear fit represents the linear nature of the sinusoidal quasi-static field at low values. Points lying on this line result from stripline limited switching and any points above this line would represent switching limited by the propagation field for the wire.

This experiment was repeated with an increased pulse voltage to obtain a greater pulsed field amplitude, this had the effect of lowering the line in figure 5.14(d). If the reversal field was then measured above the new line, this is a measurement of the propagation field for that structure. For the remaining points that still lie on the new line, they give a reduced value for the upper bound to the reversal field. By repeating the process of increasing the pulse voltage and repeating the measurements, better estimates of the magnetic properties are obtained. However, the increase in voltage above 50 V resulted in damage to the striplines. The results presented in chapter 9 therefore show a combination of propagation fields for modulated wire structures along with the best estimates of the upper bound to the propagation field in other structures.

5.6.4   Micromagnetic simulations

To aid with the interpretation of the experimental results for the magnetisation reversal in nanowire structures, micromagnetic simulations of these structures were performed. This section describes the specific simulations that were performed to give the results needed for comparison in this investigation. Two different versions of the OOMMF package were used to perform the magnetic simulations in this investigation. The mmSolve2D solver offers a simple and fast way to simulate 2D structures and was used for the simulation of edge modulated

structures presented in chapter 9. The eXtensible solver is more versatile and allows for a more complicated structure configurations that can be defined on a 3D grid. This solver was used for simulations including local variations in M_s to represent regions of local irradiation where the results are presented in chapter 8.

Experimental methods mainly involve the characterisation of a sample by examining its hysteresis loop. In a simulated system the interesting properties all appear in one quadrant of the hysteresis loop. Therefore, the computation load can be reduced by just simulating the increasing field section from a negatively saturated starting point. This shows the spin structure moving to its remanent state followed by an increase in magnetisation from an adjustment of the spin structure up to the reversal field. At this point the magnetisation in the structure switches to the opposite magnetised state. In these simulations the material parameters for permalloy were used, these are $M_s = 860 \times 10^3$ A/m and $A = 13 \times 10^{-12}$ J/m.

Static simulations

Micromagnetic simulations were performed on edge modulated nanowires with an average width of 250 nm and a thickness of 5 nm and 10 nm to compare the switching and domain wall properties with those found from experiments. The simulated nanowires were shortened to 3 μm compared to the experimental structures. This is long enough to simulate several wavelengths of the edge modulation but still small enough to perform micromagnetic simulations on a reasonable timescale.

Various techniques for removing the effect of the nanowire ends were discussed in chapter 4. Here the varying geometry of the modulated nanowires renders the fixed spins end correction not applicable because the wire cannot be represented as a continuous charge plate due to the magnetic structuring that arises in these structures (see chapter 9). Instead the nanowire ends were terminated with 0.5 μm long tapered ends to reduce the chance of nucleation so that the nucleation field was dominated by the edge modulation geometry of the wire. These tapered ends join to the modulated structure at the minimum width to give a smooth connection. The edge modulation structures were defined from an image generated with the minimum, 2 nm pixel size.

The reversal field of a structure was investigated with static simulations starting with an initially saturated structure where the spins were allowed to relax to the lowest energy configuration in zero field (with a 0.1 Oe asymmetry in the y and z direction). An axial field

was then increased in 1 Oe steps until the magnetisation switched at the reversal field.

This simulation was then repeated with the same structures but with an initial magnetisation containing an abrupt 180° change in orientation at the centre of the wire. Upon relaxation in zero field, this transformed into a transverse domain wall structure located at the centre of the wire. The magnetisation reversal field for the wire then corresponds to the de-pinning or propagation field of the domain wall within the wire.

Similar simulations were performed on unmodulated nanowires to investigate the effect of local regions of reduced M_s along the nanowire in order to represent the effects of ion irradiation. In this case the fixed spin approach was used to simulate an effectively infinitely long nanowire which in fact used a simulation window 1 μm long, 150 nm wide and 10 nm thick. Domain walls were formed from the relaxation of an abrupt change in magnetisation as above. An axial field then allowed for the propagation of a domain wall through the regions of reduced M_s. The field was increased until the domain wall structure de-pinned from the reduced M_s region.

Dynamic simulations

Dynamic simulations were performed on longer, 5 μm, edge modulated structures to give information on the behaviour of domain walls as they propagate along an edge modulated nanowire structure. For these simulations a domain wall was introduced as above, but this was moved to the left hand end of the nanowire by the application of a field to create the starting condition. This allowed a greater distance for investigating the domain wall dynamic properties as large acceleration distances were required before dynamic measurements commenced. During the simulations a constant axial field was applied to the wire. This was maintained until the domain wall propagated to the end of the wire or the field was found to be insufficient for domain wall propagation. The micromagnetic spin configuration and magnetisation data was recorded every 0.2 ns during the simulation. For simulations focussing on spin wave emission the wire length was reduced to 2.8 μm to reduce the computation load and the fine step size was reduced to 15 ps to achieve suitable temporal resolution.

5.7 Summary

This chapter described all the experiments performed during this investigation using the techniques for fabricating and characterising samples that were introduced in chapters 3 and 4. The results from these experiments are presented and discussed in the remainder of this thesis, starting with the structural properties in chapter 6 leading on to the magnetic changes that result from this structuring in chapter 7. These effects were then combined and the results from both interface structuring (chapter 8) and edge structuring (chapter 9) on the domain wall properties in nanowires are discussed.

Chapter 6

Effect of irradiation on the structure of NiFe/Au bilayers

6.1 Introduction

In this chapter the effect of the focussed ion beam Ga^+ irradiation on the structure of thin NiFe/Au bilayer films was investigated. This brings together experimental work including grazing incidence x-ray reflectivity (XRR) and angular dependent x-ray fluorescence (XRF) to investigate the layered structure and composition of the samples as a function of Ga^+ ion irradiation. These techniques are surface sensitive and give an accurate description of the depth dependence to the sample structure. These experiments are performed alongside simulations based on collision cascades from ion-target interaction using TRIDYN[234] to aid the interpretation of the results. These simulations predict the atomic rearrangement taking place during the irradiation and provide convenient visualisations of the structure to compare with experimental results.

Initially the damaging effects of high dose irradiation were investigated including the sputtering of surface material and implantation of Ga^+ ions. The investigation then moves towards the analysis of the regime where these effects are minimal and where structural changes are associated with intermixing at the interfaces. This was analysed through XRR measurements and TRIDYN simulations.

The results of this study were published in our work[245] and has been extended here to confirm the structural modifications using an alternative data fitting approach with a similar model for XRR and the more robust peak fitting approach of the XRF measurements.

Variations in the approach to the analysis affect the results of the fitting somewhat, showing that these techniques do not give a single unique solution, although the conclusions drawn from both analyses are consistent. The differences allow for a discussion of the validity of the conclusions that can be drawn from these measurements.

The structure is further investigated through fluorescence analysis allowing the sample to be characterised according to the element specific atomic relocation taking place during the irradiation. Pseudo-simultaneous analysis of both XRR and XRF data shows how the structural results agree between the two techniques; however the analysis was limited by the current state of development of the available data fitting software which do not currently support the required simultaneous fitting required for a full analysis of this data. Instead, more useful conclusions from the XRF data were drawn from a more primitive analysis approach based on the continuous variation in composition through the sample.

The ability to modify the interfacial structure through Ga^+ ion beam irradiation provides a mechanism to locally change the properties of a material. This is of great advantage for technological applications where material properties can be modified without significant roughening or damage to the sample surface and allows for the possibility to deposit multiple stacked layers without the significant build-up of surface roughness.

6.2 Surface sputtering by Ga^+ irradiation

One of the most common uses of focussed ion beam systems is for the sputtering of localised regions of material in order to mill patterns into a material. This requires a relatively large irradiation dose and therefore the effect on the structure of the sample is quite dramatic. This is illustrated by the scanning electron microscope images in figure 6.1 which are used to characterise the high dose regime.

This preliminary analysis of surface degradation of the samples shows the shape of the irradiation window is visible as a lighter coloured region at low dose which then develops roughness and ultimately results in the removal of material from the sample surface with increasing dose. By $625 \times 10^{15} \, Ga^+/cm^2$, enough material has been removed in the irradiated window such that a square shape has been milled into the sample surface.

The light contrast of the irradiated window at low dose can result from charging by implanted Ga^+ ions. As the level of irradiation is increased, small amounts of surface sputtering
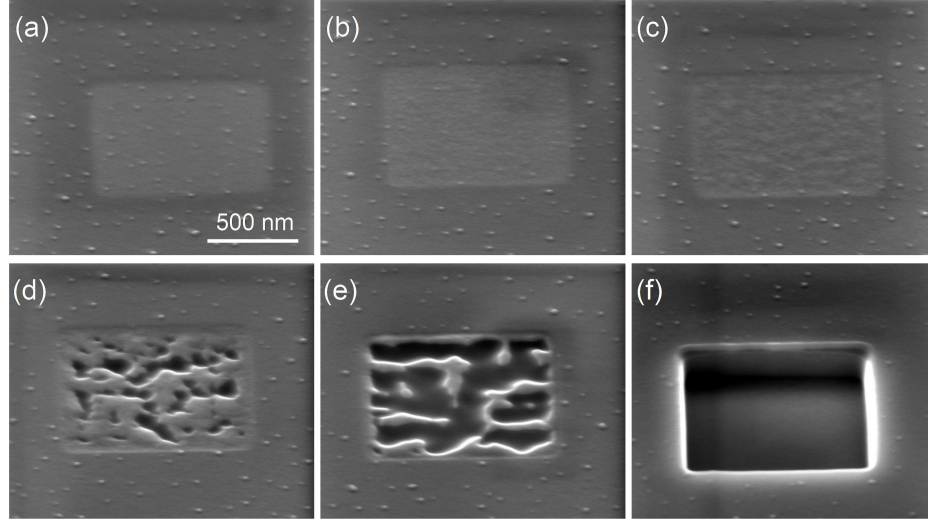
Figure 6.1: NiFe (20 nm)/Au (3 nm) surface structure after the irradiation of 1×1 μm windows with doses a) 3.1, b) 6.3, c) 12.5, d) 31.2, e) 62.5 and f) 625 $\times 10^{15}$ Ga$^+$/cm^2 at normal incidence with a beam current of 1.5 pA and an acceleration voltage of 30 keV.

lead to the development of roughness. Since these films are polycrystalline, grains are orientated in different crystal directions which leads to the non-isotropic milling observed between 12.5×10^{15} Ga$^+$/cm^2 and 62.5×10^{15} Ga$^+$/cm^2. This is explained by different sputter rates from the orientation of crystal axes in the film in an effect termed the channelling effect. After 62.5×10^{15} Ga$^+$/cm^2 significant sputtering results in the recession of the surface which increases with irradiation dose.

6.2.1 Surface recession from sputtering

These preliminary results give an indication of the regime in which surface sputtering dominates so here the low dose irradiation avoids this regime. Simulations of ion-solid interactions performed using TRIDYN for lower irradiation doses give predictions of the surface sputtering rate from NiFe, Au and NiFe/Au bilayer samples with normal incidence 30 keV Ga$^+$ irradiation. This indicates the recession of the sample surface which is shown in figure 6.2 as a function of irradiation dose for NiFe and Au samples along with NiFe/Au bilayers with a 3 nm Au cap.

These models show a linear increase in the recession of the surface with irradiation dose where the gradient represents the amount of material sputtered from the surface per incident ion. The steeper gradient for Au shows that it is more easily sputtered than NiFe, due to Au having a lower surface binding energy than Ni and Fe (see table 5.1). The surface recession
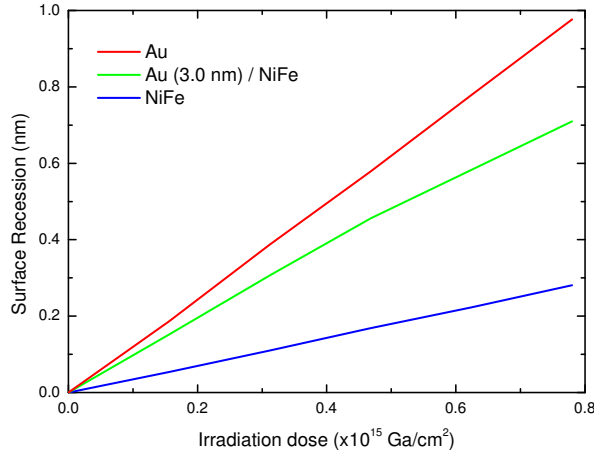
Figure 6.2: Surface recession predicted from TRIDYN simulations of the sputtering from NiFe, Au, or bilayer NiFe / (3 nm) Au samples with normal incidence 30 keV Ga$^+$ ions.

predicted for the bilayer structure with 3 nm Au lies between the Au and NiFe samples.

From these simulations the maximum surface recession is $\approx$ 1 nm, giving reasonable confidence that for the investigation of the material properties in this low dose regime, a consistent Au cap will remain after the small amount of sputtering from an initial 3 nm Au cap. Confidence in this analysis is due to previous studies that have also shown the reliability of these simulations at predicting the sputtering of capping layers in similar materials.[40]

6.3 Implantation of Ga$^+$ ions

The implantation of ions within the sample following irradiation is another important effect. This is significant in determining the properties of the material as the implanted ions can be described as defects resulting in physical changes due to stress in the lattice of the sample. Implanted ions can also give rise to chemical changes due to alloying in the material. This section presents grazing incidence x-ray fluorescence results that quantify the depth dependence to the Ga$^+$ implantation occurring as a function of the irradiation dose.

6.3.1 Total Ga$^+$ implantation with irradiation dose

X-ray fluorescence spectra for ion-beam irradiated NiFe/Au structures were collected with x-rays incident at 1° (above the critical angle) with an energy of 11.8 keV and 12.5 keV as a function of position over the width of the samples. An example of the fluorescence energy spectra is shown for 11.8 keV x-rays in figure 6.3 with peaks representing the atomic transi-
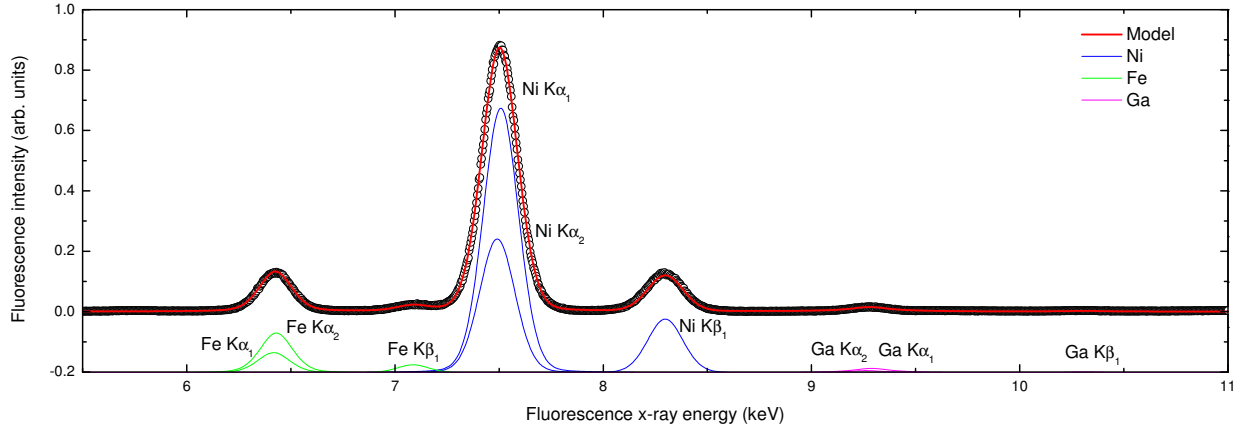
Figure 6.3: X-ray fluorescence spectrum of a NiFe/Au bilayer irradiated with a dose of 0.78×10^{15} Ga$^+$/cm^2 measured at $1°$. The spectrum is shown for 11.8 keV x-rays.

tions fitted to determine the fluorescence intensity from each element present. In the 11.8 keV data the Au peaks are missing as 11.8 keV is below the Au ionisation edge (11.919 keV[235]). This allows the Ga fluorescence to be determined more accurately as the Ga peak is not superimposed on an Au peak.

The Ga$^+$ implantation was found from the average fluorescence intensity of the Ga Kα_1 peak taken from multiple points over the width of each 1.3×5.5 mm strip sample. This fluorescence intensity from the measurements at 11.8 keV is shown as a function of irradiation dose in figure 6.4(a) where a linear increase was observed with increasing irradiation dose. This was interpreted as a linear relationship between the number of incident Ga$^+$ ions and
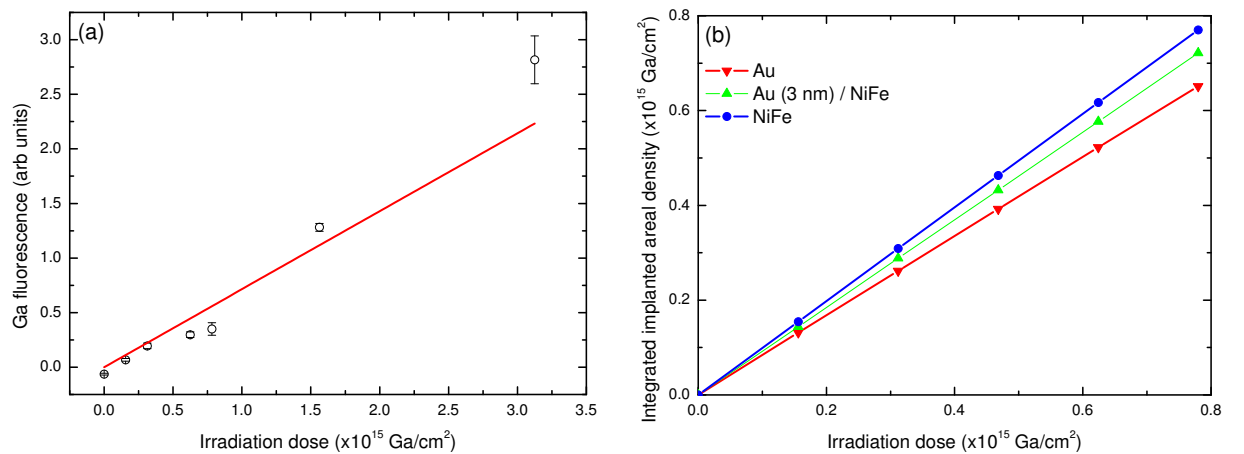
Figure 6.4: Linear increase in implanted Ga$^+$ with irradiation dose shown a) experimentally from x-ray fluorescence results at 11.8 keV with the best fit through the origin and b) by TRIDYN simulations on Au, NiFe and NiFe / (3 nm) Au models.

the number of resulting implanted Ga^+ ions.

TRIDYN simulations also predict a linear increase in implanted Ga^+ content with irradiation dose for Au, NiFe and NiFe / (3 nm) Au bilayer samples shown in figure 6.4(b). The proportion of incident Ga^+ ions that become implanted is nearly 100% showing that very few of the ions are sputtered or reflected from the sample during irradiation. Also, more Ga^+ becomes implanted in NiFe than Au as Ni and Fe have a higher surface binding energy than the Au, requiring more energy to displace a Ga atom from a NiFe matrix (see table 5.1). In the bilayer samples with a thin Au cap and thick NiFe layer the proportion of incident Ga^+ ions that remain implanted lies between that of the Au and NiFe slab. These results show the average Ga^+ implantation throughout the thickness of the film but by combining this fluorescence analysis with grazing incidence x-ray techniques, depth sensitivity can be obtained.

6.3.2 Depth profile of Ga^+ implantation

The grazing incidence angular dependence of the x-ray fluorescence intensity for the Ga peaks is shown in figure 6.5 as a function of irradiation dose for incident x-rays at both a) 11.8 keV and b) 12.5 keV. A sharp rise in the fluorescence intensity at the critical angle is followed by a gradual decrease that is typical of the signal from a thin layer of material near the surface of a sample. The height of the fluorescence intensity curves represents the amount of Ga^+ implantation within the sample; this increases with the irradiation dose, consistent with the results in figure 6.4.

The figure shows the results for incident x-ray energies at both 11.8 keV and 12.5 keV, above and below the Au L ionisation edge respectively. The results with 11.8 keV x-rays show much clearer behaviour than that found for 12.5 keV x-rays. This is due to artefacts in the fitting that arise as the Au and Ga peaks are close in energy and both have a relatively weak fluorescence intensity making it hard to differentiate between the two contributions. At 11.8 keV there is no Au fluorescence so the peak can be attributed entirely to Ga fluorescence giving more understandable results. This figure also shows interference fringes just above the critical angle for the lowest dose irradiation, indicating that the Ga is found within a thin layer at the surface of the samples.

The results shown in figure 6.5 vary as a function of incident x-ray angle; however a measure of the implantation as a function of depth is more useful and can be obtained from
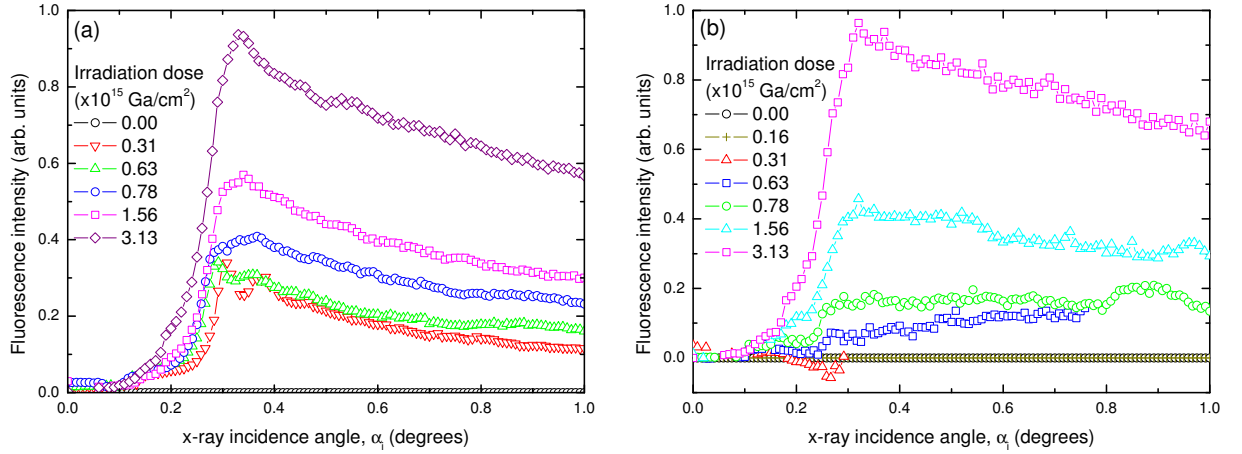
Figure 6.5: Angular dependence of the x-ray fluorescence intensity of Ga at a) 11.8 keV and b) 12.5 keV x-rays for various irradiation doses on 20 nm NiFe / 2.5 nm Au thin films.

the penetration depth shown in figure 4.8(a). Figure 6.6(a) shows the data presented in this way and has been differentiated to give an approximation to the fluorescence from each depth interval within the sample. Here a peak at the near surface region is shown which increases in area with incident irradiation dose. The high sensitivity of the penetration depth to the incident x-ray angle and additional features such as interferences from the layered nature of the sample and re-absorption of fluorescent x-rays make quantitative analysis of these results unreliable. However, the graph does show an implantation profile with a realistic shape showing an increase in the Ga^+ implantation at the near surface region with increasing dose.

This implantation depth is compared to TRIDYN simulations, shown in figure 6.6(b),
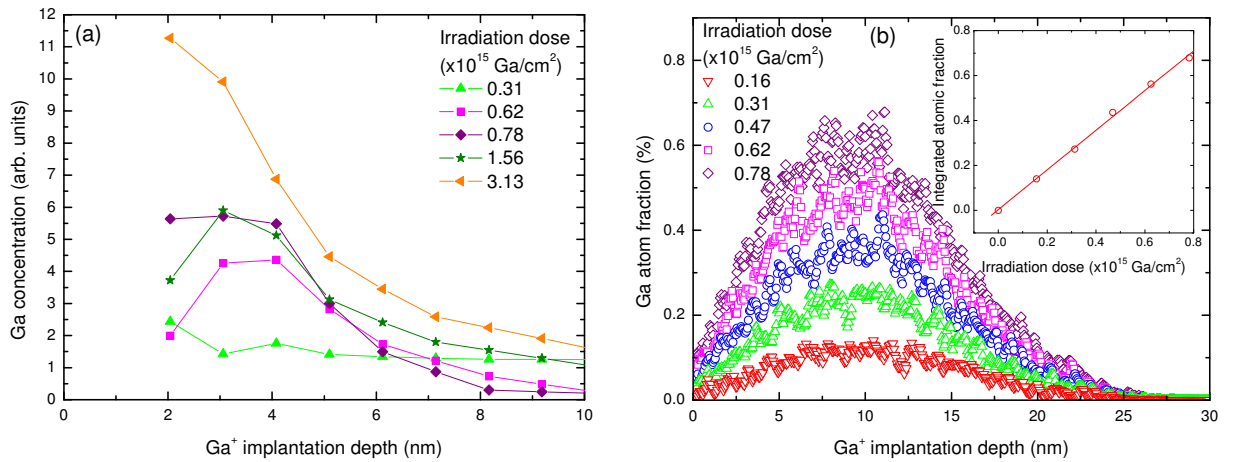
Figure 6.6: Depth dependence of the atomic fraction of implanted Ga^+ a) derived from angular dependent x-ray fluorescence and b) from TRIDYN simulations. The inset shows the maximum Ga^+ atomic fraction through the film as a function of irradiation dose.

which give the atomic fraction of implanted Ga as a function of depth for different irradiation doses. The results shown here have been smoothed with adjacent averaging over every 5 points to more clearly show the shape of the implantation profile.

These simulations show the profile where the concentration of Ga atoms rises to a maximum at a depth of approximately 10 nm followed by the decay in concentration up to a maximum implantation depth of $\approx$ 30 nm. This region of high Ga concentration near the sample surface is consistent with the shape of the implantation profile from the fluorescence results but these cannot be compared quantitatively. The maximum concentration from the TRIDYN implantation profiles is plotted in figure 6.6(b) as a function of the irradiation dose showing a linear increase in Ga concentration with dose as predicted for the low dose regime.[138]

The NiFe/Au interface at the 3 nm position in figure 6.6(b) has no obvious effect on the implantation profile of the Ga$^+$ ions. This is consistent with the relatively small difference between the implantation in NiFe, Au and NiFe/Au samples shown in figure 6.4 and can explain the negligible change in implantation due to the Au cap.

6.4 Layer structure of the samples

During irradiation, as well as the implantation and surface sputtering, the energy of the beam resulted in modifications of the initial structure of the thin film. In order to investigate these changes, grazing incidence x-ray reflectivity measurements were performed.

Figure 6.7 shows the grazing incidence x-ray reflectivity curves for the NiFe/Au bilayer samples with a range of low dose Ga$^+$ irradiation. The curves show both Kiessig fringes representing the thin layered structure of the sample with decreasing amplitude representing the roughness of the sample.

The features seen in the experimental data below 0.5° are not expected from the reflectivity of a layered structure but are explained by the finite length of the samples compared with the extended footprint of the beam at low angles. Here, the reflectivity includes a reflection from the SiO$_2$ substrate with no deposited material, leading to a complication in the results. This angle is very low so the fitting below this angle has been ignored.
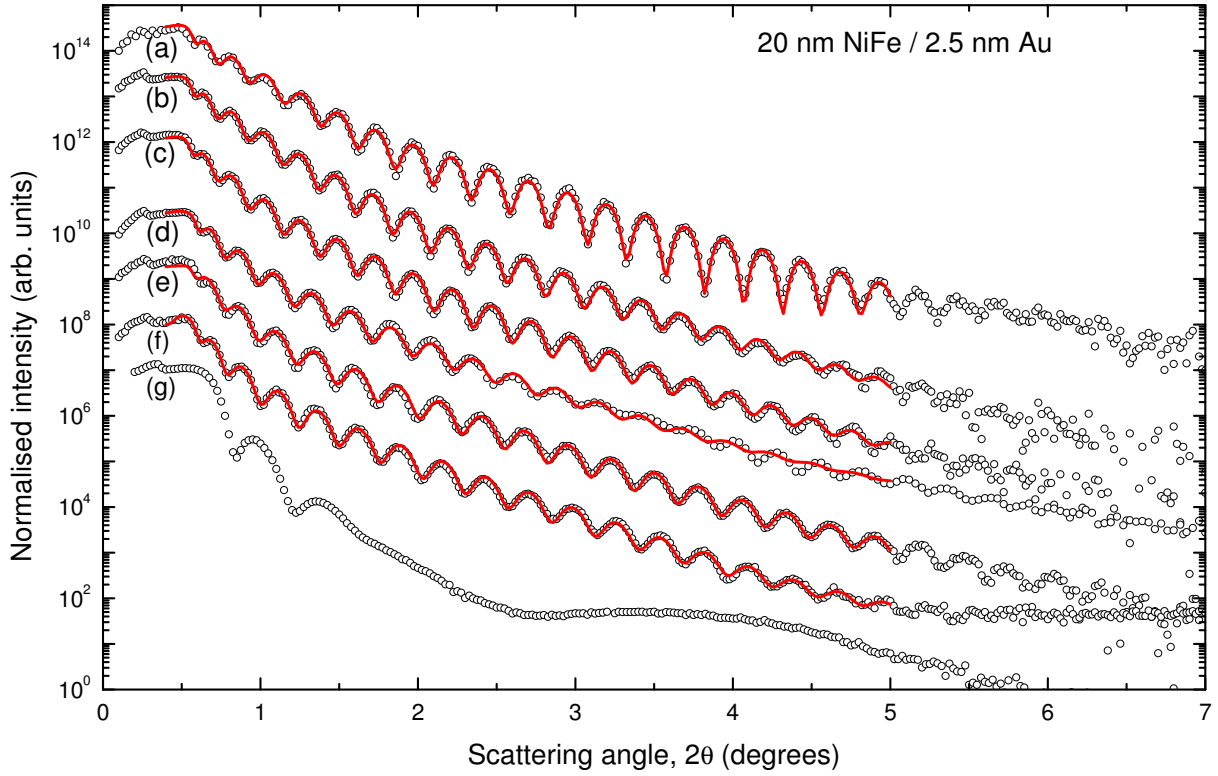
Figure 6.7: Fitted grazing incidence x-ray specular reflectivity curves for samples irradiated with doses: a) 0.00, b) 0.16, c) 0.31, d) 0.47, e) 0.63, f) 0.78, g) 4.68 $\times 10^{15}$ Ga$^+$/cm^2. (Curves are offset on intensity axis for clarity).

6.4.1 Model layered structure with interfaces

The data was analysed by fitting simulations using the Bede REFS software package[238] which fits the reflectivity data to a layered structure model with parameters representing the thickness, roughness and density of each layer. A good fit with the experimental data is shown by the red lines in figure 6.7. The good agreement between the fits and the data gives confidence that the layered model is applicable to these samples and that the fitted parameters are representative of the sample.

For higher doses, such as 4.68×10^{15} Ga$^+$/cm^2 (figure 6.7(g)), the reflectivity curve shows different behaviour without the repeating Kiessig fringes at higher angles. This indicates that the layered description of the sample is no longer appropriate and not actually possible. Here, amorphisation and damage to the sample structure resulting from the ion beam irradiation has occurred.

The simulation model in figure 6.7 was based on a nominal layered structure (20 nm NiFe / 3 nm Au) on an infinite SiO$_2$ substrate where the thickness, interface width and density

of each layer and the incident intensity were allowed to vary as free parameters. The x-ray reflectivity was mostly insensitive to the NiFe composition so this was fixed on the basis of the fluorescence measurements that are discussed in more detail in section 6.5.

Preliminary fits using this model did not give a satisfactory fit around the critical angle where the data represents the surface of the sample. This was improved by the inclusion of an additional Au surface layer to the model which had a reduced density in order to represent surface effects such as roughness or the formation of an oxide layer.[246] Figure 6.8(a) shows the improved quality of the fit for a bilayer sample irradiated with a dose of 0.16×10^{15} Ga$^+$ /cm^2. The goodness of fit parameter in this case was lowered from 0.12 to 0.06 without significant increase in the complexity of the model, therefore this revised layered structure was adopted as a reasonable representation of the system.

The NiFe/Au interface width was represented by the roughness parameter determined from the modification to the Fresnel coefficients by the Debye-Waller factor in the model.[175] This approach is valid only for interface widths below 5 nm,[247] so here a wider effective interface was created by including an additional NiFeAu alloy layer between the NiFe and Au layers for higher doses.[248;249] The models with an initially sharp interface, an interface width and interface alloy layer are shown schematically in figure 6.8(b). Table 6.1 shows a summary of the fit parameters for the best fitting models for the bilayers as a function of ion beam dose shown in figure 6.7.
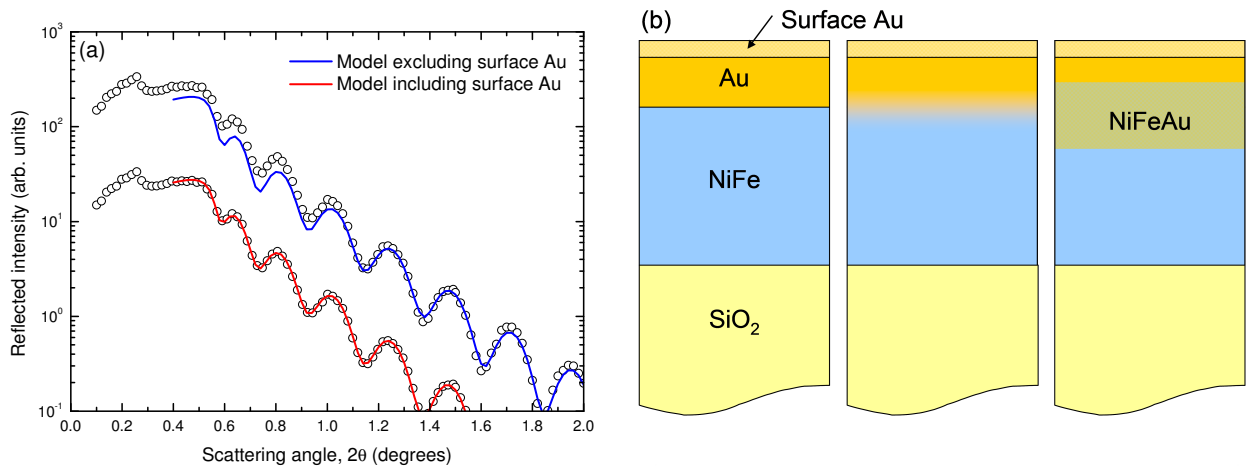
Figure 6.8: a) Improvements to the fit by the addition of a low density surface Au layer. b) Different model schematics showing the inclusion of interfacial alloy layer at high doses.

Irradiation dose ($\times 10^{15}$ Ga$^+$/cm^2)	Layer	Thickness (nm)	Interface width (nm)	Density (%)
0.00	Au	0.45 ± 0.04	0.28 ± 0.04	20 ± 10
	Au	2.7 ± 0.1	0.40 ± 0.03	90.6 ± 0.9
	NiFe	21.09 ± 0.08	1.14 ± 0.07	87 ± 1
	SiO$_2$	∞	0.313 ± 0.004	100
0.16	Au	0.1 ± 0.1	0.390 ± 0.006	37 ± 2
	Au	2.5 ± 0.4	0.82 ± 0.05	89 ± 6
	NiFe	21.4 ± 0.4	1.6 ± 0.3	85 ± 2
	SiO$_2$	∞	0.560 ± 0.009	100
0.31	Au	0.5 ± 0.1	0.65 ± 0.04	45 ± 6
	Au	2.8 ± 0.5	0.39 ± 0.01	80 ± 2
	NiFe	20.8 ± 0.5	2.6 ± 0.5	80 ± 1
	SiO$_2$	∞	0.554 ± 0.007	100
0.47	Au	0.5 ± 0.2	0.45 ± 0.07	46 ± 20
	Au	1.7 ± 0.7	0.28 ± 0.03	90 ± 1
	NiFe	20.5 ± 0.7	3.0 ± 0.4	92 ± 1
	SiO$_2$	∞	0.62 ± 0.01	100
0.63	Au	0.6 ± 0.1	0.40 ± 0.06	30 ± 10
	Au	2.0 ± 0.4	0.33 ± 0.02	89.5 ± 0.8
	NiFe	19.6 ± 0.4	4.1 ± 0.1	80 ± 2
	SiO$_2$	∞	0.451 ± 0.006	100
0.78	Au	0.5 ± 0.1	0.44 ± 0.05	59 ± 20
	Au	0.3 ± 0.3	0.27 ± 0.05	96 ± 1
	NiFe/Au	2.1 ± 0.3	3.5 ± 0.1	112 ± 6
	NiFe	19.2 ± 0.3	1.7 ± 0.2	93 ± 1
	SiO$_2$	∞	0.519 ± 0.005	100

Table 6.1: Table showing the layered structure models along with the best fitted model parameters.

6.4.2   Analysis of layer thickness from the fitted model

Figure 6.9(a) shows the layer thicknesses from these models plotted as a function of the irradiation dose. The position of the points represents the centre of the interfaces and their separation represents the layer thickness giving a graphical representation of the sample profile as a function of irradiation dose. To simplify this analysis, the thicknesses of the two Au layers were combined and for the higher doses where an alloy layer is included in the model, the thickness of this was divided between the NiFe and Au layers to improve the figure clarity.

The x-ray reflectivity technique confirms the original nominal 20 nm NiFe / 3 nm Au layered structure. A reduction in the sample thickness with dose also occurs but this is more clearly illustrated in figure 6.9(b) when the total Au thickness is plotted as a function of
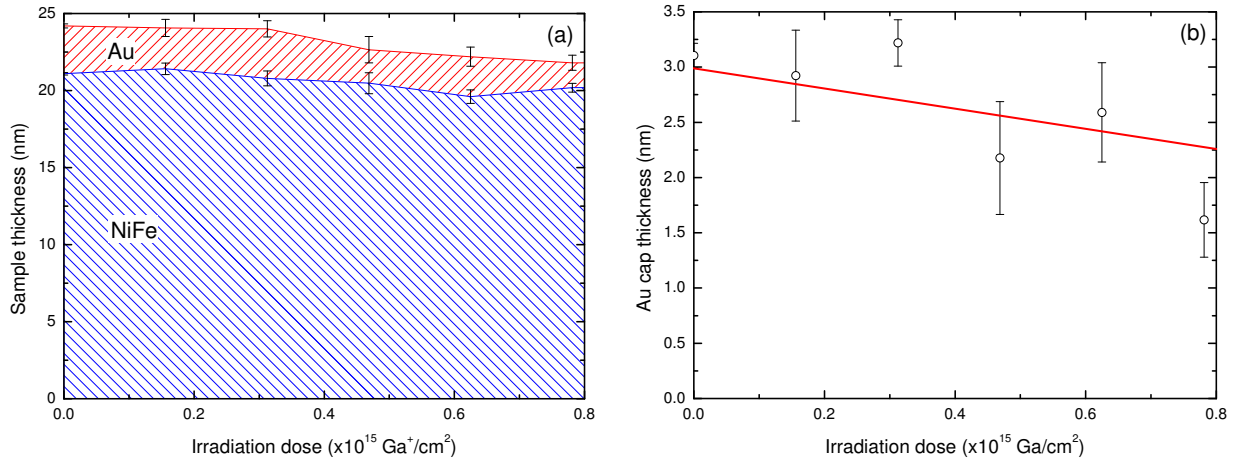
Figure 6.9: a) The variation in total sample thickness as a function of dose determined from x-ray reflectivity is composed of a NiFe layer with an Au cap. b) The thickness of the Au cap decreases slowly as a function of irradiation dose shown by the points fo x-ray reflectivity measurements and the line from TRIDYN simulations.

irradiation dose. This reduction in thickness results from a small amount of surface sputtering of the Au cap. TRIDYN simulations, shown by the line in figure 6.9(b), agree reasonably well with the experimental results. Here, the sputter rate was determined from the experimental results at 0.14 ± 0.04 nm^3/Ga$^+$ which is close to the simulated predictions from TRIDYN at 0.091 ± 0.002 nm^3/Ga$^+$. Even though the Au cap thickness reduces, x-ray reflectivity and TRIDYN simulations both show a consistent Au cap remains on the sample surface for the whole low dose region of interest.

6.4.3   Interfacial broadening with increasing irradiation dose

X-ray reflectivity also gave information about the interfaces between the layers using the interface width parameter. This was used to determine the amount of intermixing taking place as a result of the irradiation on the sample. For high doses where an alloy layer was included in the model, the total interface width was defined as the width of this layer convolved with the interface widths at the bottom and top interfaces.[149,248]

Figure 6.10 shows this width extracted from the x-ray reflectivity analysis as a function of Ga$^+$ irradiation dose. This has been squared as the irradiation induced contribution to the interface width is a more convenient parameter for the explanation of the intermixing mechanism as ballistic mixing leads to a linear increase proportional to this quantity with dose (see section 3.4.3). The irradiation induced component of interfacial mixing, σ_f, was
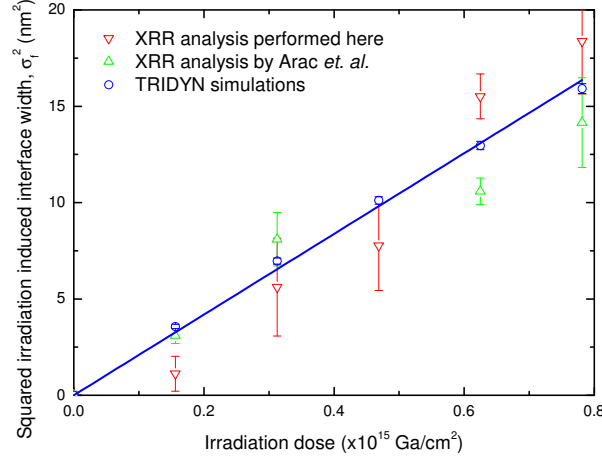
Figure 6.10: Broadening of the squared irradiation induced contribution to the interface width between NiFe and Au as a function of Ga^+ irradiation dose determined from specular x-ray reflectivity analysis. The points show the spread in the data by different fitting protocols where both agree with the line showing the linear increase predicted by TRIDYN simulations. [245]

separated from the total interface width, σ, by subtracting the interface width of the un-irradiated sample, σ_0, in quadrature: [149]

$$\sigma^2 = \sigma_0^2 + \sigma_f^2. \tag{6.1}$$

This square of the irradiation induced interface width in figure 6.10 is presented alongside the analysis of the x-ray reflectivity data performed by Arac et.al. [245] and an estimate of the interface width from TRIDYN simulations defined as a change from 5% to 95% composition which is discussed further in section 6.5.2. All the datasets show an increase in the square of the irradiation induced intermixing width and the spread of the data gives the best indication of the errors associated with the different methods used to determine the interface width.

The linear increase shown in figure 6.10 suggests that the mixing here is governed by a diffusion limited process. This is likely to have a contribution from ballistic mixing effects but be dominated by thermal spike mixing effects, these are important for $Z > 20$ and with a high damage energy, F_D. [144] This behaviour is consistent with that found in other ion beam intermixing in other similar metal/metal systems. [250,251]

The chemical effects predicted for preferential de-mixing between NiFe and Au are small in comparison to the mixing induced by the ion beam energy. [146] This explains why the results follow a linear increase rather than a trend that falls below this which is expected for preferential de-mixing.

6.4.4 Interfacial structure

Analysis of the specular x-ray reflectivity data showed an increase in the total interface width with irradiation dose. This interfacial width has two components: the topological roughness and the chemical intermixing. These are indistinguishable in specular x-ray reflectivity. However, transverse diffuse x-ray scattering experiments have been performed to distinguish between these two contributions to the interfacial structure.

Figure 6.11(a) shows transverse diffuse scans for the samples as a function of irradiation dose. A peak at the specular condition is found on top of a broad background of diffuse scatter. At the critical angles for incidence and exit, small Yoneda wings are observed. The effect of dose on these scans appears minimal. The specular peak is wide giving it a large contribution in comparison to the relatively small diffuse background. This is expected for films with large amounts of intermixing.[181]

By integrating the specular and diffuse intensities under the curve from the transverse diffuse scans, the topological roughness contribution to the interface width can be determined.[179] Figure 6.11(b) shows this contribution as a function of the irradiation dose. Combining this with the total interface width from specular x-ray reflectivity data allows the intermixing component to be determined. This is shown in figure 6.11(b) where a relatively small and constant contribution from interfacial roughness is found. Therefore, an increase in intermixing at the interface is responsible for the increase in total interface width with irradiation dose.
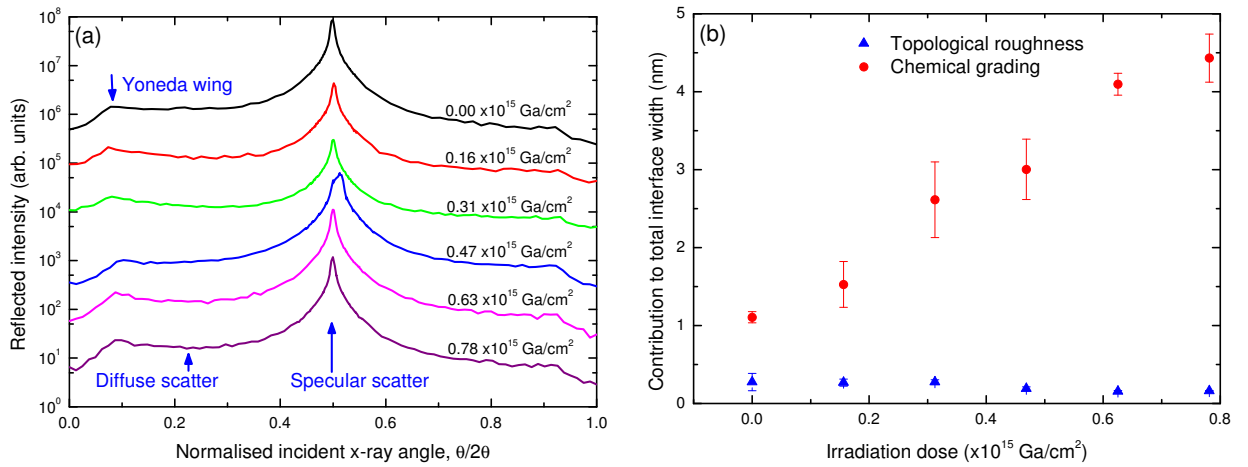

Figure 6.11: a) Transverse diffuse scans of the reflectivity from the NiFe/Au bilayers shifted for clarity. b) Integration of the specular and diffuse contributions gives the topological roughness which is used to find the amount of intermixing as a function of dose.

This simple analysis method involving the integration of the peaks in the transverse diffuse data incorporates the scattering from all layers and interfaces in the sample. Therefore this method can give only a general indication of the roughness contribution averaged over all of the interfaces. It is also not obvious how to identify separate contributions from the specular and diffuse scatter from the scans in figure 6.11(a). In this analysis, a linear fit to the extremities of the transverse diffuse scan (inside the Yoneda wings) gave a division. This is likely to overestimate the specular scatter, leading to systematic errors, but this would only adjust the size of the roughness contribution to the interface width and not affect the fact that chemical intermixing is the increasing component. Fitting of the transverse-diffuse scans would enable a more accurate description of the contribution to each interface to be determined but this is computationally intensive, dependent on many free parameters and was considered not to be a reasonable analysis method for this data.

The errors in the interface roughness contribution are taken from repeat analysis of two different transverse diffuse scans performed at a different fixed detector angle. These are combined in quadrature with the errors in the specular x-ray reflectivity fitting associated with the total interface width parameter to give errors on the intermixing contribution to the interface width.

In summary, the analysis of the specular x-ray reflectivity on a model with layers of different electron density is appropriate for these thin film samples. The fitting of a layered model to the reflectivity data gave parameters describing the thickness of the layers and their interfaces which agrees with results extracted from TRIDYN simulations of ion-solid interactions. This approach does not return one unique solution but the choice of model can influence the results obtained. Here, the results from two models on the same data give different analysis but both agree on the same linear increase in the squared intermixing width with irradiation dose. The analysis is consistent with the predicted ballistic and thermal spike mixing being the dominant intermixing processes with only a small thermodynamic chemical effect. A comparison between the specular and diffuse scattered intensity leads to the interpretation that an increase in interface width with dose is due to an increase in intermixing where samples contain a relatively constant roughness contribution.

6.5 NiFe composition in the samples

The x-ray reflectivity measurements show that focussed ion-beam irradiation has a significant effect on the interfacial intermixing in these samples. This analysis was based on a model with layers of different electron densities associated with layers of different elemental composition. Further analysis of the composition at the interfaces and the variation in the composition depth profile through the sample resulting from ion beam irradiation are presented here. This analysis combines TRIDYN simulations and analysis of grazing incidence x-ray fluorescence measurements.

6.5.1 Bulk composition of the NiFe layer

X-rays incident at a fixed angle of $\theta = 1°$, well above the critical angle, produce fluorescence from the entire thickness of the sample probing the entire NiFe layer. Scans over the width of each strip give the average fluorescence signal from multiple positions as well as being useful for aligning the sample. Figure 6.12(a) shows the fluorescence from two NiFe/Au strips irradiated with different doses where the fluorescence intensity was found from the peak area in the energy spectra as described in chapter 5. This clearly shows the position of the strips and their relative composition for an unirradiated and highly dosed sample.

The NiFe ratio was found by dividing the Ni fluorescence intensity with that of Fe and correcting by their respective fluorescence yields. Figure 6.12(b) shows the change in compo-
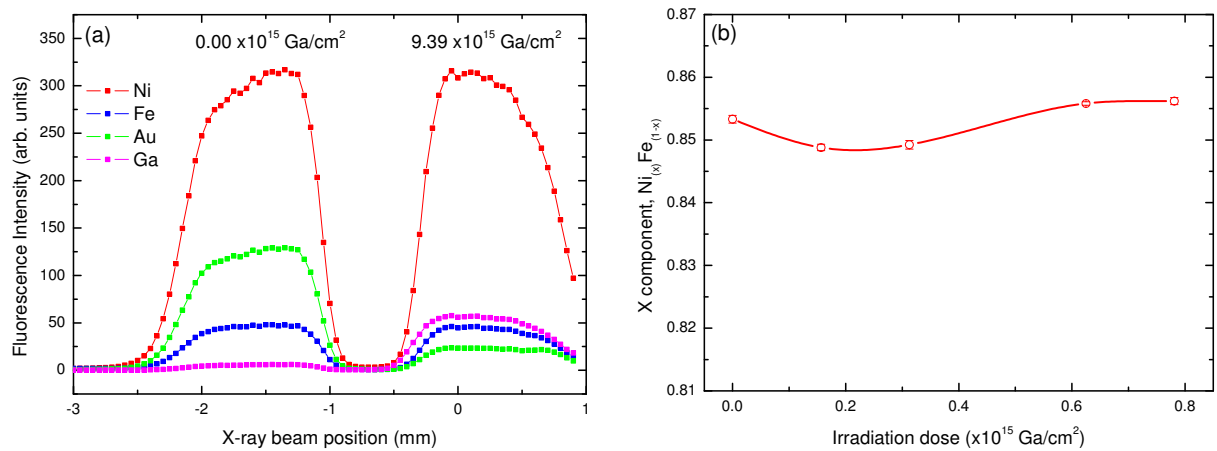
Figure 6.12: Fluorescence at an x-ray incident angle of 1° measured a) as a function of position across a strip sample and b) used to determine the NiFe ratio as a function of irradiation dose where the line is a guide to the eye.

sition measured as a function of irradiation dose where the composition is close to $Ni_{85}Fe_{15}$ showing very small dose dependent changes compared with the depth dependent changes discussed later.

6.5.2 Depth dependent composition of the samples

Element specific depth profiles from TRIDYN simulations provide a convenient way to model the depth dependent compositional variation resulting from ion beam irradiation. The relative concentration of each atomic species was extracted from the simulations as a function of depth into the sample. This is shown in figure 6.13 for a range of irradiation doses in the low dose regime for a NiFe sample with a 3 nm Au cap.

Initially a sharp interface separates the 3 nm thick Au cap layer from the NiFe layer. With increasing irradiation the composition at the interface shows diffusion-like behaviour and broadens as the atomic species relocate over the interface and become intermixed. Due to the loss of momentum during the many interactions in a collision cascade, this broadening becomes isotropic where Ni and Fe atoms move into the Au layer as well as Au atoms
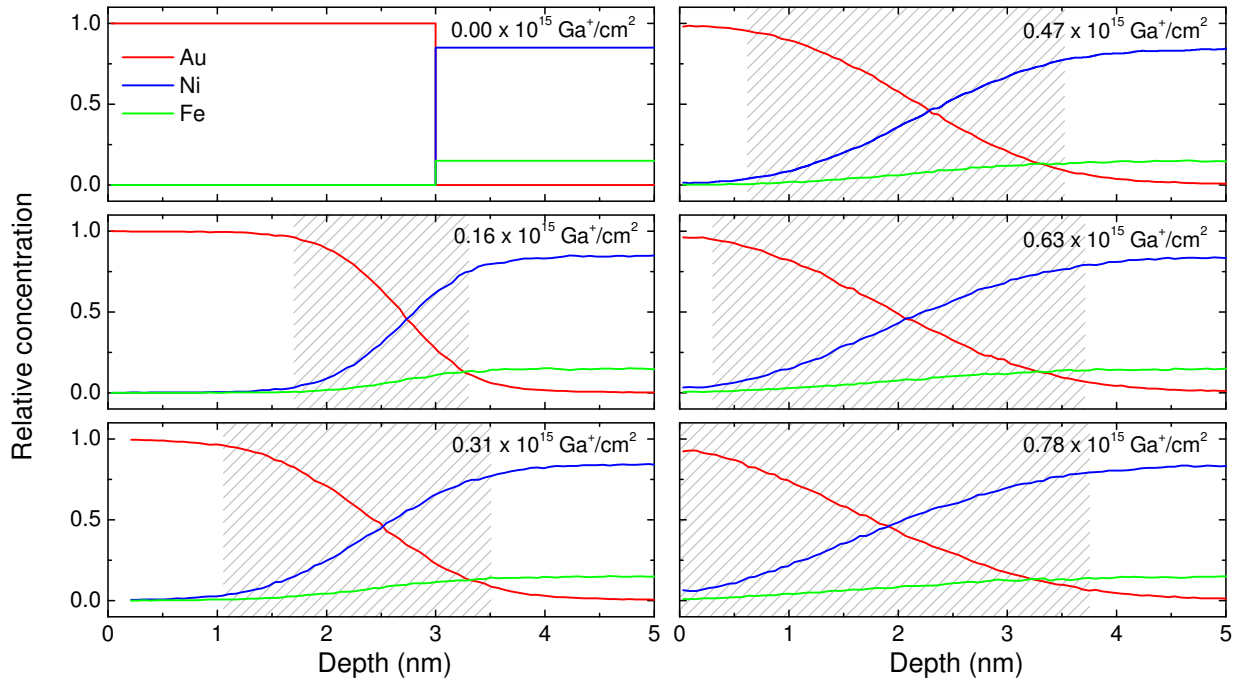
Figure 6.13: TRIDYN simulations showing the depth dependence to the relative atomic composition in an initial $Ni_{85}Fe_{15}$ film with 3 nm Au cap. The profiles show broadening of the initially sharp interface as a function of low dose Ga^+ irradiation. The hatched area represents the interface defined by the width over which the concentration changes from 5% to 95%.

moving into the NiFe layer. The centre of the interface also travels towards the sample surface with increasing dose representing the small amount of Au sputtered from the surface of the structure.

An estimate of the interface width was obtained from these simulations, defined as the width over which the composition varies from 5% to 95%, as illustrated by the shaded regions in figure 6.13. The average width was found from estimates of both the Au and Ni composition profiles and this width was persented earlier as a function of dose in figure 6.10(b).

For the highest dose simulated here at 0.78×10^{15} Ga$^+$/cm^2, a small amount of NiFe has intermixed so far that it has migrated through the Au layer and is found at the sample surface. This could result in the loss of NiFe by sputtering but this is expected to be small due to the low concentration of NiFe in the Au layer and the limited sputtering of the Au layer in this dose regime (figure 6.2).

Angle dependent x-ray fluorescence measurements provide an experimental technique to investigate the depth dependence to this elemental composition as a function of dose. The fluorescence spectra obtained have been fitted to the elemental transitions and the areas of the Ni, Fe and Au peaks give the fluorescence intensity as a function of the grazing incidence angle. This data was normalised against the beam monitor and is shown in figure 6.14.

The fluorescence intensity for each element shows an initial increase as the incident x-
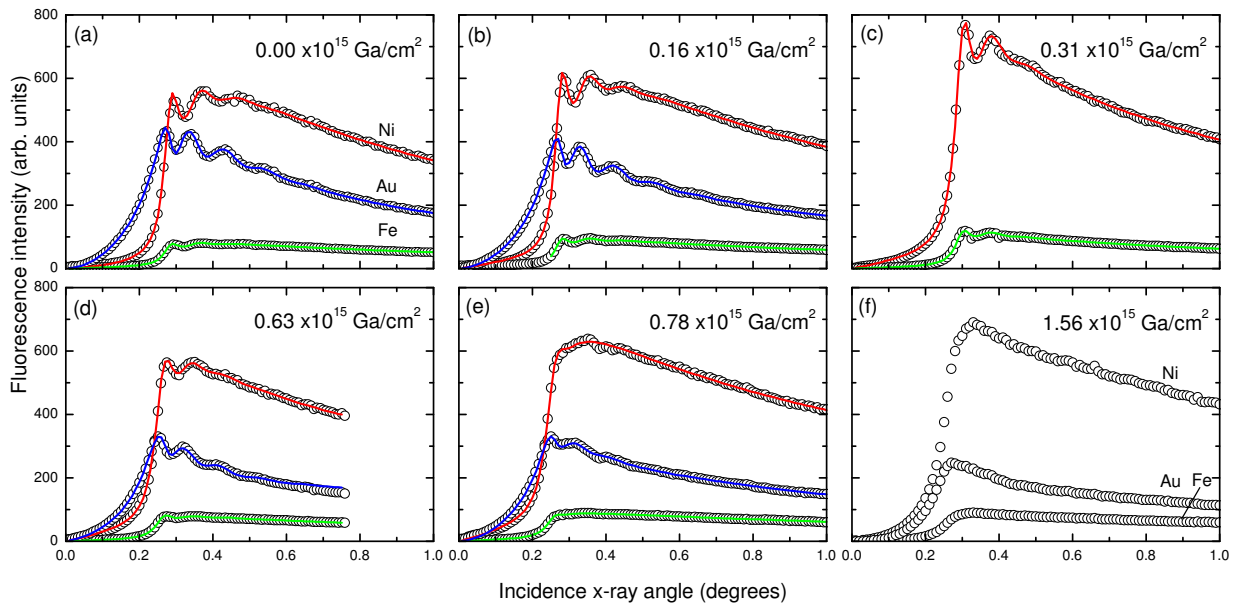
Figure 6.14: Grazing incidence x-ray fluorescence showing the depth dependence to the elemental composition as a function of Ga$^+$ irradiation dose. This is measured with 12.5 keV (11.8 keV for the 0.31×10^{15} Ga$^+$/cm^2 sample) incident x-rays and the solid lines show the best fit to the data.

ray angle passes through the critical angle. This is followed by interference fringes at the maximum intensity and then a gradual decrease in intensity towards higher angles.

This angular dependence results from the penetration depth where just an evanescence wave probes the surface of the sample below the critical angle. This region shows an increase in Au fluorescence consistent with the Au capping layer on the sample. Increasing the angle beyond the critical angle allows the beam to penetrate the entire sample thickness, explaining the sharp increase in Ni and Fe fluorescence at a greater angle than the rise in Au.

The details of the interference fringes and the decay in the fluorescence signal for higher angles contain additional information about the structure of the film. With increasing dose the fringes become less pronounced, indicating the loss of the discrete layered nature of the samples as the interface becomes intermixed, this is consistent with the x-ray reflectivity analysis and TRIDYN simulations presented in figure 6.13.

This change in behaviour is more easily seen in figure 6.15(a) where the Au fluorescence intensities at different doses are compared. Changes can also be observed below the critical angle for the higher doses where the increase in fluorescence intensity is shifted towards higher angles. This is an indication that sputtering effects on the sample surface become apparent for high irradiation doses.

To gain further understanding from the subtle changes in fluorescence intensity data has been fitted to a model in a similar approach used for the analysis of the x-ray reflectivity data.

Figure 6.15: a) Angular dependence to the x-ray fluorescence of Au for a variety of different irradiation doses. b) Composition of NiFe layer obtained from fitting the angular dependent x-ray fluorescence data where the line is a guide to the eye.

6.6   Layer model for fitting composition

The solid lines in figure 6.14 show a model fitted to the fluorescence data using REFS. This is based on the structure obtained from the x-ray reflectivity measuremen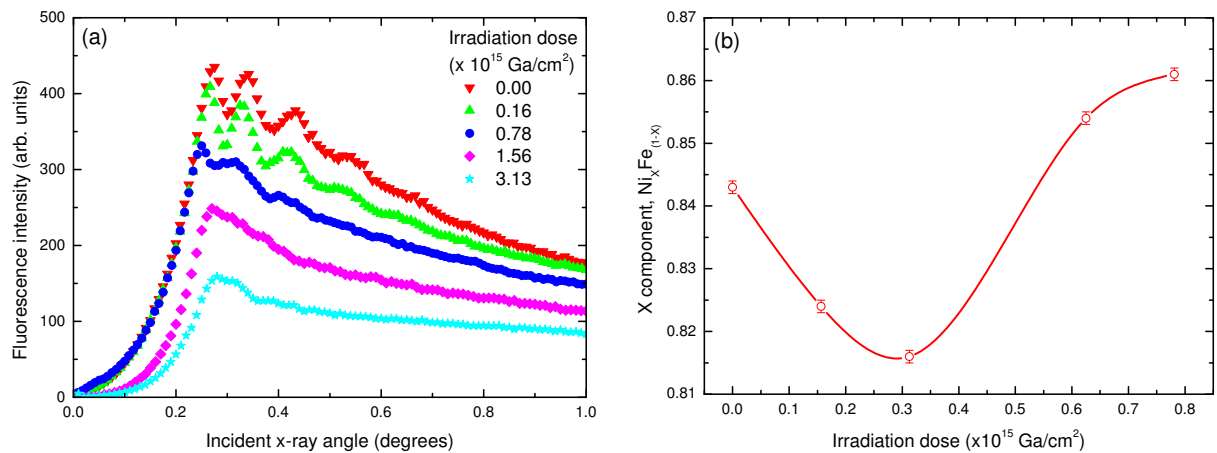ts presented earlier. Ideally the same model should fit to all the data sets from the different experimental techniques used to describe the structure, but, in reality current developments in fitting packages only allow for fitting a single set of fluorescence or reflectivity data independently and the use of both techniques for a single sample is rarely performed. The fitting of the fluorescence data here is heavily constrained around the layer structure from the reflectivity measurements but was fitted based on the composition parameters for which the fluorescence data is most sensitive.

The composition profile predicted by the TRIDYN simulations (figure 6.13) shows a gradual dependence on the composition across the interfaces. To reflect this, the alloy region in the reflectivity model was substituted by a layer where the composition varied as an error function across the layer. This graded composition approach for fluorescence analysis has been shown to give an improvement over reflectivity models based on discrete layers and roughness.[247] To obtain a good fit, this compositionally graded layer was introduced to the model at a lower irradiation dose than was necessary with the reflectivity fitting.

This model was also more sensitive to the surface Au which affects how the beam travels into the film due to the refractive index at the surface. A low density Au layer was included in the reflectivity model. This made little difference to the quality of fits for the fluorescence model so was removed at high dose irradiation, but the inclusion of a $NiFe_2O_3$ layer between the substrate and permalloy layer did give an improvement to the fits at high irradiation dose.[252]

As previously mentioned the simultaneous fitting of all the data with a single model is desirable, but was not possible with the fitting packages currently available. Here, a fitting procedure was developed where iterative fitting of the fluorescence data for Ni and Fe was performed on the structural model based on the x-ray reflectivity results described above.

The genetic algorithms built into REFS gave a best fit of the model to Ni and Fe fluorescence data with a fixed incident beam intensity and NiFe composition. Combining the goodness of fit parameters gave a parameter indicating the combined best fit for both data sets which was minimised with respect to the choice of beam intensity and NiFe composition

parameters. Once the stoichiometry was fixed from iterative fitting with the Ni and Fe data, the same model was fitted to the Au fluorescence data and the results illustrated by the lines in figure 6.14 and the parameters in table 6.2.

This technique can only find a local minimum so the fitting of many parameters may degrade the usefulness of this technique as it becomes limited by the choice of initial parameters. For this reason just the stoichiometry and incident beam intensity, the two parameters most sensitive to the fluorescence measurements, fitted using this technique with surprisingly good results. There are slight variations between the optimum structure from reflectivity and fluorescence models due to different descriptions of the layers and interfaces but the results from both models agree on the same trends for low dose irradiation. They also agree on the breakdown in the model for representing the sample as a layered structure towards higher irradiation doses.

These models are best interpreted by taking layer structure and interface width information from the reflectivity fitting and the compositional information from the fluorescence results. Ideally all x-ray reflectivity and fluorescence data would be fitted simultaneously, using a single model which can be fitted to minimise an overall goodness of fit parameter. However, this is beyond what can be achieved with currently available computational packages for fitting these complex models.

The NiFe composition which gave the best overall combined goodness of fit is shown in figure 6.15(b) as a function of the irradiation dose. Here, the composition is approximately $Ni_{85}Fe_{15}$ with a dip indicating a Fe enrichment at a dose of 0.5×10^{15} Ga/cm^2. These results agree with the fluorescence results in figure 6.12(b) but where a more significant dip occurs this may be related to the fact that these results are highly sensitive to the fitting at the critical angle whilst the previous results represent the entire NiFe thickness.

Irradiation dose ($\times 10^{15}$ Ga/cm^2)	Transition	Layer	Thickness (nm)	Interface width (nm)	Density (%)
0.00	Ni $K\alpha_1$	Au	0.4 ± 0.2	0.2 ± 0.2	17 ± 3
		Au	2.2 ± 0.1	0.2 ± 0.1	107 ± 3
		NiFe	19.53 ± 0.06	2.0 ± 0.1	90.9 ± 0.3
		SiO$_2$	∞	1.5 ± 0.1	100
	Fe $K\alpha_1$	Au	0.2 ± 0.2	0.2 ± 0.8	14 ± 10
		Au	1.7 ± 0.1	0.4 ± 0.2	110 ± 6
		NiFe	20.5 ± 0.1	2.5 ± 0.2	91.0 ± 0.5
		SiO$_2$	∞	1.5 ± 0.2	100
	Au Lm_1	Au	0.2 ± 0.1	0.2 ± 0.2	21 ± 2
		Au	2.65 ± 0.04	1.08 ± 0.05	110 ± 1
		NiFe	19.5 ± 0.1	1.32 ± 0.04	91.0 ± 0.4
		SiO$_2$	∞	1.22 ± 0.07	100
0.16	Ni $K\alpha_1$	Au	0.6 ± 0.1	3.9 ± 0.5	23 ± 2
		Au	3.2 ± 0.1	0.2 ± 0.1	85 ± 2
		NiFe	19.96 ± 0.04	1.8 ± 0.1	88.1 ± 0.2
		SiO$_2$	∞	1.19 ± 0.09	100
	Fe $K\alpha_1$	Au	0.36 ± 0.09	2.7 ± 0.3	31 ± 3
		Au	2.51 ± 0.09	0.3 ± 0.1	86 ± 2
		NiFe	20.78 ± 0.05	2.8 ± 0.1	88.0 ± 0.2
		SiO$_2$	∞	1.1 ± 0.1	100
	Au Lm_1	Au	0.32 ± 0.06	1.46 ± 0.05	44 ± 2
		Au	3.46 ± 0.04	0.52 ± 0.08	83.9 ± 0.5
		NiFe	19.39 ± 0.05	1.43 ± 0.04	88.4 ± 0.2
		SiO$_2$	∞	0.98 ± 0.05	100
0.31	Ni $K\alpha_1$	Au	3.51 ± 0.07	0.8 ± 0.1	72 ± 2
		NiFe/Au	0.24 ± 0.08	2.25 ± 0.05	89 ± 7
		NiFe	19.1 ± 0.1	1.5 ± 0.2	92 ± 0.2
		NiFe$_2$O$_4$	0.8 ± 0.2	0.7 ± 0.2	86 ± 9
		SiO$_2$	∞	0.9 ± 0.2	100
	Fe $K\alpha_1$	Au	3.8 ± 0.1	0.9 ± 0.09	71 ± 1
		NiFe/Au	0.22 ± 0.06	2.12 ± 0.07	83 ± 10
		NiFe	18.9 ± 0.3	1.5 ± 0.3	91.9 ± 0.3
		NiFe$_2$O$_4$	0.8 ± 0.1	0.7 ± 0.4	90 ± 10
		SiO$_2$	∞	0.9 ± 0.5	100
					Continued on next page

Irradiation dose ($\times 10^{15}$ Ga/cm^2)	Transition	Layer	Thickness (nm)	Interface width (nm)	Density (%)
0.78	Ni $K\alpha_1$	Au	3.2 ± 0.1	0.3 ± 0.1	73 ± 2
		NiFe/Au	0.7 ± 0.1	1.98 ± 0.07	92 ± 7
		NiFe	16.7 ± 0.3	1.2 ± 0.2	77.4 ± 0.7
		NiFe$_2$O$_4$	0.7 ± 0.1	5.0 ± 0.7	90 ± 10
		SiO$_2$	∞	5.0 ± 0.9	100
	Fe $K\alpha_1$	Au	4.2 ± 0.2	0.8 ± 0.1	72 ± 2
		NiFe/Au	0.72 ± 0.08	1.50 ± 0.08	89 ± 6
		NiFe	17.5 ± 0.8	1.2 ± 0.2	90 ± 7
		NiFe$_2$O$_4$	0.8 ± 0.1	5.0 ± 0.8	90 ± 7
		SiO$_2$	∞	5 ± 2	100
	Au Lm_1	Au	4.5 ± 0.3	0.2 ± 0.1	76 ± 4
		NiFe/Au	0.7 ± 0.2	1.57 ± 0.08	90 ± 10
		NiFe	17.3 ± 0.7	1.2 ± 0.3	75.5 ± 0.7
		NiFe$_2$O$_4$	0.8 ± 0.3	5 ± 1	84 ± 9
		SiO$_2$	∞	1.7 ± 0.4	100

Table 6.2: Table showing the best fit parameters to the model for the x-ray fluorescence data.

6.6.1   Interfacial NiFe composition

The analysis of the NiFe composition in figures 6.12(b) and 6.15(b) reveals that there may be a depth dependence to the composition throughout these films. This has been analysed using a more primitive technique where analysis of the variation in the composition through the critical angle assumes the samples have a continuously varying composition with depth without considering the effects of the layered structure.

In figure 6.14, the Ni and Fe fluorescence intensities were presented as a function of incidence x-ray angle. Dividing the fluorescence intensity of Ni with that of Fe and correcting for their respective fluorescence yields gives an indication of the composition as a function of incident x-ray angle. This analysis was performed for the data at both 11.8 keV and 12.5 keV and the average NiFe composition determined for each incidence angle is shown in figure 6.16 where the lines are included as a guide to the eye.

At large angles where the beam penetrates the entire film thickness, the results give a constant composition but as the angle is reduced through the critical angle, dose dependent variations in the composition indicate a reduced Ni/Fe ratio when the beam probes only the surface of the sample. In this surface region the quantities of Ni and Fe are low, which gives rise to the increased errors in the data at lower angles. The data for the lowest angles is
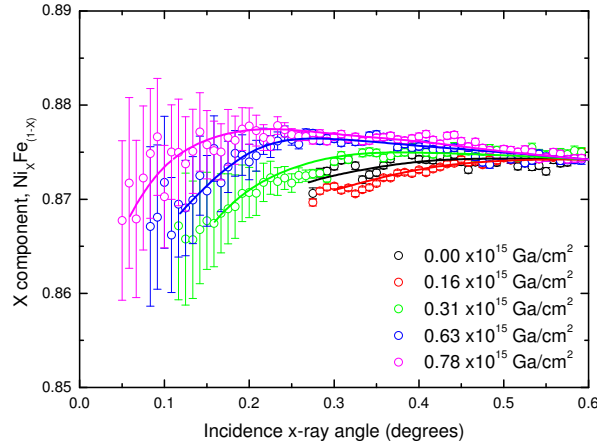
Figure 6.16: NiFe ratio as a function of x-ray incidence angle for various irradiation doses. The lines are a guide to the eye.

omitted when the errors become very large and distract from the trends in the data.

The overall higher Ni content indicated by this data over the entire angular range is likely to be a result of a systematic error introduced through the simplistic analysis of this data. This may be explained by the fact that this analysis does not take into account any re-absorption of the fluorescent x-rays transmitted through the surface Au layer.[186] Since Fe transitions are at a lower energy than Ni,[183] Fe fluorescent photons are more easily absorbed giving the appearance of a higher Ni content.

Similar analysis has been performed on the TRIDYN simulations in figures 6.13 which also shows a variation in Ni and Fe composition as a function of depth into the sample. The NiFe ratio from this analysis is shown in figure 6.17(a) as a function of depth for a range

Figure 6.17: TRIDYN simulations showing the variation in NiFe composition at the surface of a NiFe film with a) a 3 nm Au cap and b) no Au cap, for various ion irradiation doses.

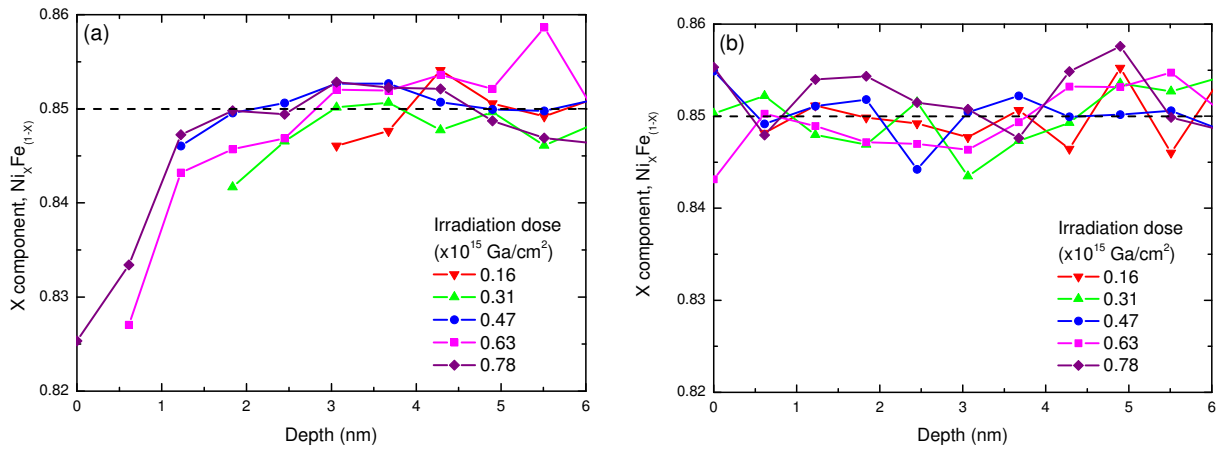of irradiation doses where binning was used to reduce the noise on the data and highlight the behaviour taking place. Here a constant NiFe composition at $Ni_{85}Fe_{15}$ was found in the deep regions in the sample which is consistent with the initial starting parameters for the simulation. However, at the near surface region a reduced Ni/Fe ratio was found to result from the ion irradiation which is similar to the experimental results.

As the NiFe concentration in the Au layer at the surface was low, the data is only shown for depths where the NiFe accounts for over 10% of the composition. The broadening of the intermixed region then explains the shift in the start of the data towards shallower depths as a function of increasing dose.

Figure 6.17(b) shows similar simulations for NiFe with no Au cap. In this case no changes to the NiFe composition are found at the near surface region resulting from ion irradiation. Instead these simulations show the sample maintains its initial composition reaching to the sample surface. Here the data is displayed all the way to the surface as there is always 100% NiFe and therefore no problems with finding the ratio of two small numbers.

Comparison between these two simulations shows that the change in surface composition of the samples is an effect that only occurs with the presence of the Au cap. This suggests that this is a property of the interface rather than due to any preferential sputtering which has been associated with similar behaviour in an uncapped sample.[41]

Instead it is possible that there could be a preferential atomic rearrangement at the near surface region where the migration of Fe into the Au layer occurs at a greater rate than Ni. This explains the resulting Fe rich surface found from both simulations and experimental results on Au capped NiFe samples. To maintain a constant ratio of Ni:Fe in the sample, a corresponding region with depleted Fe content is to be expected. Figure 6.17 shows a wide region with a higher Ni:Fe ratio that could correspond to this although it is hard to see any equivalent effect in the results of the simulations.

6.7 Summary

In this chapter the structure of thin NiFe/Au bilayer structures has been investigated using both grazing incidence x-ray reflectivity and x-ray fluorescence techniques. This has been used to quantify the structural changes in the samples resulting from focussed ion beam irradiation and the structural changes are compared with TRIDYN simulations of ion-solid

interactions.

Initially the damaging effects of high dose irradiation were investigated which result in roughening of the surface where sputtering of material is significant. This gave an upper bound on the dose range and subsequent measurements were performed at lower doses where the effects of sputtering were not significant. Here, the amount of implanted Ga^+ increased linearly with irradiation dose and was distributed around an implantation depth of ≈ 10 nm from the surface. The maximum concentration predicted from this implantation was about 0.7% Ga, which is a very small effect and unlikely to give rise to the changes in magnetism that are presented in chapter 7.

A much more significant effect is the energy transfer of the initial Ga^+ beam into the sample which gives rise to intermixing at the NiFe/Au interface. Analysis of the x-ray reflectivity of irradiated samples based on a layered model shows an increasing width for the interface region with dose. This fits to a square root relationship with the irradiation dose showing the mixing mechanism to be ballistic with additional effects of a thermal spike model. Thermodynamic considerations predict a de-mixing effect between NiFe and Au but this is small in comparison to the ion beam induced mixing and was not identified from experiments or simulations here.

Further analysis of the interfaces through measurements of the transverse diffuse x-ray scatter has shown that the topological roughness contribution to the overall interface width is small and constant. Therefore, an increasing width of intermixed region at the interface is concluded to be the dominant mechanism leading to the increase in total interface width.

The elemental composition of the samples was also investigated by angular dependent x-ray fluorescence measurements giving a depth dependent probe for the sample composition. Measurements of the total thickness of the samples gave a composition comparable with the nominally prepared NiFe film with the inclusion of a slight Fe enrichment for doses around $\approx 0.5 \times 10^{15}$ Ga/cm^2. More detailed analysis of this composition and comparison to simulations suggests this may be due to an interface effect with Au, where the Fe is mixed into the Au layer more strongly than the Ni.

Chapter 7

Modification of magnetic properties by focussed ion beam irradiation

7.1 Introduction

The modification of the magnetic properties of perpendicular magnetic anisotropy (PMA) materials by ion irradiation has been extensively explored and showed how structural modifications of an interface result in changes of the magnetic properties. However, significantly less work has been performed on materials with in-plane anisotropy. This is the theme of the results presented in this chapter where the effect of Ga^+ ion irradiation on the magnetic properties of NiFe/Au bilayer structures was investigated. The results have been analysed in terms of the structural changes taking place at the interface that were identified in chapter 6.

The chapter starts with an investigation of the magnetic properties measured using MOKE magnetometry to cover a broad range of irradiation conditions; this identified some interesting magnetic changes that occur for low dose Ga^+ ion irradiation. The remainder of the chapter focusses on detailed measurements which investigate the physical mechanisms that give rise to these effects. The measurement techniques include SQUID magnetometry, to give a direct measure of the magnetic moment, and XMCD, to give information about the relative contribution to the moment from the spin and orbital contributions. Magnetoresistance measurements were used to investigate the spin-orbit interaction and the induced moment on Au was also investigated through x-ray magnetic resonance scattering.

These techniques were introduced in chapter 4 and the experimental procedures described

in detail in chapter 5. The results presented here provide the understanding relevant for the local FIB control of the magnetic behaviour in nanowires presented in chapter 8.

7.2 Magnetic properties as a function of dose

This investigation started with the magnetic characterisation of NiFe/Au elliptical (50 × 10 μm) structures fabricated by electron beam lithography. These were irradiated with Ga^+ ions using the dual beam FIB system and the magnetic properties were investigated by MOKE magnetometry as a function of irradiation dose.

7.2.1 Magnetisation reversal in irradiated NiFe/Au ellipses

Example hysteresis loops in figure 7.1 show hysteretic behaviour, typical of a ferromagnetic sample. The coercivity is $\approx$ 15 Oe and the loops showed a relatively high remanence which indicated a magnetic easy axis along the MOKE sensitivity direction (aligned with the long axis of the ellipses). The changes in loop shape are subtle in comparison to previous studies with ion irradiation on NiFe; however these previous measurements were performed with an order of magnitude higher dose.[253] Here, the most significant difference in the magnetic behaviour was found from the variation in the maximum Kerr signal, which represents the saturation magnetisation of the sample and has been normalised with the data from the unirradiated sample. This variation is the main subject of the discussion in this chapter.

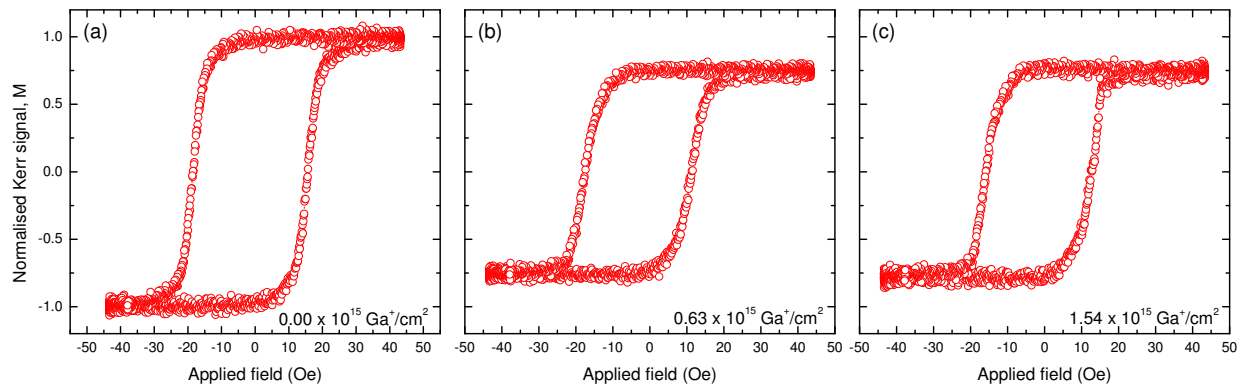**Figure 7.1:** Variation of the hysteresis loop shape with dose for 50 μm ×10 μm elliptical samples measured in a MOKE magnetometer. The samples have a layer structure of 15 nm NiFe / 3 nm Au and have been irradiated with doses of a) 0.00×10^{15} Ga^+/cm^2, b) 0.63×10^{15} Ga^+/cm^2 and c) 1.54×10^{15} Ga^+/cm^2.

7.2.2 High dose modification of magnetic properties

Initially a study over a wide range of irradiation doses up to 13×10^{15} Ga$^+$/cm^2 was performed on 10 nm NiFe / 7 nm Au bilayer elliptical structures. The results obtained were associated with damage to the magnetic thin film structure at higher doses. From these measurements the Kerr signal and coercivity were extracted from the hysteresis loops and are shown as a function of Ga$^+$ irradiation dose in figure 7.2. Here, the coercivity remains constant over a wide dose range before rising dramatically when the dose increases above 7×10^{15} Ga/cm^2. In contrast, the Kerr signal shows a linear decrease with dose, and for doses below 4×10^{15} Ga$^+$/cm^2 a decrease followed by a recovery in the Kerr signal is observed.

The changes in coercivity can be explained by an increasing density of domain wall pinning sites throughout the film. This results from an increasing number of implanted defects and damaged regions within the film that occur as a function of dose.[165]

The Kerr signal gives an indication of the magnetisation in the sample. In this case the saturation magnetisation is represented by the Kerr signal obtained from the maximum height of the hysteresis loops. The decrease in this Kerr signal with irradiation dose indicates a loss in the saturation magnetisation to the point where a ferromagnetic hysteresis loop can not be detected beyond a dose of 13×10^{15} Ga/cm^2. The loss in magnetisation is explained as a result of the amorphisation and degradation of the surface of the thin film structure. This is consistent with the results for high dose irradiation previously investigated through
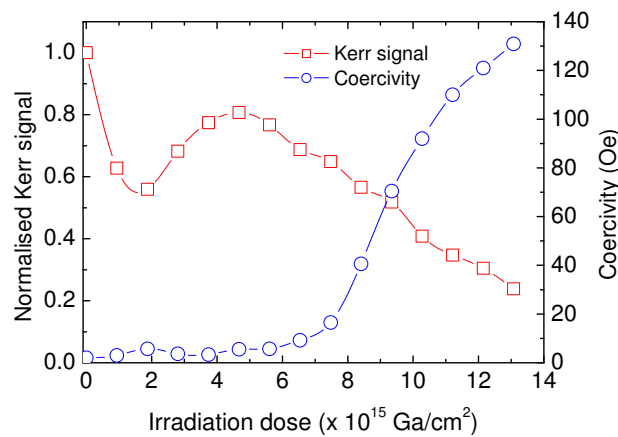
Figure 7.2: Coercivity and normalised Kerr signal as a function of Ga$^+$ dose for irradiated 10 nm NiFe / 7 nm Au bilayer ellipses. A linear decrease in Kerr signal with dose is found with an additional dip for low dose irradiation. The coercivity shows little variation until a dose of 7×10^{15} Ga$^+$/cm^2 at which point a sharp rise in coercivity occurs. Beyond 13×10^{15} Ga$^+$/cm^2 the ferromagnetic properties of the sample cannot be determined. The lines are a guide to the eye.

ion beam irradiation on similar materials.[37]

More interestingly, at very low doses, figure 7.2 shows a decrease, followed by a recovery in the Kerr signal suggesting that complex changes in the magnetic properties of these structures occur for low dose Ga^+ irradiation. This behaviour is the focus of the rest of the investigation in this chapter.

7.2.3   Complex Kerr signal behaviour for low dose irradiation

Changes in the Kerr signal may result from other factors in addition to the magnetic moment. These need to be eliminated before conclusions can be drawn from these MOKE measurements. One such artefact arises due to the alignment of a sample in the MOKE system. This means that it is common to normalise hysteresis loops from the MOKE system as they give only a relative measure of the magnetisation. However, in this case each structure was nominally identical and fabricated on the same substrate so it was reasonable to assume consistent alignment of the MOKE laser on each sample.

Magnetic changes may also result from any deviations occurring during the fabrication stages of the investigation. However, these should not be reproducible with repeat measurements. Figure 7.3(a) shows the behaviour of the Kerr signal for another bilayer sample with a thicker magnetic layer of 15 nm NiFe and a thinner capping layer of 3 nm Au. In this case the Ga^+ ion irradiation doses was focussed around the low dose regime and these results repeatably show complex low dose Kerr signal response in this case with the minimum shifted
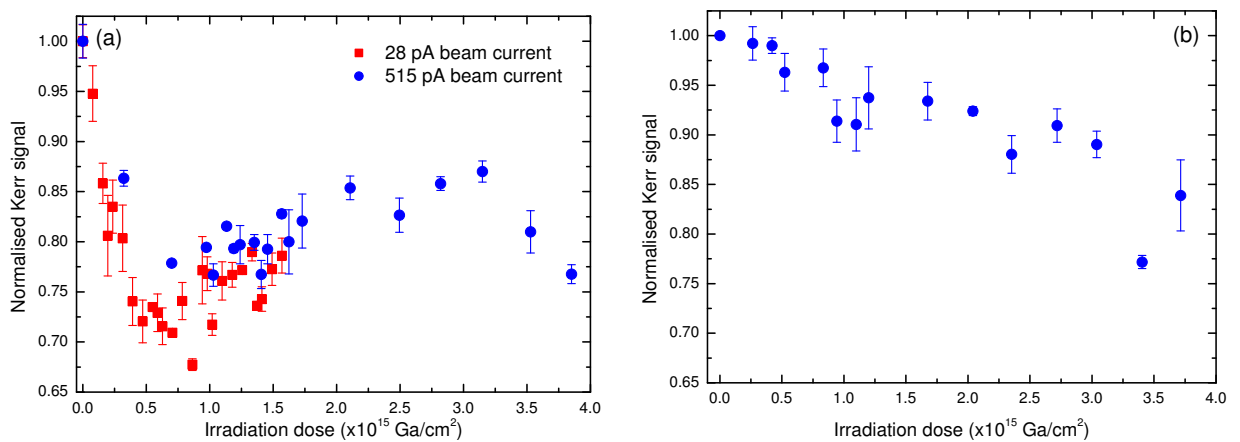

Figure 7.3: Normalised Kerr signal as a function of Ga^+ irradiation dose for 15 nm thick NiFe ellipses, a) with and b) without a 3 nm Au cap.

to lower dose compared to the previous sample with a thicker capping layer.

In figure 7.3 the errors on the data points represent the standard error between repeat measurements of an irradiated structure which also includes experimental errors associated with the repeat alignment of the structure within the MOKE system. Different points at the same dose represent the results from different elliptical structures that were irradiated with a nominally identical dose. Both of these sources of error are small in comparison to the trends observed here which suggest these results originate from the samples and not from any noise or lack of precision in the measurements.

Figure 7.3(a) also shows the effect of irradiation dose performed with two different beam currents. The results overlap, indicating that the changes arising here are due to the total quantity of Ga^+ ions involved in the irradiation rather than an effect of the rate of irradiation. This suggests that the changes in the magnetic properties do not result from any temperature rise in the sample (beyond the expected thermal spike mixing discussed in chapter 6) as the dose rate differs by nearly a factor of 20.

In figure 7.2 the minimum Kerr signal occurs at a dose of 2×10^{15} Ga^+/cm^2 whilst in figure 7.3(a) this minimum point is shifted to 0.6×10^{15} Ga^+/cm^2. This shift can be explained by the differences in the Au cap thickness. In the first case, the thicker 7 nm Au cap provides more attenuation to the Ga^+ beam than the 3 nm Au cap. This means that a greater incident dose is required to achieve the same amount of energy transfer to the NiFe/Au interface to achieve the same level of interfacial intermixing. This is also supported by TRIDYN simulations which shows that a similar interface width develops for lower doses with a thinner Au cap.

A sample thickness argument can also explain the relative size of the initial drop in the Kerr signal for these samples where the thinner 10 nm NiFe sample shows a 45% decrease in the Kerr signal compared to a 30% decrease for the 15 nm NiFe sample. The MOKE measurements probe to a skin depth of $\approx 10 - 20$ nm[207] and therefore give a measure of the entire magnetic thickness of both samples. The change in Kerr signal then represents the ratio of the magnetic response from the interface in comparison to the response from the volume of the NiFe layer.

Assuming a similar magnetic response from the interface at the minimum point in both of these samples, the difference in magnetic signal can be approximated by the ratio of the magnetic layer thicknesses: $(10 \text{ nm}/15 \text{ nm})^{-1} = 1.5$. This is the same as the difference in the

decrease in Kerr signal between the two samples: $45\%/30\% = 1.5$.

Ga^+ ion irradiation was also performed on similar samples prepared with no Au capping layer and the effect of low dose irradiation on the Kerr signal in these samples is shown in figure 7.3(b). Here, a linear decrease in Kerr signal was found throughout the low dose region and can be explained by degradation of the film quality and an increase in defect density that is consistent with the explanation of the high dose behaviour. This contrasting behaviour shows that the capping layer is important to produce this complex dose dependent magnetisation behaviour.

Although the focus here was upon an Au capping layer, the effect of other capping layers were also considered. Measurements made on a 20 nm NiFe film capped with 2.5 nm Cu also show a dose dependent change in the magnetic properties which is shown in figure 7.4. In this case the minimum magnetic signal occurs at 0.2×10^{15} Ga^+/cm^2 which is consistent with the discussion based on attenuation of the beam with the cap thickness. Also, a $\approx 30\%$ change in signal is consistent with the previous discussion of the MOKE skin depth into the sample and the sample thickness. At higher doses this sample also shows a gradual decrease in the Kerr signal associated with sample damage.

The NiFe sample with a Cu capping layer shows similar complex magnetic behaviour to those obtained with the Au capping layer. This contrasts with the gradual decrease in moment that occurs in an uncapped NiFe film. Therefore, the complex behaviour can be strongly associated with the presence of the capping layer and attention is drawn towards
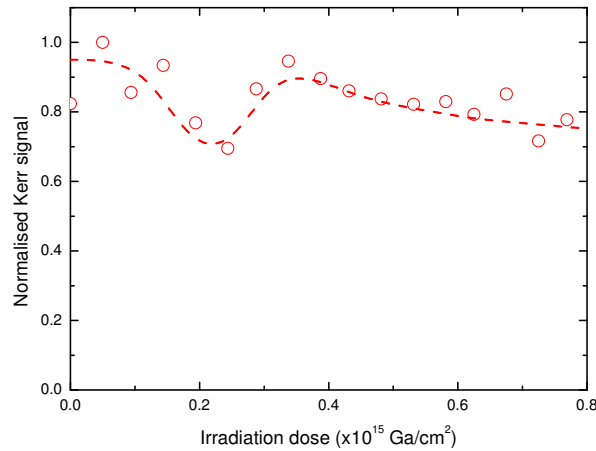

Figure 7.4: Variation of the normalised Kerr signal with irradiation dose measured using the MOKE magnetometer for 20 nm NiFe thick elliptical structures with a 2.5 nm Cu cap. The line is a guide to the eye.

the interface between the layers as the origin of this magnetic behaviour. Although this effect has been demonstrated with both Cu and Au capping layers, further investigation was continued with the Au capped samples to investigate the origins of this behaviour.

7.2.4 A direct measure of the magnetic moment from SQUID measurements

The MOKE results rely on magneto-optical interactions as the origin of the magnetic sensitivity. To a first order approximation these interactions depend linearly on the change in the ellipticity of polarisation of incident laser light upon reflection from a magnetised material. However, it may be possible that the Ga^+ irradiation was having an effect on the more complex magneto-optical properties of the sample and therefore this approximation might be less valid. A change in surface roughness of the samples may also have an effect on the reflected intensity which may also add complications to the results.

Therefore, to eliminate these potential issues, another measure of the change in the magnetisation resulting from Ga^+ irradiation was obtained using SQUID measurements performed on samples with selected irradiation doses covering the complex low dose regime. The sensitivity of the SQUID meant that these measurements required larger samples (1.3 mm $\times$ 5.5 mm) to be prepared with 20 nm NiFe / 2.5 nm Au as discussed in chapter 5.

Three example hysteresis loops from the SQUID measurements are shown in figure 7.5 for irradiation doses of 0.00×10^{15} Ga^+/cm^2 , 0.31×10^{15} Ga^+/cm^2 and 0.78×10^{15} Ga^+/cm^2. As well as the decrease in saturation magnetisation, these loops show variations in the loop
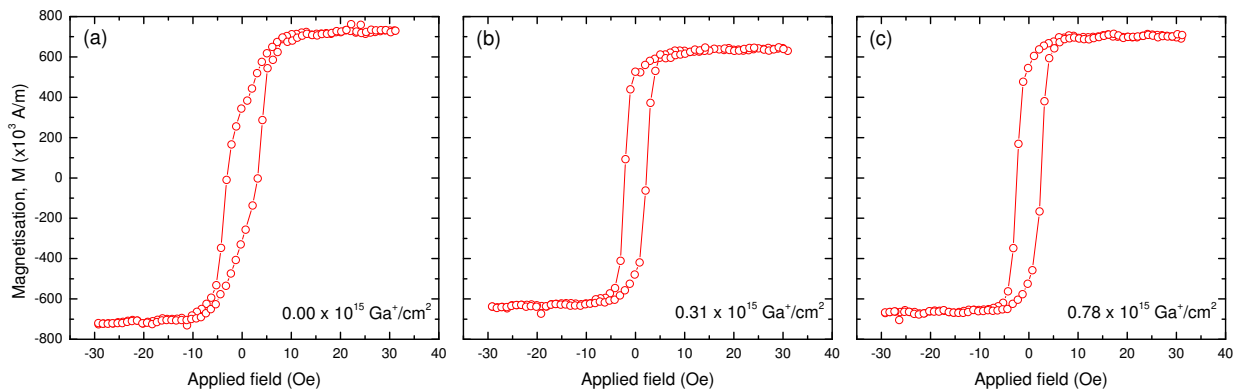

Figure 7.5: Variation of M_S with dose for the 1.3 $\times$ 5.5 mm, 20 nm NiFe / 2.5 nm Au samples measured by SQUID magnetometry. Example hysteresis loops are shown for doses of a) 0.00×10^{15} Ga^+/cm^2, b) 0.31×10^{15} Ga^+/cm^2 and c) 0.78×10^{15} Ga^+/cm^2.

shape that were not found with the elliptical structures in the MOKE measurements.

For the unirradiated sample, a more gradual reversal with reduced remanence was observed compared to the irradiated loops which show more square shaped behaviour with a rapid reversal. This may be an artefact from alignment of the sample during the SQUID measurements. The rectangular samples used here were placed with the long axis along the SQUID sensitivity direction; however, any movement of the sample could result in measurements being performed with the field applied off-axis from the easy axis of the sample. This loop shape is typical of the magnetisation response along an axis not aligned with an easy axis.[253]

Another noticeable difference between the MOKE hysteresis loops in figure 7.1 and the SQUID hysteresis loops in figure 7.5 is the value of the coercivity. The much greater value measured in the MOKE system can be explained as the MOKE is measuring microscale elliptical structures compared to larger quasi thin film structures in the SQUID measurements. In microscale structures the reversal field is dominated by energy considerations of the sample geometry, but in larger geometries there is a greater distribution of defects and roughness within the sample creating localised disturbances in the magnetostatic energy landscape. This can lead to the nucleation of a reverse domain and hence magnetic reversal with a reduced magnetic field.[114]

The saturation magnetisation of these samples was extracted from the SQUID hysteresis loops and is shown as a function of dose in figure 7.6. This figure shows a dip in saturation magnetisation confirming that this complex behaviour originates from the magnetisation of
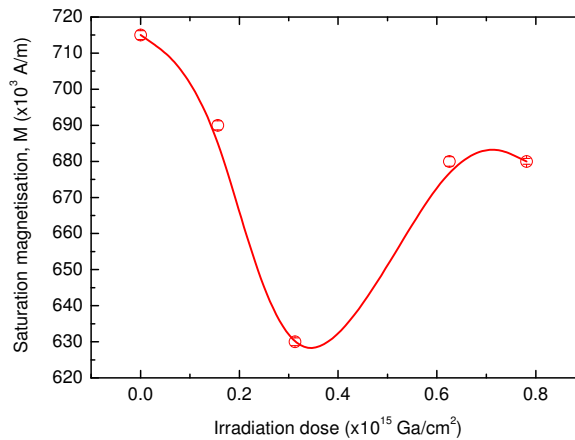

Figure 7.6: Variation of M_S with dose for the 1.3×5.5 mm samples with a 20 nm NiFe / 2.5 nm Au bilayer structure measured using SQUID magnetometry. The line is a guide to the eye.

the samples and not from any magneto-optical, surface reflectivity or sample alignment issues that may also have an influence on the MOKE measurements.

The minimum in the saturation magnetisation of these samples occurs at a similar dose of $\approx 0.35 \times 10^{15}$ Ga$^+$/cm^2, slightly lower than in figure 7.3(a) which may be attributed to a thinner Au capping layer giving less attenuation of the Ga$^+$ beam. The 12% change in the magnetic signal measured here is less that that measured for the 10 nm and 15 nm films as expected for a thicker 20 nm NiFe layer. However, this value is lower than the 22% decrease expected from the ratio of the layer thicknesses. Even though the MOKE skin depth may probe the entire magnetic thickness, there is enhanced sensitivity towards the surface which will result in a greater difference in the magnetic signal. However, the SQIUD system is equally sensitive to the entire sample thickness with no enhanced sensitivity at the sample surface. Alternatively, the minimum in figure 7.6 may not represent the greatest change in moment. A slight variation in dose may give rise to a greater moment change leading to a better agreement with the layer thickness model.

As well as confirming the magnetic origin of these changes, the SQUID gives a true measure of the magnetisation compared to the relative measurements from MOKE results. Figures 7.5 and 7.6 show the magnetisation with units of A/m. These were obtained from the SQUID measurements of the magnetic moment and divided by the volume of the magnetic material in each sample.

7.2.5 Structural influence on the interfacial magnetism

The results from high dose irradiation and the irradiation of uncapped samples agree with existing observations where heavy ion irradiation leads to amorphisation of the crystalline structure of a material at the near surface region. This damage leads to the development of a magnetically dead surface region due to a transition from ferromagnetic to paramagnetic states, in agreement with the conclusions on structure from the results in chapter 6. However, at lower doses, these damaging effects are significantly reduced and only subtle modifications to the samples occur due to the other physical mechanisms introduced in chapter 3.

The direct implantation of Ga can lead to the introduction of point defects, and eventually alloying in the sample for higher doses. In Fe-Ga alloys, a decrease in moment of 0.014 $\mu_B/at.$ per % Ga is found from the initial 2.218 μ_B per atom in Fe.[254] Similar behaviour was also found for Ni-Ga alloys with a change of 0.03 $\mu_B/at.$ per % Ga.[160] The change in moment

due to the $\approx 0.7\%$ Ga$^+$ fraction predicted from TRIDYN simulations for these low doses is therefore very small. This change unlikely to be a significant factor for magnetisation changes observed here.

The magnetic material in the samples was also enclosed by an Au cap and it is expected that this remains covering the sample in the low dose irradiation regime.[245] Therefore, the volume of ferromagnetic material does not vary sufficiently to account for the changes in magnetisation observed here. Furthermore, if there were a loss of magnetic material by sputtering this would only account for a dose dependent reduction in moment and would not explain the subsequent increase in magnetisation with further increasing dose. Dose dependent differential sputter rates for Ni and Fe have been suggested to explain changes in NiFe composition but these are significant only at higher doses.[41] The effects of sputtering on the magnetic properties are likely to be more significant for the sample with no Au cap where magnetic material resides at the surface. However, the dose dependent magnetisation changes observed here only occur with the presence of a capping layer. This indicates that the changes are not a direct result of ion induced damage from energy transfer, sputtering of material or Ga$^+$ implantation; as these processes takes place regardless of the presence of a capping layer.

Along with surface sputtering and ion implantation, introduced in chapter 3, ion beam induced interfacial intermixing is another physical effect resulting from high energy ion beam irradiation. It is therefore suggested here that the complex magnetisation behaviour results from subtle structural changes occurring at the NiFe/Au interface, resulting from the transfer of momentum to the atoms at the interface by ion irradiation.[245] The discussion now turns to characterising physical changes occurring at the interface that may result in the observed behaviour that leads to a decrease followed by a recovery in the magnetic moment.

Atoms at an interface which become mixed into their neighbouring layer can be initially described as point defects. Increasing the irradiation dose leads to an increase in intermixing and hence an increased defect density in the neighbouring layer. The physical effect of these defects can lead to a change in stress in the lattice structure that may bring about changes to the magnetic properties through magnetostriction effects.[163,164] Additionally, chemical changes may also take place where regions with high defect density can be described as an alloy at the interface. This can give rise to local modifications to the electronic structure in Au and NiFe when they are in close proximity, leading to a modification of the magnetic

moment in the Ni and Fe or the induction of a magnetic moment on the Au atoms.

Although the interface region is comparatively thin, the modified magnetic properties may be exchange coupled to regions of magnetic material further from the interface which then also experience a modification of their properties associated with the changes in the neighbouring region.[255]

7.3 Magnetic moments modified by local environment at the interface

The MOKE and SQUID results have shown complex magnetic behaviour for low dose Ga^+ irradiation on NiFe/Au bilayer structures. This behaviour is attributed to intermixing taking place at the interface between the two layers. It is suggested that this leads to changes in the electronic environment of the respective atomic species which in turn affect their magnetic moment.

Previous studies have shown that for $3d$ ferromagnets, a change in the local environment can lead to a decrease in Ni moment when it forms alloys or multilayers with Ni/Pt,[256,257] Ni-metalloid,[43] NiFe/Pt[258] or NiFeTa.[259] This is due to the corresponding increase in number of non-magnetic nearest neighbours around Ni and has been explained by the formation of non-polarisable p-d hybrid bonds from polarisable $3d$ transition metal states.[43] In Fe the moment behaviour is more complex showing an increasing Fe moment in fcc FeAu,[42] bcc Fe(Sn, Sb, Ga, As,Ge)[43] and NiFe/Pt[258] that is attributed to a volume expansion of the unit cell with the addition of larger atoms.[43,260] This analysis also fits with the lattice contraction found from the addition of smaller adatoms in bcc FeB[261] and Fe(V/Cr)[262,263] leading to a decrease in Fe moment. Theoretical predictions show that these volume effects lead to narrowing of the Fe $3d$ band in FeAu resulting in an increase in Fe exchange and hence the increased moment.[264] Analysis of the various phases of Ni and Fe have shown that discontinuous changes in magnetic moment can result from volume expansion in these alloys.[264]

To further investigate the changes in the magnetic moment and identify any modifications to the relative contributions from the Ni and Fe, XMCD measurements have been performed. These measurements give an element specific probe into the sample magnetisation that is also sensitive to the orbital and spin angular momentum contributions to the magnetic moment.

7.3.1 Moment contributions from Ni and Fe

XMCD measurements were performed at the Ni and Fe $L_{3,2}$ edges for selected low dose irradiation conditions on the NiFe/Au bilayer structures. For each sample, the different spectra for each combination of x-ray helicities and applied magnetic fields were combined to give difference spectra that were integrated over the $L_{3,2}$ edges to give the curves shown in figure 7.7.

A selection of different irradiation doses are shown for both Ni and Fe where an initial large drop corresponds to the negative area difference between the two L_3 absorption peaks shown in figure 4.11(a). This is followed by a partial recovery corresponding to a positive difference between the areas of the two L_2 absorption peaks. These two transitions separate three plateau regions where no dichoric effects occur between absorption edges.

Each of these integrated difference spectra holds information about the spin and orbital contribution to the moments of each element. The area difference at the L_3 edge is determined by a combination of the spin and the orbital moments whilst the L_2 edge represents only the spin contribution.

For the low dose irradiation at 0.52×10^{15} Ga$^+$/cm^2 the Fe spectra shows a decrease at the L_3 edge which is almost equal to the recovery at the L_2 edge. A similar effect is seen at 0.72×10^{15} Ga$^+$/cm^2 for the Ni spectra. These results contrast with the behaviour observed for other doses showing a recovery of approximately half the size of the initial decrease. At these low doses the shape of the integrated spectra is indicative of quenching of the orbital momentum contribution to the total magnetic moment.
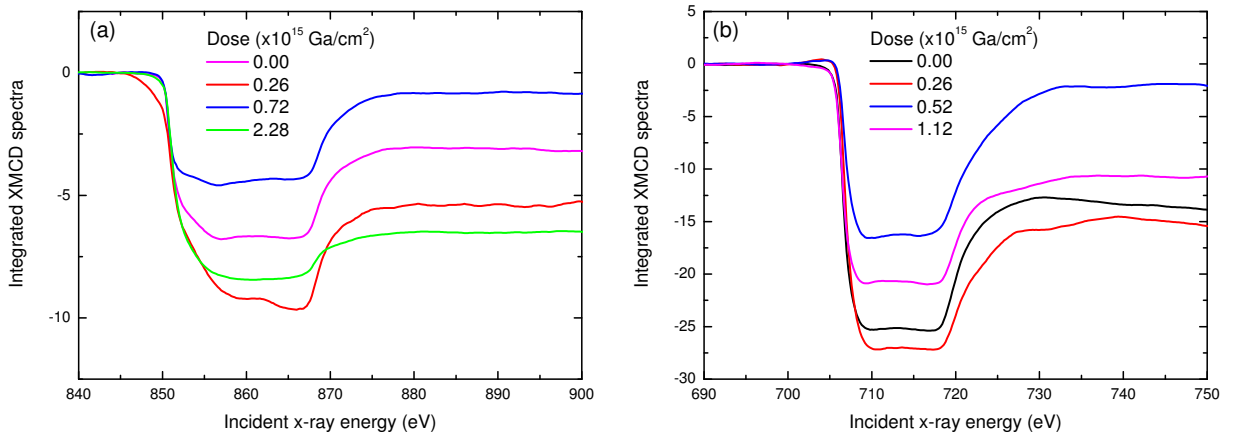

Figure 7.7: Integrated XMCD difference spectra at the $L_{3,2}$ edges in a) Ni and b) Fe, shown for a selection of Ga$^+$ ion irradiation doses.

More in-depth analysis of the relative contributions to the moment was achieved by applying the sum rules[197] to each of these integrated curves. The ratio of the orbital to spin moment extracted from this analysis is shown in figure 7.8 as a function of the irradiation dose for both Ni and Fe atoms in the sample.

This figure gives an approximate ratio for the orbital to spin contributions to the magnetic moment with a value of ≈ 0.2. As suggested by the simple analysis of the integrated spectra these graphs also show a decrease in this ratio for doses around 0.5×10^{15} $\mathrm{Ga^+/cm^2}$ indicating the occurrence of orbital quenching in these samples. However, due to the uncertainties on these derived quantities in figure 7.8 it is hard to draw any conclusions about any differences in behaviour between Ni and Fe.

The points on these graphs represent the different values obtained for the ratio after repeated analysis with multiple pairs of absorption spectra obtained with either opposite helicity or opposite magnetic field. The errors on these points represent the standard error between the different estimates of the ratio and are most likely to originate from variations in the polarisation of the x-ray beam occurring due to the movement of insertion devices around the synchrotron ring. This also appears to have a more significant impact on the results obtained at the Ni energies.

The enhanced orbital quenching suggests that the crystal field becomes more significant over the spin-orbit interaction in this low dose regime. This leads to a change in the energetics where the ground state becomes one in which the orbital angular momentum contribution to the magnetic moment is minimised. This has the effect of reducing the total moment, which
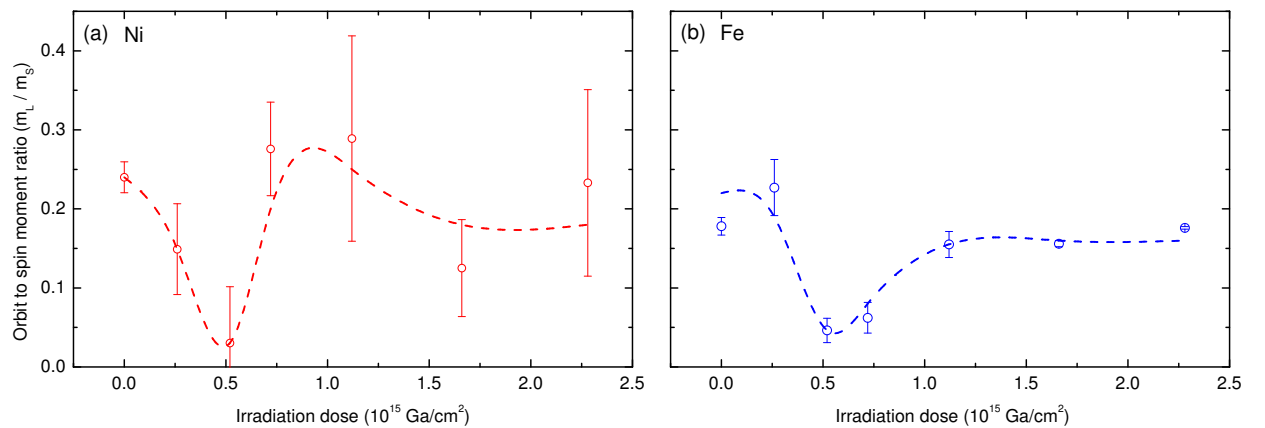

Figure 7.8: Orbit to spin ratio of the contribution to the magnetic moment for a) Ni and b) Fe atoms as a function of $\mathrm{Ga^+}$ ion irradiation in a NiFe/Au bilayer sample. The lines are a guide to the eye.

is consistent with a decrease in the total magnetic moment observed with both the MOKE and SQUID analysis. This is also consistent with the decrease in Ni and Fe moment found in previous studies, due to polarisation effects from the proximity of non-ferromagnetic atoms.

The XMCD technique was also used to give element specific magnetisation behaviour as a function of magnetic field and is shown by the hysteresis loops in figure 7.9 for Ni. The low coercivity measured in these samples agrees with the results obtained from the SQUID measurements on similar quasi thin film samples. Another effect that may contribute to the difference in the coercivity observed with these samples could be due to the different substrates on which the samples are grown.[128] An electron transparent SiN substrate was required for the XMCD measurements, however, additional measurements find no significant effect of the substrate on the magnetic properties measured here.

7.3.2   Magnetoresistance behaviour: a proxy for the spin-orbit interaction

Changes in the strength of the spin-orbit interaction can be investigated through measurements of the electrical resistance of the sample. The difference in resistance for current flowing perpendicular and parallel to an applied magnetic field is strongly linked to the spin-orbit interaction in an effect known as the *anisotropic magnetoresistance* (AMR) of a material. As this additional measurement adds value to this discussion, but does not form a substantial part of the understanding of this thesis, a detailed discussion of the theory associated with this technique has not been included but a can be found elsewhere.[265]

AMR measurements were performed in a four point geometry with a current of 1 mA
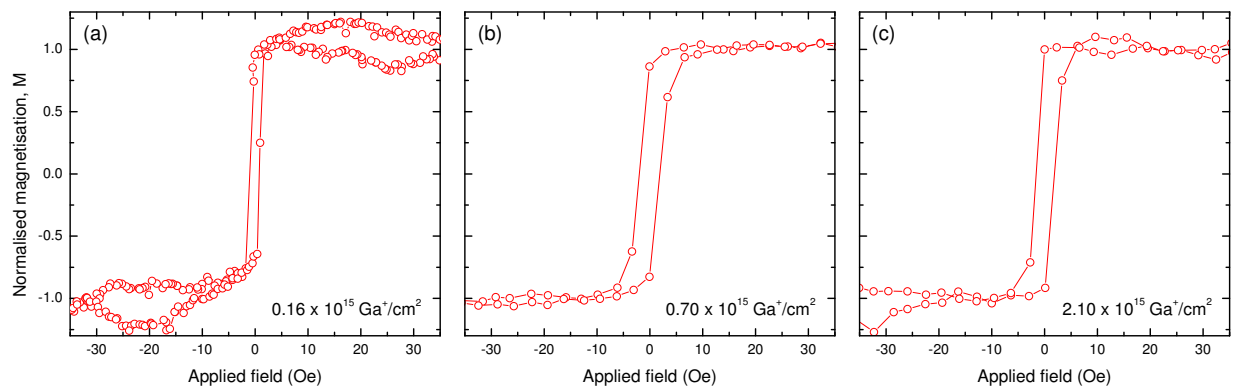

Figure 7.9: Ni XMCD hysteresis loops from 1.2×1.6 mm NiFe/Au samples irradiated with dose of a) 0.16×10^{15} Ga$^+$/cm^2 , b) 0.70×10^{15} Ga$^+$/cm^2 and c) 2.10×10^{15} Ga$^+$/cm^2.

applied along the long axis of 1.3×5.5 mm samples. This axis was aligned both parallel and perpendicular to a saturating magnetic field and the resistance in each orientation, $R_{\parallel}$ and $R_{\perp}$ respectively, was used to determine the anisotropic magnetoresistance ratio. This was found from: $\mathrm{AMR} = \Delta R / R_{av}$, where ΔR is the difference in resistance between the parallel and perpendicular geometries and R_{av} is the baseline resistance of the sample, given by $R_{av} = \frac{1}{3}R_{\parallel} + \frac{2}{3}R_{\perp}$.

The AMR ratio for these samples, along with the variation of the baseline resistance is shown in figure 7.10 as a function of Ga^+ irradiation dose. Here, a linear increase in the baseline resistance (figure 7.10(b)) was observed, while more significantly the corresponding AMR response (figure 7.10(a)) shows a peak which rises to a maximum at a dose of 0.47×10^{15} $\mathrm{Ga}^+/\mathrm{cm}^2$.

The linear increase in the resistance is about 8% and may again be attributed to a linear increase in defect density and development of the alloy region within the film. This leads to more scattering of the conduction electrons and hence a higher resistance.[62] A further contribution could also arise from any sputtered thinning of the Au cap. This acts as a shunt for some of the current and if thinned, a larger proportion of the current would then flow through the more resistive NiFe layer resulting in the observed increase in total resistance.

The AMR ratio shows a complex response in the same low dose regime associated with the changes observed in the magnetic moment of this sample. The peak in the AMR ratio suggests a complex change in the spin-orbit interaction in the low dose regime. These results tie in
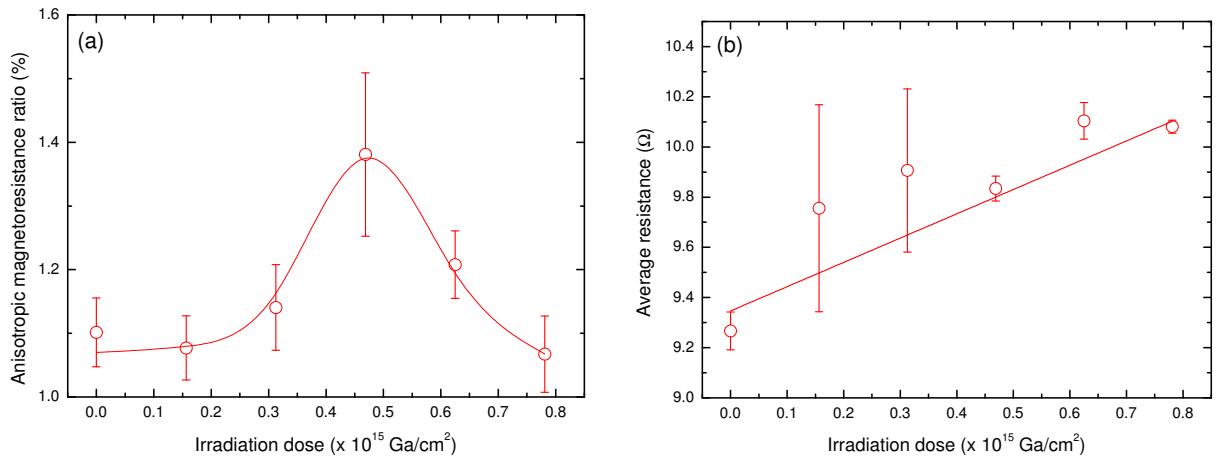

Figure 7.10: a) Anisotropic magnetoresistance ratio and b) baseline resistance measurements for a 20 nm NiFe / 2.5 nm Au bilayer sample as a function of Ga^+ irradiation dose. The dashed line is a guide to the eye and the solid line is a linear fit to the data.

with other experimental results which demonstrate an increase in magnetoresistance from the interface effects in NiFe/Au.[266] This was explained by the strong spin-orbit coupling of Au leading to an enhanced spin-dependent scattering for the electrons in NiFe. Theoretical work also demonstrates an increased spin-orbit coupling on Fe atoms as a result of the proximity with non-ferromagnetic $5d$ atoms with high spin-orbit coupling such as Pt.[267] This transfer of spin-orbit coupling shows a dependence on the proximity between the atoms, with a decreasing effect with distance away from an interface in a multilayered sample.

7.3.3   Induced moment on interfacial Au atoms

The previous discussion has shown that both the magnetic moment on Ni and Fe as well as the spin-orbit interaction are affected by changes in the local environment at the interface resulting from the intermixing. In addition to the Ni and Fe, the Au atoms may also give rise to a contribution to the magnetic response of these samples. This section presents element specific results for Au that suggest the appearance of a magnetic moment on the Au atoms.

Atomic Au is non-magnetic as it has completely filled $5d$ states; however, hybridisation in its metallic form can lead to the generation of a few $5d$ holes. When in proximity with $3d$ ferromagnets this leads to exchange spin polarisation giving rise to an induced magnetic moment.[53,55,268] This feature is common amongst other $4d$; Ag,[269] and 5d; W,[56,255] Ir[56] and Pt[257,258,270] atoms in layers interfaced to a $3d$ layer.

The induced moment on Au in a bcc AuFe alloy increases with the number of Fe nearest neighbours, becoming a maximum with Au as an impurity, totally surrounded by Fe.[42] This moment also decreases with distance away from an interface in a layered material.[55,255]

The possibility of an induced magnetic moment on the Au in these samples was investigated here through the use of a resonant scattering x-ray technique. This provides element specific sensitivity to the Au atoms and employs the dichoric absorption to give sensitivity to the magnetisation of these atoms. In addition to this, the experiment was performed as a function of grazing incidence x-ray beam angle to investigate the depth dependence to any magnetic signal that may be originating from the Au in these bilayer samples.

X-ray reflectivity scans of irradiated NiFe/Au bilayer samples were performed with circularly polarised x-rays whilst flipping the applied magnetic field at the sample. From this, an average value of the reflectivity was found for both positive and negative fields at each angle in the reflectivity scan. Figure 7.11 shows the results of these scans on two different samples
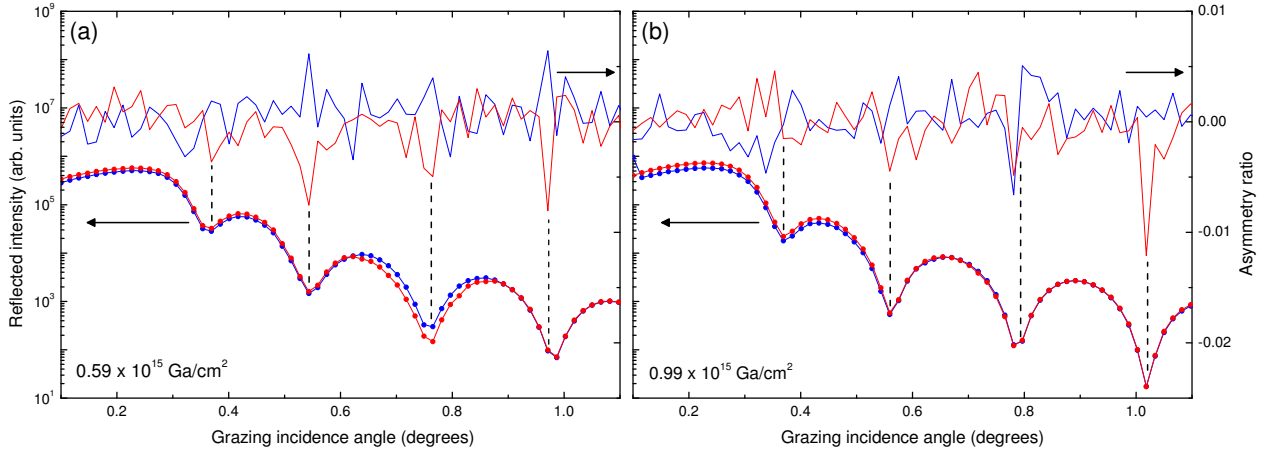
Figure 7.11: The sum, $(I^+ + I^-)$, and asymmetry ratio, $(I^+ - I^-)/(I^+ + I^-)$, between the reflectivity in opposite magnetic fields as a function of grazing incidence x-ray angle. This is repeated for both x-ray helicities at the Au L_3 edge (11.919 keV[235]) and with two samples irradiated with a dose of a) 0.59×10^{15} Ga$^+$/cm^2 and b) 0.99×10^{15} Ga$^+$/cm^2.

with irradiation doses of 0.59×10^{15} Ga$^+$/cm^2 and 0.99×10^{15} Ga$^+$/cm^2. The reflectivity curves come from the sum of the reflected intensities at each field, $(I^+ + I^-)$, whilst the asymmetry ratio, $(I^+ - I^-)/(I^+ + I^-)$, shows the spectral difference normalised to the sum of the reflected intensities at each field. The two colours on the graph represent repeat analysis of the sample with opposite x-ray helicity.

The sum of the reflected intensities contains only the structural information from the sample and shows typical grazing incidence x-ray reflectivity with an α_i^{-4} decrease in the intensity superimposed with Kiessig fringes resulting from interference effects.

The asymmetry ratio represents the scattering when the structural effects have been removed so only magnetic contributions to the scattering remain. Here the signal shows only small variations from zero at a similar level to the noise. However, when analysed alongside the reflectivity curve, significant peaks can be identified, corresponding in angle to the Kiessig minima. These peaks occur in opposite directions when repeated with the opposite x-ray helicity, suggesting the presence of a small dichoric signal originating from the Au magnetic moment in these samples.

Kiessig minima represent the angles where destructive interference occurs between x-rays reflected from the interfaces. This correlation in angle between the asymmetry ratio and the structural reflectivity suggests that there may be a small magnetic signal associated with the interfaces in these samples. Similar results in other samples also show peaks in the asymmetry ratio which are found at Kiessig minima relating to the interfaces.[195]

Further investigation was performed where the samples were positioned at the specular condition that gave the largest asymmetry ratio in the reflectivity scans. This occurred at $\theta = 0.75°$, $2\theta = 1.5°$ for the 0.59×10^{15} Ga$^+$/cm^2 sample and $\theta = 0.81°$, $2\theta = 1.62°$ for the 0.99×10^{15} Ga$^+$/cm^2 sample. The size of the asymmetry ratio was then investigated where the difference in reflectivity due to flipping helicity was investigated as a function of the applied magnetic fields; these results are shown in figure 7.12(a).

The position of the boxes represent the average asymmetry ratio and the height represents the standard error in the measurements. This figure shows that a difference in the asymmetry ratio is discernible between positive and negative fields for both samples investigated, indicating a change in the dichoric signal from Au as a function of applied magnetic field. This suggests a change in magnetisation state of the Au between positive and negative applied fields, further indicating the existence of a small induced magnetic moment. Differences in this magnetic response between the doses 0.59×10^{15} Ga$^+$/cm^2 and 0.99×10^{15} Ga$^+$/cm^2 shown in figures 7.11 and 7.12(a) are apparent but are small in comparison to the errors.

The changes in the asymmetry ratio have also been investigated as a function of the incidence x-ray energy over the Au L edge. The results shown in figure 7.12(b) show the asymmetry ratio, centred around zero, which includes a peak at the Au L edge. This is opposite in sign for the two opposite helicities and confirms that these effects originate from the Au in the sample.
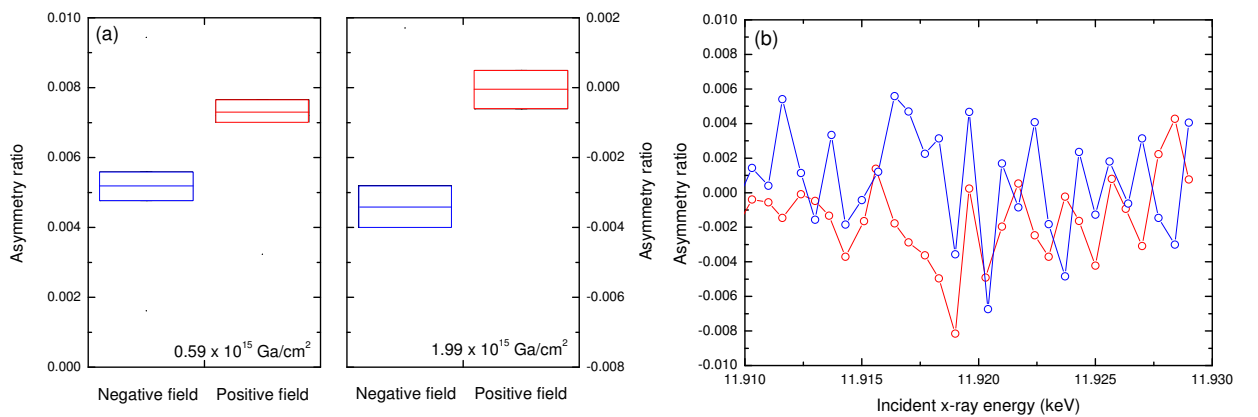
Figure 7.12: a) Asymmetry ratio in the reflection for lcp and rcp circularly polarised x-rays from irradiated samples in both positive and negative magnetic fields. The position of the boxes represent the average asymmetry ratio with a standard error represented by their height. b) Asymmetry ratio in the reflected intensity from a 0.59×10^{15} Ga$^+$/cm^2 irradiated sample measured as a function of incident x-ray energy. These measurements were performed at a Keissig minima: $\theta = 0.75°$ for the 0.59×10^{15} Ga$^+$/cm^2 sample and $\theta = 0.81°$ for the 0.99×10^{15} Ga$^+$/cm^2 sample.

The combination of these results suggest the presence of a very small magnetic dichoric effect associated with the Au atoms in these samples. This effect is very small and hard to measure but shows qualitatively that this effect occurs, although no further quantitative analysis can be performed on this data.

In summary, the analysis of the magnetic moments at the interfaces has shown that intermixing at the interfaces results in a change in local environment of the Ni, Fe and Au atoms. This leads to a reduction in Ni and Fe moment due to polarisation effects whilst a finite moment is induced on Au due to polarisation effects. XMCD analysis has shown that this reduction in moment results from the enhancement in orbital quenching in this low dose regime. This is closely linked with the spin-orbit coupling which also shows complex changes in the low dose regime in the magnetoresistance results and has been associated with the transfer of the large spin-orbit coupling of Au onto the Fe and Ni atoms.

7.4 Origins of the complex magnetic behaviour

The experiments performed in this chapter have uncovered various different contributions to the magnetism of these samples which all display the complex changes in behaviour for low dose Ga^+ ion irradiation. These have all been explained by modifications to the local environment at the interface but so far no explanation for the change in direction of this behaviour has been identified. This section discusses the possible explanations for how the complex changes occur in the low dose irradiation regime.

A complex effect like this may be expected to result from either an effect that follows a complex varying cause, or result from a combination of multiple physical processes, each varying consistently, but when combined, giving rise to complex behaviour. Structural results in chapter 6 show a steady increase to the interface width with irradiation dose. This does not reveal any complex changes in the low dose regime and implies the latter case where the behaviour is due to a combination of effects leading to a more complex overall behaviour.

7.4.1 Effect of interfacial stress on the magnetism

During the sample fabrication, the deposition of the layers produced a relatively sharp initial interface separating the Au and NiFe layers. Since these layers have different lattice parameters, a lattice mismatch will generate stress at the interface. In the initial stages of

irradiation a broadening of the interface width allows the stress to be more evenly distributed over the wider interface width. Other investigations have previously applied this to explain the improvement in crystallinity upon the initial irradiation of other samples.[253,271,272] This process takes place during the initial stages of irradiation and is counteracted later by the increase in lattice stress due to the intermixing of larger Au atoms into the NiFe layer. This stress can lead to an expansion of the NiFe unit cell, resulting in an increased moment on Au[273] similar to the increased moment on Fe seen for a volume expansion of the unit cell with the addition of larger atoms.[42,43,43,258,260]

Other works suggested an alternative possibility where the initial interfacial roughness from the deposition process can be smoothed out during the initial stages of irradiation. This is explained as an effective annealing based on the initial ion beam energy transferred to the sample.[40,165] The positive heats of mixing of Au in Ni and Fe show that the separation of NiFe and Au layers in an effective annealing process can be expected.[148,149] Further increase in dose follows the same idea that intermixing of larger Au atoms leads to an increase in stress.

Here the structural results agree with the first case, where a gradual increase in interface width takes place over the entire dose range. However, for the second case, the structural results do not report an initial interface smoothing with the onset of irradiation. Even though this has not been identified from the x-ray reflectivity studies, the sensitivity of this technique may be insufficient to exclude this possibility.

7.4.2 Interfacial composition effect on magnetism

More in-depth analysis of the interfaces considers the element specific nature of each layer and the atomic relocation over the interface that occurs during intermixing. Following an initial low dose of irradiation, the NiFe layer contains a low concentration of Au atoms. These atoms have a large number of ferromagnetic nearest neighbours and therefore gain a large induced magnetic moment.[42] With increasing dose the density of Au on the NiFe side of the interface increases, giving a greater contribution to the total magnetic moment as more Au atoms contribute. However, as the Au density increases, the number of ferromagnetic neighbours decreases, leading to a reduction in the induced Au moment per atom in a competing effect. A decrease in the polarisation also occurs due to the increased separation of the nearest neighbours.[55,255]

A further effect must also be taken into consideration as the induced moment on Au due to the polarisation occurs at the expense of a reduced moment on the Ni and Fe atoms. A similar situation is described with competing contributions to the magnetic moment at NiFe/Pt interfaces that give rise to complex overall behaviour.[258] Here, polarisation effects lead to an induced moment on Pt at the expense of the moment on the Ni and Fe, whilst the Fe also displays an increasing moment due to the volume expansion of the unit cell.

Further complications may also arise due to the preferential rearrangement of Ni and Fe atoms at the near interface region which was suggested from the x-ray fluorescence results presented in chapter 6. With the increase in irradiation there is a small preference for Fe to move into the Au layer leading to a variation in the composition of NiFe at the near interface region. These local changes in composition could move away from the condition for vanishing magnetocrystalline and magnetostriction properties for $Ni_{81}Fe_{19}$. This would lead to an effect on the magnetic anisotropy which is easily affected by fluctuations in the composition or from defects.[253] Significant changes in local composition could also lead to partial ordering of the magnetic material. The ordered state of NiFe occurs at $NiFe_3$ which shows degraded magnetic properties.[62] Therefore a transition into the ordered state or transitions between other phases could result in discontinuous changes in magnetic moment.

7.5   Summary

This chapter presents the results of an experimental study into the effects of ion beam irradiation on the magnetic properties of NiFe/Au bilayer structures. The changes in the magnetic properties are the result of the structural changes taking place at the interface between the layers that were described fully in chapter 6.

Initially, the magnetic behaviour with high dose irradiation was investigated and confirmed the effects reported in the literature whilst also identifying the dose range of interest for this investigation. At these high doses: sputtering of material, damage to the crystal structure and significant amounts of ion implantation lead to a degradation in the magnetic properties. Beyond a certain quenching dose the material undergoes a ferromagnetic to paramagnetic transition. This behaviour is coupled with an increase in the coercivity of thin-films due to an increasing density of domain wall pinning defects throughout the film as a function of dose.

For low dose ion irradiation more complex behaviour was observed with both MOKE and SQUID techniques. An initial decrease in the magnetisation of the samples was followed by a recovery. This effect is much more significant than the gradual decrease in the magnetic signal resulting from the damaging effects of the higher dose irradiation. In this low dose regime the irradiation induced damage from sputtering and ion implantation are greatly reduced and are not considered to be responsible for the complex low dose effects. Instead intermixing at the interface provides the most appropriate explanation for the origin of these changes.

Contributions to the magnetic moment investigated through XMCD measurements reveal complex changes in the orbital to spin moment ratio for both Ni and Fe. This is interpreted as orbital quenching which results from the significance of the crystal field increasing with respect to the spin-orbit coupling in the material. This effect may also explain the loss in the total moment of the samples. Further investigation into the spin-orbit interaction through magnetoresistance measurements also revealed complex behaviour, showing a peak in the low dose irradiation regime. This indicates that the spin-orbit interaction is also strongly linked with the changes in environment from intermixing at the interface.

Additionally a small induced moment was detected on the Au atoms. Analysis alongside the structural component of these results suggests the Au moment originates from the interface of the material. This agrees with the understanding that the NiFe/Au interface is the origin of this complex magnetic behaviour.

Further analysis of the magnetisation response to magnetic field gave hysteresis loops from the various techniques. These mainly showed the effect on the coercivity of the various different sample sizes used for each technique, revealing a lower coercivity for the larger samples.

This chapter has shown that complex changes in the magnetic behaviour of these samples results from intermixing at the NiFe/Au interface, where a change in moment on all of the atoms involved as well as a change in spin-orbit interaction have been identified. These complex changes are associated with multiple factors due to polarisation affects as well as variations in the stress present at the interface. Although a complete description of behaviour of the magnetic properties could not be characterised, it is expected that the complex interplay between these competing effects are likely to be the source of the complex magnetic behaviour that has been revealed.

Chapter 8

Local irradiation control of domain wall behaviour in nanowires

8.1 Introduction

In this chapter the effect Ga^+ irradiation on the magnetic properties and domain wall behaviour in NiFe/Au nanowires was investigated. This builds on the understanding of the ion beam modifications to magnetic bilayer materials described in the previous chapter along with the nanofabrication techniques discussed in chapter 3. The use of a focussed ion beam system gives the capability to perform localised modifications to a magnetic material on a nanoscale length scale comparable with the dimensions of domain walls in nanowires. Although there is a well established understanding of the magnetic properties of domain walls in permalloy nanowires, the use of Ga^+ ion irradiation for their control via the modification of magnetic properties has not been exploited as an significant patterning technique.

First, magnetic nanowires were fabricated and their magnetic behaviour was investigated. The magnetisation behaviour was dominated by a strong shape anisotropy along the wire axis and magnetisation reversal takes place by the nucleation and propagation of a domain wall which can be controlled via the inclusion of a domain wall injection pad at one end of the structure. Following localised irradiation the properties of these nanowire structures were modified and the effects of focussed Ga^+ irradiation on domain wall behaviour were investigated. In particular, the effect of the irradiation dose and the dimensions of the irradiated area upon the domain wall behaviour were of significant interest.

The domain wall behaviour in nanowire structures was also investigated through micro-

183

magnetic simulations where the irradiated region was represented by a region with a reduced M_S. These simulations show some agreement with the trends seen in the experimental results and give some insight into the domain wall pinning processes taking place. Extending these simulations reveals that pinning is also affected by the relationship between the domain wall structure and the geometry of the boundary between regions of different magnetic properties along the nanowire.

Finally, the pinning of propagating and stationary domain walls at a material property boundary was compared using micromagnetic simulations. This provided an understanding of the different pinning strengths for the more complex features observed in the experimental measurements of the nanowires.

8.2 Magnetisation reversal in nanowires

Figure 8.1 shows scanning electron microscope images of some example nanowires of different widths fabricated by electron beam lithography, thermal evaporation, and lift-off techniques. In this case the nanowires are 20 μm long with a 10 nm NiFe / 2.5 nm Au bilayer structure and are grouped in arrays of identical nanowires with a pitch of 800 nm.

The magnetisation reversal in these nanowire structures was investigated experimentally through MOKE measurements with field applied along the nanowire axis. This gave hysteresis loops representing the magnetisation which are shown in figure 8.2 for wires of different widths. These are compared with and without a domain wall nucleation pad at one end of the nanowire.
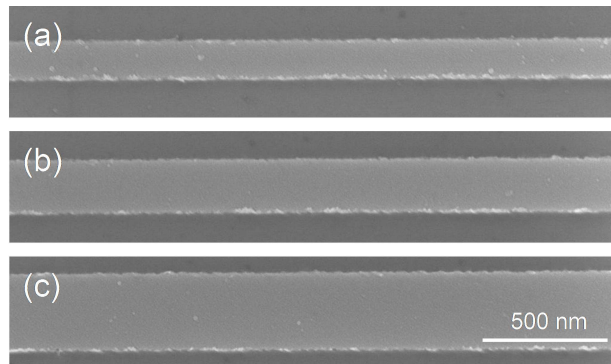

Figure 8.1: Scanning electron microscope images of 20 μm long, 10 nm NiFe / 2.5 nm Au nanowires with widths of a) 150 nm, b) 200 nm and c) 300 nm prepared by electron beam lithography, deposition and lift-off.
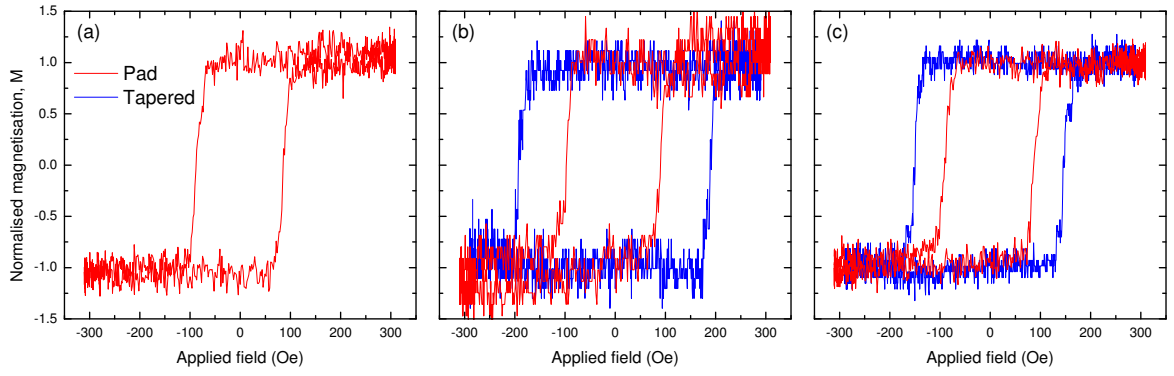
Figure 8.2: MOKE hysteresis loops showing the magnetisation reversal for an array of identical 20 μm long, 10 nm NiFe / 2.5 nm Au nanowires with a pitch of 800 nm which include either two tapered ends; or a nucleation pad at one end and a tapered end at the other. Various different wire widths are shown: a) 180 nm, b) 300 nm and c) 350 nm.

The magnetisation reversal in these structures gives square shaped hysteresis loops where an abrupt change in magnetisation occurs at a certain reversal field. For the wires with two tapered ends the figure showed a strong width dependence where a greater field is required for magnetisation reversal in thinner wires. In contrast, with the inclusion of a nucleation pad, this reversal field was reduced and the behaviour changes to show a slight reduction in reversal field for thinner wires. For the case of the nanowire with two tapered ends, with a width of 180 nm, no hysteresis loop was obtained as the reversal field was beyond the maximum field obtainable from the MOKE system ($\approx$ 300 Oe).

The reversal field from these hysteresis loops is plotted in figure 8.3 as a function of the nanowire width, clearly showing the trends in the reversal field for both datasets. The
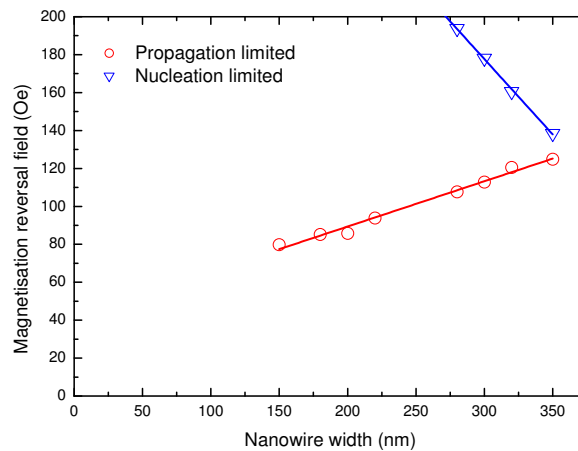

Figure 8.3: Magnetisation reversal field as a function of wire width for 20 μm long, 10 nm NiFe / 2.5 nm Au nanowires with and without a domain wall nucleation pad on one end of the nanowire structures.

wire structures with two tapered ends have a reversal field which is limited by nucleation events. Increasing the wire width leads to a decrease in the reversal field which is due to the increased anisotropy distribution[114] and a reduction in shape anisotropy associated with larger structures. These effects lower the energy of spins aligned off-axis, increasing the field torque and giving rise to a reduction in the energy barrier and field for reversal.

With the inclusion of a 1 μm long, 500 nm wide nucleation pad structure onto one end of the nanowires, the figure shows a reduced reversal field which increases with the wire width. In this case, nucleation occurs in the pad as it is the widest part of the structure. However, the reversal field measured for the wires was limited by the field required for the injection of domain walls into the nanowire structure. Interestingly, this field shows an increase with increasing nanowire width.

8.3 Localised irradiation of NiFe/Au nanowires

Now that the magnetisation reversal behaviour in nanowires has been established, knowledge about the modification of the magnetic properties from chapter 7 and techniques for localised patterning with ion irradiation from chapter 3 are combined. This allows for the control of domain walls to be explored through localised ion irradiation along a nanowire.

In this section, an individual 400 nm wide, 100 μm long nanowire with a 15 nm NiFe / 2.5 nm Au bilayer structure was investigated. This included a 4 μm long, 2 μm wide domain wall nucleation pad at one end and a 4 μm long tapered end at the other. An example structure is shown in figure 8.4 where a locally irradiated region across the nanowire width is shown in figure 8.4(b). The irradiated window was 4 μm long and 500 nm wide and was imaged shortly after irradiation where the effect of the charged surface gives rise to the contrast in the image.

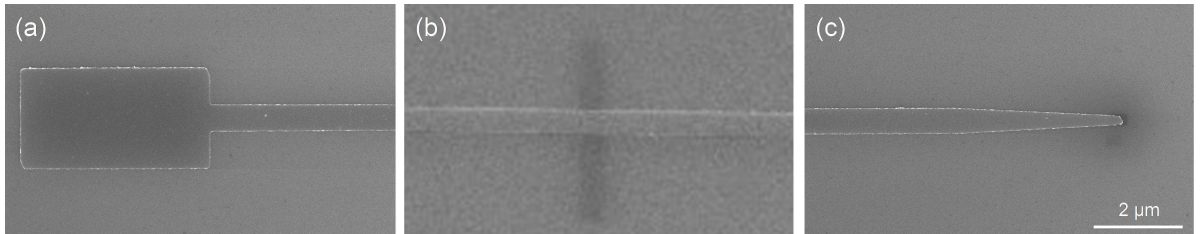**Figure 8.4:** Scanning electron microscope images of an individual 100 μm long, 400 nm wide nanowire including a) a 4 μm long, 2 μm wide domain wall nucleation pad, b) 4 μm high, 500 nm wide irradiated regions and c) a 4 μm long tapered end.

The effect of these irradiated regions upon the domain wall behaviour in the nanowire was characterised with MOKE measurements at different positions along the length of the nanowire. The change in the magnetisation reversal of the wires either side of the irradiated regions provided a useful measure of the interaction between the domain walls and the irradiated regions.

8.3.1 Effect of irradiation dose on domain wall behaviour

The results presented in chapter 7 show that the saturation magnetisation of a magnetic material can be modified through control of the irradiation dose. When performed locally within nanowire structures this localised reduction of M_S may create an artificial domain wall pinning site following from the theory introduced in chapter 2. To investigate the effects of the irradiated regions within a nanowire as a function of irradiation dose, an initial irradiation window was chosen with a width of 2 μm. This was larger than the dimensions of an expected domain wall structure, of the order of 100's nanometres, but still small enough to constrain the domain wall structure in comparison to the footprint of the MOKE laser spot $\approx$ 10 μm.

Examples of the MOKE hysteresis loops are shown in figure 8.5 for three different positions along a nanowire that includes three irradiated regions with increasing dose. Figure 8.5(a) corresponds to the magnetisation behaviour of the wire between the nucleation pad and the first irradiated region with a dose of 1.9×10^{15} Ga$^+$/cm^2. Figure 8.5(b) is measured after this irradiated region and figure 8.5(c) is measured after a second irradiated region with a
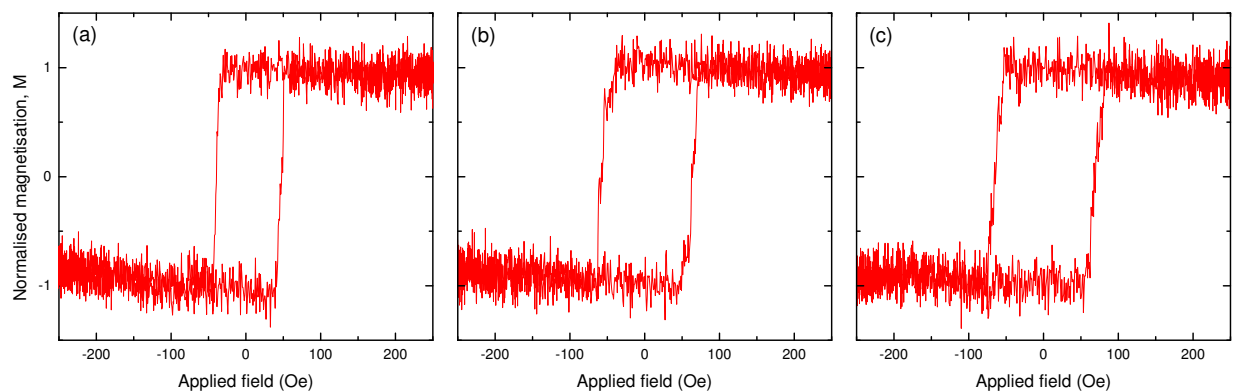
Figure 8.5: MOKE hysteresis loops showing magnetisation reversal in an individual 100 μm long, 400 nm wide, 15 nm NiFe / 2.5 nm Au nanowire. The loops correspond to positions along the nanowire: a) before and after a 2 μm wide region irradiated with a dose of b) 1.9×10^{15} Ga$^+$/cm^2 and c) 3.8×10^{15} Ga$^+$/cm^2. Following the higher dosed regions, the loops show a more gradual reversal at an increased coercivity.

higher dose of 3.8×10^{15} Ga$^+$/cm^2. These figures show an increase in the coercivity and also a gradual change in loop shape from an initially sharp reversal towards a more gradual reversal following regions with increasing dose.

A small distribution in the reversal field between each field cycle can result in the slight change in loop shape due to the averaging in these measurements. The reversal field for comparison between different irradiation conditions was then taken as the field needed to complete the magnetisation reversal for every field cycle.

This field was investigated further, as a function of position along the nanowire as shown in figure 8.6(a). The positions of the irradiated regions were easily identified by a discrete change in the reversal field separating regions along the nanowire which display a constant reversal field. The low reversal field measured in the vicinity of the nucleation pad also show the reduced reversal field associated with the wider structure as discussed above.

The domain wall nucleation pad on these nanowires dictates the domain wall propagation from left to right. In this case, the nucleation of a reverse domain and injection of a domain wall took place at ≈ 45 Oe as shown by the reversal field along the wire before the first irradiated region. Beyond this irradiated region with a dose of 1.9×10^{15} Ga$^+$/cm^2, the reversal field rose to 67 Oe. Therefore a domain wall can propagate with a field of 45 Oe before this region, but the field must increase to 67 Oe for the domain wall to propagate beyond this irradiated region. A further irradiated region with a higher dose of 3.8×10^{15} Ga$^+$/cm^2
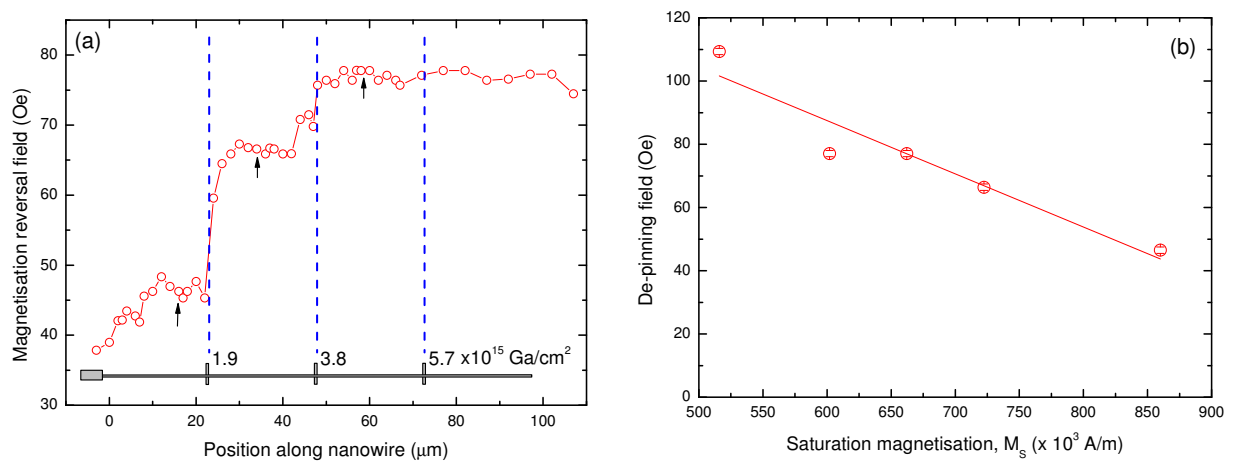
Figure 8.6: a) Variation in reversal field with position along a 100 μm long, 400 nm wide, 15 nm NiFe / 2.5 nm Au nanowire including 2 μm wide irradiated regions with various irradiation doses. The arrows show the measurements corresponding to the hysteresis loops in figure 8.5. b) The reversal field following an irradiated region represents the de-pinning field for a domain wall which increases linearly with a reduction in M_S.

required a further increase in the applied field to propagate the domain wall through this region, but little change in the pinning was observed with a dose of 5.7×10^{15} Ga$^+$/cm^2.

This abrupt change in the reversal field of a domain wall at the irradiated region suggests that the domain wall becomes pinned during its propagation along the nanowire. The pinning strength of these irradiated regions can be characterised by the field required to de-pin the domain wall. This field is shown in figure 8.6(b) as a function of the the value of M_S expected in each irradiated region. These values of M_S were estimated from the results presented in figure 7.3(a) based on the irradiation of microscale elliptical structures where an unirradiated structure was assumed to have a value of $M_S = 860 \times 10^3$ A/m. Even though these doses extend above the low dose regime where complex changes in M_S are observed, the properties here are still dominated by the changes in M_S.

Figure 8.6(b) shows that the domain wall de-pinning field increases as the saturation magnetisation is decreased from higher irradiation doses. A linear fit to this data shows a shift in the de-pinning field by 44 ± 6 Oe from the unirradiated sample ($M_S = 860 \times 10^3$ A/m). This shift is attributed to the field required for the nucleation of a reverse domain and injection of a domain wall into the nanowire which is also included in this measurement. The linear fit also gives a dimensionless gradient of -14 ± 2 showing the change in de-pinning field with M_S, to be discussed later in this chapter.

8.3.2   Effect of the width of the irradiated region on domain wall pinning

In addition to the investigation into the effect of different irradiation dose, the effect of the width of the irradiated region was also investigated at a constant dose of 7.6×10^{15} Ga$^+$/cm^2. This dose was chosen as it gave the highest de-pinning field in figure 8.6(b) and was therefore likely to show the most significant changes as the width is varied.

Again, a nanowire with irradiated regions along its length was investigated and example MOKE hysteresis loops are shown in figure 8.7. These show sharp reversal behaviour before the first irradiated region in figure 8.7(a), which becomes broadened and has a greater reversal field following the irradiated regions in figures 8.7(b) and (c). The change in loop shape again suggests a greater distribution to the reversal field of the wire. When averaged over many field cycles this leads to a broadening of the hysteresis loop.
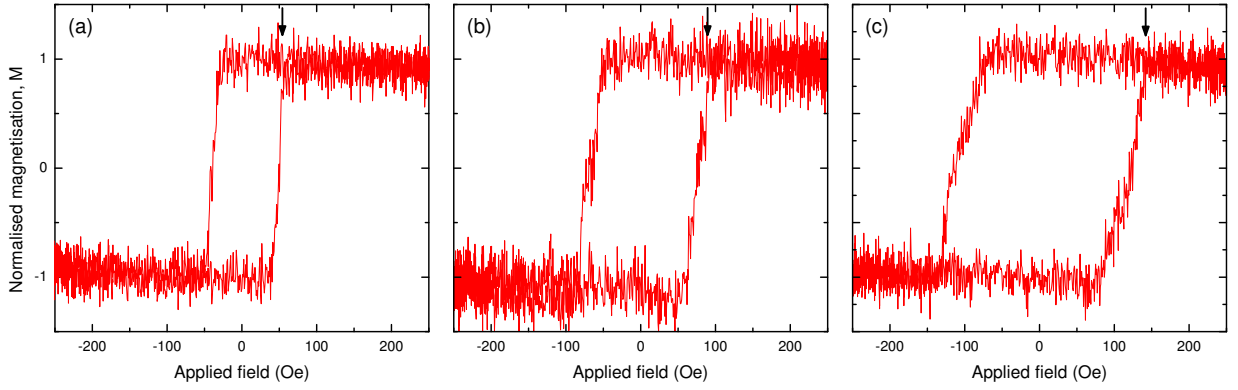
Figure 8.7: MOKE hysteresis loops showing magnetisation reversal in an individual 100 μm long, 400 nm wide, 15 nm NiFe / 2.5 nm Au nanowire. The loops correspond to positions along the nanowire: a) before and after a b) 1 μm and c) 4 μm wide region irradiated with a dose of 7.6×10^{15} Ga$^+$/cm^2. The magnetisation reversal becomes more gradual and occurs at an increased reversal field (indicated by the arrows) following the irradiated regions.

The reversal field from the hysteresis loop was extracted as the field required to achieve complete magnetisation reversal in every field cycle. This is shown by the arrows in figure 8.8(a) as a function of measurement position along the nanowire.

The abrupt changes in the reversal field are attributed to domain wall pinning which increases with the width of the irradiated region. Figure 8.8(b) shows this more clearly where the de-pinning field is shown as a function of the width of the irradiated region. Initially an increase in the de-pinning field occurs up to a width of ≈ 2 μm which then settles to a constant
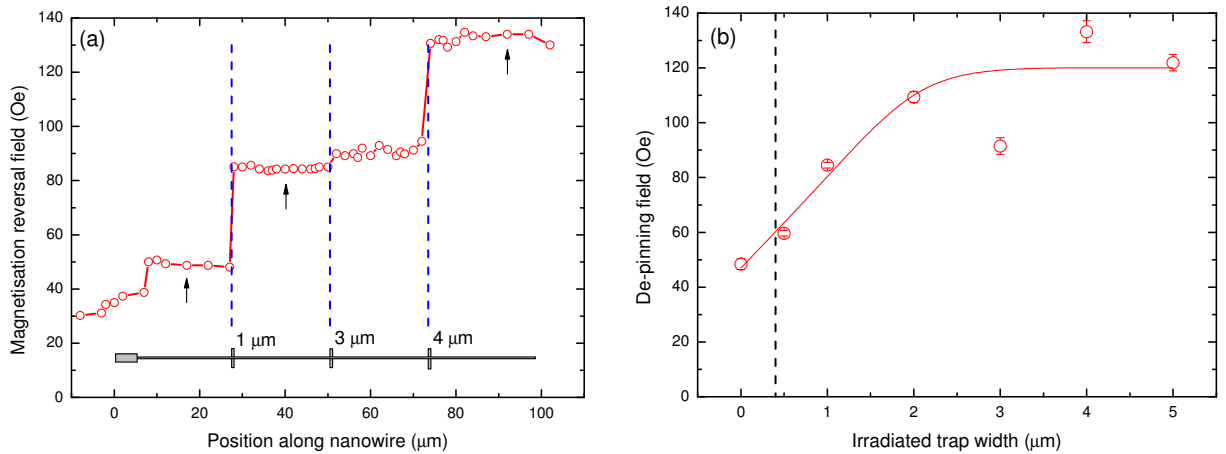
Figure 8.8: a) Variation in reversal field with position along a 100 μm long, 400 nm wide, 15 nm NiFe / 2.5 nm Au nanowire with various width regions irradiated with a dose of 7.6×10^{15} Ga$^+$/cm^2. The arrows show the measurements corresponding to the hysteresis loops in figure 8.7. b) This reversal field is plotted as a function of the width of the irradiated region where the line is a guide to the eye.

de-pinning field for wider irradiated regions. This agrees with the theoretical understanding of domain wall pinning where the pinning potential does not depend on defect size once the defect is sufficiently larger than the domain wall width. In this case, the domain wall width is expected to be of a comparable size to the nanowire width,[12] which is indicated by the vertical line in figure 8.8(b). The domain wall width is on the same order of magnitude but still noticeably smaller than the trap width associated with the change in behaviour. Possible reasons for this are associated with the dynamic properties of domain walls and are discussed later in this chapter. In addition to the irradiation induced de-pinning field, this figure also shows the same ≈ 45 Oe de-pinning field associated with the nucleation of the reverse domain and injection of the domain wall into the nanowire in these measurements.

8.4   Micromagnetic simulations of domain wall behaviour in nanowires with locally varying M_S

To model the domain wall behaviour using micromagnetic simulations, the irradiated region was initially considered as a 200 nm wide region with a reduced saturation magnetisation, $M_S = 800 \times 10^3$ A/m, in the centre of a 10 μm long, 150 nm wide, 10 nm thick nanowire. The saturation magnetisation was chosen as it is the dominant factor found from the results in chapter 7 and provides the most simplistic modelling approach that may explain the relevant physical processes observed in the experimental results. A more complete modelling approach including the effects of other magnetic parameters such as the exchange stiffness, A, or the damping parameter, α, may lead to a improved predictions by the model, but would bring additional modelling complexity.

An initial transverse domain wall structure at the left side of the nanowire structure was propagated to the right side under the influence of either a 6 Oe or 8 Oe applied axial field in a dynamic simulation as a function of the simulation time. Figure 8.9(a) shows the variation in the normalised magnetisation of the system as a function of time that represents the position of the domain wall along the nanowire. Since the simulations start with an initial domain wall structure in the nanowire, the de-pinning field in these micromagnetic results appears considerably lower. This is because the simulations do not include the ≈ 45 Oe intrinsic contribution due to the nucleation of the reverse domain and injection of a domain wall into the nanowire.
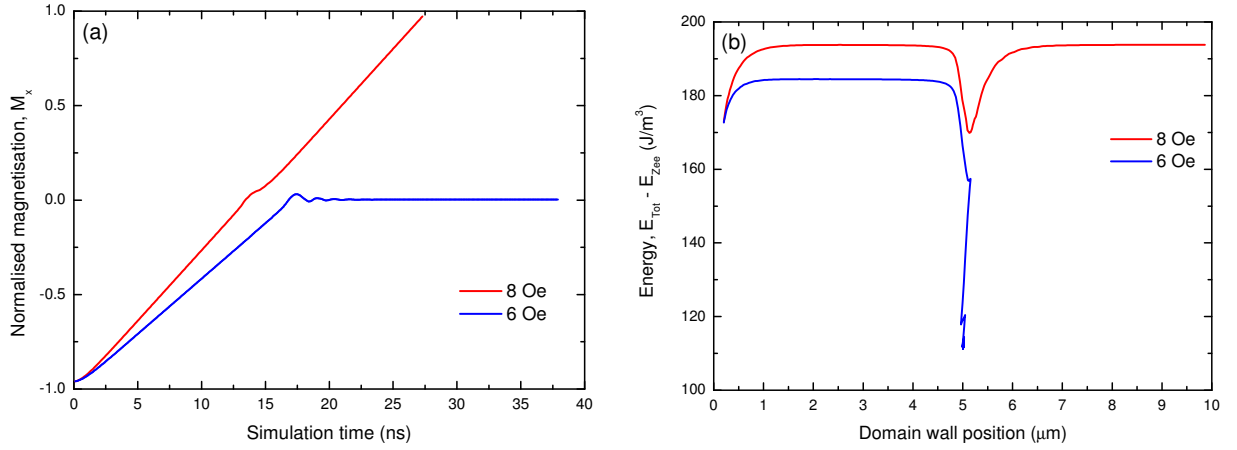
Figure 8.9: Dynamic micromagnetic simulations of a domain wall propagating along a nanowire including a 200 nm wide region of reduced $M_S = 800 \times 10^3$ A/m in the centre of a 10 μm long wire. The a) magnetisation of the wire and b) energy dependence of the domain wall are shown for propagation with both 8 Oe and 6 Oe driving fields.

With the 8 Oe applied field, the domain wall propagates to the end of the nanowire and is able to pass through the region of reduced M_S. However, with a 6 Oe applied field the domain wall propagates to the centre of the wire and becomes pinned by the region of reduced M_S. This figure also shows a difference in domain wall velocity for the two applied fields where both are below the Walker field.

The change in energy associated with the structure of the domain wall has been extracted from these simulations by subtracting the field energy from the total energy of the system. This is shown in figure 8.9(b) for both fields as a function of the domain wall position along the nanowire. An initial increase in energy is associated with the domain wall structural changes during the acceleration phase of the simulation (discussed in chapter 5). This is followed by a regime where constant energy is associated with a uniform spin structure of the wall during propagation. As the domain wall arrives at the region of reduced M_S, it adopts a structure with reduced energy.

For the 8 Oe applied field, the field energy was sufficient to overcome the energy barrier associated with the region of reduced M_S and the domain wall continues to propagate along the second half of the wire. However, for the 6 Oe applied field, the field energy is not sufficient to allow the wall to continue propagation beyond the region of reduced M_S and instead the domain wall finds a state of minimised energy by structural rearrangements within the reduced M_S region.

The reduction in the domain wall energy as it enters the region of reduced M_S shows that

192

this region acts as an energy well. The domain walls at both fields can enter the well however only the the energy associated with the 8 Oe field is sufficient to overcome the energy barrier to escape this well. Therefore, the de-pinning of a domain wall from a region of reduced M_S is associated with the domain walls leaving the well. Further investigation of this de-pinning field was performed as a function of applied field, using static micromagnetic simulations, with an initial domain wall structure inside the energy trap.

These static simulations were performed with an increasing axial field applied to a transverse domain wall initially in the centre of a trap region of reduced M_S. The axial magnetisation of the nanowire obtained from these simulations is shown in figure 8.10(a) as a function of applied field for various different values for M_S.

This net nanowire magnetisation was initially zero when the domain wall was initiated in the centre of the wire and rose gradually to ≈ 0.3 due to spin rearrangements in the domain wall structure and the movement of the domain wall within the trap. A further increase in field shows an abrupt transition in the magnetisation associated with the de-pinning of the domain wall from the trap at the de-pinning field.

The de-pinning field plotted as a function of M_S is shown in figure 8.10(b) which can be compared with the experimental results in figure 8.6(b). Both show a linear increase in the de-pinning field as M_S in the trap is reduced. For the micromagnetic simulations the de-pinning field vanishes for traps where M_S approaches the value of the unirradiated
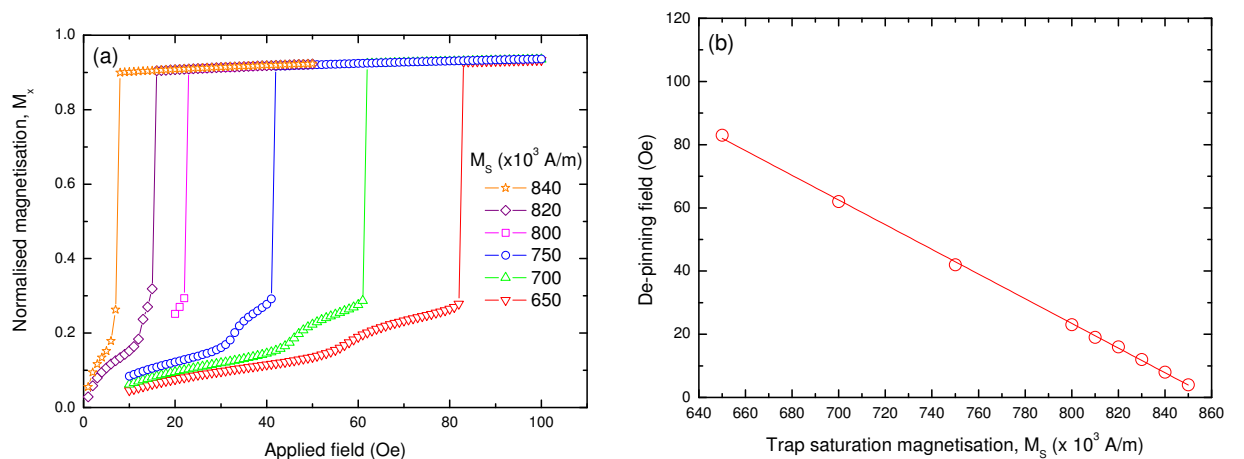

Figure 8.10: a) Increasing field section of the hysteresis loops for a transverse wall in the centre of a 2 μm long nanowire containing a 200 nm wide region of reduced $M_S = 800 \times 10^3$ A/m. b) The de-pinning field of a domain wall from these regions is plotted as a function of the value of M_S and is fitted by a linear relationship.

wire, $M_S = 860 \times 10^3$ A/m. However, in the experimental case a ≈ 45 Oe shift in the de-pinning field was found showing an additional de-pinning field contribution associated with the injection of the domain wall. This additional field was not included in the micromagnetic simulations as they start with an initial domain wall structure and neglects the magnetisation processes that takes place within the nucleation pad.

This linear relationship has a dimensionless gradient of 31.1 ± 0.2 which is over twice as steep as that obtained for the experimental results. This difference may be due to fabricational roughness, slight differences between the magnetic parameters, wire geometry and stochastic thermal effects which are not accounted for in the micromagnetic simulations. These could all result in a greater de-pinning field from micromagnetic simulations in comparison to experimental results with the same reduction in M_S.

The gradual increase in the magnetisation shown for low fields in figure 8.10(a) was further investigated through the images of the micromagnetic spin configuration to gain insight into the domain wall pinning by such traps of reduced M_S. These images are shown in figure 8.11 with an increasing field applied to a domain wall in a nanowire with a trap of $M_S = 750 \times 10^3$ A/m. In these simulations the domain wall pins towards the right hand side of the reduced M_S region, outlined by the black box. This is consistent with pinning associated with the exit of the domain wall from the trap. It is interesting to note that the domain wall was pinned inside the trap for low applied fields, but the majority of the domain wall structure was outside of the trap at 40 Oe where the domain wall was still pinned.

The effect of the width of the reduced M_S region was also investigated through micromagnetic simulations and the increasing field sections from the hysteresis loops are shown in
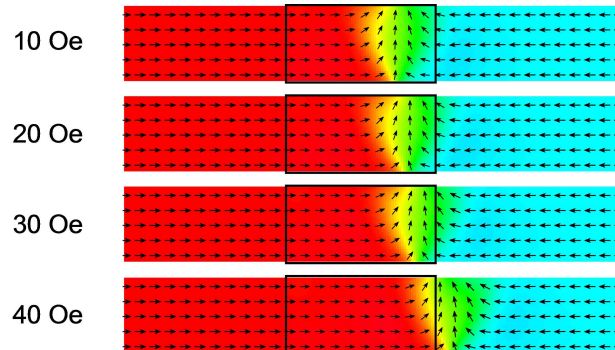

Figure 8.11: Micromagnetic spin configuration of a transverse domain wall in a nanowire pinned by a 200 nm wide region of reduced $M_S = 750 \times 10^3$ A/m with various applied magnetic fields along the nanowire axis.

figure 8.12. These simulations were performed with both transverse and vortex domain wall structures, and the two figures show some differences in the behaviour.

For the transverse domain wall structure a gradual increase in magnetisation occurs corresponding to the change of position of the domain wall within the trap. This is followed by a sharp transition in the magnetisation as the domain wall de-pins and completes the magnetisation reversal. For a vortex domain wall the gradual increase in magnetisation is more complex, showing multiple transitions and extending to a greater magnetisation before de-pinning. However, the behaviour of both domain walls can still be characterised by a de-pinning field where the domain wall de-pins and completes the magnetisation reversal of the nanowire.

This de-pinning field is shown in figure 8.13 for both transverse and vortex walls as a function of the width of the reduced M_S region. The horizontal lines indicate the reversal field for an effectively infinite trap width, calculated from a simulation with only one boundary.

For wide traps, the de-pinning field was a similar value to that of the infinitely wide trap. However, as the width of the trap was reduced below ≈ 150 nm the de-pinning field reduced as the domain wall was larger than the trap and only a small region of the domain wall structure was involved in the pinning. This figure shows a similar trends to those seen in the experimental results in figure 8.8(b). As previously discussed, the micromagnetic simulations show a lower initial de-pinning field as they do not take into account the ≈ 45 Oe field required for the injection of the domain wall from the nucleation pad. Another significant difference

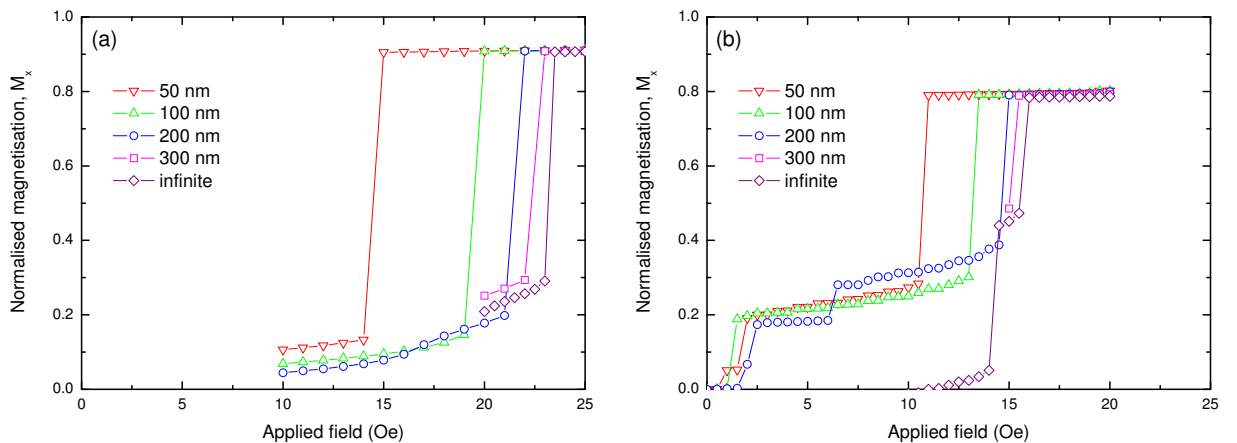**Figure 8.12:** Increasing field sections of hysteresis loops from micromagnetic simulations of the magnetisation reversal in a 1 μm long, 150 nm wide, 10 nm thick nanowire including a region of reduced $M_S = 800 \times 10^3$ A/m. These are shown for a variety of different widths to the irradiated regions for both a) transverse and b) vortex domain wall structures.
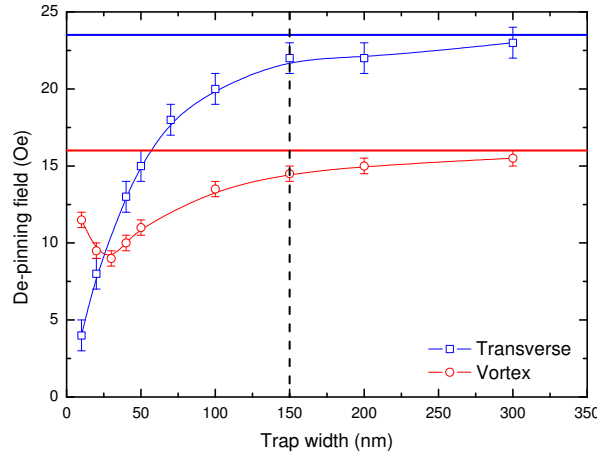
Figure 8.13: The de-pinning field from a reduced M_S trap for transverse and vortex domain walls as a function of the width of the reduced M_S region along a 1 μm long, 150 nm wide, 10 nm thick nanowire. The two horizontal lines show the de-pinning field of a domain wall from a single boundary representing an effectively infinite wire and the vertical line shows the expected domain wall size.

is the agreement between the expected domain wall size and the change in behaviour of the de-pinning field. This agreement is better for the micromagnetic simulations compared to the experimental results and is discussed later in this chapter in relation to the pinning of a static domain wall in the micromagnetic simulations compared to a dynamically propagating domain wall in the experimental measurements.

The micromagnetic simulations allow for the differences in the pinning of transverse and vortex walls to be investigated. Figure 8.13 shows that transverse walls experience a greater de-pinning field than vortex walls except for irradiated traps with widths < 30 nm where the de-pinning field for vortex walls shows a complex rise. The transverse walls are also more affected by the width of the irradiated region showing a greater change in de-pinning field over the range of dimensions investigated. The difference in the de-pinning field for the two wall structures is similar to the pinning of domain walls based on their structure from different notch geometries.[14,93–96]

The micromagnetic spin structure of the two different domain wall structures are shown in figure 8.14 as a function of the width of the reduced M_S trap at a field just below the de-pinning field. For transverse domain walls, the majority of the wall structure was outside the trap region, which is consistent with the behaviour found in figure 8.11 and also explains the greater extent of gradual magnetisation increase for wider traps in figure 8.12(a).

The vortex domain wall structures experience a more complex interaction with the reduced
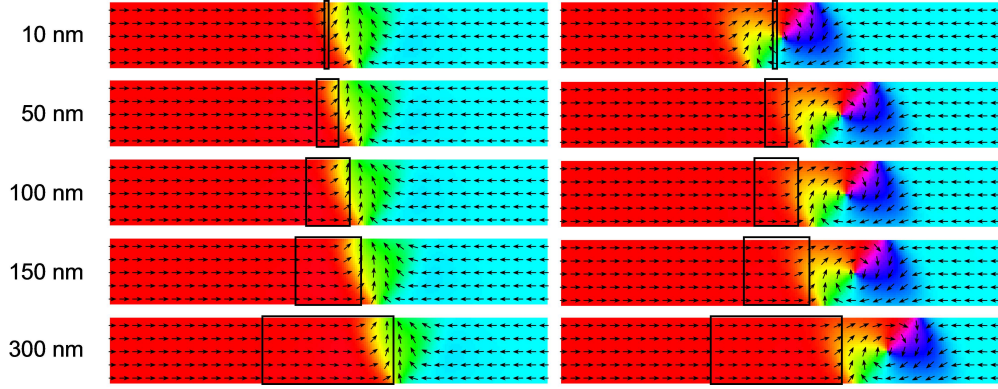
Figure 8.14: Micromagnetic simulations of transverse and vortex domain wall structures at a field just below the de-pinning field for various width reduced M_S regions within a nanowire structure.

M_S trap and can become pinned from different regions within their spin structure. For the 10 nm wide trap the centre of the vortex was pinned by the trap. However, for the wider traps, at the field just below the de-pinning field, the vortex walls are pinned mainly outside the trap, similar to the transverse walls. The more complex interaction between the vortex walls and the traps can explain the more complex gradual increase in magnetisation before the de-pinning field found in figure 8.12(b).

The micromagnetic simulations in figures 8.11 and 8.14 show how the interaction of a domain wall with an reduced M_S region is complex. This incorporates multiple pinning stages at different positions across the boundary of the magnetic property variation and also shows a dependence on domain wall structure. This leads on to the discussion about the pinning of domain walls in relation to the geometry of the reduced M_S region.

8.4.1 Effect of the irradiation geometry on domain wall pinning

Micromagnetic simulations have shown that pinning depends on the micromagnetic structure of the domain wall and its interaction with the boundary between regions of different M_S at the edges of the trap. The results presented so far have all been performed with M_S regions bounded at 90° to the nanowire axis. The relationship between the domain wall pinning and micromagnetic structure was investigated further by comparing pinning at boundaries rotated at different angles with respect to the nanowire axis. These simulations used an initial domain wall structure in the centre of the nanowire where a boundary was offset to the right of the domain wall. Only one boundary was considered for simplicity, in a simulation scheme following the results from the effectively infinite traps presented in figure 8.13.

Figure 8.15 shows the variation of the de-pinning field as a function of the boundary angle for both transverse and vortex domain wall structures. At 90°, the boundary was perpendicular to the nanowire and the domain walls showed the behaviour previously discussed in this chapter. Rotating the boundary in either direction leads to a complex angular dependence showing an initial increase in de-pinning field to a maximum at $\approx 45°$ and 135°. A further rotation leads to a decrease in the de-pinning field as the boundary approaches a more parallel configuration with the nanowire.

At angles around 90° the de-pinning field for transverse walls was greater than for vortex domain walls. However with rotation of the boundary this difference decreases and even inverts, giving rise to a greater de-pinning field for vortex walls below 50°. The transverse domain walls have a 'V' shaped structure so it is expected that they may experience a difference in the de-pinning field with angle associated with the domain wall chirality. This also explains the different behaviour associated with either an increase or decrease in angle from 90°. More interestingly the asymmetry in the de-pinning field for the transverse structure was not as significant as that observed for the more symmetrical vortex structure.

The spin structures obtained from the micromagnetic simulations shown in figure 8.16 give more insight into the pinning of these domain wall structures, these are shown for a field just below the de-pinning field. The lines superimposed on the figure show the location of the boundary between normal M_S on the right and reduced M_S region on the left.
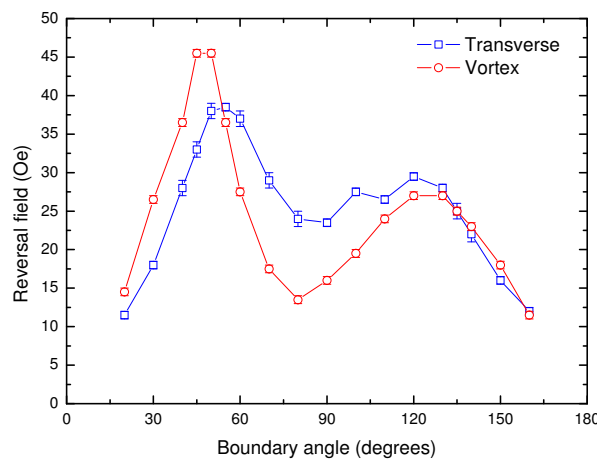

Figure 8.15: Micromagnetic simulations of the de-pinning field of a domain wall from a boundary into a region of reduced M_S which is rotated at an angle to the nanowire axis. The de-pinning field is compared for both transverse and vortex domain wall structures in a 1 μm long, 150 nm wide, 10 nm thick nanowire.
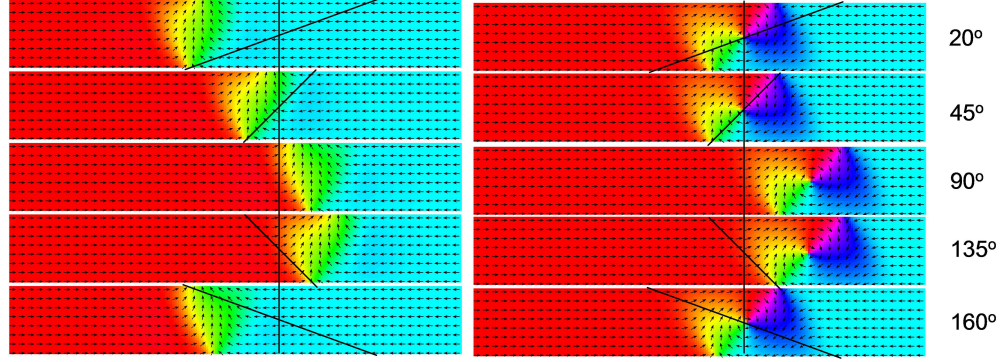
Figure 8.16: Micromagnetic spin structure showing the domain wall position just before de-pinning from the boundary of the region of reduced M_S. This is shown for a 1 μm long, 150 nm wide, 10 nm thick nanowire structure. The lines show the positions of the boundary with the reduced M_S region on the left.

The domain walls become pinned at the boundary by different parts of the domain wall structure, similar to the vortex pinning at the perpendicular boundary. At 20°, 45°, and 160°, the transverse domain wall was pinned on the reduced M_S side of the trap. This contrasts with the previous behaviour with the perpendicular boundary where the domain wall was pinned largely outside of the trap for fields just below the de-pinning field. For the vortex walls, at most angles, the vortex structure was pinned at the centre of the boundary; however for 90°, and 135°, the structure was also pinned on the outside of the reduced M_S region.

8.4.2   Influence of the sharpness of the irradiation boundary on the domain wall pinning

The micromagnetic simulations so far have modelled the irradiated region as a sharply defined region of reduced M_S with an abrupt change in the value of M_S at the boundary. However, experimentally a more gradual transition between the properties of the wire and the irradiated regions are expected to result from the irradiation process.[116] In this section the effect of the boundary sharpness on the domain wall de-pinning field was investigated through micromagnetic simulations.

The boundary between regions of different magnetic properties will have a gradual transition associated with the profile of the ion beam irradiation that is known to be approximately Gaussian for the focussed Ga^+ beam used here.[240] Therefore, the boundary of an irradiated region made up of multiple irradiated pixels has a profile described by the convolution of many Gaussian distributions forming an error function at the boundary.

For the simulation of these boundaries, the micromagnetic problem was based on a structure that could be described analytically. Therefore the error function was approximated by the sigmoidal function:

$$y = \frac{M_1 - M_2}{1 + exp(\frac{x - x_0}{\mathrm{d}x})}. \tag{8.1}$$

This function varies between two values of the saturation magnetisation, $M_1 = 800 \times 10^3$ A/m and $M_2 = 860 \times 10^3$ A/m, around a centre point, $x_0 = 500$ nm. The variation in the shape of this function for various width parameters, $\mathrm{d}x$, is plotted in figure 8.17(a).

Micromagnetic simulations were used to determine the domain wall de-pinning fields from these graded boundaries which are shown in figure 8.17(b) for both transverse and vortex domain wall structures. Here, the vortex wall has a lower de-pinning field than the transverse wall, again consistent with the previous results. The de-pinning field for both structures decreases as the width parameter describing the boundary is increased from the initial abrupt interface to the broadened sigmoidal profile. This decrease is consistent with the theory associated with the de-pinning of domain walls from a large 'fuzzy defect' described in chapter 2.

The focussed Ga$^+$ beam is expected to have a beam diameter of 17 nm,[170] dependent on the alignment, focussing and the condition of the beam apertures at the time. For a gradual transition in magnetic properties over this width, the micromagnetic simulations predict a ≈ 1 Oe reduction in the reversal field in comparison to the simulations on the

Figure 8.17: a) A boundary between regions with different M_S can be described by a sigmoidal function which is shown for a variety of different width parameters. b) Micromagnetic simulations show the effect of the width parameter on the domain wall de-pinning field for both transverse and vortex walls at the boundary in a 1 μm long, 150 nm wide, 10 nm thick nanowire.

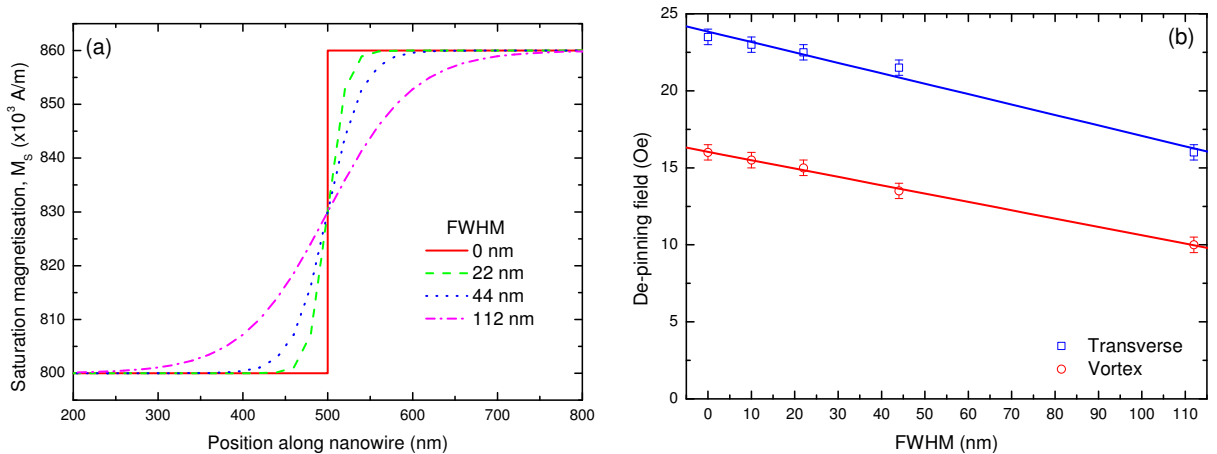abrupt interface. This is a small difference and is not considered to be a significant effect on the domain wall de-pinning from these traps.

8.5   Static and dynamic pinning effects on domain walls

In figure 8.9 the results of a dynamic micromagnetic simulation on a 10 μm long wire show the interaction of a transverse domain wall with a 200 nm wide, $M_S = 800 \times 10^3$ A/m trap. This showed that the domain wall was pinned at 6 Oe, but could propagate over the trap with an 8 Oe field and hence the de-pinning field of the trap lies between 6 Oe and 8 Oe. In figure 8.10, a static simulation on a 1 μm long wire showed that the de-pinning field with the same trap parameters was 23 ± 1 Oe and in figure 8.12(a) it was 22 ± 1 Oe. These results are obviously different to the 6 - 8 Oe de-pinning field, however they represent traps defined by the same parameters, both in 150 nm wide, 10 nm thick nanowire structures with $M_S = 860 \times 10^3$ A/m.

These simulations have been performed as a function of time in the dynamic case using a value of $\alpha = 0.01$ and as a function of field in the static case with $\alpha = 0.5$. However, results previously presented in figure 4.16 show that there are no noticeable differences between the de-pinning fields predicted by these two simulation methods.

All these simulations use fixed spins at the nanowire ends to correct the simulations so the wires appear as infinitely long nanowires (see chapter 5). Therefore the length of the simulation should not affect the results of the simulation. This is confirmed by additional dynamic simulations comparing figure 8.9 with a shorter 2 μm long wire shown in figure 8.18(a). The de-pinning field in this case was found to be between 7 Oe and 8 Oe, showing no significant dependence on the length of the wire used in the simulation.

The difference between these simulations is then associated with the state of the domain wall prior to the pinning/de-pinning at the irradiated region. In the dynamic simulations, the domain wall arrives at the trap travelling at a finite velocity and in the case of the static de-pinning simulations, the domain wall is initially at rest within the trap.

This leads to a possible description of domain wall pinning that is similar to mechanical friction where a static domain wall may experience a greater pinning effect compared to the propagating domain wall.[274] In the case of slow moving or stationary domain walls in an irradiated region, a de-pinning field is required to de-pin the domain wall from the trap region
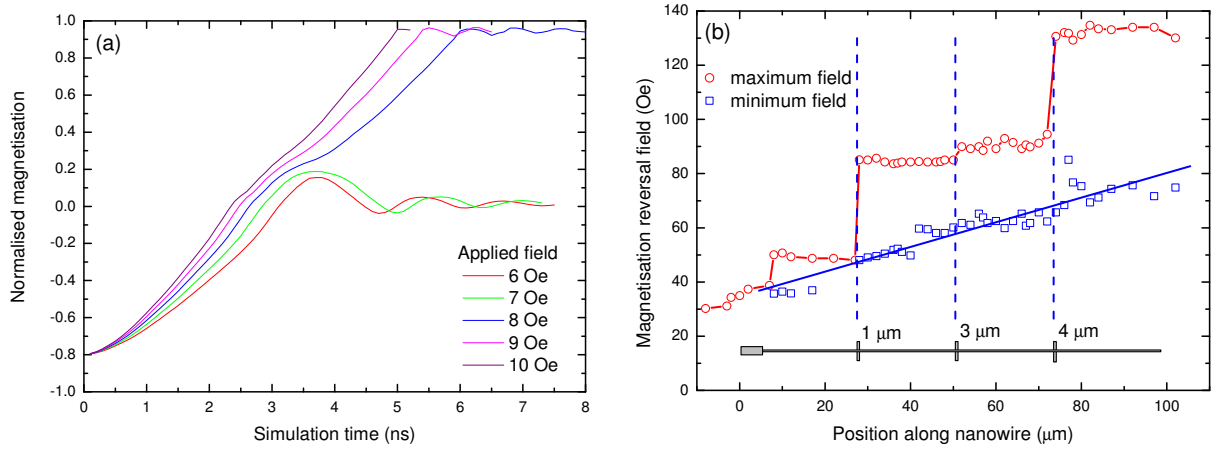
Figure 8.18: a) Dynamic simulations showing the magnetisation of a 2 μm long nanowire where a domain wall either propagates over, or gets pinned by a 200 nm wide, $M_S = 800 \times 10^3$ A/m trap. b) MOKE measurements of the minimum and maximum reversal fields as a function of position along a nanowire with irradiated regions of increasing width.

allowing it to continue propagation. With faster domain wall dynamics, the domain walls may not 'feel' the full pinning potential of the trap, allowing the wall to propagate over the irradiated region at a lower field than for the slower moving walls.

This description also provides an explanation for the variation in the hysteresis loop shape found in the experimental results shown in figures 8.5 and 8.7. The more gradual reversal transition is associated with a distribution of reversal fields averaged over many field cycles. The earlier analysis of these results compared the reversal field taken as the applied field required to achieve complete magnetisation reversal in the nanowires. However, the lowest field at which any magnetisation reversal takes place is also an important parameter as it represents the lowest field at which magnetisation reversal can take place.

Figure 8.18(b) shows the variation in both the maximum and minimum reversal field as a function of position along a nanowire with various width irradiated regions. The maximum reversal field shows discrete jumps at the location of the irradiated regions which separate regions of constant reversal field. This behaviour may originate from the slow moving domain walls which experience the full pinning effect of the irradiated traps. In contrast, the minimum reversal field shows a linear increase with little effect of the irradiated regions. This may represent the behaviour of faster moving domain walls that do not experience the full pinning effect of the irradiated regions.

The results in figure 8.8(b) show that the pinning of domain walls is affected by irradiated regions larger than the domain wall width. However, the theoretical explanation and the

micromagnetic results in figure 8.13 show no significant changes in de-pinning field occur when the irradiated region is larger than the width of a domain wall. This difference may be explained as dynamic propagating domain walls does not 'feel' the full pinning effect of the irradiated region. Therefore, a larger irradiated region may be required to achieve the same pinning effect as for domain walls in the static regime.

8.6 Summary

In summary this chapter shows how localised Ga^+ irradiation of bilayered magnetic nanowires can be used to locally modify the magnetic properties, giving control over the behaviour of magnetic domain walls within nanowires. This incorporates conventional methods for the manipulation of domain walls in nanowires, along with less well established methods for the modification of the magnetic properties in bilayered magnetic material. The results presented here may be beneficial for the development of future technological devices operating through the manipulation of domain walls.

The investigation commenced with the analysis of the magnetisation reversal in nanowire structures. Here, shape anisotropy gives rise to the behaviour leading to a decreasing reversal field with increasing wire width, governed by the nucleation of domain walls in these structures. The inclusion of a domain wall nucleation pad lowers the reversal field of the wire and shows a reversal field of the wire which increases with wire width.

Localised regions of Ga^+ irradiation have been used to modify the magnetic properties of the nanowire to act as artificial defects that pin the domain walls at the irradiated regions. A greater field was then required to de-pin the domain wall and allow propagation to continue. This de-pinning field increased linearly with the irradiation dose and showed an initial increase followed by a plateau with respect to the width of the irradiated region.

This behaviour was analysed using micromagnetic simulations where the irradiated region was represented as a region of reduced saturation magnetisation. Here, the domain walls experience a local energy minimum where the de-pinning field behaviour with trap width and depth shows qualitative agreement with the experimental results. Further insight gained from the micromagnetic simulations shows the effect of domain wall structure on the pinning mechanisms for the domain wall. This leads to some level of selective pinning through the relation between the geometry of the boundary and the structure of the domain wall.

Finally, considering the differences in pinning behaviour between dynamic propagating domain walls in comparison to stationary domain walls reveals a substantial difference in the de-pinning energy of the domain wall from the trap. This understanding helps suggest possible explanations for the more complex results obtained from the experimental study.

Chapter 9

Magnetic reversal behaviour in structurally modulated nanowire

9.1   Introduction

The modification of the magnetic material by focussed ion beam irradiation has been discussed as one method for control of domain walls in nanowires. However, a more established approach to gain such control can be achieved through geometrical patterning of the magnetic material through lithographic techniques. This method has led to many advances in the understanding and control of domain walls, particularly their static properties, based on the energetics of the interactions between individual domain walls and localised geometrical features. The dynamic properties of domain walls are not so well understood, but recent work on the inclusion of periodic structuring along a nanowire has demonstrated both experimental[113] and theoretical[275–277] improvements to the domain wall dynamics. This has significance for future technological devices where the operation by the manipulation of domain walls in a fast reliable manner is the key to their functional operation.

These improvements in domain wall dynamics arise due to the suppression of Walker breakdown in the domain wall motion at higher fields and the key to controlling this suppression lies in the understanding of the nature of the breakdown process. This breakdown arises due to spin precessional frequency limitations in the magnetic material resulting in complex periodic transitions of the domain wall from a transverse wall structure to a vortex core wall structure during its propagation along the wire. The different wall structures affect the dynamics and even result in retrograde motion during the propagation which leads a

dramatic reduction in the time-averaged domain wall velocity. Using modern lithographic techniques, periodic structuring is now a realistic approach for the improvement in domain wall dynamics.

This chapter includes a detailed series of experimental measurements and micromagnetic simulations that investigate the nucleation and propagation of domain walls, and ultimately the mechanism for the suppression of Walker breakdown in these structures. The investigation starts with an analysis of the static properties of the magnetic reversal behaviour in an edge modulated nanowire structure. These properties are compared with the magnetisation reversal by domain wall propagation in the same nanowire structures. The micromagnetic investigation is then extended to focus on the structural transformations that take place during the Walker breakdown process, in particular the relationship between the periodicity of micromagnetic structural transformations and geometrical edge modulations of the nanowire. This identifies a route to control Walker breakdown which is then further explained by the dissipation of energy in the form of spin waves to stabilise the domain wall.

9.2   Edge modulation geometry

The nanowires in this chapter can be considered as planar nanowires with the inclusion of sinusoidal modulation to both edges. This modulation is characterised by a wavelength, λ_m, amplitude, A_m, and average width, w, which was fixed at 250 nm. Examples of lithographically defined nanowires are shown in figure 9.1 where the parameters are overlaid on figure
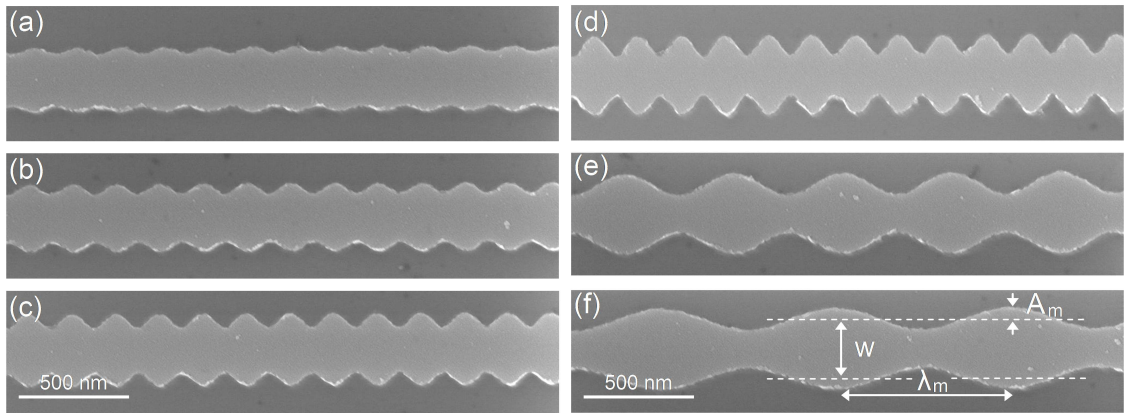

Figure 9.1: Scanning electron microscope images of edge modulated nanowires with a) 15 nm, b) 25 nm, c) 35 nm and d) 50 nm amplitude with a 0.2 μm wavelength; e) 0.5 μm and f) 0.8 μm wavelength with 50 nm amplitude.

9.1(f).

These wires were 20 μm long, 10 nm thick NiFe structures with a 2.5 nm Au cap that were fabricated by electron beam lithography and thermal evaporation. The wires were patterned in arrays with a pitch of 800 nm to cover an area appropriate for MOKE measurements and for nucleation studies, 1 μm tapered ends were included to prevent the nucleation of domains at the ends of the nanowires. Figure 9.2(a) shows a scanning electron microscope image of a typical array of wires and figure 9.2(b) shows one of the tapered ends at a higher magnification. Multiple arrays of wires were fabricated with different edge modulation parameters and with wavelengths varying from 0.2 μm up to 2.0 μm and with amplitudes from 15 nm up to 50 nm. These structural features were chosen to be in the size range comparable to that expected for the dimensions of domain walls in these structures.

9.3   Nucleated magnetisation reversal in edge modulated wires

The investigation of structures with both ends tapered aimed to understand the magnetisation reversal behaviour that is governed by nucleation within the modulated wire structure. The influence of the edge modulation parameters on the magnetisation behaviour was investigated using focussed MOKE magnetometry and micromagnetic simulations.

Examples of the MOKE hysteresis loops are shown in figure 9.3 with a selection of wavelengths for a nanowire with 35 nm edge modulation amplitude. The figure shows a wavelength dependence to the reversal field along with subtle differences in the loop shape. For long wavelengths, sharp magnetisation reversal between the two saturated magnetisation states was observed. However, for wavelengths below 0.8 μm, a more gradual increase in the
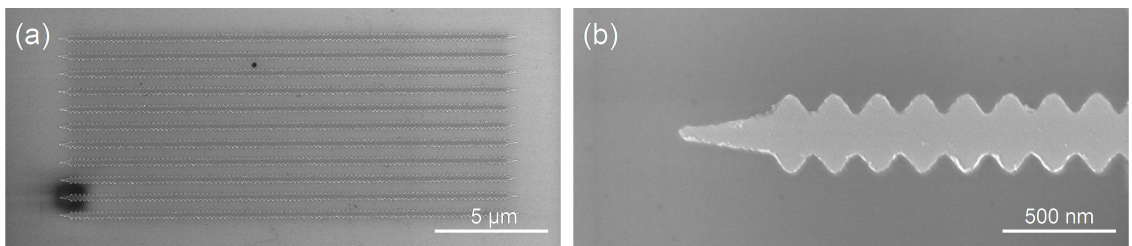
Figure 9.2: Scanning electron microscope images showing a) an array of 20 μm long nanowires with a pitch of 800 nm and b) a magnified section of a nanowire showing details of the tapered end.
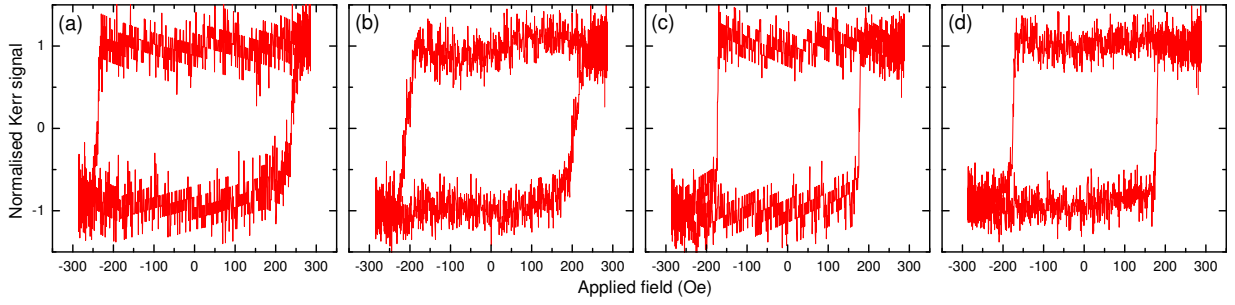
Figure 9.3: Magnetisation response to applied field for a 35 nm amplitude 10 nm NiFe / 2.5 nm Au wire with wavelengths: a) 0.3 μm, b) 0.4 μm, c) 0.8 μm and d) 1.0 μm measured using the MOKE.

magnetisation was observed prior to the sharp switching at the reversal field.

From these hysteresis loops, the reversal field was extracted and has been plotted as a function of the edge modulation wavelength in figure 9.4. This gives a better understanding of the changes in the reversal field as a result of the edge modulation parameters.

For longer wavelengths, where the wire structures approach that of an unmodulated nanowire, the reversal field shows little dependence on the wavelength. At shorter wavelengths, the reversal field gradually decreases to a minimum and then rises more sharply for the shortest wavelengths. In this short wavelength regime there is little amplitude dependence to the reversal field, whilst for the longer wavelengths the amplitude dependence becomes significant, leading to a reduced reversal field for the nanowires with larger amplitude edge modulation. The wavelength corresponding to the minimum reversal field also shifts towards longer wavelengths as the modulation amplitude is increased.
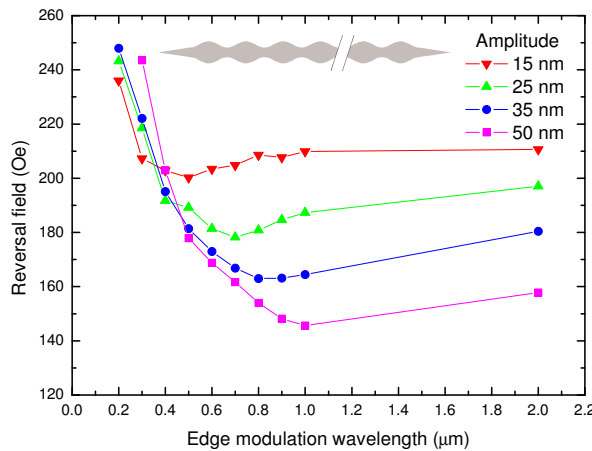
Figure 9.4: Magnetisation reversal field as a function of wavelength for 10 nm NiFe / 2.5 nm Au modulated nanowires with two tapered ends obtained from MOKE hysteresis measurements.

These results have been compared with detailed micromagnetic simulations performed on similar wire structures (5 nm thick), with a 2 μm long modulated wire section and additional 0.5 μm tapered ends. Examples of sections of the hysteresis loops from these simulations show the behaviour just before the magnetisation reversal in figure 9.5(a) for $\lambda_m \geq 0.7$ μm and 9.5(b) for $\lambda_m < 0.7$ μm with a 5 nm thick structure and 35 nm amplitude modulation.

The figures show the magnetisation initially at negative saturation where a positive applied field is increased until the magnetisation switches to the positive saturation state (not shown) at the reversal field. This behaviour was characterised into two regimes. For longer wavelengths, sharp switching of the magnetisation occurs between the two saturated states at the reversal field (figure 9.5(a)). However, for shorter wavelengths, more complex reversal incorporates a gradual increase in magnetisation until the eventual sharp switching occurs at the reversal field (figure 9.5(b)).

This reversal field shows a dependence upon the edge modulation parameters that was extracted from the simulations and is plotted in figure 9.6 as a function of edge modulation wavelength for a selection of different amplitudes. These results are shown for simulations with both 5 nm and 10 nm thick nanowires.

The dependence of the reversal field on the modulation parameters obtained from the micromagnetic simulations shows very similar behaviour to that found from the experimental MOKE measurements. For long wavelengths, little change in the reversal field was found. As the wavelength was reduced, the reversal field reduces to a minimum before a sharper
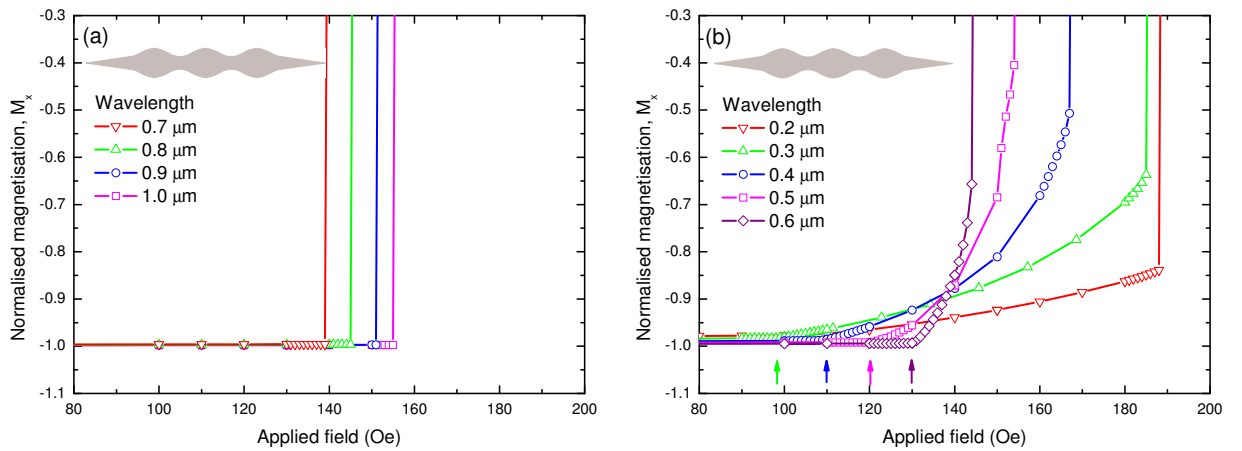
Figure 9.5: Micromagnetic simulations of magnetisation reversal in a 250 nm wide nanowire with 35 nm edge modulation amplitude and both ends tapered, as a function of magnetic field. The effect of the edge modulation wavelength is compared for the a) long and b) short wavelength regimes.
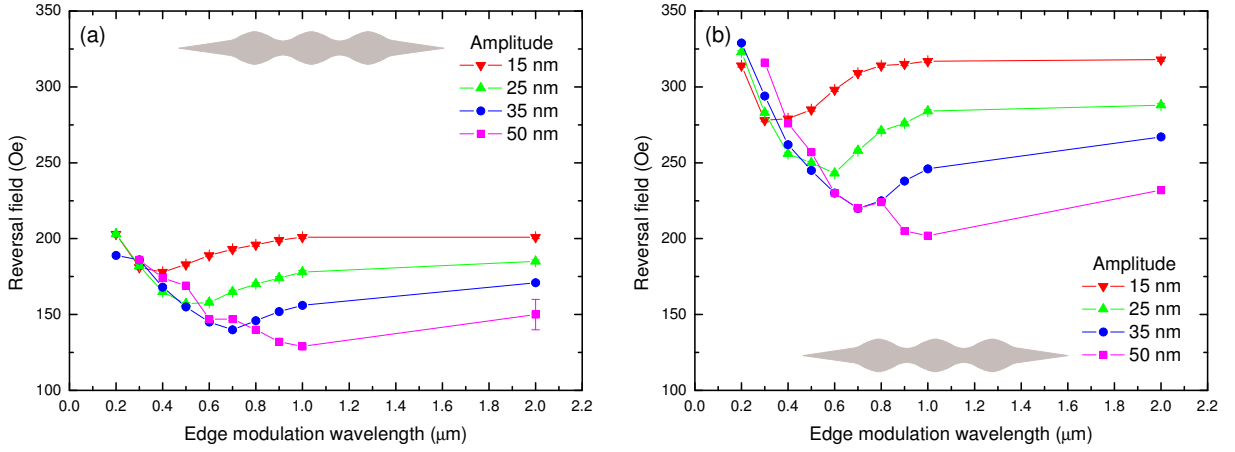
Figure 9.6: Magnetisation reversal field obtained from micromagnetic simulations as a function of the edge modulation wavelength for a selection of amplitudes with both a) 5 nm and b) 10 nm thick structures.

towards shorter wavelengths. The reversal field behaviour also depends on the modulation amplitude in the longer wavelength regime, giving a reduction in the reversal field for wires with larger modulation amplitude. The wavelength at which the reversal field is a minimum also shifts towards longer wavelengths with increasing amplitude.

A comparison between the two simulated thicknesses shows that the reversal field is greater and the changes are more pronounced for the thicker structures. However, the minimum reversal field remains at the same wavelength in both cases.

Although there is good agreement in the behaviour between the experimental results and the micromagnetic simulations, there is still a discrepancy between the absolute values of the reversal field. The experimental results show a shift towards higher reversal fields and a less significant drop in reversal field with decreasing wavelength. These differences may be due to the fabricational roughness, slight differences between the magnetic parameters and due to stochastic thermal activation effects which are not accounted for in the micromagnetic simulations.

9.4 Magnetisation reversal field dependence on wavelength

Further examination of the magnetisation reversal behaviour reveals a wavelength dependence to the minimum reversal field in figure 9.6. This behaviour has been explained by the

combination of two processes, one which governs the sharp magnetisation reversal at long wavelengths and another that leads to the gradual increase in magnetisation in the short wavelength regime.

Looking in more detail at figure 9.5(b), the onset of the gradual magnetisation increase occurs at a clearly identified field (indicated by the arrows on the figure), which decreases with the modulation wavelength. By plotting this field along with the abrupt reversal field from wires with longer modulation wavelength, figure 9.7 shows a continuous variation in field over the two wavelength regimes.

This suggests that the physical mechanism responsible for the abrupt reversal in longer wavelength nanowires is also responsible for the onset of the gradual magnetisation increase in the shorter wavelength nanowires. The increase in the reversal field for short wavelength modulation is dominated by an alternative process which leads to a stabilisation of the magnetisation, driving the magnetisation reversal towards higher fields with a gradual increase in the magnetisation.

The decreasing trend in the reversal field with the modulation parameters has been explained here using a simple analytical model based on the torque acting on the spins due to their angle relative to the applied field along the nanowire axis. In the unmodulated nanowire, the spins align parallel to the nanowire due to the shape anisotropy of the wire. However, the inclusion of edge modulation gives rise to a local demagnetising effect where spin alignment at the nanowire edges essentially tracks the contours of the edge modulation.
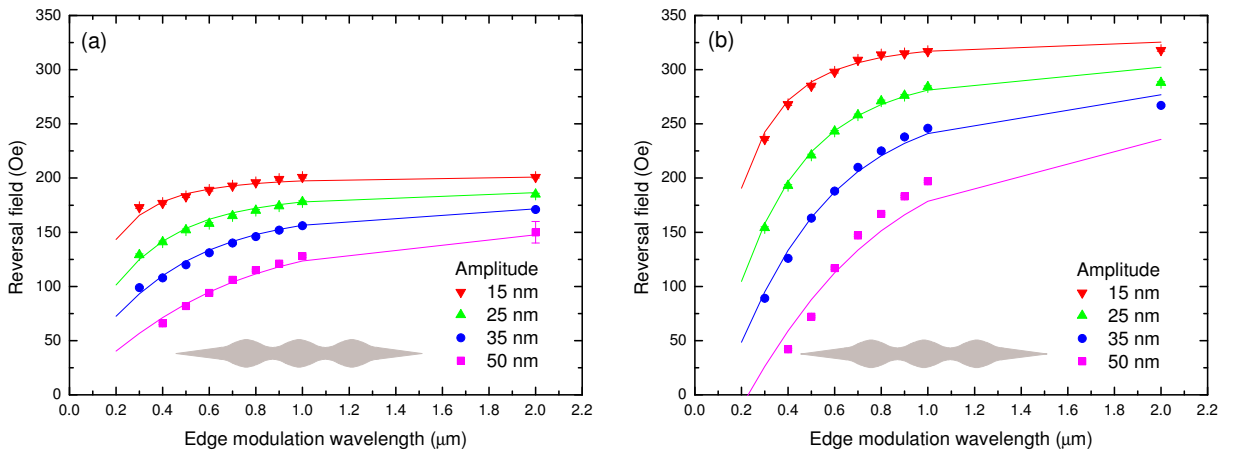
Figure 9.7: The abrupt reversal field obtained for long modulation wavelengths plotted along with the field corresponding to the onset of the magnetisation increase for wires with short wavelength modulation. This is shown for simulations on nanowires with a) 5 nm and b) 10 nm thick wires. The lines show best fits to the data.

Since the field was applied along the nanowire axis, these spins are at an angle, θ, with respect to the field as illustrated in figure 9.8. These spins then experience a torque given by $\boldsymbol{m} \times \boldsymbol{B}$, which scales as the sine of the angle, θ, between the spin and the applied field.

The energy required to rotate the spin is then given by the integral of this torque, $mB \int \sin \theta \, \mathrm{d}\theta$, evaluated between its initial and final angle. Taking the final angle to be parallel with the field gives a Zeeman contribution to the energy barrier that scales with $- \cos \theta$. For long wavelength low amplitude edge modulation, this angle is close to 180°, giving a large energy barrier that must be overcome to complete the switching. For shorter wavelength, high amplitude modulation this angle approaches 90° and provides a lower energy barrier for switching. This effect is best illustrated by the comparison between two edges of different modulation amplitude in figure 9.8.

The energy barrier for magnetisation switching can be related to the edge modulation parameters where the shape of the sinusoidal edge modulations is described by:

$$y = A_m \sin \left(\frac{2\pi x}{\lambda_m} \right) \tag{9.1}$$

where A_m is the amplitude, λ_m is the wavelength and x is the position along the nanowire. The differential of this edge geometry gives the gradient of the edge as a function of the position:

$$\frac{\mathrm{d}y}{\mathrm{d}x} = \frac{2\pi A_m}{\lambda_m} \cos \left(\frac{2\pi x}{\lambda_m} \right) \tag{9.2}$$

where the maximum (at $x = 0$) is given by:

$$\frac{2\pi A_m}{\lambda_m}. \tag{9.3}$$
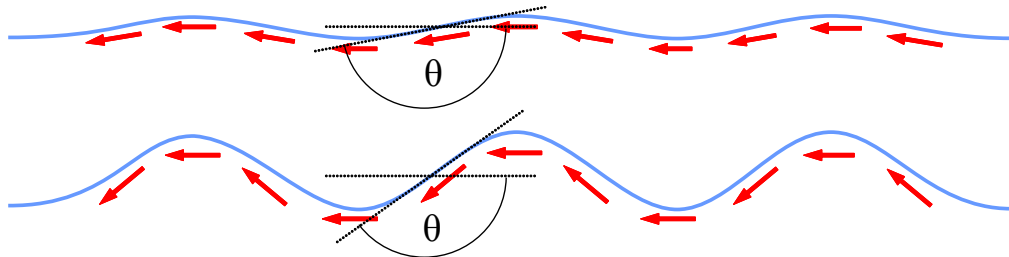
Figure 9.8: Two schematic illustrations of spins following the contours of the edge modulation. The maximum gradient of the wire gives the angle, θ, of the spin which becomes more orthogonal to the long axis of the nanowire with increasing amplitude of modulation.

Assuming that the spins follow the contours of the edge modulation, the maximum spin angle is found from the arc tangent of the maximum gradient. This then leads to an expression for the energy barrier which is proportional to the cosine of this angle, given by:

$$H = A_m\gamma + \beta\cos\left(\arctan\left(\frac{2\pi\delta A_m}{\lambda_m}\right)\right). \tag{9.4}$$

Here the factor, β, scales the angular term dependence, $A_m\gamma$, represents an additional amplitude dependent offset field and, δ, scales the angle term. This expression was fitted to both the experimental and micromagnetic datasets, with just β, γ and δ as free parameters, shown by the solid lines in figures 9.7 and 9.9 which represent the fit of this model to the data. In the case of the experimental MOKE dataset, only the reversal fields determined from the long wavelength modulation were included in the fitting as the identification of the field associated with the onset of curling in figure 9.3 is not reliable. The fits of the experimental results gave the values: $\beta = 234 \pm 1$ Oe, $\gamma = -1.5 \pm 0.1$ Oe/nm and $\delta = 1.8 \pm 0.1$. In comparison the micromagnetic simulations of the 5 nm thick wires: $\beta = 216 \pm 1$ Oe, $\gamma = -1.2 \pm 0.1$ Oe/nm and $\delta = 1.9 \pm 0.1$ whilst for the 10 nm thick wires: $\beta = 356 \pm 4$ Oe, $\gamma = -1.8 \pm 0.2$ Oe/nm and $\delta = 2.7 \pm 0.1$.

The values of β represent the variation in the reversal field of an unmodulated nanowire which incorporates the effect of any width and thickness dependence. The increase in this value for the 10 nm thick micromagnetic simulations is consistent with the higher reversal

Figure 9.9: Reversal field as a function of modulation parameters obtained from MOKE measurements. The data for the long wavelengths has been fitted by a model indicated by the solid lines.

fields expected for thicker nanowires. However, in the experimental data this parameter is lower than expected from simulations of t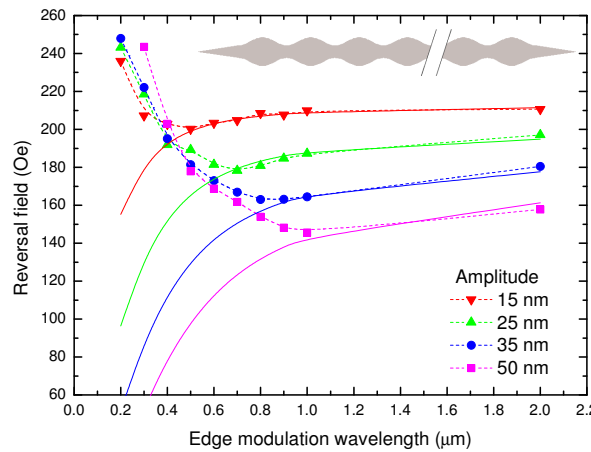he 10 nm nanostructure. This difference may be due to the fabricational roughness, slight differences in magnetic parameters and stochastic thermal effects which are not accounted for in the micromagnetic simulations. The other two parameters show similar values when fitted to the different datasets where γ shows a well defined amplitude depend contribution. δ acts as a correction to the ratio, A_m/λ_m, and it is interesting to note that it takes the value $\delta \approx 2$ showing this effect is actually governed by twice the ratio of A_m/λ_m for reasons that are not completely understood. A similar factor of 2 also appears in figures 9.6 and 9.9 where the minimum reversal field occurs at $\lambda_m/2A_m \approx 10$.

9.5   Magnetisation stabilisation with short wavelength edge modulation

This model gives a good explanation of the magnetisation reversal behaviour for long wavelength modulation; however both the experimental results and micromagnetic simulations show a sharp increase in reversal field for short wavelength modulation that is not explained by the model. This increase in reversal field is associated with the gradual increase in magnetisation shown by the hysteresis loops in figures 9.3 and 9.5. This suggests a transition in spin structure towards a lower energy configuration that stabilises the magnetisation, requiring a further increase in the field to overcome the energy barrier for magnetisation reversal.

Further analysis of this short wavelength regime was performed on the micromagnetic spin structures. Examples of the spin configuration in a $\lambda_m = 0.4$ μm, $A_m = 35$ nm and 5 nm thick structure are shown in figure 9.10 for various applied fields. With no applied field the spins appear symmetric about the wire axis where small deviations from the axial alignment occur due to the edge contours as previously discussed. An increase in field up to 120 Oe, which is beyond the onset of the gradual magnetisation increase, leads to a spin rearrangement to a state with magnetisation components orthogonal to the nanowire axis in the lobed sections. These orthogonal components develop with a further increase in field before the eventual reversal of the magnetisation at the reversal field (168 Oe in this case).

The more complex spin configuration for the short wavelength modulation appears to be related to the wider geometry of the lobed sections of the nanowire. To further understand this effect, these lobed sections were modelled as a series of ellipses as illustrated in figure
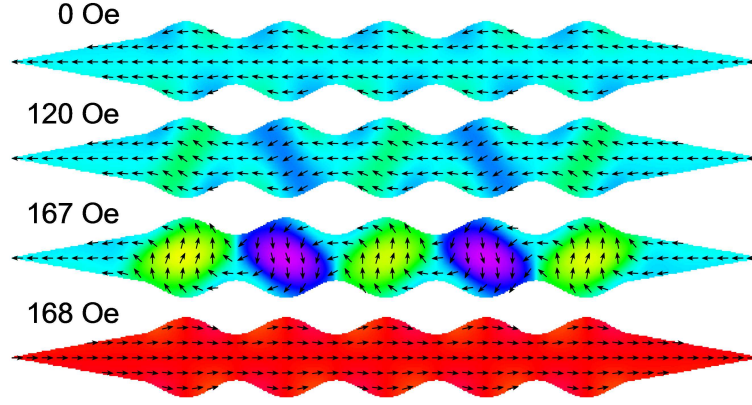
Figure 9.10: Micromagnetic simulations of the spin structure for a 5 nm thick structure with $\lambda_m = 0.4\,\mu$m and $A_m = 35$ nm. The effect of increasing field on an initially saturated structure shows a transition to a spin configuration with localised orthogonal magnetisation before the eventual magnetisation reversal at the reversal field.

9.11. The shape anisotropy associated with the ellipse is linked to the modulation parameters where a reduction in wavelength or an increase in the amplitude reduce the shape anisotropy contribution along the length of the nanowire. In the extreme case, the shape anisotropy of the ellipse can give rise to a preferential magnetisation which lies orthogonal to the nanowire axis. The changes in this behaviour are best illustrated by the comparison between two modulated wires of different wavelength with the same modulation amplitude. In figure 9.11, for long wavelengths the long axis of the ellipses lie along the nanowire axis, but with the reduction in wavelength, the long axis of the ellipses are now orthogonal to the nanowire.

Micromagnetic analysis was performed on individual ellipses with a height equal to the average wire width plus twice the amplitude, and the length of the ellipse was approximated by the wavelength of the modulation. Figure 9.11 shows that the wavelength is an overestimate of the length of the ellipse; however this simplified model still reproduces some of the
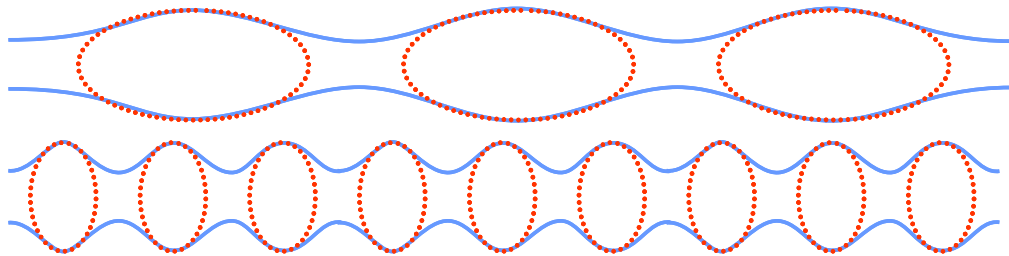
Figure 9.11: Schematic diagram showing how nanowire edge modulation leads to lobed regions in the geometry which can be represented by a series of ellipses. Comparison between two different wavelengths shows how the long axis of the ellipse, and hence the shape anisotropy, can transition from parallel to orthogonal alignment with the nanowire.

interesting behaviour observed in the edge modulated nanowires.

Figure 9.12(a) shows the increasing field section of the hysteresis loops obtained from micromagnetic simulations performed on ellipses with a height of 320 nm with various lengths. The hysteresis loop shape shows a similar behaviour including sharp reversal for long ellipses and a more gradual magnetisation increase followed by the sharp reversal for the ellipses with a shorter length. In the extreme case when the ellipse length decreases below 0.4 μm, the height of the ellipse becomes greater than the width. This swaps the easy and hard shape anisotropy axes of the system and the hysteresis loop then shows the behaviour of the magnetisation along the hard axis of the ellipse. This behaviour is quite different showing the immediate rotation of the magnetisation at zero field to a state with only a small x-axis magnetisation component. A much larger field is then needed to achieve magnetic saturation in these samples which is achieved through a gradual magnetisation increase.

Figure 9.12(b) shows the micromagnetic spin structure for 5 nm thick, 320 nm high, 0.2 μm and 0.6 μm wide structures shown with 0 Oe and 100 Oe applied fields. The 0.6 μm wide structure shows the magnetisation initially oriented to the left. At 100 Oe, beyond the reversal field, the magnetisation has reversed and is orientated to the right. For the 0.2 μm wide structure the magnetisation initially rotates as it is more energetically stable along the vertical direction. The application of the field acts to rotate the spins along the axis of the field but even at 100 Oe a vertical magnetisation component is still present.

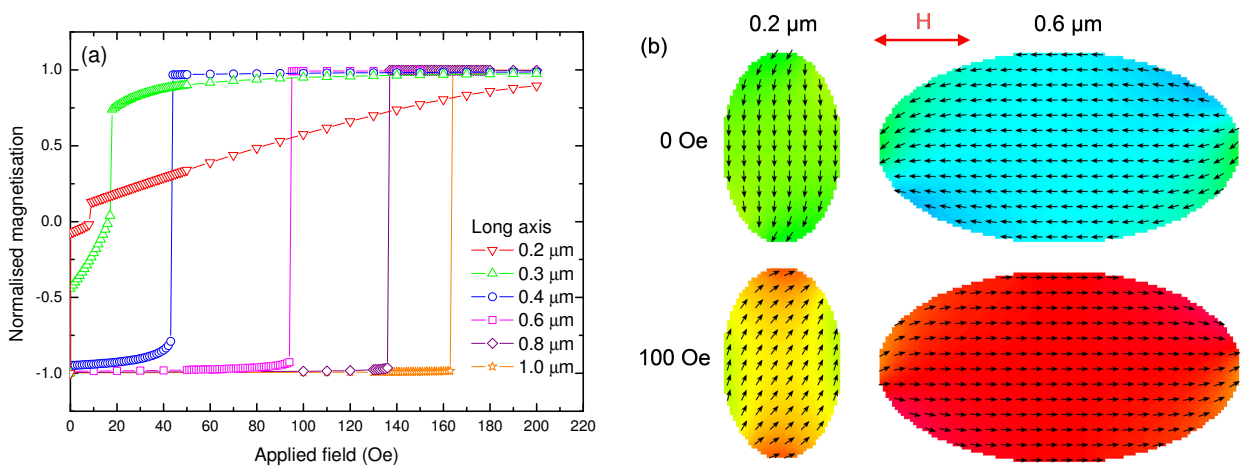**Figure 9.12:** a) Increasing field sections from the hysteresis loops and b) micromagnetic spin structures of the elliptical structures at 0 Oe and 100 Oe axial field, showing the effect of the different shape anisotropy directions. These simulations are performed on a 5 nm thick elliptical structures with various lengths and a width of 320 nm, corresponding to a 250 nm wide nanowire with 35 nm edge modulation amplitude,

The reversal fields for the elliptical structures extracted from figure 9.12(a) are shown in figure 9.13(a) as a function of the width and length of the ellipse. Here, for the larger width ellipses, similar behaviour is observed to that in the long wavelength edge modulated wires which is again accounted for by the spins following the edge contours of the structure. For the case of shorter ellipse width, an obvious reversal field does not exist, instead a gradual increase in magnetisation is found to occur up to much greater fields.

This change in easy axis shape anisotropy in the ellipses gives rise to the physical phenomenon behind the increase in reversal field at short wavelengths. However, for the edge modulated nanowires an abrupt switching at low wavelengths was observed which contrasts with the more gradual magnetisation reversal found for the ellipses. This difference can be explained by the additional global shape anisotropy associated with the nanowire structure which competes with the localised shape anisotropy of the lobes. The observed effect is likely to be a combination of the behaviours of both structures and can explain the abrupt reversal behaviour and the shift towards higher fields.

Another difference between the simplistic ellipse model and the modulated nanowire structure is due to the magnetisation orientation along the easy axis of the ellipse. In the case of one elliptical structure, the magnetisation has a energy preference to align along the easy axis where both orientations along the axis are energetically equivalent. When multiple elliptical lobed regions along a nanowire are considered, the demagnetisation of one lobe has a small effect on the energy of its neighbouring lobe. This leads to the large scale ordering that can
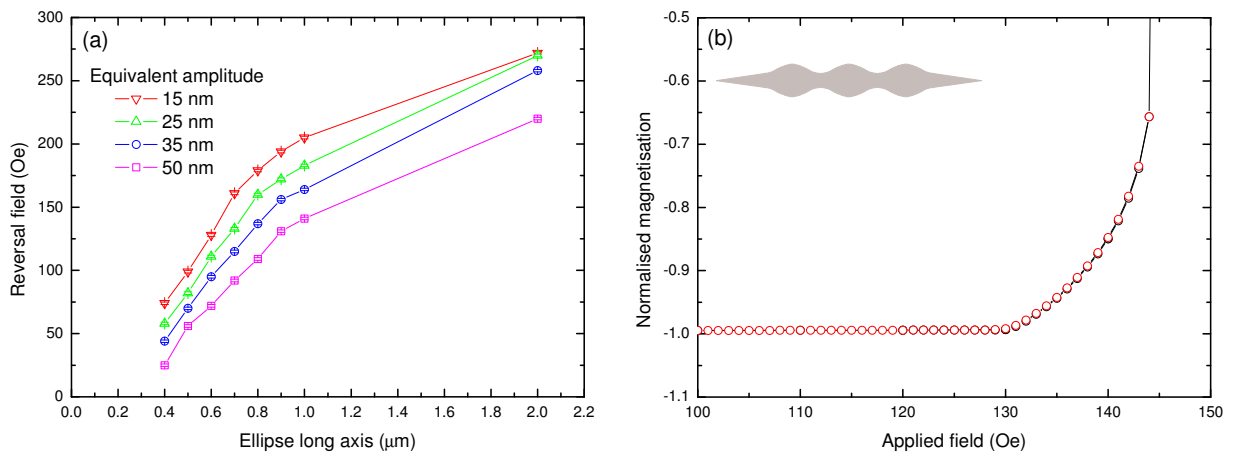

Figure 9.13: a) The reversal field obtained from micromagnetic simulations of elliptical structures as a function of their geometry. b) The magnetisation behaviour obtained from micromagnetic simulations of a 35 nm amplitude, 6 μm wavelength, 5 nm thick nanowire structure with field increased to 144 Oe followed by a decrease in the field.

217

be seen in figure 9.10 giving neighbouring lobes an opposing magnetisation orientation.

This figure shows the alternating magnetisation direction across every lobe; however, in some cases, there are defects in this ordering which are likely to be due to the initial magnetisation direction set at two different lobes at different places in the wire before the effect propagates to fill the whole wire. In these cases, there is no significant effect on the reversal field of the wire and therefore this large scale ordering is believed to give only a small perturbation to the energy of the system.

The analysis here has shown that the shift in localised shape anisotropy to an orthogonal alignment with the nanowire means that a greater field is required for the magnetisation reversal with low wavelength, high amplitude edge modulations. This occurs due to the development of a micromagnetic spin arrangement with magnetisation orthogonal to the nanowire axis. The onset of this new spin state is governed by the spin angle model but it is unclear what governs the eventual reversal field for these structures.

Figure 9.13(b) shows the magnetisation response of the modulated wire structures with increasing then decreasing fields across the region of gradual magnetisation change. There is no significant difference in magnetisation behaviour between increasing and decreasing fields, indicating that this process is reversible with no energy barrier separating the two states.

To explain the preference for the system to adopt the new spin state with increasing field without overcoming an energy barrier, the new spin state must be at a lower energy configuration. This is surprising since an increase in field should lead to an increase in energy of the system. It is however the total energy that is the important quantity and the previous simulations give the micromagnetic spin configurations where the total energy is minimised by the transition into the new spin state for each field value.

The variation in total energy of these different spin states was calculated from micromagnetic simulations for a range of applied fields. In these simulations the system was not allowed to evolve, enabling the determination of the energy for a non-equilibrium fixed-spin configuration. The total energy for a selection of fixed-spin configurations are plotted as a function of the applied field in figure 9.14, showing a linear increase in energy for each spin structure. A Zeeman energy contribution gives rise to the linear increase in energy with field where the gradient is governed by the micromagnetic spin structure. Additionally, exchange and demagnetisation energy contributions give rise to a constant energy term leading to an offset in the energy. The figure shows how a gradual transition between spin states allows
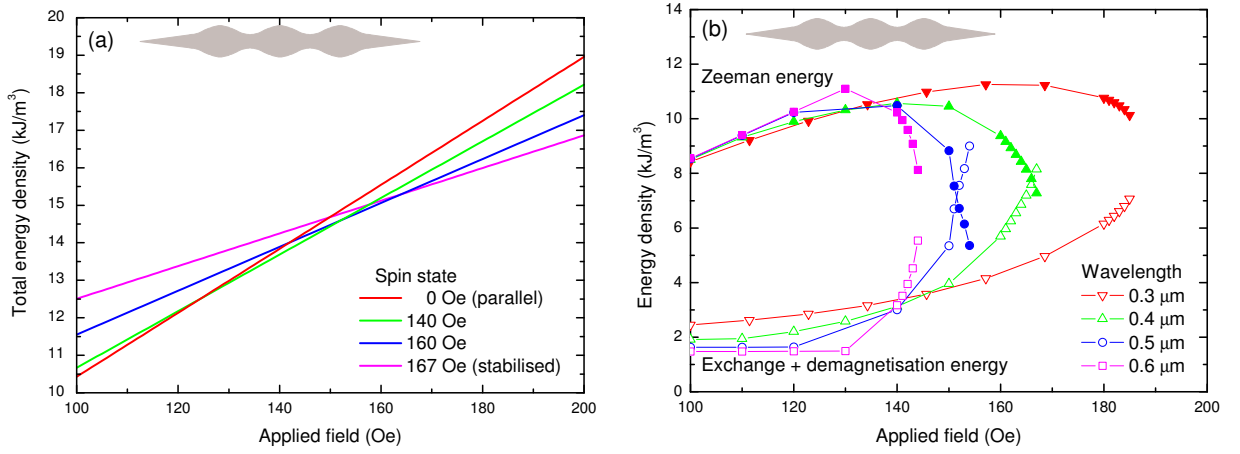
Figure 9.14: a) Total energy of a 5 nm thick modulated nanowire with $A_m = 35$ nm and $\lambda_m = 0.4~\mu$m as a function of magnetic field. The micromagnetic spin structure is fixed in the equilibrium state obtained from previous simulations at various applied fields. b) The contributions to the minimised total energy for the $A_m = 35$ nm structure at various wavelengths as a function of applied field showing changes in the contribution to the total energy before the reversal field.

the system to maintain a minimum total energy when the applied field is increased.

The contributions to total energy from the Zeeman, exchange and demagnetisation energies are shown separately in figure 9.14(b) as a function of field for various different modulation wavelengths. Here, the decrease in the total energy is explained by a reduction in the Zeeman contribution which outweighs the increase in exchange and demagnetisation energy associated with the more complex spin structure. These contributions show that a discontinuity arises at the reversal field where the Zeeman contribution approaches zero and the exchange and demagnetisation contributions approach ∞. This goes some way to explaining the increased reversal field in these structures.

The combination of these physical mechanisms explains the complex behaviour of the reversal field as a function of edge modulation wavelength. For long modulation wavelengths and low amplitudes the reversal field is explained by a model based on the spins following the nanowire edge contours which are at an angle relative to the field along the nanowire axis. This accurately describes the reversal field down to shorter wavelengths where competition between the localised shape anisotropy of the lobes competes with the long axis shape anisotropy of the wire, leading to an increase in reversal field. This comes with a change in behaviour showing a gradual magnetisation increase with a micromagnetic spin configuration including regions of magnetisation orthogonal to the wire axis in the lobed regions. This provides a qualitative explanation for the increase in reversal fields.

9.6 Domain wall mediated reversal in edge modulated nanowires

So far this chapter has considered the magnetisation reversal behaviour in edge modulated nanowire structures governed by the nucleation along the wire. In this section, magnetisation reversal mediated by domain wall propagation is investigated as a function of the edge modulation parameters.

9.6.1 Domain wall injection from a nucleation pad

To investigate the properties of domain walls in these structures, nominally identical arrays of edge modulated nanowires were fabricated with the inclusion of a domain wall nucleation pad on one end of each nanowire, as illustrated in figure 9.15. This allowed the controlled formation of a reverse domain and associated domain wall that could be injected into the nanowire at a relatively low field to investigate reversal via domain wall propagation. These structures were fabricated in the same lithographic and deposition process, on the same substrate as the previous structures. Therefore the possibility of any changes in behaviour resulting from differences in the growth quality, film thickness or development procedure can be ignored. This also allowed a direct comparison between the domain wall mediated behaviour and the nucleation field dependence in nominally identical modulated structures.

Investigation into the magnetic properties of these arrays of wires by MOKE magnetometry yielded hysteresis loops from which the reversal field was extracted. This is shown in figure 9.16 as a function of the edge modulation parameters where the magnetisation reversal occurs at ≈ 120 Oe and was largely independent of the edge modulation wavelength and amplitude for the majority of the wires investigated. Towards shorter wavelengths an increase in the reversal field was found that was more significant with larger amplitude modulation.
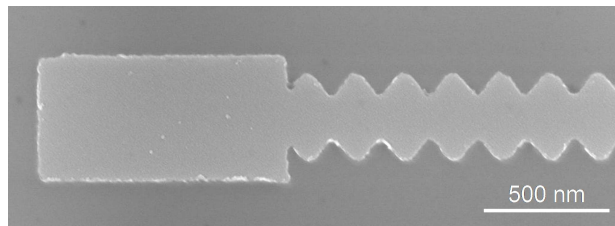
Figure 9.15: Scanning electron microscope image of an edge modulated nanowire with the inclusion of a 1 μm long, 500 nm wide domain wall nucleation pad at one end.
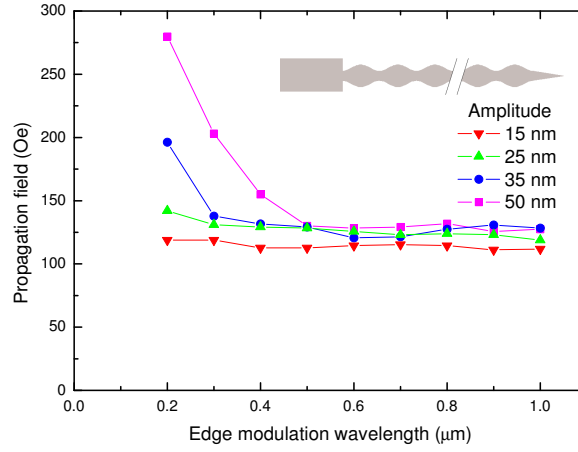
Figure 9.16: Magnetisation reversal field obtained from MOKE measurements representing the domain wall propagation field in edge modulated nanowires. Domain walls were introduced from a 1 μm long, 500 nm wide domain wall nucleation pad.

In comparison to the structures with two tapered ends, the reversal of the nanowires with the nucleation pad occurs at a lower field. This difference is due to the injection of a domain wall from the domain wall nucleation pad, followed by the reversal of the magnetisation by domain wall propagation at a lower field than that required for direct nucleated reversal in the structures without nucleation pads.

In these experimental results the reversal field describes the magnetisation reversal for the whole system. This includes both the propagation characteristics of the domain wall in the edge modulated nanowire structures and the domain wall injection characteristics of the nucleation pad. For the case when the propagation field is greater than the injection field of the pad, the measured reversal field is limited by the propagation field of the nanowire. However, if the injection field of the pad is the greater of these two factors, this becomes the limiting factor and the reversal field represents only the injection field from the pad.

The plateau in figure 9.16 showing no dependence on edge modulation parameters suggests these measurements are limited by the injection field of the pad. This ≈ 120 Oe field is also typical of the injection field expected from this sized pad structure.[1] The nanowires with short wavelength edge modulation show a reversal field that rises above the injection field limited data. This represents the real propagation field for domain walls in these structures.

9.6.2   Domain wall injection through localised pulsed fields

Further investigation into the domain wall propagation in these structures requires the injection of domain walls at lower fields. To achieve this, an alternative domain wall injection stripline technique was adopted where domain walls were injected into the nanowires by a localised pulsed magnetic field. This field is generated from a current flowing along a stripline, perpendicular to the nanowires, such that a domain wall was nucleated at the intersection point. Since this pulsed injection field was separated from the quasi-static field used to drive the reversal in the whole structure, domain wall propagation at lower quasi-static fields could be investigated.

Striplines were fabricated on top of the edge modulated nanowire structures with two tapered ends which were measured for their intrinsic switching behaviour. This additional fabrication step is described in section 5.6.3. In principle, a sufficiently large pulsed current can create a domain wall without the need for additional external applied fields. The later addition of a quasi-static field can be used to propagate the domain wall. However, the stripline fabricated here required a small additional quasi-static field so that the sum of the pulsed and quasi-static fields was sufficient to overcome the field for domain wall nucleation at the localised intersection point. The pulsed fields were synchronised with the quasi-static field applied during MOKE measurements resulting in a change to the hysteresis loops based on the trigger point and magnitude of the pulsed field. A measurement scheme, explained in more detail in section 5.6.3 gives the reversal field for these structures which is shown as a function of the edge modulation parameters in figure 9.17.

Figure 9.17: Magnetisation reversal field obtained from MOKE measurements on edge modulated nanowires where domain walls are introduced through a pulsed magnetic field stripline approach.

This figure also shows a plateau in the reversal field, independent of modulation parameters for the longer wavelength modulation but at a lower field compared to the plateau obtained with the pad injection. At shorter wavelengths the reversal field incr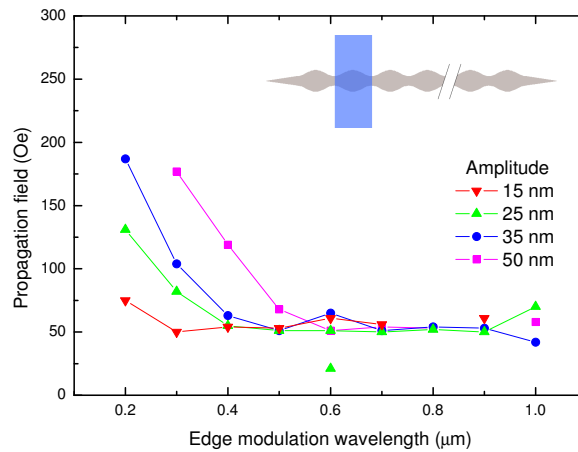ease is most significant for the large amplitude modulation. This agrees with the limited results obtained from the nucleation pad domain wall injection technique.

The reduced reversal field of the plateau confirms that the previous plateau originated due to an artefact of the nucleation pad domain wall injection and therefore does not represent the properties of the edge modulated nanowires. With the domain wall injection stripline the plateau is lowered, revealing more of the low wavelength results that show propagation field limited behaviour. Even though this pulsed field technique gives significant improvements in the results, the measurements are still limited by the maximum pulsed fields that can be obtained from the stripline. By pushing the limits of the pulsed field magnitude from the stripline, additional measurements were performed on the 25 nm amplitude, 0.6 μm wavelength structure. This allowed the lower bound on the propagation field for this wire to be reduced to 21 Oe; however, this led to burn-out of the stripline so measurements could not be repeated for other structures. Therefore, the data in the long wavelength region represents an upper bound for the propagation field of domain walls in these structures.

9.6.3 Micromagnetic analysis of domain wall de-pinning fields

The de-pinning field for domain wall motion in edge modulated nanowire structures has also been investigated using micromagnetic simulations. Starting with a transverse domain wall in a nanowire structure, an increasing axial field was applied until the domain wall de-pinned from any localised pinning potentials along the wire and completed the magnetisation reversal. The de-pinning fields found from a detailed series of simulations are shown in figure 9.18 as a function of the edge modulation parameters for both a) 5 nm and b) 10 nm thick nanowires.

These results show a constant de-pinning field, independent of modulation parameters, for longer wavelength modulation with an increase in the de-pinning field towards shorter wavelengths that is more significant for the larger amplitude modulation. The de-pinning field for the 10 nm thick nanowires is greater than that of the equivalent 5 nm thick nanowire. The trends agree with those found from experimental results; however the values of the modulation limited de-pinning fields are greater in the micromagnetic simulations. This is
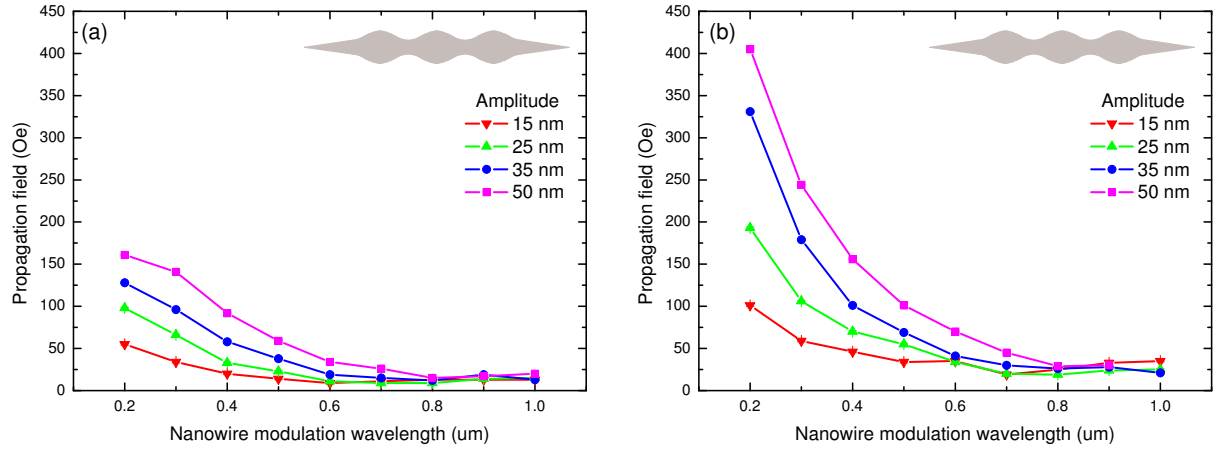
Figure 9.18: Micromagnetic simulations of the domain wall de-pinning field as a function of edge modulation parameters for a a) 5 nm and b) 10 nm thick modulated nanowire.

consistent with the overestimates obtained from the micromagnetic simulations of the direct switching in modulated structures with two tapered ends.

The de-pinning field for long and short wavelengths measured by this technique agree with the micromagnetic simulations as far as the experiments show. The behaviour at long wavelengths is unaffected by the edge modulation but as the wavelength is reduced an increase in de-pinning field occurs which is greater for the larger amplitude modulation.

With infinite wavelength, the edge modulation can be considered as a planar wire with no edge modulation. Here, the de-pinning field is low and represents unhindered domain wall propagation along a nanowire. As the wavelength is decreased the de-pinning field increases which is more significant for the larger amplitude modulation. This is accounted for by an increase in domain wall pinning resulting from the local effects of the edge modulation.

9.6.4 Local pinning from nanowire modulations

This behaviour is investigated through further analysis of the micromagnetic simulations which show the spin configuration of the domain walls in the nanowire structures. Examples of these are shown in figure 9.19 for 5 nm thick wires with 0.3 μm wavelength modulation at various amplitudes. These domain wall spin structures are shown at an energetic minimum in zero field and just below their de-pinning field.

At zero field the domain wall adopts an asymmetric transverse wall structure and traverses one of the lobed wire sections of the nanowire. The spin structure of this wall is then modified by the application of the axial magnetic field bringing it to a more symmetrical configuration,
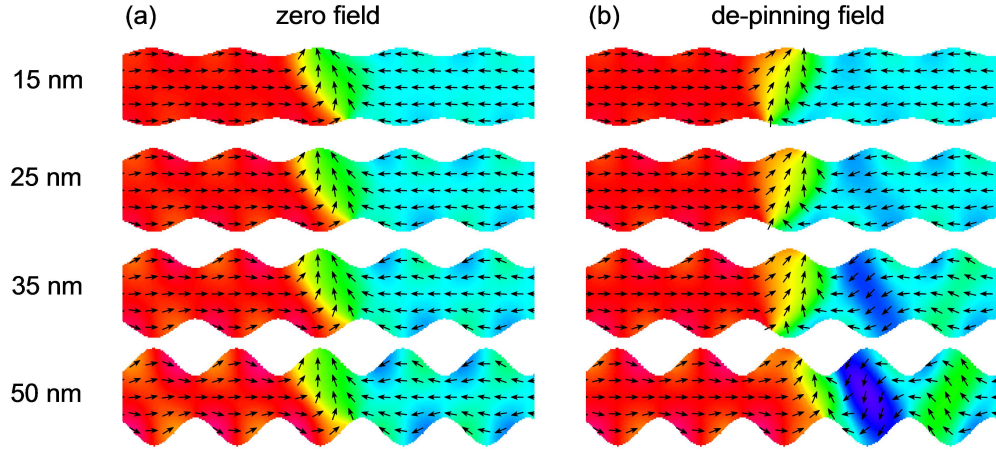
Figure 9.19: Micromagnetic spin structure of transverse domain walls in a 0.3 μm wavelength nanowire with various modulation amplitudes at a) zero field and b) just below the de-pinning field.

before eventually de-pinning from the lobe. For 50 nm modulation amplitude, the domain wall shifts towards the constriction forming an additional state of reduced energy before de-pinning. The structure of this domain wall depends on the relative contributions to the energy from the demagnetisation and exchange terms. A domain wall pinned within an edge modulated nanowire feels the effect of the periodic effective field and has a reduced energy when the orthogonal component of magnetisation of the domain wall is coincident with a wider lobe section. However, this leads to a competing effect where an increase in the area of the domain wall leads to an increased exchange contribution. A minimum equilibrium energy configuration is established by the transition into an asymmetrical domain wall structure.[278–280]

As modulation wavelength is decreased or the amplitude increased, the lobed regions along the nanowire have increased localised orthogonal shape anisotropy. This will further reduce the energy of the domain wall leading to increased pinning and therefore a greater de-pinning field for the shorter wavelength, higher amplitude modulation.

This pinning behaviour results from the effect of the localised orthogonal anisotropy in the lobed sections along the wire. However, the experimental results only interrogate the magnetisation state following the propagation of the domain wall over many wavelengths of edge modulation. The consistency of this propagation was confirmed in an extended 40 μm long nanowire with 1 μm wavelength and an amplitude of 100 nm shown in figure 9.20. Here, the samples were fabricated and the measurements performed by E. Arac. The magnetisation switching was found to be consistent from multiple positions along the nanowire indicating
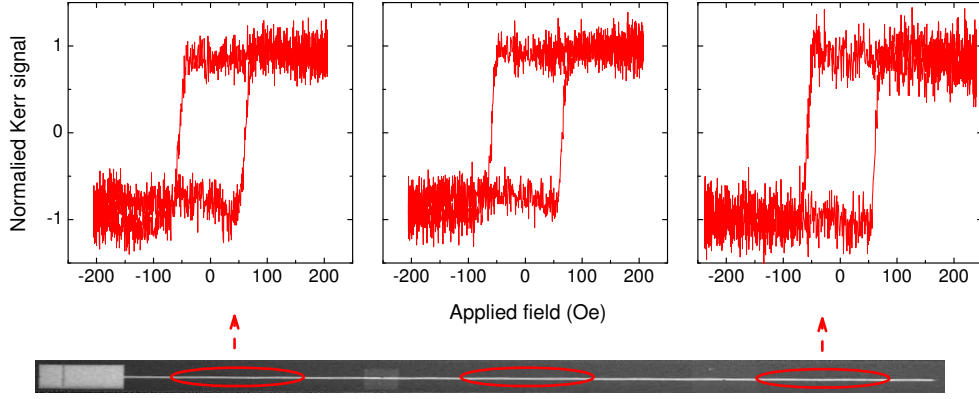
Figure 9.20: MOKE measurements at three positions along a 40 μm long edge modulated nanowire with $\lambda_m = 1$ μm and $A_m = 100$ nm that indicates the consistency of the domain wall propagation along the modulated structure.

that once a domain wall de-pins from one section of the modulated wire, the wall propagates through all subsequent lobes at the same field.

9.7 Domain wall dynamics in edge modulated nanowires

So far this chapter has considered the quasi-static magnetisation reversal behaviour for edge modulated nanowire structures. This has included the magnetic reversal of the structures due to nucleation and also the reversal mediated by the propagation of domain walls. The variation in the propagation field for domain wall motion has been attributed to the interaction between the wall spin structure and the localised geometrical structures along the nanowire resulting from the edge modulation. The remainder of this chapter considers the dynamic properties of these domain walls as they propagate along the edge modulated nanowire structure. These are examined through further detailed micromagnetic modelling where additional considerations are taken into account due to the dynamic nature of these simulations. These considerations are detailed in chapter 5 where the Gilbert damping parameter is of particular importance and is set to a more realistic value of $\alpha = 0.01$.

9.7.1 Unmodulated nanowires

Initially the domain wall dynamics in an unmodulated, 5 nm thick, 250 nm wide nanowire were investigated in a 5 μm long wire with two tapered ends. A transverse domain wall structure was introduced towards the left edge of the nanowire and allowed to propagate in

an axial magnetic field, maintained at a fixed value throughout the duration of the simulation. Further details of the simulations are described in chapter 5.

The domain wall propagation is shown as a function of elapsed time in figure 9.21 for fields of 10 Oe and 20 Oe, directed along the nanowire axis, below and above the Walker field respectively. Below the Walker field, a transverse domain wall propagates consistently along the nanowire structure, maintaining its transverse domain wall structure. However, above the Walker field, the effects of Walker breakdown become evident. The initial transverse domain wall structure is modified by an antivortex core which nucleates on one end of the domain wall structure. This core traverses the wire width, reversing the wall chirality, and annihilates on the opposite edge. The domain wall, then proceeds to propagate until the whole process is repeated. Note, in figure 9.21 the snapshots are not performed with the same time intervals and indicate that the propagation at 20 Oe is on average much slower than that at 10 Oe.

During propagation of the domain wall, the size of the domain aligned with the field increases at the expense of the other domain leading to an increase in the magnetisation. This allows the domain wall position to be extracted from the magnetisation component along the nanowire axis. This position is shown in figure 9.22(a) as a function of time during the application of the field.

For fields below the Walker field, a linear increase in magnetisation represents uniform domain wall motion where the velocity can be determined from the gradient. However, when the applied field exceeds the Walker field, the magnetisation shows the periodic behaviour in
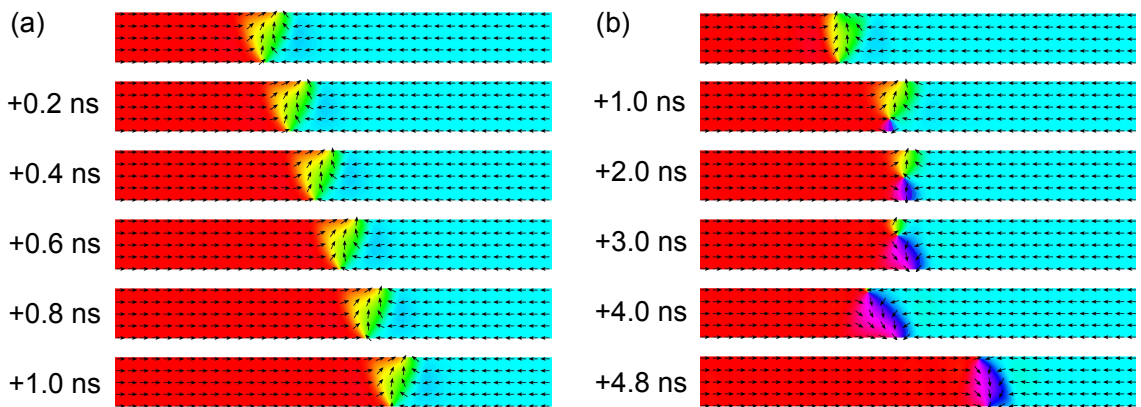
Figure 9.21: Micromagnetic simulations of a domain wall spin structure a) 10 Oe undergoing uniform motion and b) at 20 Oe undergoing Walker breakdown which includes periods of retrograde motion.
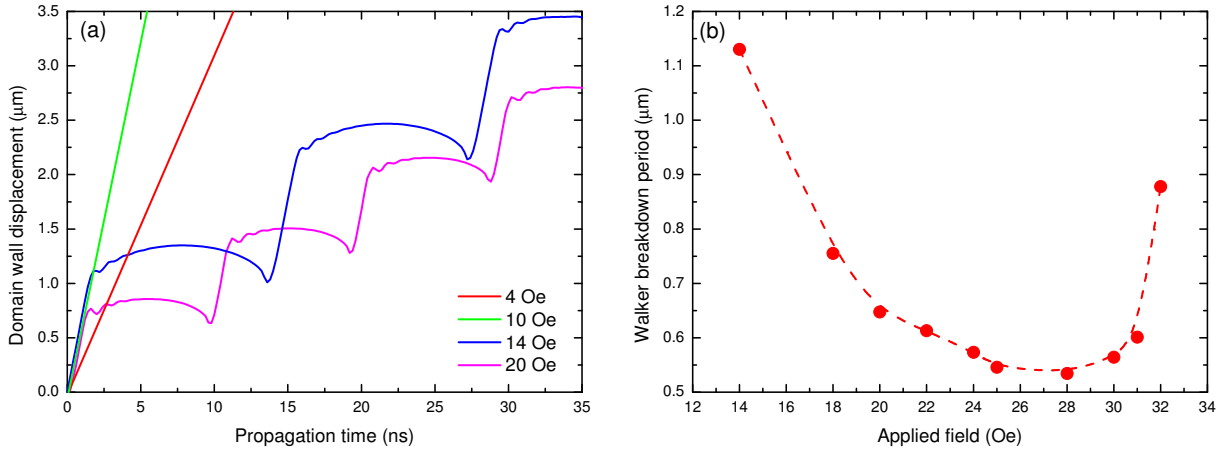
Figure 9.22: Micromagnetic simulations showing a) the change in magnetisation as a function of time and b) variation of Walker breakdown period for domain wall motion in a 5 nm thick, 250 nm wide unmodulated nanowire for different magnitudes of the magnetic field.

the position of the domain wall which includes periods of fast motion and then a prolonged period of little change in position followed by a period of retrograde motion. The domain wall velocity at these fields is taken from the time-averaged gradient of magnetisation over several periodic cycles. This figure also shows that the periodicity of this effect remains constant during propagation and has a field dependence that shows an increase in the periodicity for larger fields.

In figure 9.22(a) this periodicity appears as a temporal periodicity; however it is more useful to represent this periodicity as a spatial periodicity. This results in Walker breakdown with a more frequent temporal periodicity due to an increase in field leading to a shorter spatial periodicity.

By comparing the domain wall propagation from many dynamic simulations, the field dependence to the Walker breakdown periodicity was found and is presented in figure 9.22(b). A decrease in the spatial periodicity was found to correspond to an increase in applied field until it reaches a minimum at ≈ 0.55 μm for a field of ≈ 30 Oe. At higher fields, further effects lead to an increase in periodicity associated with an increase in domain wall velocity but where the spin structure of the domain wall becomes noticeably distorted. In this case the definition of this spin structure as a domain wall may not hold true.[281] This periodicity dependence of the domain wall propagation is determined from the parameters such as the saturation magnetisation, M_s, exchange constant, A, and the Gilbert damping parameter, α, for the material.

Following this analysis of the periodic Walker breakdown behaviour in a plain nanowire structure it is interesting to investigate the behaviour in nanowires with periodic edge modulations. Here, the relationship between the periodic domain wall structural transformations during domain wall motion is affected by the periodic geometry which will lead to a variation in the energy landscape along the nanowire structure. This section investigates the effects of the structural modulation parameters on the dynamic domain wall behaviour in edge modulated structures.

9.8 Dependence of domain wall velocity on modulation amplitude

In the first instance the effect of edge modulation amplitude on the dynamic properties was investigated for nanowires with a fixed wavelength of 0.4 μm. This value was chosen to be below the minimum Walker breakdown periodicity of ≈ 0.55 μm for the unmodulated nanowire. Figure 9.23 shows how the field dependence to the time-averaged domain wall velocity is affected by the modulation amplitude.
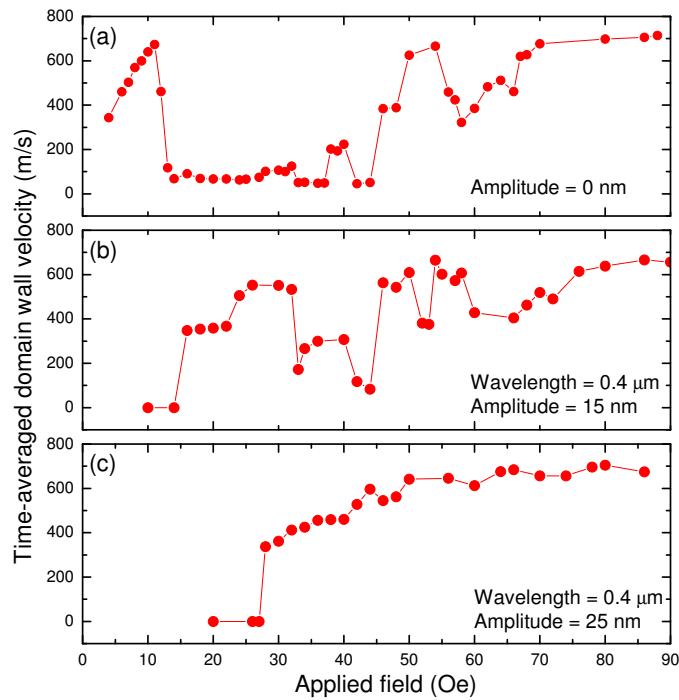
Figure 9.23: Micromagnetic simulations of domain wall velocity as a function of applied field for different edge modulation amplitudes in a 5 nm thick nanowire with an average width of 250 nm and a modulation wavelength of 0.4 μm. The effect of a) an unmodulated nanowire is compared to a nanowire with b) 15 nm and c) 25 nm edge modulation amplitude.

In the unmodulated case a linear increase in velocity occurs before a dramatic reduction at the Walker field. This is followed by a regime of slow domain wall motion with little effect from the applied field. Above 30 Oe, chaotic Walker breakdown occurs, where the domain walls can propagate faster but the structure of the domain wall is complex and the periodicity is hard to define.[281]

An edge modulation amplitude of 15 nm gives rise to regions of high domain wall velocity which appear for fields where Walker breakdown behaviour occurs in the unmodulated nanowire. These regions of fast motion are interrupted by low velocity regions showing the effects of Walker breakdown. The combination of these regions results in a complicated field dependence to the velocity. An amplitude of 25 nm allows a high domain wall velocity to be maintained over a wide field range where the effects of Walker breakdown have been suppressed. The velocity is high and has little variation over a wide field range. This behaviour presents significant improvement over the domain wall dynamics for the unmodulated nanowire.

This improvement in the domain wall velocity is however associated with an increase in the de-pinning field with modulation amplitude. This is the field required to overcome the pinning potential for a domain wall in the edge modulated structures and is the same de-pinning field discussed earlier in this chapter with the results in figures 9.16 and 9.17.

9.8.1 Nanowire modulation wavelength affect on domain wall Walker breakdown dynamics

In figure 9.23, nanowires with a 0.4 μm wavelength were chosen to be below the Walker breakdown periodicity of the plain nanowire structure. However, this may not be the optimum periodicity for enhanced domain wall dynamics. This section presents simulations where the domain wall velocity was investigated as a function of the edge modulation wavelength.

A detailed series of dynamic micromagnetic simulations were used to explore this relationship between edge modulation wavelength and Walker breakdown periodicity. The structures all contained 25 nm amplitude modulation with a range of wavelengths both above and below the ≈ 0.5 μm period of Walker breakdown. The results of these simulations are combined into the phase diagram shown in Figure 9.24 which presents the domain wall velocity as a function of both applied field and structural wavelength.
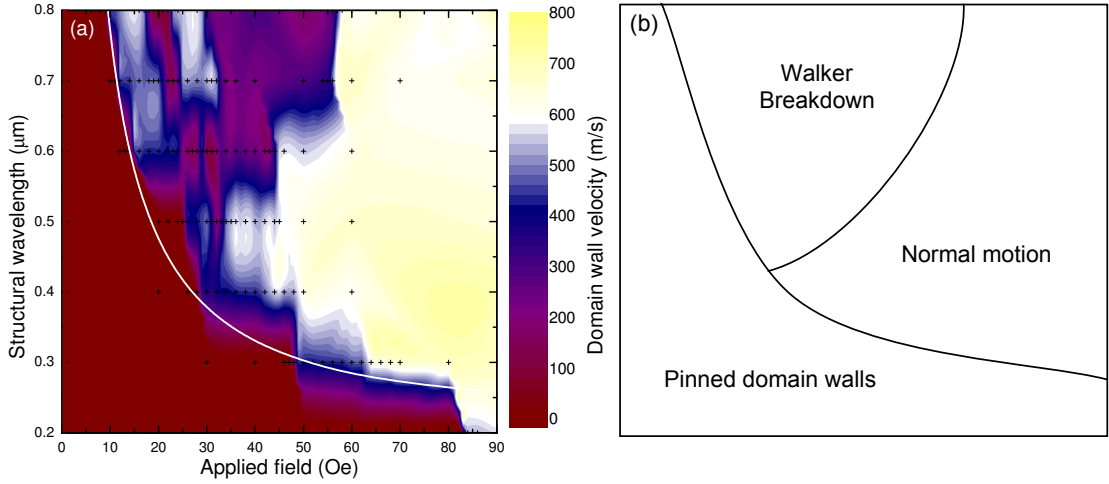
Figure 9.24: Phase diagram showing the time-averaged domain wall velocity in a 25 nm amplitude modulated nanowire as a function of the modulation wavelength and applied field. Three different regimes of behaviour are identified a) in the micromagnetic simulations and b) shown more clearly by the schematic illustration. These include pinned domain walls at low applied fields, propagating domain walls above the de-pinning field (shown by the solid line) and a regime showing complex dynamics for the longer wavelength modulation above the de-pinning field.

At low fields the dark regions represent pinned domain walls whilst the lighter regions towards higher fields represent fast domain wall motion. At intermediate fields for $\lambda_m > 0.5$ μm a region showing complex domain wall dynamics is observed.

The de-pinning field behaviour seen in figures 9.16, 9.17 and 9.23 is also apparent in figure 9.24 as an abrupt rise in the velocity which separates the dark pinned region from the light dynamic domain wall region. The de-pinning field variation takes the form of a $1/\lambda_m$ dependence on the edge modulation wavelength and is indicated by the white line superimposed on figure 9.24(a). This is explained on the basis of competing shape anisotropy from the wire axis and the localised elliptically shaped lobes.

Above the de-pinning field the dynamic domain wall properties are revealed. For short structural wavelengths, the velocity increases rapidly above the de-pinning field and remains at a high value until the upper range of the investigated fields. This shows that the Walker breakdown behaviour found for the plain nanowire has been suppressed by the addition of subtle edge modulation. For structural wavelengths $\lambda_m > 0.5$ μm, complex changes in the domain wall velocity are found where Walker breakdown suppression becomes inconsistent and Walker breakdown behaviour reappears at certain fields.

The Walker breakdown suppression becomes consistent at $\lambda_m \approx 0.5$ μm, which interestingly is the periodicity of structural changes for the domain wall undergoing Walker break-

down. In the following sections the mechanism underpinning this Walker breakdown suppression is investigated looking at the link between the modulation wavelength and the periodicity of the micromagnetic structural changes that occur during Walker breakdown.

9.8.2   Walker breakdown suppression mechanism

As previously discussed, Walker breakdown involves the periodic transition between transverse and antivortex core domain wall structures. The mechanism for the suppression of Walker breakdown relies on inhibiting these transitions and allowing a domain wall to maintain its fast moving transverse micromagnetic structure.

The periodic edge modulations to the nanowire effectively lead to a periodic variation in the nanowire width as a function of position along the wire. In chapter 2 the energetics of different domain wall structures in different thickness and width nanowires was discussed. This showed that transverse walls are more energetically stable in thinner wires whilst vortex structures are more stable in wider wires. The combination of this with the periodic variation in nanowire width leads to a periodic energy landscape along the axis of the wire which is opposite for these two domain wall structures.

If a constriction in the wire geometry occurs at a position that coincides with the antivortex core nucleation in the Walker breakdown process, then the energy landscape at this point presents a large energy barrier for the vortex to pass the constriction. It is then energetically favourable for the vortex core structure to transform back into a transverse wall structure which is able to pass through the constriction.

The periodic disruption of the vortex core structure by the arrival of constrictions in the wire geometry, coupled with the periodic nature of vortex core nucleation is the key to the Walker breakdown suppression presented here. The successful suppression for short structural wavelengths is seen in figure 9.24 where the domain wall disruption occurs more frequently than vortex core nucleation. However, for the longer structural wavelengths this disruption misses some of the nucleation events explaining the region of complex behaviour in this figure.

This model also explains the modulation amplitude dependence of the dynamic behaviour seen in figure 9.23. With a greater amplitude the difference in width of the wire becomes more significant, resulting in a larger difference in the energy landscape along the wire. When the amplitude increases past a certain point, the energy barrier for a vortex structure to pass

through a constriction is high enough to force the domain wall to return to its transverse structure. This shows as successful Walker breakdown suppression for amplitudes greater than a certain value.

9.9   Energy dissipation via spin wave emission

As the vortex core structure transforms into a transverse domain wall structure during Walker breakdown suppression, there is a large amount of energy associated with an out-of-plane magnetisation component of the vortex core that needs to be dissipated from the system. This process was investigated through further micromagnetic simulations performed on the dynamics of this transition.

To explain the transition from vortex to transverse domain wall structure it is convenient to examine the results for a wire that experiences normal motion, Walker breakdown and suppressed Walker breakdown as a function of field rather than as a function of wire structuring. This allows the simulation outputs to be compared as a function of just one parameter. Such an example is adopted with 0.8 μm wavelength and 25 nm amplitude modulation from the region showing complex behaviour in figure 9.24. This has been investigated with applied fields at 16 Oe, 18 Oe and 24 Oe. Figure 9.25 shows micromagnetic simulations of the time evolution of a domain wall structure in these modulated wires with these three applied fields. The simulations show an initial transverse domain structure which propagates over one wavelength of the wire structure.
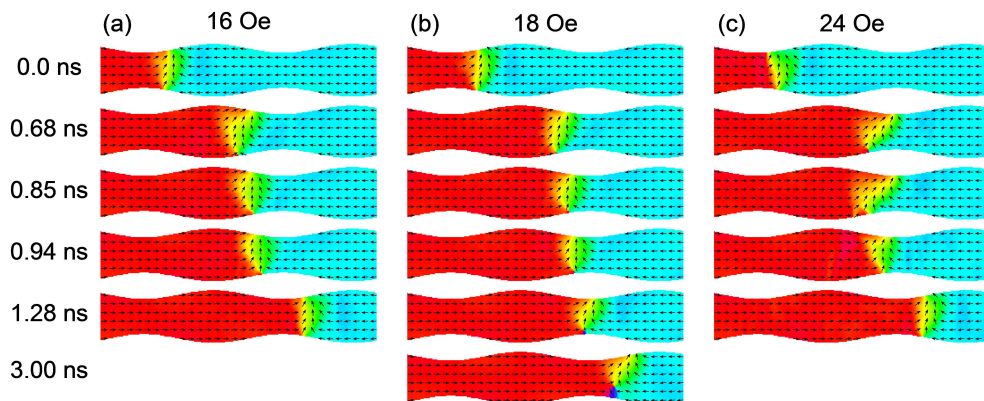
Figure 9.25: Micromagnetic simulations showing domain wall propagation in an edge modulated nanowire structure with 0.8 μm wavelength, 25 nm amplitude and 5 nm thickness. The choice of field results in normal domain wall motion, Walker breakdown and suppressed Walker breakdown behaviour at a) 16 Oe, b) 18 Oe and c) 24 Oe respectively.

At 16 Oe the domain wall propagates over the wire section without any significant changes in its velocity or micromagnetic structure. An increase to 18 Oe shows the onset of Walker breakdown with the vortex core nucleation occurring at the 0.68 ns position on the bottom edge of the wire and progressing with the traverse of the nanowire width. At 24 Oe, vortex nucleation at 0.68 ns is shortly followed by annihilation of the vortex core at 0.85 ns where a spin wave can just be seen radiating from the original vortex location. Following this, the domain wall continues to propagate with a transverse wall structure.

Further analysis of the out-of-plane M_z magnetisation component reveals the details of this process as the vortex core structure is shown by the presence of a large out-of-plane magnetisation component. The time evolution of M_z as a function of position along the nanowires is shown in figure 9.26 for the three regimes of domain wall motion discussed in figure 9.25.

At each field a disturbance in M_z corresponding to the domain wall is seen propagating in the positive x direction. At 16 Oe, the M_z disturbance represents a transverse wall structure, has a low magnitude and travels at a fast velocity. At 18 Oe, the M_z component is much greater, representing the large out-of-plane magnetisation component of a vortex core structure. The slow propagation speed of the vortex core structure shows up as a lower gradient in the figure. At 24 Oe, a spin wave can clearly be seen radiating from the vortex nucleation location and travelling in the negative x direction. The remaining transverse domain wall structure continues to propagate in the positive x direction with the same high velocity as seen in the 16 Oe case.
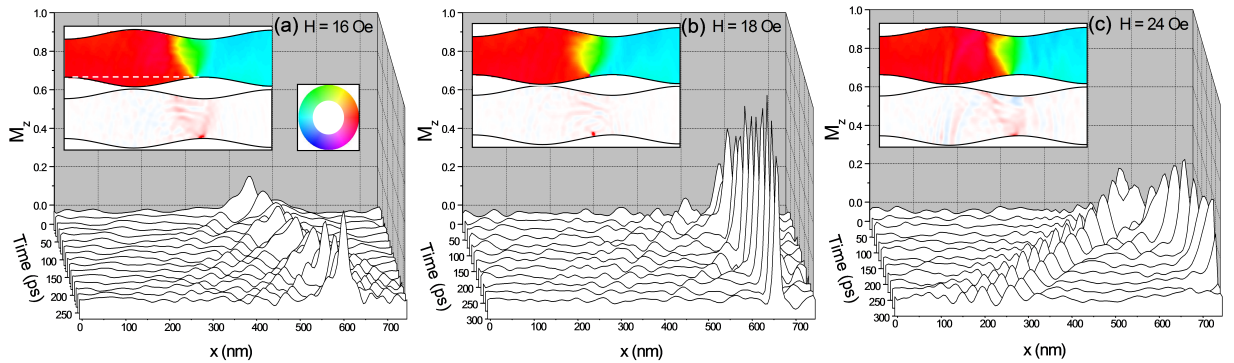
Figure 9.26: Time evolution of the M_z magnetisation component as a function of the position along the axis of a nanowire with 0.8 μm wavelength, 25 nm amplitude and 5 nm thickness. This behaviour is shown for driving fields at a) 16 Oe, b) 18 Oe and c) 24 Oe. The inserts show a snapshot of the M_{x-y} (top) and M_z (bottom) magnetisation components at the 200 ps position and the position of the linescan is illustrated by the white dashed line.

These dynamic simulations have revealed that the emission of spin waves occurs during the transition from vortex core to transverse domain wall structure. This is expected to be the channel for the dissipation of energy from the system. This energy transfer mechanism has previously been considered for the transfer of energy to domain walls by the absorption[3,282,283] and from emission[284] of spin wave energy. This has previously been suggested as a mechanism for stabilising domain wall dynamics in the limit of 'huge anisotropies'.[285,286] However, in this case, the material parameters are still representative of a permalloy structure and this emission is a result of just low amplitude edge modulation.

With a further increase in applied field, figure 9.24 shows complex behaviour with the intermittent occurrence of Walker breakdown suppression. This is explained by considering the energy of the resultant transverse domain wall structure following the emission of the spin wave energy. For greater fields the remaining energy is not adequately reduced to fully prevent the transition to a vortex core structure. This has been observed in further dynamic simulations which are not included here.

The emission of energy in the form of a spin wave from a vortex core structure can be used as a mechanism to dissipate the build up of domain wall energy. This dissipation allows a vortex core structure to return to a transverse domain wall and maintain the fast domain wall motion in the Walker breakdown suppression process.

9.10 Summary

Magnetisation reversal behaviour in nanowires with the inclusion of small amplitude sinusoidal edge modulation to both edges has been investigated. This investigation was performed through both experimental measurements by focussed MOKE magnetometry and through a detailed series of micromagnetic simulations.

The investigation started by considering the magnetisation behaviour governed by nucleation effects within the modulated nanowires. This showed a gradual reduction in reversal field to a minimum with the reduction in modulation wavelength, followed by a steeper increase in reversal field for the case of short wavelength modulation. The gradual decrease in reversal field was explained by an analytic model based upon the torque of a spin following the contours of the modulation, at an angle to the magnetic field along the nanowire axis. This model was fitted to both the experimental and micromagnetic results giving good

agreement and showing the scalability of this analysis for different modulation parameters.

The sharper increase in the reversal field for shorter wavelength modulation originates from competing anisotropies along the nanowire. This is explained in terms of the localised shape anisotropy of a series of ellipses which led to the development of regions of orthogonal magnetisation alignment along the nanowire providing a lower energy spin configuration. The competition between this effect and the global shape anisotropy of the nanowire gives rise to a shift of the reversal field towards higher fields.

The propagation behaviour of domain walls in these structures was investigated through the analysis of the de-pinning field due to the edge modulation. This results in behaviour at long wavelengths consistent with that expected for an unmodulated nanowire structure. With a reduction in modulation wavelength the de-pinning field becomes more significant, particularly for the large amplitude modulation. This effect was also explained due to the localised shape anisotropy of the lobe regions along the nanowire for which the orthogonal spin component of a transverse domain wall structure finds a localised energy minimum and hence experiences stronger pinning.

Domain wall dynamics in these structures were also investigated through further micromagnetic simulations showing that a suitable choice of edge modulation parameters with careful matching to the periodicity of magnetic spin structural transformations during Walker breakdown can be used for the suppression of Walker breakdown. This effect originates from the periodic energy landscape of the domain wall structure during its propagation along a nanowire with periodically varying geometry. The modulation opens a channel such that the build up of domain wall energy is periodically released through the emission of spin waves, maintaining the fast domain wall motion associated with a transverse domain wall structure.

These improvements in dynamic properties gained by the introduction of modulated edges are also hindered by the increase in de-pinning field resulting from the modulation. A phase diagram has shown how the domain wall velocity is affected by both structural wavelength and applied field. From this the effects of de-pinning field and Walker breakdown suppression both show how modulation parameters can be optimised to achieve the best compromise between the two behaviours. This analysis was performed with 5 nm thick nanowires with an average width of 250 nm and 25 nm amplitude modulation but this is just one example. Scaling laws demonstrated here are expected to be applicable to other geometries which may lead to further optimisation of the domain wall dynamics.

Chapter 10

Conclusions and further work

This thesis presents an investigation into the localised control of the magnetic properties in NiFe/Au bilayer systems through modifications to the structure of the material. Two approaches have been considered. First, focussed ion beam irradiation leading to interfacial intermixing, bringing about changes in the magnetic moment of the material. Second, geometrical patterning was used to manipulate the energetic landscape leading to control over the magnetisation behaviour in nanowires. Both techniques have been combined with well established techniques for the control of domain walls in nanowires and lead to a greater understanding of the static and dynamic interactions between domain walls and structuring of the nanowire.

10.1   Conclusions of this study

Focussed ion beam irradiation induced modifications to the bilayer structure were investigated in chapter 6 through grazing incidence x-ray reflectivity and fluorescence techniques. These reveal the damaging effects of high dose irradiation to the crystal structure including sputtering from the sample surface. Additionally the linear increase in the concentration of implanted Ga^+ ions within the near surface region of the material has been characterised. For low dose Ga^+ ion irradiation, intermixing at the interfaces becomes the dominant structural change, leading to the development of a compositionally graded alloy region. This alloy region has been characterised in detail through x-ray scattering techniques to determine the interface width and to differentiate between contributions from topological roughness from intermixing. Further x-ray fluorescence analysis gives an additional element specific compo-

sitional description of the modifications to the bilayer structure.

The combination of x-ray reflectivity and fluorescence analysis is not a common method and these techniques are usually analysed individually. Here, the fitting of a single model to both techniques was demonstrated; however, current computational packages available for fitting the data do not support the fitting of a model to multiple datasets with a single set of parameters. Therefore, a technique was adopted as a compromise, based on the iterative fitting of the multiple datasets, leading to a refinement of the model describing the structure of the materials.

The effect of these interfacial structural modifications on the magnetic properties of the bilayer structures was investigated in chapter 7. At high doses, damage to the structure lead to a degradation of the magnetic properties, eventually leading to a transition from a ferromagnetic to paramagnetic state. More interestingly, complex changes show a dramatic decrease followed by a recovery in the magnetic moment, associated with the development of the intermixed interface for low dose Ga^+ ion irradiation. This gives a new sensitive method to modify the magnetic properties of a material system that can be tuned through the choice of the irradiation dose, capping layer material and thickness.

The magnetic behaviour was observed through MOKE measurements which were followed by SQUID measurements to confirm the behaviour was of magnetic origin. XMCD analysis showed that orbital quenching occurs in Ni and Fe leading to a reduction in moment at a dose coincident with the minimum in the magnetic moment. This, along with anisotropic magnetoresistance measurements suggest changes also arise in the strength of the spin-orbit coupling due to intermixing in this low dose regime. In addition, the Au atoms are shown to gain a small magnetic moment at the interface due to polarisation effects. The complex dose dependent magnetic properties have been attributed to the competition between various effects including a loss in NiFe moment, a gain in Au moment, the transfer of spin-orbit coupling from Au to NiFe and the volume expansion of the unit cell due to the inclusion of defect atoms. These effects vary in significance due to the changes in the local environment of the atoms at the interface during the intermixing process where the combination of these effects lead to the observed magnetic behaviour.

The control over the magnetic properties through focussed ion irradiation was applied to magnetic nanowire systems. Chapter 8 shows how localised regions of modified magnetic material can affect the behaviour of domain walls as they propagate along the nanowires

leading to controllable pinning of the domain wall in an irradiated trap. The de-pinning field of the traps was characterised both experimentally and through micromagnetic simulations as a function of the irradiation dose and trap width. An increasing dose leads to a linear increase in the de-pinning field whilst an increase in trap width leads to a rapid increase in the de-pinning field when the width is comparable to the domain wall width. A further increase in trap width brings about little additional increase in the de-pinning field from the trap.

Further investigation into the pinning of domain walls reveals that the geometry of the irradiated region and the micromagnetic structure of the domain wall can give rise to different de-pinning fields. This gives the ability to select specific domain wall types based on nanowire design and may prove useful for further exploitation in domain wall based devices. In addition to their structure, experimental and micromagnetic results both reveal a difference in pinning associated with the dynamic properties of domain walls in the irradiated traps. This behaviour is also associated with the modified domain wall structure during its propagation which 'feels' a different pinning strength to a stationary domain wall.

New methods for the control of the behaviour of domain walls in nanowires have also been explored through the inclusion of small amplitude periodic geometrical modulations to both edges of a nanowire (see chapter 9). These modulations lead to improvements in the domain wall dynamics but also give rise to less desirable domain wall pinning behaviour. This part of the investigation characterised these effects, uncovering a possible route towards the optimisation of both these effects.

The magnetisation reversal behaviour of nanowires was modified by the inclusion of the edge modulation giving rise to a nucleation dominated reversal field dependence governed by the combination of two physical processes. A model, based on the torque on the spins that follow the contours of the edge modulation of the nanowire with respect to their angle with an applied field, brings about a Zeeman contribution to the energy barrier for switching. This model accurately describes the reversal field in the long wavelength limit in both the experimental and micromagnetic results and is found to be scalable with the modulation parameters. In the short wavelength limit the reversal field was dominated by an additional process leading to a sharp rise in the reversal field. This additional process is due to regions of localised orthogonal shape anisotropy resulting from the geometry of the modulation, which is most significant in the small wavelength, large amplitude regime. This localised anisotropy

competes with the global axial shape anisotropy of the wire and leads to a more complex spin structure that stabilises the magnetisation of the system, leading to an increase in the reversal field.

The modulation also leads to an increase in the domain wall de-pinning field for transverse domain wall structures. This is explained by a reduced energy configuration where the orthogonal spins in a transverse domain wall micromagnetic structure coincide with the regions of localised orthogonal shape anisotropy along the nanowire. This pinning becomes most significant with small wavelength, large amplitude modulation and a good agreement is found between micromagnetic simulations and experimental results with domain walls injected both with domain wall nucleation pad structure and through localised pulsed field domain wall injection techniques.

The micromagnetic investigation was extended to consider the dynamic properties of domain walls that experience Walker breakdown with strong magnetic fields, where periodic structural transitions of the domain wall lead to a significant reduction in the time-averaged domain wall velocity. Matching the wavelength of the structural modulations to the periodicity of the domain wall structural transitions demonstrates the suppression of the Walker breakdown. The suppression mechanism has been elucidated and is due to the periodic energy landscape along the nanowire which shows a strong preference for a transverse domain wall structure coincident with the expected transition towards a vortex core structure as part of the Walker breakdown process. This allows a transverse domain wall structure to be maintained where excess energy associated with the perpendicular magnetisation component of the vortex structure is dissipated through the emission of spin wave energy.

The careful selection of modulation properties allows for the optimisation of this effect where the improved domain wall mobility can be achieved over a wide field range. This must be balanced by minimising the pinning effects that also arise due to the inclusion of the edge modulation. A phase diagram was presented showing the route towards the optimum of these properties based on the modulation parameters.

10.2 Further work

This study has demonstrated methods for the control of domain wall behaviour in nanowires through modifications to both the interfacial and geometrical structuring of the nanowires.

This has led to novel findings, however, further scientific investigation is still required before this knowledge can be applied in technological applications. This section highlights some possible areas of research that could be continued and may lead to further advances in the fundamental understanding in magnetisation processes or may contribute towards the development of novel technological devices.

The study of the ion beam induced modifications to the structural and magnetic properties have focussed on NiFe/Au bilayer structures. A similar effect has been demonstrated in a Cu capped sample which suggests that further investigation in other layered materials may be beneficial. This could lead to the discovery of other layered structures that may give a greater level of control over the magnetisation and may also add to the understanding of the physical processes taking place.

The changes in magnetic behaviour of these samples has been attributed to changes in the magnetic moment and the spin-orbit interaction for the atoms at the near interface region. These provide an explanation for the observed variation in the saturation magnetisation of the samples which shows the most dramatic changes. For a complete understanding of the magnetic properties the effect on other magnetic parameters such as the damping or exchange stiffness also need to be investigated.

The behaviour of domain walls in irradiated nanowires has been compared with micro-magnetic models that include a region of reduced M_S along the nanowire length. These models show the same trends as those observed in experimental results, however, there are still obvious discrepancies between the measured and simulated values of the de-pinning of a domain wall from the irradiated regions. These differences are greater than what can reasonably be expected due to the omission of thermal effects from the simulation as experimental and simulated results from the edge-modulated nanowires are within much closer agreement. Further insight into changes in the damping or exchange stiffness in these materials may be a useful inclusion to the model to lead to a much closer agreement between the models and the experimental results.

Several of the results presented here suggest that the pinning of domain walls shows a dependence on their dynamic properties where stronger pinning is experienced by slower moving domain walls. This difference is likely to be of great importance in the development of domain wall devices and deserves a great deal of further attention. The pulsed field stripline domain wall injection approach, adopted for the edge modulated nanowire investigation,

provides a possible route for further experimental investigation into the differences between static and dynamic pinning. The ability to introduce domain walls at an arbitrary bias field allows their velocity on arrival at the irradiated region to be controlled. This would then allow for measurements on the magnetisation in nanowires to determine the de-pinning field of a domain wall as a function of its incident velocity. The dynamic properties are strongly influenced by the damping in the material. To accurately model the dynamic properties in the irradiated regions will require the effect of the damping parameter to be well understood and to be included in the simulations.

Micromagnetic simulations have been used to extend the understanding of the domain wall behaviour beyond what has been measured experimentally in this investigation. This includes simulations of the de-pinning field of domain walls which show a relationship between the domain wall structure and the geometry of the irradiated region along the nanowire. Also, the mechanism for the suppression of Walker breakdown through the inclusion of small amplitude edge modulations has been determined through micromagnetic simulations. An experimental investigation to confirm these micromagnetic results would be an ideal next step in to further understand this domain wall behaviour.

Finally, the domain wall motion investigated here has been driven by applied magnetic fields. This techniques is well suited for laboratory based investigation in test structures, and has direct applications in sensor technology. However, for other future device applications, spin transfer torque driven domain wall motion is a more appropriate technique for the manipulation of domain walls. Further work needs to be performed to verify that the behaviour demonstrated here can be reproduced with STT driven domain wall motion.

Collectively this thesis reveals novel methods for the manipulation and control of magnetic domain walls in nanowire structures. This includes significant advances in the understanding of the interactions between domain walls and nanowire structures which is predicted to be valuable for both future research and industrial exploitation. The deeper understanding into the dynamic domain wall processes is particularly relevant and can be directly applied to the work of many others in the field. Techniques demonstrated here show how domain wall mobility can be enhanced and how chirality can be preserved through the suppression of Walker breakdown. These properties are very significant in reaching the harsh demands of speed and reliability that is highly sought after for novel technological devices.

References

[1] R.P. Cowburn, D.A. Allwood, G. Xiong and M.D. Cooke. Domain wall injection and propagation in planar Permalloy nanowires. *Journal of Applied Physics* **91**, 6949 (2002).

[2] G.S.D. Beach. Current-induced domain wall motion. *Journal of Magnetism and Magnetic Materials* **320**, 1272 (2008).

[3] D-S. Han, S-K. Kim, J-Y. Lee, S.J. Hermsdoerfer, H. Schultheiss, B. Leven and B. Hillebrands. Magnetic domain-wall motion by propagating spin waves. *Applied Physics Letters* **94**, 112502 (2009).

[4] D.A. Allwood, G. Xiong, M.D. Cooke, C.C. Faulkner, D. Atkinson, N. Vernier and R.P. Cowburn. Submicrometer ferromagnetic NOT gate and shift register. *Science* **296**, 2003 (2002).

[5] N. Vernier, D.A. Allwood, D. Atkinson, M.D. Cooke and R.P. Cowburn. Domain wall propagation in magnetic nanowires by spin-polarized current injection. *Europhysics Letters* **65**, 526 (2004).

[6] A. Torti, V. Mondiali, A. Cattoni, M. Donolato, E. Albisetti, A.M. Haghiri-Gosnet, P. Vavassori and R. Bertacco. Single particle demultiplexer based on domain wall conduits. *Applied Physics Letters* **101**, 142405 (2012).

[7] C.C. Faulkner, D.A. Allwood, M.D. Cooke, G. Xiong, D. Atkinson and R.P. Cowburn. Controlled switching of ferromagnetic wire junctions by domain wall injection. *Journal of Applied Physics* **39**, 2860 (2003).

[8] Y. Yokoyama, Y. Suzuki, S. Yuasa, K. Ando, K. Shigeto, T. Shinjo, P. Gogol, J. Miltat, A. Thiaville, T. Ono and T. Kawagoe. Kerr microscopy observations of magnetization process in microfabricated ferromagnetic wires. *Journal of Applied Physics* **87**, 5618 (2000).

[9] D. Lacour, J.A. Katine, L. Folks, J.R. Childress, M. Carey and B.A. Gurney. Experimental evidence of multiple stable locations for a domain wall trapped by a submicron notch. *Applied Physics Letters* **84**, 1910 (2004).

[10] A. Himeno, T. Ono, S. Nasu, K. Shigeto, K. Mibu and T. Shinjo. Dynamics of a magnetic domain wall in magnetic wires with an artificial neck. *Journal of Applied Physics* **93**, 8430 (2003).

[11] C.C. Faulkner, M.D. Cooke, D.A. Allwood, D. Petit, D. Atkinson and R.P. Cowburn. Artificial domain wall nanotraps in $Ni_{81}Fe_{19}$ wires. *Journal of Applied Physics* **95**, 6717 (2004).

[12] Y. Nakatani, A. Thiaville and J. Miltat. Head-to-head domain walls in soft nano-strips: A refined phase diagram. *Journal of Magnetism and Magnetic Materials* **290-291**, 750 (2005).

[13] D.A. Allwood, G. Xiong and R.P. Cowburn. Domain wall diodes in ferromagnetic planar nanowires. *Applied Physics Letters* **85**, 2848 (2004).

[14] M.T. Bryan, T. Schrefl and D.A. Allwood. Symmetric and asymmetric domain wall diodes in magnetic nanowires. *Applied Physics Letters* **91**, 142502 (2007).

[15] A. Himeno, S. Kasai and T. Ono. Current-driven domain-wall motion in magnetic wires with asymmetric notches. *Applied Physics Letters* **87**, 243108 (2005).

[16] H.G. Piao, H-W. Lee and J. Yoon. Ratchet effect of domain wall motion by GHz AC magnetic field in asymmetric sawtooth-shaped ferromagnetic nanowires. *IEEE Transactions on Magnetics* **46**, 1844 (2010).

[17] A. Himeno, T. Okuno, S. Kasai, T. Ono, S. Nasu, K. Mibu and T. Shinjo. Propagation of a magnetic domain wall in magnetic wires with asymmetric notches. *Journal of Applied Physics* **97**, 066101 (2005).

[18] D. Atkinson, D.A. Allwood, G. Xiong, M.D. Cooke, C.C. Faulkner and R.P. Cowburn. Magnetic domain-wall dynamics in a submicrometre ferromagnetic structure. *Nature Materials* **2**, 85 (2003).

[19] D. Atkinson, D.A. Allwood, C.C. Faulkner, M.D. Cooke and R.P. Cowburn. Magnetic domain wall dynamics in a permalloy nanowire. *IEEE Transactions on Magnetics* **39**, 2663 (2003).

[20] G.S.D. Beach, C. Nistor, C. Knutson, M. Tsoi and J.L. Erskine. Dynamics of field-driven domain-wall propagation in ferromagnetic nanowires. *Nature Materials* **4**, 741 (2005).

[21] N.L. Schryer and L.R. Walker. The motion of 180° domain walls in uniform dc magnetic fields. *Journal of Applied Physics* **45**, 5406 (1974).

[22] D.M. Burn and D. Atkinson. Complex pulsed field magnetization behavior and Walker breakdown in a NiFe thin-film. *Journal of Applied Physics* **108**, 073926 (2010).

[23] D.A. Allwood, G. Xiong, C.C. Faulkner, D. Atkinson, D. Petit and R.P. Cowburn. Magnetic domain-wall logic. *Science* **309**, 1688 (2005).

[24] S.S.P. Parkin, M. Hayashi and L. Thomas. Magnetic domain-wall racetrack memory. *Science* **320**, 190 (2008).

[25] P. Vavassori, V. Metlushko, B. Ilic, M. Gobbi, M. Donolato, M. Cantoni and R. Bertacco. Domain wall displacement in Py square ring for single nanometric magnetic bead detection. *Applied Physics Letters* **93**, 203502 (2008).

[26] M. Donolato, P. Vavassori, M. Gobbi, M. Deryabina, M.F. Hansen, V. Metlushko, B. Ilic, M. Cantoni, D. Petti, S. Brivio and R. Bertacco. On-chip manipulation of protein-coated magnetic beads via domain-wall conduits. *Advanced materials* **22**, 2706 (2010).

[27] E. Rapoport and G.S.D. Beach. Dynamics of superparamagnetic microbead transport along magnetic nanotracks by magnetic domain walls. *Applied Physics Letters* **100**, 082401 (2012).

[28] G. Ruan, G. Vieira, T. Henighan, A.P. Chen, D. Thakur, R. Sooryakumar and J.O. Winter. Simultaneous magnetic manipulation and fluorescent tracking of multiple individual hybrid nanostructures. *Nano letters* **10**, 2220 (2010).

[29] A.D. West, K.J. Weatherill, T.J. Hayward, P.W. Fry, T. Schrefl, M.R.J. Gibbs, C.S. Adams, D.A. Allwood and I.G. Hughes. Realization of the manipulation of ultracold atoms with a reconfigurable nanomagnetic system of domain walls. *Nano letters* **12**, 4065 (2012).

[30] C. Chappert, H. Bernas, J. Ferre, V. Kottler, J.P. Jamet, Y. Chen, E. Cambril, T. Devolder, F. Rousseaux, V. Mathet and H. Launois. Planar patterned magnetic media obtained by ion irradiation. *Science* **280**, 1919 (1998).

[31] T. Devolder. Light ion irradiation of Co/Pt systems: Structural origin of the decrease in magnetic anisotropy. *Physical Review B* **62**, 5794 (2000).

[32] Y.G. Wang and Y.Z. Huang. Magnetic patterning of Co/Pt multilayers by Ga^+ ion irradiation. *Journal of Electronic Materials* **38**, 468 (2008).

[33] C. Vieu, J. Gierak, H. Launois, T. Aign, P. Meyer, J.P. Jamet, J. Ferre, C. Chappert, T. Devolder, V. Mathet and H. Bernas. Modifications of magnetic properties of Pt/Co/Pt thin layers by focused gallium ion beam irradiation. *Journal of Applied Physics* **91**, 3103 (2002).

[34] J.K. Tripathi, D. Kumar, P. Malar, T. Osipowicz, V. Ganesan, A. Gupta and T. Som. Effect of ion beam irradiation on magnetic and structural properties of Pt/Cr/Co multilayers. *Nuclear Instruments and Methods in Physics Research B* **266**, 1247 (2008).

[35] J.K. Tripathi, A. Gupta and T. Som. Ion induced modification in structural and magnetic properties of Pt/Cr/Co multilayers. *Solid State Communications* **150**, 333 (2010).

[36] C.M. Park and J.A. Bain. Focused-ion-beam induced grain growth in magnetic materials for recording heads. *Journal of Applied Physics* **91**, 6830 (2002).

[37] C.C. Faulkner, D. Atkinson, D.A. Allwood and R.P. Cowburn. Rapid tuning of $Ni_{81}Fe_{19}$/Au bilayer magnetic properties by focused ion beam intermixing. *Journal of Magnetism and Magnetic Materials* **319**, 9 (2007).

[38] C.M. Park and J.A. Bain. Local degradation of magnetic properties in magnetic thin films irradiated by Ga^+ focused-ion-beams. *IEEE Transactions on Magnetics* **38**, 2237 (2002).

[39] J. Fassbender and J. McCord. Control of saturation magnetization, anisotropy, and damping due to Ni implantation in thin $Ni_{81}Fe_{19}$ layers. *Applied Physics Letters* **88**, 252501 (2006).

[40] W.M. Kaminsky, G.A.C. Jones, N.K. Patel, W.E. Booij, M.G. Blamire, S.M. Gardiner, Y.B. Xu and J.A.C. Bland. Patterning ferromagnetism in $Ni_{80}Fe_{20}$ films via Ga^+ ion irradiation. *Applied Physics Letters* **78**, 1589 (2001).

[41] L.D. Ozkaya, R.M. Langford, W.L. Chan and A.K. Petford-Long. Effect of Ga implantation on the magnetic properties of permalloy thin films. *Journal of Applied Physics* **91**, 9937 (2002).

[42] F. Wilhelm, P. Poulopoulos, V. Kapaklis, J.-P. Kappler, N. Jaouen, A. Rogalev, A. Yaresko and C. Politis. Au and Fe magnetic moments in disordered Au-Fe alloys. *Physical Review B* **77**, 224414 (2008).

[43] B.W. Corb, R.C. O'Handley and N.J. Grant. Chemical bonding, magnetic moments, and local symmetry in transition-metalmetalloid alloys. *Physical Review B* **27**, 636 (1983).

[44] D. Bagayoko and J. Callaway. Lattice-parameter dependence of ferromagnetism in bcc and fcc iron. *Physical Review B* **28**, 5419 (1983).

[45] K.J. Lee, T.H.Y. Nguyen and K.H. Shin. Reduction in critical current density of current-induced magnetization switching. *Journal of Magnetism and Magnetic Materials* **304**, 102 (2006).

[46] J. Crangle. *The magnetic properties of solids.* Arnold London (1977).

[47] D. Jiles. *Introduction to magnetism and magnetic materials.* Chapman & Hall (1998).

[48] R.C. O'Handley. *Modern magnetic materials principles and applications.* Wiley (2000).

[49] S. Blundell. *Magnetism in condensed matter.* Oxford University Press (2001).

[50] R.M. Bozorth and J.G. Walker. Magnetic crystal anisotropy and magnetostriction of iron-nickel alloys. *Physical Review* **89**, 624 (1953).

[51] H. Ebert, R. Zeller, B. Drittler and P.H. Dederichs. Fully relativistic calculation of the hyperfine fields of 5d-impurity atoms in ferromagnetic Fe. *Journal of Applied Physics* **67**, 4576 (1990).

[52] R. Tyer, G. van der Laan, W. Temmerman, Z. Szotek and H. Ebert. Systematic theoretical study of the spin and orbital magnetic moments of 4d and 5d interfaces with Fe films. *Physical Review B* **67**, 104409 (2003).

[53] J.W. Cable and E.O. Wollan. Magnetic-moment distribution in NiFe and AuFe alloys. *Physical Review B* **7**, 2005 (1973).

[54] G.Y. Guo and H. Ebert. Band-theoretical investigation of the magneto-optical Kerr effect in Fe and Co multilayers. *Physical Review B* **51**, 12633 (1995).

[55] F. Wilhelm, M. Angelakeris, N. Jaouen, P. Poulopoulos, E. Papaioannou, C.H. Mueller, P. Fumagalli, A. Rogalev and N.K. Flevaris. Magnetic moment of Au at AuCo interfaces: A direct experimental determination. *Physical Review B* **69**, 220404 (2004).

[56] F. Wilhelm, P. Poulopoulos, H. Wende, A. Scherz, K. Baberschke, M. Angelakeris, N.K. Flevaris and A. Rogalev. Systematics of the induced magnetic moments in 5d layers and the violation of the third Hund's rule. *Physical Review Letters* **87**, 207202 (2001).

[57] P. Langevin. Magnétisme et théorie des électrons. *Annales de Chimie et de Physique* **5**, 70 (1905).

[58] A. Aharoni. *Introduction to the theory of ferromagnetism.* Oxford University Press (2000).

[59] B.D. Cullity. *Introduction to magnetic materials*. Addison Wesley (1972).

[60] P. Weiss. La variation du ferromagnetisme du temperature. *Comptes Rendus* **143**, 1136 (1906).

[61] P.A.M. Dirac. On the theory of quantum mechanics. *Proceedings of the Royal Society of London* **112**, 661 (1926).

[62] R.M. Bozorth. *Ferromagnetism*. D. Van Nostrand New York (1951).

[63] L Néel. Influence des fluctuations des champs moléculaires sur les propriétés magnétiques des corps. *Annalen der Physique* **18**, 5 (1932).

[64] L Néel. Propriétées magnétiques des ferrites; férrimagnétisme et antiferromagnétisme. *Annales de Physique* **3**, 137 (1948).

[65] M. Klaui and C.A.F. Vaz. *Handbook of magnetism and advanced magnetic materials v.2 - magnetic configurations in small elements, magnetization processes and hyesteretic properties*. Wiley (2007).

[66] A.P. Malozemoff and J.C. Slonczewski. *Magnetic domain walls in bubble materials*. Academic Press New York (1979).

[67] W.F. Brown. *Micromagnetics*. Interscience Publishers New York (1963).

[68] J. Fidler. Micromagnetic modelling-the current state of the art. *Journal of Physics D: Applied Physics* **33**, R135 (2000).

[69] L. Landau. On the theory of the dispersion of magnetic permeability in ferromagnetic bodies. *Physikalische Zeitschrift der Sowjetunion* **8**, 153 (1935).

[70] T.L. Gilbert. A Lagrangian formulation of the gyromagnetic equation of the magnetization field. *Physical Review* **100**, 1243 (1955).

[71] J.O. Rantschler, R.D. McMichael, A. Castillo, A.J. Shapiro, W.F. Egelhoff, B.B. Maranville, D. Pulugurtha, A.P. Chen and L.M. Connors. Effect of 3d, 4d, and 5d transition metal doping on damping in permalloy thin films. *Journal of Applied Physics* **101**, 033911 (2007).

[72] T.L. Gilbert. Classics in magnetics a phenomenological theory of damping in ferromagnetic materials. *IEEE Transactions on Magnetics* **40**, 3443 (2004).

[73] R.D. McMichael and A. Kunz. Calculation of damping rates in thin inhomogeneous ferromagnetic films due to coupling to lattice vibrations. *Journal of Applied Physics* **91**, 8650 (2002).

[74] E. Rossi, O. Heinonen and A.H. MacDonald. Dynamics of magnetization coupled to a thermal bath of elastic modes. *Physical Review B* **72**, 174412 (2005).

[75] V. Kambersky and C.E. Patton. Spin-wave relaxation and phenomenological damping in ferromagnetic resonance. *Physical Review B* **11**, 2668 (1975).

[76] R.D. McMichael, D. Twisselmann and A. Kunz. Localized ferromagnetic resonance in inhomogeneous thin films. *Physical Review Letters* **90**, 227601 (2003).

[77] J. Fassbender, J.V. Borany and A. Mücklich. Structural and magnetic modifications of Cr-implanted permalloy. *Physical Review B* **73**, 184410 (2006).

[78] G.M. Sandler, H.N. Bertram, T.J. Silva and T.M. Crawford. Determination of the magnetic damping constant in NiFe films. *Journal of Applied Physics* **85**, 5080 (1999).

[79] W.E. Bailey, P. Kabos, F. Mancoff and S. Russek. Control of magnetization dynamics in $Ni_{81}Fe_{19}$ thin films through the use of rare-earth dopants. *IEEE Transactions on Magnetics* **37**, 1749 (2001).

[80] E. Heinonen. Finite temperature micromagnetic modeling applied to spin valves. *IEEE Transactions on Magnetics* **38**, 10 (2002).

[81] A. Hubert and R. Schäfer. *Magnetic domains*. Springer Berlin (1998).

[82] Y. Nakatani, A. Thiaville and J. Miltat. Faster magnetic walls in rough wires. *Nature materials* **2**, 521 (2003).

[83] A. Hirohata, Y.B. Xu, J.A.C. Bland, S.N. Holmes, E. Cambril, Y. Chen and F. Rousseaux. Influence of crystalline structures on the domain configurations in controlled mesoscopic ferromagnetic wire junctions. *Journal of Applied Physics* **91**, 7308 (2002).

[84] R.D. McMichael and M.J. Donahue. Head to head domain wall structures in thin magnetic strips. *IEEE Transactions on Magnetics* **33**, 4167 (1997).

[85] M. Klaui, C.A.F. Vaz, J.A.C. Bland, L.J. Heyderman, F. Nolting, A. Pavlovska, E. Bauer, S. Cherifi, S. Heun and A. Locatelli. Head-to-head domain-wall phase diagram in mesoscopic ring magnets. *Applied Physics Letters* **85**, 5637 (2004).

[86] M.D. Cooke, D.A. Allwood, D. Atkinson, G. Xiong, C.C. Faulkner and R.P. Cowburn. Thin single layer materials for device application. *Journal of Magnetism and Magnetic Materials* **257**, 387 (2003).

[87] M.T. Bryan, D. Atkinson and R.P. Cowburn. Experimental study of the influence of edge roughness on magnetization switching in Permalloy nanostructures. *Applied Physics Letters* **85**, 3510 (2004).

[88] R. Friedberg and D.I. Paul. New theory of coercive force of ferromagnetic materials. *Physical Review Letters* **34**, 1234 (1975).

[89] D.I. Paul. General theory of the coercive force due to domain wall pinning. *Journal of Applied Physics* **53**, 1649 (1982).

[90] L.J. Dijkstra and C. Wert. Effect of inclusions on coercive force of iron. *Physical Review* **79**, 979 (1950).

[91] K.J. O'Shea, S. McVitie, J.N. Chapman and J.M.R. Weaver. Direct observation of changes to domain wall structures in magnetic nanowires of varying width. *Applied Physics Letters* **93**, 202505 (2008).

[92] L.J. Chang, Y.D. Yao and P. Lin. Magnetic interaction in domain wall depinning at square notch and antinotch traps. *IEEE Transactions on Magnetics* **47**, 2519 (2011).

[93] L.K. Bogart, D.S. Eastwood and D. Atkinson. The effect of geometrical confinement and chirality on domain wall pinning behavior in planar nanowires. *Journal of Applied Physics* **104**, 033904 (2008).

[94] L.K. Bogart, D. Atkinson, K.J. O'Shea, D. McGrouther and S. McVitie. Dependence of domain wall pinning potential landscapes on domain wall chirality and pinning site geometry in planar nanowires. *Physical Review B* **79**, 054414 (2009).

[95] D. Atkinson, D.S. Eastwood and L.K. Bogart. Controlling domain wall pinning in planar nanowires by selecting domain wall type and its application in a memory concept. *Applied Physics Letters* **92**, 022510 (2008).

[96] D.S. Eastwood, J.A. King, L.K. Bogart, H. Cramman and D. Atkinson. Chirality-dependent domain wall pinning in a multinotched planar nanowire and chirality preservation using transverse magnetic fields. *Journal of Applied Physics* **109**, 013903 (2011).

[97] H.G. Piao, X. Zhang and H.C. Choi. Condition of the ratchet effect of a magnetic domain wall motion under an asymmetric potential energy. *Journal of Applied Physics* **111**, 07D301 (2012).

[98] A. Aziz, S.J. Bending, H. Roberts, S. Crampin, P.J. Heard and C.H. Marrows. Artificial domain structures realized by local gallium focused ion-beam modification of PtCoPt trilayer transport structure. *Journal of Applied Physics* **98**, 124102 (2005).

[99] A. Vogel, S. Wintz, T. Gerhardt, L. Bocklage, T. Strache, M-Y. Im, P. Fischer, J. Fassbender, J. McCord and G. Meier. Field- and current-induced domain-wall motion in permalloy nanowires with magnetic soft spots. *Applied Physics Letters* **98**, 202501 (2011).

[100] M.A. Basith, S. McVitie, D. McGrouther and J.N. Chapman. Reproducible domain wall pinning by linear non-topographic features in a ferromagnetic nanowire. *Applied Physics Letters* **100**, 232402 (2012).

[101] T. Ono, H. Miyajima, K. Shigeto, K. Mibu, N. Hosoito and T. Shinjo. Propagation of a magnetic domain wall in a submicrometer magnetic wire. *Science* **284**, 468 (1999).

[102] D.A. Allwood, G. Xiong, M.D. Cooke, C.C. Faulkner, D. Atkinson and R.P. Cowburn. Characterization of submicrometer ferromagnetic NOT gates. *Journal of Applied Physics* **95**, 8264 (2004).

[103] A. Thiaville, Y. Nakatani, J. Miltat and N. Vernier. Domain wall motion by spin-polarized current: A micromagnetic study. *Journal of Applied Physics* **95**, 7049 (2004).

[104] K.J. Sixtus and L. Tonks. Propagation of large Barkhausen discontinuities. *Physical Review* **37**, 930 (1931).

[105] K.J. Sixtus and L. Tonks. Propagation of large Barkhausen discontinuities. II. *Physical Review* **42** (1932).

[106] M.T. Bryan, T. Schrefl, D. Atkinson and D.A. Allwood. Magnetic domain wall propagation in nanowires under transverse magnetic fields. *Journal of Applied Physics* **103**, 073906 (2008).

[107] A. Thiaville and Y. Nakatani. Domain-wall dynamics in nanowires and nanostripes. In B. Hillebrands and A. Thiaville, editors, *Spin Dynamics in confined magnetic structures III*. Springer (2006).

[108] E. Martinez, L. Lopez-Diaz, L. Torres, C. Tristan and O. Alejos. Thermal effects in domain wall motion: Micromagnetic simulations and analytical model. *Physical Review B* **75**, 174409 (2007).

[109] A.A. Thiele. Steady-state motion of magnetic domains. *Physical Review Letters* **30**, 230 (1973).

[110] K. Richter, R. Varga, G.A. Badini-Confalonieri and M. Vazquez. The effect of transverse field on fast domain wall dynamics in magnetic microwires. *Applied Physics Letters* **96**, 182507 (2010).

[111] K. Weerts, W. Van Roy, G. Borghs and L. Lagae. Suppression of complex domain wall behavior in $Ni_{80}Fe_{20}$ nanowires by oscillating magnetic fields. *Applied Physics Letters* **96**, 062502 (2010).

[112] J-Y. Lee, K-S. Lee and S-K. Kim. Remarkable enhancement of domain-wall velocity in magnetic nanostripes. *Applied Physics Letters* **91**, 122513 (2007).

[113] E.R. Lewis, D. Petit, L. O'Brien, A. Fernández-Pacheco, J. Sampaio, A-V. Jausovec, H.T. Zeng, D.E. Read and R.P. Cowburn. Fast domain wall motion in magnetic comb structures. *Nature Materials* **9**, 980 (2010).

[114] T. Thomson, G. Hu and B. Terris. Intrinsic distribution of magnetic anisotropy in thin films probed by patterned nanostructures. *Physical Review Letters* **96**, 257204 (2006).

[115] R. Lavrijsen, J.H. Franken, J.T. Kohlhepp, H.J.M. Swagten and B. Koopmans. Controlled domain-wall injection in perpendicularly magnetized strips. *Applied Physics Letters* **96**, 222502 (2010).

[116] J.H. Franken, M. Hoeijmakers, R. Lavrijsen, J.T. Kohlhepp, H.J.M. Swagten, B. Koopmans, E. van Veldhoven and D.J. Maas. Precise control of domain wall injection and pinning using helium and gallium focused ion beams. *Journal of Applied Physics* **109**, 07D504 (2011).

[117] K. Shigeto, T. Shinjo and T. Ono. Injection of a magnetic domain wall into a submicron magnetic wire. *Applied Physics Letters* **75**, 2815 (1999).

[118] M. Hayashi, J. Ieda, Y. Yamane, J-I. Ohe, Y. Takahashi, S. Mitani and S. Maekawa. Supplementary information: Time domain observation of spinmotive force in permalloy nanowires. *Science And Technology* **108**, 147202 (2012).

[119] M. Hayashi, L. Thomas, Y. Bazaliy, C. Rettner, R. Moriya, X. Jiang and S.S.P. Parkin. Influence of current on field-driven domain wall motion in permalloy nanowires from time resolved measurements of anisotropic magnetoresistance. *Physical Review Letters* **96**, 197207 (2006).

[120] M. Hayashi, L. Thomas, R. Moriya, C. Rettner and S.S.P. Parkin. Current-controlled magnetic domain-wall nanowire shift register. *Science* **320**, 209 (2008).

[121] M. Hayashi, L. Thomas, C. Rettner, R. Moriya, Y. Bazaliy and S.S.P. Parkin. Current driven domain wall velocities exceeding the spin angular momentum transfer rate in permalloy nanowires. *Physical Review Letters* **98**, 037204 (2007).

[122] C. Kittel. *Introduction to solid state physics*. Wiley Hoboken (2005).

[123] X. Chen, H. Qiu, H. Qian, P. Wu, F. Wang, L. Pan and Y. Tian. Characteristics of Ni_xFe_{100x} films deposited on $SiO_2/Si(100)$ by DC magnetron co-sputtering. *Vacuum* **75**, 217 (2004).

[124] R.R. Verderber. Texture of evaporated NiFe thin films. *Journal of Applied Physics* **30**, 1359 (1959).

[125] J. Venables. *Introduction to surface and thin film processes.* Cambridge University Press (2000).

[126] K. Luo, D.Y. Kim and D.W. Goodman. The nucleation and growth of gold on silica. *Journal of Molecular Catalysis A: Chemical* **167**, 191 (2001).

[127] M.S. Blois. Preparation of thin magnetic films and their properties. *Journal of Applied Physics* **26**, 975 (1955).

[128] M.A. Akhter, D.J. Mapps, Y.Q. Ma Tan, A.K. Petford-Long and R. Doole. Thickness and grain-size dependence of the coercivity in permalloy thin films. *Journal of Applied Physics* **81**, 4122 (1997).

[129] M. Nastasi, J.W. Mayer and J.K. Hirvonen. *Ion-solid interactions: Fundamentals and applications.* (1996).

[130] J. Lindhard, M. Scharff and H.E. Schioett. *Range concepts and heavy ion ranges (Notes on atomic collisions, II)* volume 33. Ejnar Munksgaard Copenhagen (1963).

[131] J.P. Biersack. Calculation of projected rangesanalytical solutions and a simple general algorithm. *Nuclear Instruments and Methods* **183**, 199 (1981).

[132] J.F. Ziegler, J.P. Biersack and U. Littmark. *The stopping and range of ions in solids.* Pergamon New York (1985).

[133] O. Ikeda. Phase equilibria and stability of ordered b.c.c. phases in the Fe-rich portion of the FeGa system. *Journal of Alloys and Compounds* **347**, 198 (2002).

[134] P. Sigmund. Theory of sputtering. I. Sputtering yield of amorphous and polycrystalline targets. *Physical Review* **184**, 383 (1969).

[135] Q. Wei, K-D. Li, J. Lian and L. Wang. Angular dependence of sputtering yield of amorphous and polycrystalline materials. *Journal of Physics D: Applied Physics* **41**, 172002 (2008).

[136] L.A. Giannuzzi and F.A. Stevie. *Introduction to focused ion beams: Instrumentation, theory, techniques, and practice.* Springer (2005).

[137] M.T. Robinson and O.S. Oen. The channeling of energetic atoms in crystal lattices. *Applied Physics Letters* **2**, 30 (1963).

[138] B.Y. Tsaur, S.S. Lau, Z.L. Liau and J.W. Mayer. Ion-beam-induced intermixing of surface layers. *Thin Solid Films* **63**, 31 (1979).

[139] F. Besenbacher and J. Bø ttiger. Short-and long-range ion-beam mixing in Cu: Al. *Applied Physics A Solids and Surfaces* **29**, 141 (1982).

[140] T. Banwell, B.X. Liu, I. Golecki and M-A. Nicolet. Chemical effects in ion mixing of transition metals on SiO_2. *Nuclear Instruments and Methods* **209**, 125 (1983).

[141] P. Sigmund and A. Gras-Marti. Distortion of depth profiles during sputtering: I. General description of collisional mixing. *Nuclear Instruments and Methods* **168**, 389 (1980).

[142] A. Fick. On liquid diffusion. *Philosophical Magazine* **10**, 30 (1995).

[143] H.H. Andersen. The depth resolution of sputter profiling. *Applied Physics* **18**, 131 (1979).

[144] P. Sigmund and A. Gras-Marti. Theoretical aspects of atomic mixing by ion beams. *Nuclear Instruments and Methods* **182**, 25 (1981).

[145] W. Bolse. Ion-beam induced atomic transport through bi-layer interfaces of low-and medium-Z metals and their nitrides. *Materials Science and Engineering: R: Reports* **12**, 53 (1994).

[146] J. Desimoni and A. Traverse. Model for compound formation during ion-beam mixing. *Physical Review B* **48**, 13266 (1993).

[147] S.J. Kim, M-A. Nicolet, R.S. Averback and D. Peak. Low-temperature ion-beam mixing in metals. *Physical Review B* **37**, 38 (1988).

[148] M. Homma, M. Imakawa, M. Okada and S. Tsutsumi. Au-Fe-Ni permanent magnet alloys. *IEEE Transactions on Magnetics* **21**, 1245 (1985).

[149] A. Traverse, M.G. Le Boite, L. Nevot, B. Pardo and J. Corno. Initial stages of the ion beam mixing process. *Applied Physics Letters* **51**, 1901 (1987).

[150] J.A. Brinkman. On the nature of radiation damage in metals. *Journal of Applied Physics* **25**, 961 (1954).

[151] T.W. Workman, Y.T. Cheng, W.L. Johnson and M-A. Nicolet. Effect of thermodynamics on ion mixing. *Applied Physics Letters* **50**, 1485 (1987).

[152] J.M. MacLaren and R.H. Victora. Perpendicular magnetic anisotropies of (Pt/Co/Pt)/X superlattices. *Applied Physics Letters* **66**, 3377 (1995).

[153] P.F. Carcia, S.I. Shah and W.B. Zeper. Effect of energetic bombardment on the magnetic coercivity of sputtered Pt/Co thin-film multilayers. *Applied Physics Letters* **56**, 2345 (1990).

[154] T. Blon, G. Ben Assayag, J.C. Ousset, B. Pecassou, A. Claverie and E. Snoeck. Magnetic easy-axis switching in Co/Pt and Co/Au superlattices induced by nitrogen ion beam irradiation. *Nuclear Instruments and Methods in Physics Research B* **257**, 374 (2007).

[155] R. Hyndman, P. Warin, J. Gierak, J. Ferre, J.N. Chapman, J.P. Jamet, V. Mathet and C. Chappert. Modification of Co/Pt multilayers by gallium irradiation - Part 1: The effect on structural and magnetic properties. *Journal of Applied Physics* **90**, 3843 (2001).

[156] C. Rettner, S. Anders, J.E.E. Baglin, T. Thomson and B.D. Terris. Characterization of the magnetic modification of Co/Pt multilayer films by He^+, Ar^+, and Ga^+ ion irradiation. *Applied Physics Letters* **80**, 279 (2002).

[157] A. Maziewski, P. Mazalski, Z. Kurant, M.O. Liedke, J. McCord, J. Fassbender, J. Ferre, A. Mougin, A. Wawro, L.T. Baczewski, A. Rogalev, F. Wilhelm and T. Gemming. Tailoring of magnetism in Pt/Co/Pt ultrathin films by ion irradiation. *Physical Review B* **85**, 054427 (2012).

[158] D. Weller, J.E.E. Baglin, A.J. Kellock, K.A. Hannibal, M.F. Toney, G. Kusinski, S. Lang, L. Folks, M.E. Best and B.D. Terris. Ion induced magnetization reorientation in Co/Pt multilayers for patterned media. *Journal of Applied Physics* **87**, 5768 (2000).

[159] K. Zhang, K.P. Lieb, V. Milinovic, M. Uhrmacher and S. Klaumünzer. Interface mixing and magnetism in Ni/Si bilayers irradiated with swift and low-energy heavy ions. *Nuclear Instruments and Methods in Physics Research B* **249**, 167 (2006).

[160] B.W. Corb. Magnetic moments and coordination symmetry in bcc Fe-M alloys. *Physical Review B* **31**, 2521 (1985).

[161] J. Fassbender, A. Mucklich, K. Potzger and W. Möller. Mixing and subsequent amorphization of ultrathin $Ni_{81}Fe_{19}$/Ta bilayers by 30keV Ni implantation. *Nuclear Instruments and Methods in Physics Research B* **248**, 343 (2006).

[162] Q. Leng, H. Han, M. Mao, C. Hiner and F. Ryan. Magnetic dead layers in NiFe/Ta and NiFe/Si/diamond-like carbon films. *Journal of Applied Physics* **87**, 6621 (2000).

[163] R. Grossinger, R.S. Turtelli and N. Mehmood. Magnetostriction of Fe-X (X = Al, Ga, Si, Ge) inter-metallic alloys. *IEEE Transactions on Magnetics* **44**, 3001 (2008).

[164] R.C. Hall. Single crystal anisotropy and magnetostriction constants of several ferromagnetic materials including alloys of NiFe, SiFe, AlFe, CoNi, and CoFe. *Journal of Applied Physics* **30**, 816 (1959).

[165] G. Xiong, D.A. Allwood, M.D. Cooke and R.P. Cowburn. Magnetic nanoelements for magnetoelectronics made by focused-ion-beam milling. *Applied Physics Letters* **79**, 3461 (2001).

[166] J. Gierak, A. Madouri, A.L. Biance, E. Bourhis, G. Patriarche, C. Ulysse, D. Lucot, X. Lafosse, L. Auvray, L. Bruchhaus and R. Jede. Sub-5nm FIB direct patterning of nanodevices. *Microelectronic Engineering* **84**, 779 (2007).

[167] J. Orloff. High-resolution focused ion beams. *Review of Scientific Instruments* **64**, 1105 (1993).

[168] L.W. Swanson. Liquid metal ion sources: Mechanism and applications. *Nuclear Instruments and Methods in Physics Research* **218**, 347 (1983).

[169] G. Taylor. Disintegration of water drops in an electric field. *Proceedings of the Royal Society of London* **280**, 383 (1964).

[170] Helios NanoLab 600i. Technical report FEI.

[171] Schottky Field Emission Electron Source. Technical Report 503 FEI.

[172] D. Gehriger. Private communications.

[173] O. Wilhelmi, S. Reyntjens, C. Mitterbauer, L. Roussel, D.J. Stokes and D.H.W. Hubert. Rapid prototyping of nanostructured materials with a focused ion beam. *Japanese Journal of Applied Physics* **47**, 5010 (2008).

[174] E. Hecht. *Optics*. Addison Wesley San Francisco (2002).

[175] J. Als-Nielsen and D. McMorrow. *Elements of modern x-ray physics*. Wiley (2001).

[176] L.G. Parratt. Surface studies of solids. *Physical Review* **95**, 359 (1954).

[177] H. Kiessig. Untersuchungen zur totalreflexion von röntgenstrahlen. *Annalen der Physik* **402**, 715 (1931).

[178] L. Névot and P. Croce. Caractérisation des surfaces par réflexion rasante de rayons X. Application à l'étude du polissage de quelques verres silicates. *Revue de Physique Appliquée* **15**, 761 (1980).

[179] K. Bowen and B.K. Tanner. *X-ray metrology in semicondictor manufacturing*. Taylor & Francis (2006).

[180] J.B. Kortright. Nonspecular x-ray scattering from multilayer structures. *Journal of Applied Physics* **70**, 3620 (1991).

[181] E.P. Bertin. Principles and practice of x-ray spectrometric analysis. (1975).

[182] M.O. Krause. Atomic radiative and radiationless yields for K and L shells. *Journal of Physical and Chemical Reference Data* **8**, 307 (1979).

[183] D.R. Lide. *CRC handbook of chemistry and physics*. The Chemical Rubber Company (1969).

[184] S.I. Salem, S.L. Panossian and R.A. Krause. Experimental K and L relative x-ray emission rates. *Atomic Data and Nuclear Data Tables* **14**, 91 (1974).

[185] M.O. Krause. Natural widths of atomic K and L levels, Ka X-ray lines and several KLL Auger lines. *Journal of Physical and Chemical Reference Data* **8**, 329 (1979).

[186] D.K.G. De Boer. Glancing-incidence x-ray fluorescence of layered materials. *Physical Review B* **44**, 498 (1991).

[187] M. Birkholz. *Thin film analysis by x-ray scattering*. Wiley (2006).

[188] M.G. Samant, J. Stöhr, S.S.P. Parkin, G.A. Held, B.D. Hermsmeier, F. Herman, M. Van Schilfgaarde, L.C. Duda, D.C. Mancini, N. Wassdahl and Others. Induced spin polarization in Cu spacer layers in Co/Cu multilayers. *Physical review letters* **72**, 1112 (1994).

[189] J.L. Erskine and E.A. Stern. Calculation of the M23 magneto-optical absorption spectrum of ferromagnetic nickel. *Physical Review B* **12**, 5016 (1975).

[190] G. Schütz, W. Wagner, W. Wilhelm and P. Kienle. Absorption of circularly polarized x rays in iron. *Physical review letters* **58**, 737 (1987).

[191] C.T. Chen, Y.U. Idzerda, H.J. Lin and N.V. Smith. Experimental confirmation of the x-ray magnetic circular dichroism sum rules for iron and cobalt. *Physical review letters* **75**, 152 (1995).

[192] C. Kapusta, P. Fischer and G. Schütz. Magnetic x-ray absorption spectroscopy. *Journal of Alloys and Compounds* **286**, 37 (1999).

[193] J. Stöhr. X-ray magnetic circular dichroism spectroscopy of transition metal thin films. *Journal of Electron Spectroscopy and Eelated Phenomena* **75**, 253 (1995).

[194] R.P. Feynman, R.B. Leighton and M. Sands. *The Feynman lectures on physics.* Addison Wesley Reading (1964).

[195] C-C. Kao, C.T. Chen, E.D. Johnson, J.B. Hastings, H.J. Lin, G.H. Ho, G. Meigs, J-M. Brot, S.L. Hulbert, Y.U. Idzerda and C. Vettier. Dichroic interference effects in circularly polarized soft-x-ray resonant magnetic scattering. *Physical Review B* **50**, 9599 (1994).

[196] W.L. O'Brien and B.P. Tonner. Orbital and spin sum rules in x-ray magnetic circular dichroism. *Physical Review B* **50**, 12672 (1994).

[197] P. Carra, B.T. Thole, M. Altarelli and X. Wang. X-ray circular dichroism and local magnetic fields. *Physical review letters* **70**, 694 (1993).

[198] B.T. Thole, P. Carra, F. Sette and G. van der Laan. X-ray circular dichroism as a probe of orbital magnetization. *Physical review letters* **68**, 1943 (1992).

[199] J.P. Hannon, G.T. Trammell, M. Blume and D. Gibbs. X-ray resonance exchange scattering. *Physical review letters* **61**, 1245 (1988).

[200] D. Gibbs, D.R. Harshman, E.D. Isaacs, D.B. McWhan, D. Mills and C. Vettier. Polarization and resonance properties of magnetic x-ray scattering in holmium. *Physical Review Letters* **61**, 1241 (1988).

[201] J.M. Tonnerre, L. Seve, D. Raoux and G. Soullié. Soft x-ray resonant magnetic scattering from a magnetically coupled Ag/Ni multilayer. *Physical Review Letters* **75**, 740 (1995).

[202] C-C. Kao, J.B. Hastings and E.D. Johnson. Magnetic-resonance exchange scattering at the iron L_{II} and L_{III} edges. *Physical Review Letters* **65**, 373 (1990).

[203] M. Faraday. On the magnetization of light and the illumination of magnetic lines of force. *Philosophical Transactions of the Royal Society of London A* **136**, 1 (1846).

[204] J. Kerr. On rotation of the plane of polarization by reflection from the pole of a magnet. *Philosophical Magazine* **3**, 321 (1877).

[205] J. Kerr. On reflection of polarized light from the equatorial surface of a magnet. *Philosophical Magazine* **5**, 161 (1878).

[206] J. Zak, E. R. Moog, C. Liu and S.D. Bader. Fundamental magneto-optics. *Journal of Applied Physics* **68**, 4203 (1990).

[207] J.A.C. Bland and M.J. Padgett. An intensity-stabilised He-Ne laser for measuring small magneto-optic Kerr rotations from thin ferromagnetic films. *Journal of Physics E: Scientific Instruments* **22**, 308 (1989).

[208] R.P. Cowburn, D.K. Koltsov, A.O. Adeyeye and M.E. Welland. Probing submicron nanomagnets by magneto-optics. *Applied Physics Letters* **73**, 3947 (1998).

[209] W. Webb. Superconducting quantum magnetometers. *IEEE Transactions on Magnetics* **8**, 51 (1972).

[210] B.S. Deaver and W.M. Fairbank. Experimental evidence for quantized flux in superconducting cylinders. *Physical Review Letters* **7**, 43 (1961).

[211] J. Clarke. Principles and applications of SQUIDs. *Proceedings of the IEEE* **77**, 1208 (1989).

[212] J.C. Gallop. *SQUIDs, the Josephson effects and superconducting electronics.* IOP Publishing (1991).

[213] B.D. Josephson. The discovery of tunnelling supercurrents. *Reviews of Modern Physics* **46**, 251 (1974).

[214] A.H. Silver and J.E. Zimmerman. Quantum states and transitions in weakly connected superconducting rings. *Physical Review* **43**, 317 (1967).

[215] R.P. Giffard, R.A. Webb and J.C. Wheatley. Principles and methods of low-frequency electric and magnetic measurements using an rf-biased point-contact superconducting device. *Journal of Low Temperature Physics* **6**, 533 (1972).

[216] MPMS-XL. Technical report Quantum Designs.

[217] J.O. Oti. SimulMag: Micromagnetic simulation software (1997).

[218] W. Scholz. Magpar: Parallel finite element micromagnetics package (2009).

[219] T. Fischbacher, M. Franchin, G. Bordignon and H. Fangohr. A Systematic Approach to Multiphysics Extensions of Finite-Element-Based Micromagnetic Simulations: Nmag. *IEEE Transactions on Magnetics* **43**, 2896 (2007).

[220] T. Tsukamoto, Y. Kanai, K. Koyama, K. Yoshida, Y. Uehara, K. Shimizu, S. Greaves and H. Muraoka. Micromagnetic simulation of recording write heads a comparison of various micromagnetic software. *IEEE Transactions on Magnetics* **48**, 311 (2012).

[221] M.J. Donahue and D.G. Porter. Object Oriented Micro-Magnetic Framework (OOMMF) (2002).

[222] OOMMF user's guide (release 1.2a3). Technical report (2002).

[223] M.J. Donahue and R.D. McMichael. Micromagnetics on curved geometries using rectangular cells: Error correction and analysis. *IEEE Transactions on Magnetics* **43**, 2878 (2007).

[224] A. Kunz. Simulating the maximum domain wall speed in a magnetic nanowire. *IEEE Transactions on Magnetics* **42**, 3219 (2006).

[225] K.J. Kirk, J.N. Chapman and C.D.W. Wilkinson. Lorenz microscopy of small magnetic structures (invited). *Journal of Applied Physics* **85**, 5237 (1999).

[226] D.G. Porter. Velocity of transverse domain wall motion along thin, narrow strips. *Journal of Applied Physics* **95**, 6729 (2004).

[227] W. Eckstein. *Computer simulation of ion-solid interactions.* Springer Berlin (1991).

[228] W. Möller and M. Posselt. TRIDYN_FZR user manual. Technical report Institute of ion Beam Physics and Materials Research Dresden, Germany (2002).

[229] J.P. Biersack and L.G. Haggmark. A Monte Carlo computer program for the transport of energetic ions in amorphous targets. *Nuclear Instruments and Methods* **174**, 257 (1980).

[230] W. Möller, W. Eckstein and J.P. Biersack. TRIDYN - binary collision simulation of atomic collisions and dynamic composition changes in solids. *Computer Physics Communications* **51**, 355 (1988).

[231] G. Moliere. Theorie der streuung schneller geladener teilchen I. einzelstreuung am abgeschirmten Coulomb-Feld. *Zeitschrift Naturforschung Teil A* **A2**, 133 (1947).

[232] J.F. Ziegler, J.P. Biersack and M.D. Ziegler. *SRIM - The stopping and range of ions in matter.* SRIM (2008).

[233] J. Lindhard and M. Scharff. Energy dissipation by ions in the keV region. *Physical Review* **124**, 128 (1961).

[234] W. Möller and W. Eckstein. Tridyn - A TRIM simulation code including dynamic composition changes. *Nuclear Instruments and Methods in Physics Research B* **2**, 814 (1984).

[235] J.A. Bearden and A.F. Burr. Reevaluation of x-ray atomic energy levels. *Reviews of Modern Physics* **39**, 125 (1967).

[236] S. Brandt. *Data analysis*. Springer New York (1999).

[237] Summary of BM28 technical data - www.esrf.eu/UsersAndScience/Experiments/CRG/BM28.

[238] M. Wormington, D.K. Bowen and B.K. Tanner. Principles and performance of a PC-based program for simulation of grazing incidence x-ray reflectivity profiles. *MRS Proceedings* **238**, 119 (1991).

[239] M. Wormington. Characterization of structures from x-ray scattering data using genetic algorithms. *Philosophical Transactions of the Royal Society of London A* **357**, 2827 (1999).

[240] D. Petit, C.C. Faulkner, S. Johnstone, D. Wood and R.P. Cowburn. Nanometer scale patterning using focused ion beam milling. *Review of Scientific Instruments* **76**, 026105 (2005).

[241] A. Barna, L. Kotis, J.L. Labar, Z. Osvath, A.L. Toth, M. Menyhard, A. Zalar and P. Panjan. Ion beam mixing by focused ion beam. *Journal of Applied Physics* **102**, 053513 (2007).

[242] I.A. Kowalik, G. Ohrwall, B.N. Jensen, R. Sankari, E. Wallén, U. Johansson, O. Karis and D. Arvanitis. Description of the new I1011 beamline for magnetic measurements using synchrotron radiation at MAX-lab. *Journal of Physics: Conference Series* **211**, 012030 (2010).

[243] L. Bouchenoire, S.D. Brown, P Thompson, J.A. Duffy, J.W. Taylor and M.J. Cooper. Performance of phase plates on the XMaS beamline at the ESRF. *Journal of Synchrotron Radiation* **10**, 172 (2003).

[244] D.A. Allwood, G. Xiong, M.D. Cooke and R.P. Cowburn. Magneto-optical Kerr effect analysis of magnetic nanostructures. *Journal of Physics D: Applied Physics* **36**, 2175 (2003).

[245] E. Arac, D.M. Burn, D.S. Eastwood, T.P.A. Hase and D. Atkinson. Study of focused-ion-beaminduced structural and compositional modifications in nanoscale bilayer systems by combined grazing incidence x ray reflectivity and fluorescence. *Journal of Applied Physics* **111**, 044324 (2012).

[246] Y. Lee. X-Ray fluorescence and reflectivity analysis of multiple-layer thin films. *Analytical Sciences* **11**, 529 (1995).

[247] S. Kim, Y.L. Soo, G. Kioseoglou, Y.H. Kao, K. Ramanathan and S.K. Deb. Compositional intermixing at CdS/Cu(In,Ga)Se$_2$ rough interface studied by x-ray fluorescence. *Journal of Applied Physics* **91**, 6416 (2002).

[248] J. Buchanan, T.P.A. Hase, B.K. Tanner, P. Chen, L. Gan, C. Powell and W.F. Egelhoff. Anomalously large intermixing in aluminumtransition-metal bilayers. *Physical Review B* **66**, 104427 (2002).

[249] M.G. Le Boite, A. Traverse, L. Nevot, B. Pardo and J. Corno. Grazing x-ray reflectometry and Rutherford backscattering: Two complementary techniques for the study of thin film mixing. *Nuclear Instruments and Methods in Physics Research B* **29**, 653 (1988).

[250] T. Weber and K.P. Lieb. Ion irradiation induced atomic transport and phase formation in the system nickelaluminum. *Journal of Applied Physics* **73**, 3499 (1993).

[251] P. Bø rgesen, D.A. Lilienfeld and H. Msaad. Low-temperature ion beam mixing of medium-Z metals. *Nuclear Instruments and Methods in Physics Research B* **59**, 563 (1991).

[252] T. Regan, H. Ohldag, C. Stamm, F. Nolting, J. Lüning, J. Stöhr and R. White. Chemical effects at metal/oxide interfaces studied by x-ray-absorption spectroscopy. *Physical Review B* **64**, 214422 (2001).

[253] R. Gupta, K.P. Lieb, Y. Luo, G.A. Müller, P. Schaaf and K. Zhang. Argon and krypton ion-induced changes in permalloy thin films. *The European Physical Journal B* **63**, 501 (2008).

[254] A.T. Aldred. Magnetization of iron-gallium and iron-arsenic alloys. *Journal of Applied Physics* **37**, 1344 (1966).

[255] N. Jaouen, F. Wilhelm, A. Rogalev, J.M. Tonnerre, T.K. Johal and G. van der Laan. Ag- and W-induced magnetic moment in 3d multilayer. *IEEE Transactions on Magnetics* **41**, 3334 (2005).

[256] R.E. Parra and J.W. Cable. Neutron study of magnetic-moment distribution in Ni-Pt alloys. *Physical Review B* **21**, 5494 (1980).

[257] P. Poulopoulos, F. Wilhelm, H. Wende, G. Ceballos, K. Baberschke, D. Benea, H. Ebert, M. Angelakeris, N.K. Flevaris, A. Rogalev and N.B. Brookes. X-ray magnetic circular dichroic magnetometry on Ni/Pt multilayers. *Journal of Applied Physics* **89**, 3874 (2001).

[258] Y.F. Liu, J.W. Cai and L. Sun. Large enhancement of anisotropic magnetoresistance and thermal stability in Ta/NiFe/Ta trilayers with interfacial Pt addition. *Applied Physics Letters* **96**, 092509 (2010).

[259] N. Moghadam, G.M. Stocks, M. Kowalewski and W.H. Butler. Effects of Ta on the magnetic structure of permalloy. *Journal of Applied Physics* **89**, 6886 (2001).

[260] K. Mitsuoka, H. Miyajima, H. Ino and S. Chikazumi. Induced magnetic moment in ferromagnetic Fe alloys by tetragonally elongated lattice expansion. *Journal of the Physical Society of Japan* **53**, 2381 (1984).

[261] R. Ray and R. Hasegawa. Rapidly quenched metastable ironboron solid solutions. *Solid State Communications* **27**, 471 (1978).

[262] S. Mirbt, I.A. Abrikosov, B. Johansson and H.L. Skriver. Magnetic properties of Fe embedded in V and Cr: Thin films and dilute alloys. *Physical Review B* **55**, 67 (1997).

[263] A. Scherz, H. Wende, P. Poulopoulos, J. Lindner, K. Baberschke, P. Blomquist, R. Wäppling, F. Wilhelm and N.B. Brookes. Induced V and reduced Fe moments at the interface of Fe/V(001) superlattices. *Physical Review B* **64**, 180407 (2001).

[264] V.L. Moruzzi, P.M. Marcus, K. Schwarz and P. Mohn. Ferromagnetic phases of bcc and fcc Fe, Co, and Ni. *Physical Review B* **34**, 1784 (1986).

[265] H.S. Nalwa. *Handbook of thin film materials.* Academic Press (2001).

[266] L. Ding, H. Qiu, C. Li, D. Xiang, J. Teng and G. Yu. Control of spin-polarized electron magnetoresistance in Ta/NiFe/Ta films by intercalation of Au. *Journal of Physics D: Applied Physics* **46**, 025002 (2013).

[267] G.Y. Guo and H. Ebert. On the origins of the enhanced magneto-optical Kerr effect in ultrathin Fe and Co multilayers. *Journal of Magnetism and Magnetic Materials* **156**, 173 (1996).

[268] L. Uba, S. Uba, V. Antonov, A. Yaresko, T. Ślzak and J. Korecki. Magneto-optical anisotropy study of Fe_n/Au_n superlattices. *Physical Review B* **62**, 13731 (2000).

[269] N. Jaouen, F. Wilhelm, A. Rogalev, J. Goulon, L. Ortega, J.M. Tonnerre and A. Yaresko. Electronic and magnetic interfacial states of Ag in an $Ni_{81}Fe_{19}$/Ag coupled multilayer. *Journal of Physics: Condensed Matter* **20**, 095005 (2008).

[270] F. Wilhelm, P. Poulopoulos, G. Ceballos, H. Wende, K. Baberschke, P. Srivastava, D. Benea, H. Ebert, M. Angelakeris, N.K. Flevaris, D. Niarchos, A. Rogalev and N.B. Brookes. Layer-resolved magnetic moments in Ni/Pt multilayers. *Physical review letters* **85**, 413 (2000).

[271] G.A. Muller, R. Gupta, K.P. Lieb and P. Schaaf. Determination of spin distributions in ion-beam magnetic textured iron films by magnetic orientation Mossbauer spectroscopy. *Applied Physics Letters* **82**, 73 (2003).

[272] K. Zhang, K.P. Lieb, G.A. Muller, P. Schaaf, M. Uhrmacher and M. Münzenberg. Magnetic texturing of xenon-ion irradiated nickel films. *The European Physical Journal B* **42**, 193 (2004).

[273] P. Zhang and T. Sham. X-ray studies of the structure and electronic behavior of alkanethiolate-capped gold nanoparticles: The interplay of size and surface effects. *Physical Review Letters* **90**, 245502 (2003).

[274] E.R. Lewis, D. Petit, L. O'Brien, A-V. Jausovec, H.T. Zeng, D.E. Read and R.P. Cowburn. Kinetic depinning of a magnetic domain wall above the Walker field. *Applied Physics Letters* **98**, 042502 (2011).

[275] J. Ieda, H. Sugishita and S. Maekawa. Current-induced domain wall motion in magnetic nanowires with spatial variation. *Journal of Magnetism and Magnetic Materials* **322**, 1363 (2010).

[276] H.G. Piao, J.H. Shim, S.H. Lee, D. Djuhana, S-K. Oh, S-C. Yu and D-H. Kim. Domain wall propagation in wavy ferromagnetic nanowire. *IEEE Transactions on Magnetics* **45**, 3926 (2009).

[277] H.G. Piao, J.H. Shim and D. Djuhana. Micromagnetic simulation of damped sscillatory behavior of domain wall propagation in sinusoidal ferromagnetic nanowire. *IEEE Transactions on Magnetics* **46**, 224 (2010).

[278] D. Ravelosona, F. Cayssol, J. Wunderlich, H.W. Schumacher, C. Chappert, V. Mathet, J. Ferre and J.P. Jamet. Dynamics of magnetization reversal in a mesoscopic wire. *Journal of Magnetism and Magnetic Materials* **249**, 170 (2002).

[279] J. Wunderlich, D. Ravelosona, C. Chappert, F. Cayssol, V. Mathet, J. Ferre, J.P. Jamet and A. Thiaville. Influence of geometry on domain wall propagation in a mesoscopic wire. *IEEE Transactions on Magnetics* **37**, 2104 (2001).

[280] F. Cayssol, D. Ravelosona, C. Chappert, J. Ferre and J.P. Jamet. Domain wall creep in magnetic wires. *Physical Review Letters* **92**, 107202 (2004).

[281] S. Glathe, R. Mattheis and D.V. Berkov. Direct observation and control of the Walker breakdown process during a field driven domain wall motion. *Applied Physics Letters* **93**, 072508 (2008).

[282] S-M. Seo, H-W. Lee, H. Kohno and K.J. Lee. Magnetic vortex wall motion driven by spin waves. *Applied Physics Letters* **98**, 012514 (2011).

[283] Y. Le Maho, J-V. Kim and G. Tatara. Spin-wave contributions to current-induced domain wall dynamics. *Physical Review B* **79**, 174404 (2009).

[284] X.S. Wang, P. Yan, Y.H. Shen, G.E.W. Bauer and X.R. Wang. Domain wall propagation through spin wave emission. *Physical Review Letters* **109**, 167209 (2012).

[285] R. Wieser, E.Y. Vedmedenko and R. Wiesendanger. Domain wall motion damped by the emission of spin waves. *Physical Review B* **81**, 024405 (2010).

[286] D. Bouzidi and H. Suhl. Motion of a Bloch domain wall. *Physical Review Letters* **65**, 2587 (1990).